Plasmas dans l'eau et aux interfaces

Ilya Marinov

UNIVERSITÉ PARIS SUD

Comprendre le monde, construire l'avenir®

LPP

UNIVERSITE PARIS-SUD

ÉCOLE DOCTORALE : Ondes et Matière
Laboratoire de Physique des Plasmas
DISCIPLINE Physique

THÈSE DE DOCTORAT

soutenue le 02/12/2013

par

Ilya MARINOV

Plasmas dans l'eau et aux interfaces

Directeur de thèse :	Antoine ROUSSEAU	Directeur de Recherche (CNRS-LPP)
Co-directrice de thèse :	Svetlana Starikovskaia	Directeur de Recherche (CNRS-LPP)
Composition du jury :		
Président du jury :	Catherine KRAFFT	Professeur (Paris Sud)
Rapporteurs :	Jean-Michel POUVESLE	Directeur de Recherche (CNRS-GREMI)
	Peter BRUGGEMAN	Professeur Associé (University of Minnesota)
Examinateurs :	Corinne DUPUY	Directeur de Recherche (CNRS-IGR)
	Thierry BELMONTE	Directeur de Recherche (CNRS-IJL)

ACKNOWLEDGEMENTS

This work would not have been possible without the contribution, guidance and support of dozens of people.

First and foremost I wish to thank my research advisor Dr. Antoine Rousseau for giving me the opportunity to do my PhD work on this fascinating subject. I am grateful to Antoine for his motivation, encouragement, patience and continuous scientific and emotional support.

I would like to express my deepest and sincere gratitude to my co-advisor Dr. Svetlana Starikovskaia who was guiding me during the three years of my PhD. I'm indebted to Svetlana for her great research experience and academic skills that allowed me to learn a lot and overcome the difficulties. The confidence Svetlana accorded to me during my PhD and, particularly, during the hard time of writing of this thesis is invaluable.

I gratefully acknowledge my thesis referees, Dr. Jean-Michel Pouvesle and Dr. Peter Bruggeman, and examiners Prof. Catherine Krafft, Dr. Corinne Dupuy and Dr. Thierry Belmonte for interesting discussions, their instructive criticism and explicit comments that allowed me to improve my work.

I am most grateful to Dr. Corinne Dupuy who afforded me with a chance to work in her team, for her valuable suggestions and personal attention. I am also thankful to Aurore Simon-Carré and Amélie Boichard for their help which is difficult to overestimate.

I gratefully acknowledge Dr. Anne Janin and Dr. Arnaud Duval for their expertise and implication.

I am sincerely thankful to Dr. Andrei Starikovskii and Dr. Mikhail Shneider for my unforgettable stay in Princeton University and fruitful discussions.

I wish to thank Dr. Leonid Arantchouk for his immense knowledge and everything I learned from him.

I thank everyone from Cold Plasma team, all PhD and undergraduate students for enriching discussions and memorable time we spent together in the lab and during the conferences. I wish to thank my entire laboratory, all research, technical and administrative staff for their everyday help and support.

I would like to thank my lovely family, my parents for their heart-warming care, my sister for her encouragement and my brother without whom I would have never finished this work.

CONTENTS

1 Introduction

1.1 Context of the thesis

In this thesis two main subjects have been investigated i) physics of initiation of electrical discharge in liquid medium and ii) application of cold atmospheric air plasma for treatment of living cells.

Plasma in liquids

Historically the early research on electrical breakdown of liquids followed two distinct purposes: the prevention of sparking in liquid isolators and production of thermal plasma for underwater welding and generation of strong shock waves. Experimental studies were mainly focused on formation of conductive channel in the discharge gap filled with liquid, while the initiation and prebreakdown phenomena were almost inaccessible with the experimental facilities of that time (Naugolnykh and Roy 1974). Later, electrical discharges in water were considered as a efficient source of active radical and non radical species, i.e. H_2O_2, OH, $^1O_2$, O_3 etc., for waste water treatment and removal of organic contaminants (Malik *et al* 2001).

Nowadays discharges in liquids are seen far beyond the traditional interest associated with environmental applications for water treatment and electrical insulation. The discharges in liquids are extensively studied for chemical, biotechnology and medical applications. The number of new applications increases gradually ranging from chemical synthesis (Hamdan *et al* 2013), refining of oils (Geiger and Staack 2012) and medical use for ablation of tissues (Stalder and Woloszko 2007).

However the physics underlying the complex phenomena of electric discharge formation is not fully understood. It is reported on extreme conditions in underwater discharge channels including elevated pressures, temperature and electron densities (An *et al* 2007) which makes them related with some astrophysical objects, like chromospheres

of cold stars (Cram and Mullan 1985). Let us note a creation of European working group for plasma in liquids, that is probably the best illustration of the continuous interest in this field.

Biomedical applications of plasma

The first attempt to use the therapeutic properties of electrical discharges in the ambient air has been done already in the end of 19th century using a self-induction coil transformer (Tesla coil) under the name of 'Violet Ray' (Weltmann *et al* 2012), however it is only in 1970s that the first patent for plasma based sterilization has been issued (Menashi 1968). Later on the first plasma coagulator has been introduced (Morrison 1977). It is not earlier than 2003 that the pioneering work on plasma treatment of living eukaryote cells has been done by Stoffels and coworkers (Stoffels *et al* 2003). Since that time numerous beneficial applications have been proposed and first encouraging results are now being reported. Among the most notable examples of plasma use in bio-medicine are dentistry (Yu *et al* 2012), dermatology (Heinlin *et al* 2011), plasma assisted hemostasis (Fridman *et al* 2008) and oncology (Kim *et al* 2011).

Over the last ten years application of cold plasma for biomedical purposes has developed from a subdivision of the traditional plasma chemistry into an independent multidisciplinary field. The best example of fast growing interest in plasma-medicine is the exponential increase in number of participants of a specialized biennial International conference on plasma medicine (ICPM) that has been held for already 4 times since its first issue in 2007. The most important international conferences on plasma physics have now sections and workshops entirely devoted to plasma biomedical applications. New laboratories and even entire institutions have been created over last several years in which specialists in plasma science and electrical engineers work together with biologists and medical doctors. In France since 2010 a GDR ABioPlas consolidates the efforts of numerous groups working in vast field of biomedical applications of plasmas.

1.2 Organization of the work

Study of nanosecond discharge in liquids in LPP

The first part of this thesis considers formation and properties of gaseous discharge channels produced in liquid dielectrics under HV pulse. This subject has been brought in the Laboratory of Plasma Physics (LPP) with a PhD Thesis of Paul Ceccato under supervision of Dr Antoine Rousseau. Paul performed a detailed parametric study of discharge dynamics in water under positive and negative microsecond pulses (Ceccato *et al* 2009). He has also considered the questions related to discharge initiation, however due to slowly rising voltage and difficulty of synchronization the first nanoseconds of discharge propagation were inaccessible. At the beginning of my thesis, we have developed a discharge device that enables investigation of nanosecond discharges in liquid with synchronization within 1 ns.

Biomedical applications of cold atmospheric plasma

The research on biomedical applications of plasmas has not existed in LPP before present thesis. Two collaborations have been created with group working on cancer pathophysiology (Hopital St Louis, Inserm UMR-S 728) and group studying the role of reactive oxygen species (ROS) in radiocancerogenesis (IGR, UMR 8200).

First, nanosecond dielectric barrier discharge (DBD) suitable for in-vitro and in-vivo applications was designed, fabricated and characterized.

The first tests on treatment of living cells were conducted with St Louis group under direction of Prof. Anne Janin and Dr Arnaud Duval. Tests have been carried out in vitro on two cell lines (HMEC, Jurkat) and in vivo on nude mice. Influence of plasma was characterized by induction of cell death in the colonies or in the tissues.

The second collaboration was devoted to the study of the mechanisms, namely the role of ROS in plasma action. The work was done under

supervision and with great help of Dr Corinne Dupuy and Dr Aurore Carré. Systematic measurements of plasma produced ROS in the culture medium have been done together with control of cell viability on the normal (HTori) and cancer (1205Lu) cell lines.

Treatment and handling of living cells and mice were undertaken in necessary conditions and in full compliance with rules of safety and ethics.

1.3 Organization of the thesis

This thesis consists of two separate parts considering i) initiation and dynamics of nanosecond discharge in liquids (Chapter 2-4) and ii) mechanisms of cells response to in-vitro and in-vivo plasma treatment (Chapter 5-7).

Chapter 2 gives a present state of knowledge on mechanisms of discharge initiation, describing the dynamics and properties of matter in the discharge channel.

Chapter 3 describes the experimental approach applied for the shadowgraphic and spectroscopic study of nanosecond discharge in liquid. The principle and diagnostics of the DBD for biomedical applications is also provided.

Chapter 4 deals with experimental results obtained on nanosecond discharge in water, ethanol and n-pentane. Several mechanisms of discharge initiation depending on applied positive voltage are discussed. Comparison with existing theoretical models of discharge initiation is provided. Experimental results on shadowgraphic, electrical and spectroscopic diagnostics of the discharge propagation dynamics are reported. Estimates of discharge pressure, temperature and plasma density are provided. Discharge reignition under successive reflected HV pulses is considered.

Chapter 5 provides a review on existing application of cold plasma in biology and medicine with focus on treatment of mammalian cells. The

basic notions of cellular and molecular biology, i.e. organization of a cell, existence of chemical gradients across the cell membrane, cell cycle and death are discussed.

Chapter 6 gives information on protocols and methods used for treatment of living cells and further analysis of ROS production and cell viability.

Chapter 7 provides the main results obtained on treatment of endothelial (HMEC) and circulating (Jurkat) cell lines. Analysis of apoptosis/necrosis induction has been done by means of flowcytometry with two markers AnnexinV (AV) and Propidium iodide (PI). Data on penetration depth profile of plasma applied on nude mice skin is provided. Results of quantitative measurement of hydrogen peroxide production in culture medium exposed to plasma are discussed. Analysis of normal thyroid (HTori) and cancerous melanoma (1205Lu) cells viability as a function of H_2O_2 concentration is given.

General conclusions summarize the main results obtained in this thesis.

2 Electrical discharges in liquid dielectrics

2.1 State of the art

The appearance of fast optical converter cameras and bright flash light sources together with development of fast broad band oscilloscopes made possible the visualization of prebreakdown structures in liquids and study of their dynamics (Farazmand 1961). Using shadowgraphic or schlieren visualization bushy or filamentary low density structures were found to propagate with sub or supersonic velocity depending and nature of liquid, voltage rate, amplitude and polarity and electrode configuration. As a rule, asymmetric electrodes, e.g. point-to-plane or point-to-wire configurations were used to study the effect of voltage polarity. Thus, for pure hydrocarbons and liquefied noble gases it was found that lower voltage amplitude is required for discharge formation on the negatively polarized point electrode comparing to anode initiated discharge.

The breakdown of dielectric fluid can be divided in 4 stages: initiation, propagation of discharge structures, bridging of discharge gap and postdischarge evolution. Historically, the early work focused on the high-current breakdown phase, which was registered by the drop in voltage on the high-voltage electrode and a strong light emission. The dielectric strength has been characterized by the delay time of breakdown with respect to the instant of HV application to the electrodes. Postdischarge evolution of the discharge structures has been studied in order to calculate the pressure at the time of the breakdown. It was done for acousto-mechanical applications, as well as to study the recovery of the dielectric properties in spark gaps with liquid dielectric. In a special case of underwater welding, gas bubbles formed by the decomposition of liquid were trapped in the discharge region by a special dome. It was found that the discharge developing in the gas bubbles gives a weld of a better quality.

As it was shown for water (Gavrilov *et al* 1994) and several nonpolar dielectrics (McKenny and McGrath 1984), pulsed positive discharge occurs in two distinct forms, depending on applied voltage and tip diameter, i.e. nonunifomity of the field. At lower voltages the discharge ignites in a hemispherical or bushy form propagating with subsonic or supersonic velocity depending on nature of dielectric liquid. For higher voltages and very sharp tips, the discharge ignites in a filamentary streamer-like mode, also called tree-like discharge. For microsecond HV pulses, as a rule, positive discharge first ignites in a bush-like form and then transition to filamentary mode occurs at the time scale of 1 μs. The fast filamentary discharge is always supersonic with propagation velocity in the region between 10 and 100 km/s. It is stated that different physical phenomena are responsible for the propagation of bush-like and tree-like modes, however until recently very few was known about initiation phase of these two modes.

2.2 Mechanisms of discharge initiation

By discharge initiation we will understand a formation of conductive phase on the electrode or in its vicinity. The instant of the initiation is strongly dependent on the form of the applied voltage and the electrode configuration. There is some uncertainty in determination of the instant of discharge initiation from transient current and optical registration of primary discharge structures or light emissions. So, for pure liquids under DC voltage it was found that nanosecond current pulses always precede the formation of low density structures on the submicron point cathode (Kattan et al 1989). If the point electrode had a radius of less than 100 nm, the discharge structures were not detected. Discharge produced with nanometer size electrodes in water and water salt solutions (Staack *et al* 2008) showed that the corona discharge was formed directly in liquid while boiling or liquid dissociation has been avoided. This was confirmed by the emission spectra with low

broadened atomic lines of elements of dissolved salts at the absence of atomic lines of hydrogen and oxygen for pulses shorter than 100 ns. For microsecond anode initiated discharge, the conduction current, which depends on the ionic conductivity of the water, precedes the appearance of a bubble, which plays the role of primary phase of the discharge (Ceccato et al 2009). In the case of ultra-short sub-nanosecond pulses and fields exceeding 10^{10} V/m (Starikovskiy *et al* 2011), plasma emission from the discharge was detected already at the leading edge of the HV pulse of 150 ps. It is clear that the experimental study of the mechanisms of discharge initiation requires a simultaneous optical and electrical diagnostic with sub-nanosecond time resolution.

The formation and development of discharge structures precedes the electric breakdown, but in some cases the discharge gap is not bridged, and such a discharge is called partial. Partial discharges are mainly observed for strongly asymmetric electrode configuration as point to plane or wire to plane. In asymmetrical electrode geometries the field decreases hyperbolically with the distance from the electrode and, at a given duration and amplitude of the applied voltage on the electrode, there is a minimal length of the discharge gap, which avoids the breakdown. A spark formation can be avoided by using a sufficiently long discharge gaps or by covering one of the electrodes with a dielectric. It is done in order to reduce the erosion of the point electrodes and to avoid the eventual damage of electrical and optical equipment. Partial discharges are also most commonly used for environmental (Malik *et al* 2001) and medical (Stalder and Woloszko 2007) applications, as more energy- efficient for production of reactive oxygen species (ROS), or when substantial water heating must be avoided. Discharge structures consist of conducting channels or gaseous cavities propagating in liquid. Discharge structures are characterized by their shape and propagation velocity. Among the most important parameters determining the form of the discharge structure are polarity of the electrode, the field distribution in the electrode gap, properties of the fluid, the presence of impurities and dissolved gas, hydrostatic pressure and temperature.

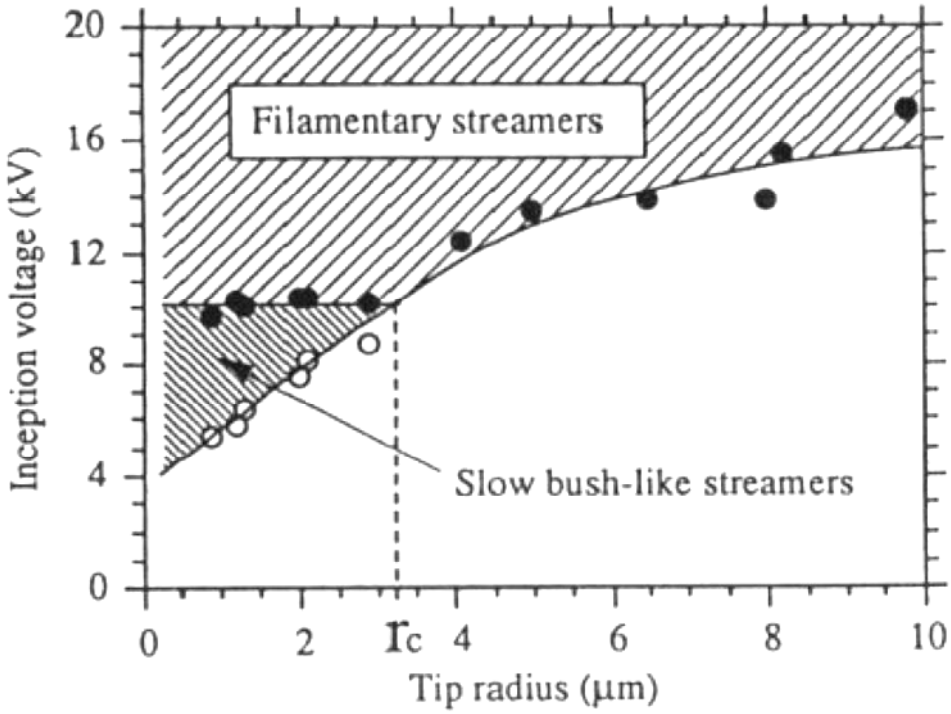

Figure 2.1 Initiation of slow (bush-like) and fast (tree-like) discharge in n-pentane as a function of applied voltage and tip radius. Taken from (Lesaint and Gournay 1994a).

For point electrode of positive polarity structures of two types, namely bush-like and tree-like modes have been observed in various liquid hydrocarbons by applying a high voltage pulse with rising slope of 10 ns. It was found that, for each value of the tip radius, there was a minimum threshold voltage when the filamentary discharge can only be detected (Figure 2.1). Impurities with low ionization potential were found to diminish the threshold voltage, while electron scavengers did not show any influence. For pulses with a longer rising slope, the discharge was initiated first as a bush-like, and then transformed into tree-like discharge. A similar situation was observed in water under microsecond pulses with a rise time of 20 ns (Ceccato *et al* 2009). Thus, the discharge structure of the first type was formed and then it turned, in a few hundred of nanoseconds, into a filamentary discharge of the second type. It is worth noting, that both discharge structures were filamentary: the first discharge mode demonstrated a fan-like structure with numerous channels of equal length and the second mode was a tree-like structure showing strong branching of channels. If the rising

front of voltage pulse was about 10 ns, the direct formation of the second type structure was detected (Ushakov *et al* 2007).

The discharge of negative polarity demonstrated a similar bush-like pattern with a rough boundary in number of liquids. For submicron pin electrodes the negative discharge was formed in the form of bubble or series of bubbles. In the case of ultra-high electric fields filamentary negative discharge has been observed. An exhaustive classification of discharge structures depending on polarity and nature of liquid was done in (Beroual *et al* 1998).

2.3 Discharge initiation in gaseous bubbles

One of widely accepted models of discharge initiation is based on assumption of a gas discharge in cavity or bubble, formed in the high field region in liquid. The bubble can occur naturally from dissolved gas or under the effect of applied electric field. Another argument for the bubble-based mechanism of discharge initiation is also supported by the damage of very sharp pin electrodes observed in inert liquids at prebreakdown fields when only emission/ionization current occurs. It is suggested that sputtering due to the bombardment by ions, accelerated inside the bubble, and cavitation process itself can be an important issue leading to tip erosion (Halpern and Gomer 1969). The possible mechanisms of bubble formation and their role in the discharge initiation will be discussed below.

For micron size bubble filled with air at atmospheric pressure and placed in the electric field of 10^7 V/m, the time delay to partial discharge formation inside the bubble is of the order of nanosecond or less (Ushakov *et al* 2007). The current, necessary to sustain the avalanche, can be as low as 10^{-10} A. As one can see, the direct observation of partial discharge in the bubble is a technically demanding task and a number of works were searching for indirect evidence of bubble mechanism. For example, it was shown that

degassing, hydrostatic pressure and viscosity of liquid increase the time lag to discharge initiation (Ushakov *et al* 2007).

Once the avalanche occurs inside the bubble, the electric field decreases due to the charge deposition on the interface between the bubble and the liquid (Gournay and Lesaint 1993). Consequently, voltage across the bubble drops below Paschen minimum and discharge extinguishes. The time necessary to remove adsorbed charges is determined by diffusion of charges through the bulk liquid and by the solvation rate. It is assumed that charges, adsorbed on the bubble wall, are predominately ions, while electrons can penetrate deeper in the liquid where they are rapidly solvated over ~ 1 ps, in the case of water. Successive discharge occurs when the voltage across the bubble recovers to the breakdown value. The total number of partial discharges in the bubble is determined by the duration of the applied field and the rate of diffusion of the charges in the fluid. After each successive breakdown, the bubble size increases due to release of Joule energy as well as the action of the Coulomb and electrostrictive forces.

If we assume that the relaxation time of the surface charge is higher than the formation of the breakdown, the bubble can be approximated by a dielectric sphere with a charged surface. Then, in the field close to a uniform, Coulomb force acting on the bubble surface may be presented in the form of additional pressure (Ushakov *et al* 2007):

$$\Delta P_e \approx \frac{3\varepsilon_0(\varepsilon-1)\varepsilon E^2}{2(2\varepsilon+1)} \qquad (2.1)$$

Coulomb forces act in the direction of electric field, inducing bubble deformation into prolate spheroid. The deformed bubble is normally not symmetrical and has higher curvature on the side closer to the cathode under uniform field conditions (Beroual 1992). Image forces and redistribution of the surface charges in the external field are thought to be the reason for bubble asymmetry. Field strengthening at the tip, formed in the process of bubble elongation, can provide the electric field amplitude exceeding the breakdown threshold. It was demonstrated (Garton and Krasucki 1964), that if the ratio of dielectric permittivity

of the bubble and that of liquid $\varepsilon_b/\varepsilon_l \geq 20$, which is valid mainly for conducting bubbles or drops of highly polar liquids, there is a critical value of bubble elongation. Therefore, if the ratio of major and minor axis of elongated conducting bubble exceeds 1.85, the bubble becomes instable and elongates until the bridging of the gap occurs or bubble disruption at the sharp extremities. Figure 2.2 shows the instability development during elongation of water droplet in silicon oil leading to breakdown. It is suggested that even for bubble as small as 100 nm in diameter, the instability can occur under the field of 10^8 V/m. For charged nanobubble in low viscous liquid, the instability can develop on the nanosecond time scale.

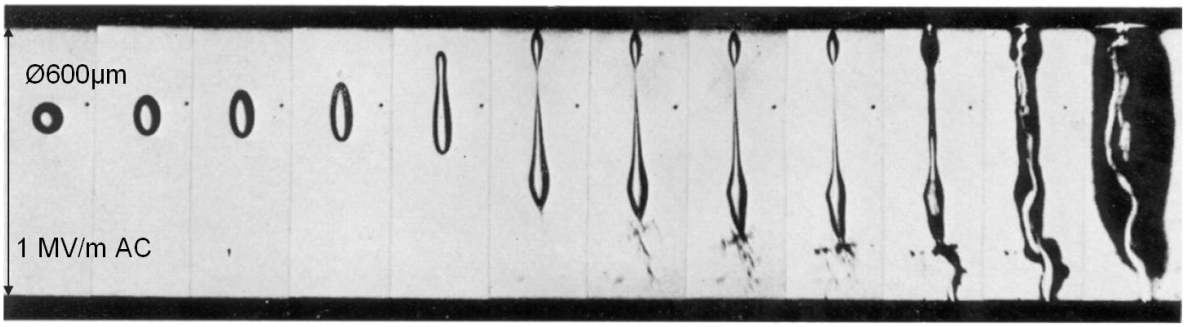

Figure 2.2 Breakdown in silicon oil due to instability development of water droplet under AC electric field of 1 MV/m. Taken from (Garton and Krasucki 1964).

As it was shown by Korobeinikov with coworkers (Korobeinikov *et al* 2002), bubbles of 40 – 100 µm, artificially produced on the electrode surface, can play a role of initiation site for positive and negative discharge in water. It was found that at maximal field amplitude of $8 \cdot 10^7$ V/m with rising time of 0.2 µs both cathode and anode bubbles elongated in the direction of the electric field. Anode bubbles were found to contract along transverse axis, and the total time of deformations was of the order of 500 ns after application of high voltage pulse. Then, bubble isotropically increased in size and supersonic streamers forming a fan-shaped structure emerged from the most remote point on bubble surface at about 1 µs (Figure 2.3, a). Ignition of positive streamers was accompanied by emission of spherical shock waves with the origin at the surface of initial bubble. Negative discharge developed from the extremity of deformed bubble in a bush-

like form with subsonic velocity below 400 m/s (Figure 2.3, b). For cathode bubbles the ionization processes manifested already 0.25 µs after application of voltage pulse as could be seen from bubble elongation with simultaneous increase of its transverse diameter (Figure 2.3, b).

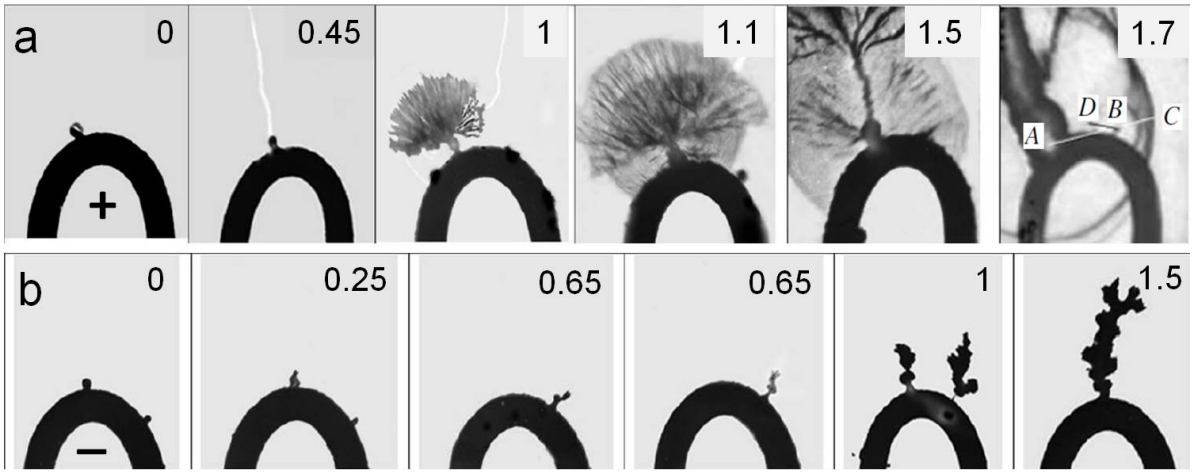

Figure 2.3 Initiation of a) positive and b) negative discharge with the aid of artificially produced bubbles. Time is given in microseconds and corresponds to delay with respect to application of HV pulse. Modified from (Korobeinikov *et al* 2002).

In order to explain the polarity effect, the authors assumed that for cathode bubbles the electron injection can produce avalanches in the bubble at the field below the peak amplitude over the rising slope of voltage pulse. The charges, being adsorbed on the bubble surface, experience the action of Coulomb force resulting in bubble expansion. The field inside the bubble is attenuated by the surface charges which prevent avalanche development and breakdown. The pressure inside the cathode structure is believed to be close to atmospheric pressure. As for anode bubbles, electron detachment from negative ions is seen as the main source of seeding electrons. However the density of negative ions adsorbed from the bulk liquid on the bubble surface is rather low and bubble elongates due to the dielectrophoretic force till the field strengthening inside the bubble would allow avalanche to streamer transition. In the case when no bubbles were produced beforehand on the electrode, the delay of breakdown of anode initiated discharge increased by several microseconds, whereas discharge structures

demonstrated the similar patterns. The propagation dynamics of positive and negative discharges will be discussed in details in the following section.

In cyclohexane electron injection from the cathode was suggested to explain initiation of the negative discharge, supported by Trichel-like current signal (Kattan *et al* 1989). The initiation of negative discharge is characterized by a very steep dependence on applied voltage with well defined threshold value of voltage amplitude. The initiation current of negative discharge was found to be insensitive on hydrostatic pressure up to 10 MPa (Dumitrescu *et al* 2001). It is believed that electrons in sufficiently high electric field are able to gain enough energy for evaporation of a small volume of liquid, leading to electron avalanche in the gaseous phase. Expulsion of the electric field from the conductive cavity acting as electrode extension ensures successive propagation of the discharge. Anode initiated discharge, investigated in the same work, demonstrated smoother dependence of initiation probability on applied voltage. Also inhibition of positive discharge initiation at high pressure and absence of transient current have been observed as opposed to negative discharge.

2.4 Bubble formation in liquid prior to discharge ignition

2.4.1 Existence of stable micro bubbles formed from dissolved gas

All liquids exposed to atmospheric conditions contain dissolved gases whereas solubility of each component mainly depends on nature of liquid, alkaline admixtures and temperature. The existence of stable nanometre scale bubbles, also called bubstons, was predicted theoretically (Bunkin and Bunkin 1992) and was demonstrated experimentally for the case of non-degassed water (Vallee *et al* 2005, Bunkin *et al* 2009). Authors suggested, to explain the bubble stabilization, a selective adsorption of the same sign ions in non-degassed water. It was shown that bubstons can be found even at very low ionic concentration of 10^{15} cm^{-3}. It is stated that autodissociation of water and dissolved carbon dioxide giving HCO_3^- ion can provide such

ionic concentration in deionized water (Vallee *et al* 2005). The charging of bubble surface by ion adsorption allows equilibrating of the pressure due to the surface tension by the negative electrostatic pressure of Coulomb repulsion:

$$\frac{2\sigma}{R} = \frac{Q^2}{8\pi\varepsilon R^4} \qquad 2.\ 2$$

Consequently, the pressure inside the charge bubble is of the order of hydrostatic pressure in liquid. Bubstons are stable and can withstand even double distillation of water. Spontaneous coagulation of bubstons leads to formation of 1 – 1.5 μm size clusters at the density of about 10^6 cm^{-3} as detected by optical and interference microscopy (Figure 2.4, a-b). The number of bubston clusters was found to increase with ionic concentration and basic pH.

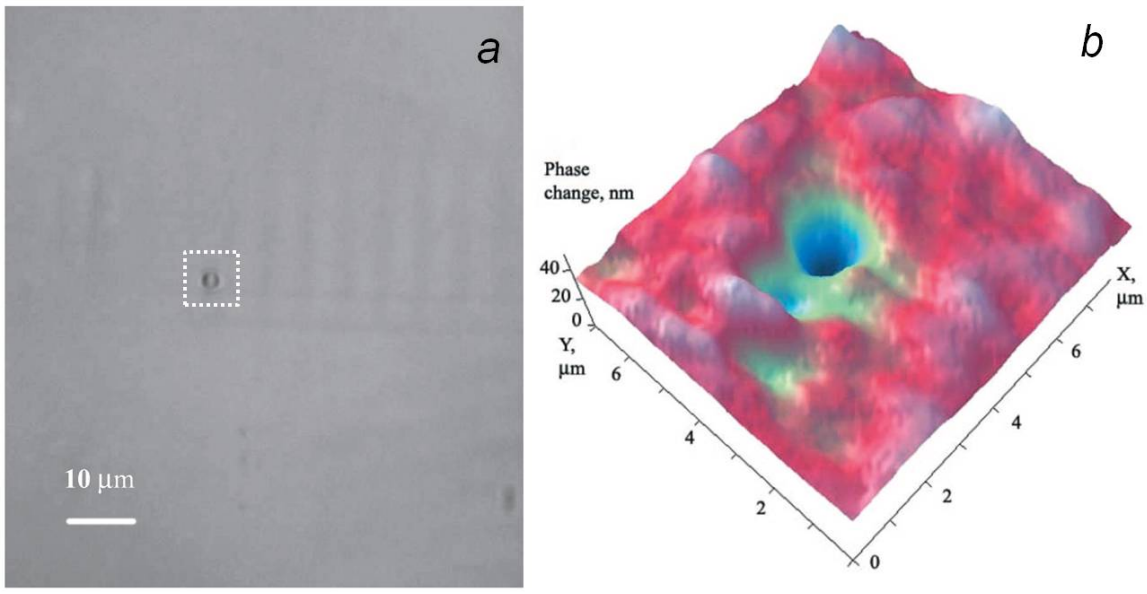

Figure 2.4 a) Micrograph demonstrating spontaneous formation of a micrometer scale particle in double distilled and filtered non deionized water. b) Interferogram corresponding to the zone highlighted on the optical image demonstrating optical density distribution. Taken from (Bunkin *et al* 2009).

Under conditions of nanosecond laser breakdown in water clusters of mechanically stabilized bubbles can play a role of seed centers of breakdown initiation (Bunkin and Bakum 2006). It is suggested that

electron oscillating in the electric field of laser pulse may inside a 10 – 20 nm bubston may gain enough energy for ionization of water molecules on the bubble surface. The development of electron avalanche induces evaporation of interfaces between individual bubstons and formation of microscopic gas bubble.

2.4.2 Gaseous traps on the electrode surface

Generally, even carefully polished electrodes or electrodes produced by electrochemical etching present microscopic and smaller asperities and cavities. Depending on wettability of the electrode surface under study, gaseous bubbles may eventually form at the roughnesses (Figure 2.5). The gas inside the microcavities is typically air at atmospheric pressure that could remain after the electrode was set in contact with ambient air or come from dissolved gas in liquid or electrode material. To give an example, tap water contains about 0.05 cm^3/g of dissolved air at atmospheric pressure and stainless steel contains about 1 mm^3/g of air at normal conditions (Ushakov *et al* 2007).

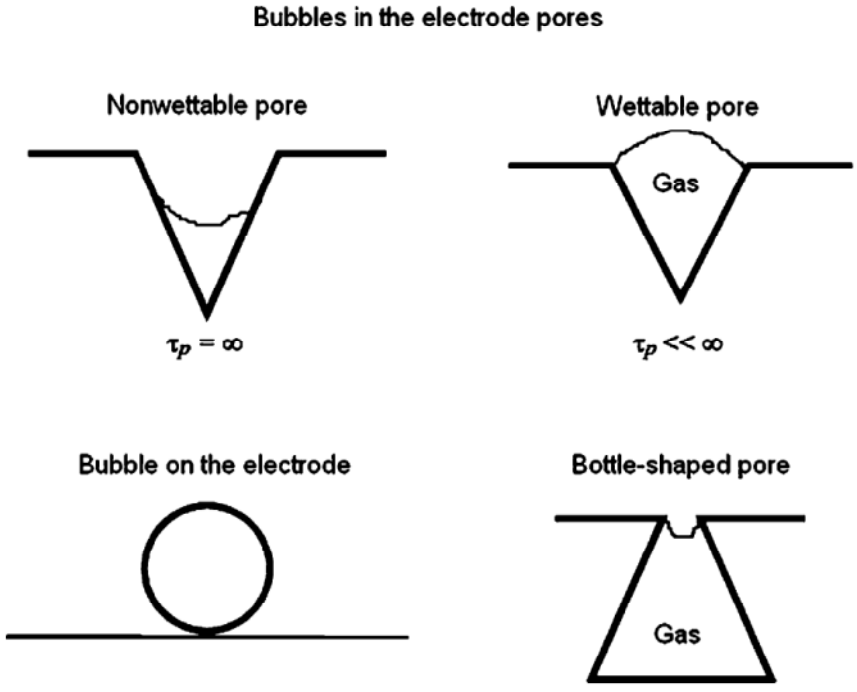

Figure 2.5 Formation of gaseous cavities on electrode surface roughnesses. Taken from (Ushakov *et al* 2007)

2.4.3 Bubble nucleation by ionization/emission currents

Electrons produced by emission from the cathode or in the process of autoionization in the anode vicinity can acquire energy in the inter-molecular spacing sufficient to excite vibrational modes of molecules of the liquid. Taking water as an example, the average distance between water molecules is equal to $4 \cdot 10^{-10}$ m and assuming maximal field strength of 10^9 V/m, we obtain for the energy gain by an electron the value of about 0.4 eV (~3200 cm^{-1}) which is comparable with vibrational energy in a bulk water (3200 – 3500 cm^{-1}, ~1600 cm^{-1}). Hence, the energy transfer between electrons and vibrational degrees of freedom of water molecules is rather probable under given electric field. Then, the vibrational energy is rapidly converted into heat during collisions between the molecules. Consequently, local heating in highly non-uniform fields due to the emission/ionization current may induce homogeneous nucleation of bubble. Temperature increase in the tip vicinity can be found from the current flux (Halpern and Gomer 1969):

$$\Delta T = iF_t r_t / 8\pi\kappa r^2 (r - r_t), \qquad (2.3)$$

where F_t – field at the tip, r_t – tip radius, k – thermal conductivity. The solution for steady-state heat transfer suggests that the maximal temperature increase (ΔT_{max}) should be at the distance equal to $2r_t$.The time required to reach ΔT_{max} can be found by equating the energy input rate to the temperature rise (Halpern and Gomer 1969):

$$\Delta\tau = \left(2C_p r_t^2 \rho\right)/\kappa \qquad (2.4)$$

In the superheated liquid the bubble nucleation occurs with the probability defined by a volumetric nucleation frequency:

$$J = N\left[exp\left(-\frac{\lambda}{kT}\right)\right]\left(\frac{2\sigma}{\pi m}\right)^{1/2} exp\left(\frac{16\pi\sigma^3}{3kT(P_v - P)}\right), \qquad (2.5)$$

where N is the number of molecules per unit volume, is the vaporization heat, is the surface tension, m is the mass of molecule of liquid, P_v is the saturated vapor pressure at T, P is the external pressure.

2.4.4 Proton hopping (Grotthuss mechanism)

In the case of water it is known that protons have anomalously elevated mobility as compared to other ions. Thus, at the absence of external field proton diffuse almost 7 times faster than Na^+. In fact, proton tunneling through the water molecules occurs via hydrogen bonds. Under the electric field of the order of 10^9 V/m the hydrogen bonds along the field axis are considerably strengthened while hydrogen bonds orthogonal to the field become weaker (Vegiri 2004). Therefore, electric current induced by proton hopping can play an important role under the electric fields typical for the discharge formation in water.

2.4.5 Auger process

Auger process is very well known for gases and solids and consists in nonradioactive energy transfer and electron emission by producing a vacancy in the atomic inner shell or valence band. It was proposed for liquids by Lewis (Lewis 2003) in order to explain production of seed charges required for avalanche ignition at both cathode and anode. For biased electrode being cathode the proposed scenario is following. Under strong electric field in the double layer free positive ions reach the cathode surface. Positive ions attached to the cathode have the energy level below Fermi energy of metal electrode. Resonance tunneling can occur between valence band and positive ion acting as a hole (Figure 2.6, a). Energy released in electronic transition from about Fermi level to vacancy is nonradiatively transferred to another electron. Hot electron with energy above Fermi level is injected to the liquid.

In the case of positively polarized electrode, electrons from negative ions and electrons with energy level above Fermi energy can tunnel to the conduction band (Figure 2.6, b). Relaxation of the electron to Fermi lever liberates energy enough to excite another electron from valence band. Finally a hole is formed in liquid by tunneling of electron to the vacancy.

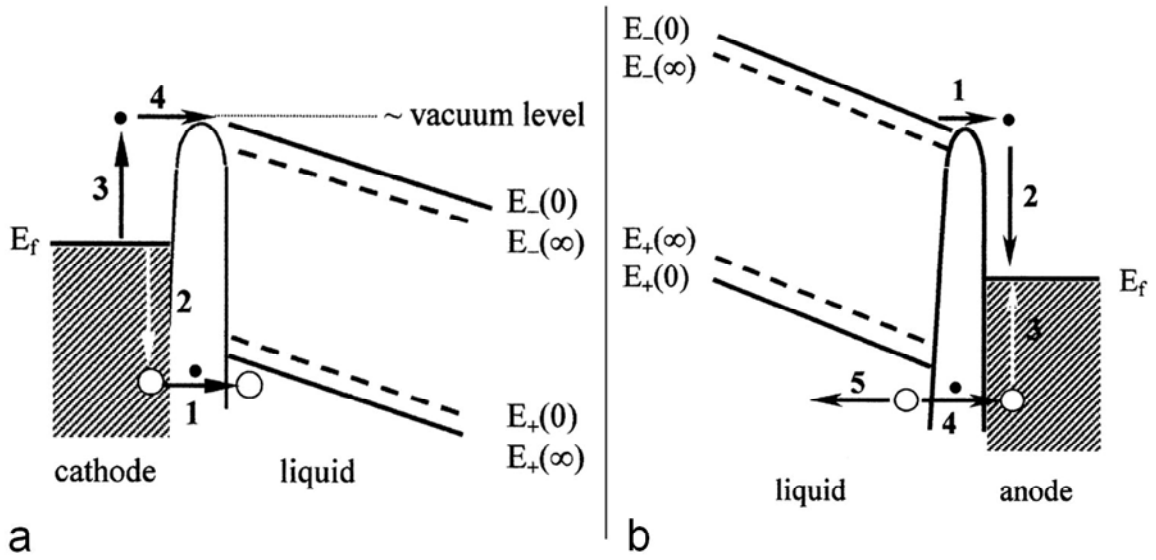

Figure 2.6 a) Generation of Auger electron from the cathode by neutralization of positive ion b) Generation of positive hole in Auger process of neutralization of negative ion or electron. Taken from (Lewis 2003)

2.4.6 Lippmann effect

An ion naturally present in liquid can form a chemical bond with electrode surface due to the difference between Fermi level and energy level in ion. Polar molecules can also be adsorbed on the metal surface by image force. Thus, the interface between liquid and metal consists of double charged layer of opposite sign, also called electric double layer. As a rule, in the double layer the substance with higher dielectric permittivity has a positive charge. Consequently, at the electrode/liquid interface liquid would have net negative charge, while for liquid/gas boundary liquid would be charged positively. Double layer consists of dense Helmholtz layer formed by adsorbed ions and molecules and diffuse (Gouy-Chapman) layer extending in the bulk liquid and screening the space charge of double layer.

It is worth noting the importance of electrode polarity on formation of double layer. For biased anode more negative ions are attracted and adsorbed on the electrode surface strengthening the double layer (Figure 2.7, a). On the contrary, for cathode negative ions are repulsed while net positive charge is increased with applied voltage. From mentioned above it directly follows that if a short pulsed voltage is

applied to the anode the interfacial tension would decrease until the liquid layer lost the cohesion. For cathode the effect would be opposite at low voltages and after the change of double layer sign the interfacial tension would drop.

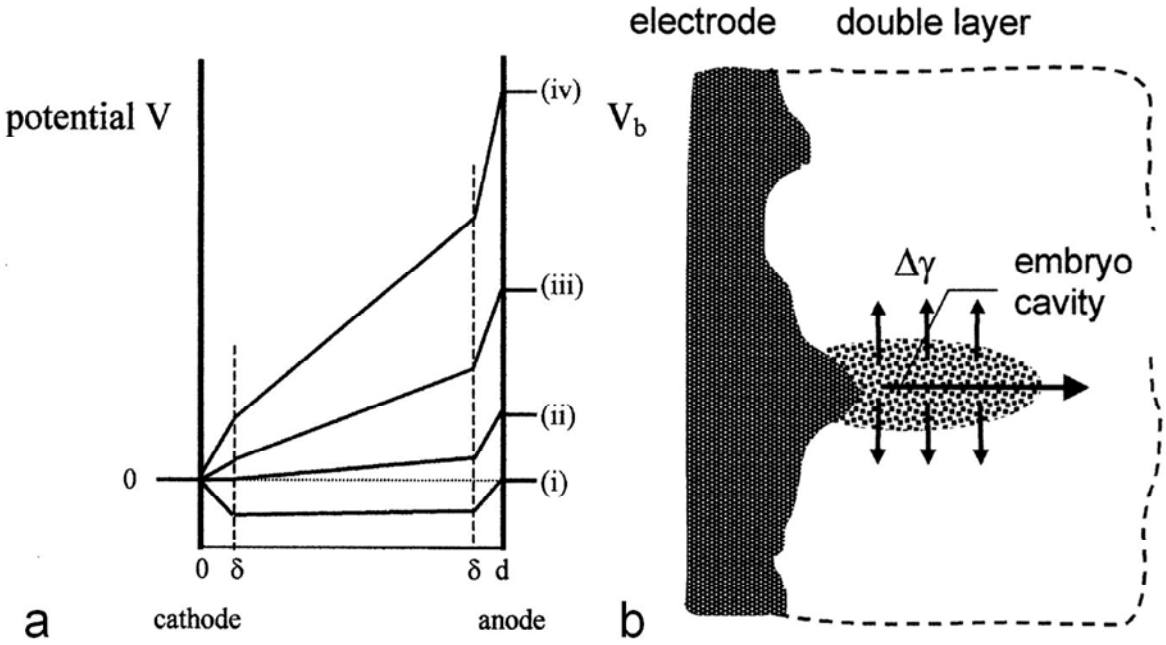

Figure 2.7 a)Distribution of potential between cathode and anode for bias increasing from i) U=0 to iv) U=Vb. b) Lost of cohesion by liquid in double layer and cavity formation under nonuniform electric field. Taken from (Lewis 2003)

Under highly nonuniform electric field at the sharp point electrode the reduction of interfacial tension and loss of cohesion lead to formation of a low density cavity (Figure 2.7, b). The evolution of the cavity is defined by competition between screening of local field by improved ion flux inside the low density region and instability development of charged interface.

2.4.7 Bubble cavitation induced by electrostrictive force

Recently Shneider and coworkers (Shneider *et al* 2012, Shneider and Pekker 2013b) stated that, at initial stage of the discharge development, for polar liquids in highly nonuniform fields, the pressure gradient due to electrostriction effect can be an important issue in streamer formation mechanism. The force acting on unit volume of

dielectric liquid placed in nonuniform electric field is given by Helmholtz equation (Ushakov *et al* 2007)

$$\vec{F} = e\delta n\vec{E} + \frac{\varepsilon_0}{2}E^2\nabla\varepsilon + \frac{\varepsilon_0}{2}\nabla\left(E^2\rho\frac{\partial\varepsilon}{\partial\rho}\right) \qquad (2.6)$$

where the first term corresponds to force acting on free charges, the second term arises in the case of inhomogeneous dielectric and the third term describes the force acting in the nonuniform electric field. For prebreakdown conditions (before discharge ignition) the first two terms can be neglected. Fast reorganization of electrical dipoles in nonuniform field leads to strong electrostriction effect. The size of area R where the rupture of liquid may occur has a typical size of the order of the tip radius and is given by (Shneider *et al* 2012)

$$R \approx r_0\left(\varepsilon_0\varepsilon\frac{V^2}{P_c r_0^2}\right)^{1/4} = 7\times10^{-5}r_0^{1/2}V^{1/2}, \qquad (2.7)$$

where $\mathrm{r_0}$ is the radius of the tip, V is the applied voltage and $\mathrm{P_c}$ is the critical pressure corresponding to rupture of liquid and cavitation induction which is about 30 MPa in case of fast stretching of water (Herbert *et al* 2006). The negative pressure arising from stretching of dielectric in nonuniform electric field by ponderomotive forces can be found using (Shneider and Pekker 2013b)

$$p_e = -0.5\alpha\varepsilon_0\varepsilon E^2, \qquad (2.8)$$

where α is empirical constant relying density variation with change in dielectric constant of polar dielectric $\left(\alpha = \frac{\rho}{\varepsilon}\frac{\partial\varepsilon}{\partial\rho}\right)$. In the case of water α equals 1.5 (Ushakov *et al* 2007).

In the discontinuities of liquid, cavitation of dissolved gas can take place while the electrons can accelerate to values exceeding the ionization energy of water (9 eV). Just few recent experimental works (Starikovskiy 2013, Dobrynin *et al* 2013) considered electrostriction mechanism to be relevant for discharge initiation in dielectric liquids.

2.5 Mechanisms of discharge propagation

2.5.1 Lipmann effect

As it was discussed above, the loss of cohesion between liquid and electrode surface under nonuniform electric field may lead to void formation in the double electric layer. It was proposed to extend this mechanism based on Lippmann effect to the bulk liquid (Lewis 1998). At each point the electric field creates a stress E^2 acting orthogonally to the field direction. As a result, the cohesiveness between molecules of liquid decreases along the field lines. It is suggested that sub-microscopic holes can be formed in liquid under the electric fields typical for discharge initiation in dielectric liquid (10^8 – 10^9 V/m). The holes in this case are seen as molecular size voids stochastically appearing in the liquid volume. At some critical holes density, available mechanical energy can satisfy the Griffith criterion inducing crack formation (Figure 2.8a). The time of crack formation is obviously depends on liquid bulk modulus and surface energy that, in the general case, are unknown functions of electric field and can be considerably decreased in the presence of nano-voids. Although, the lack of experimental data on the change in mechanical properties of liquid under electric stress prevents numerical analysis of the problem, the authors estimate that the effect can play a role in discharge propagation on the nanosecond time scale. Note, that the crack propagation is only determined by the field distribution and the generation rate of holes, while formation of the conductive plasma in the crack is not necessary for this model. However, simple estimation shows that energy gain by an electron over crack length of 10^{-8} m can achieve 10 eV which is sufficient for impact ionization of liquid molecules. Therefore, avalanche development become possible in the crack. Proposed mechanism depends on E^2 and hence should be relevant for both anode and cathode initiated discharges.

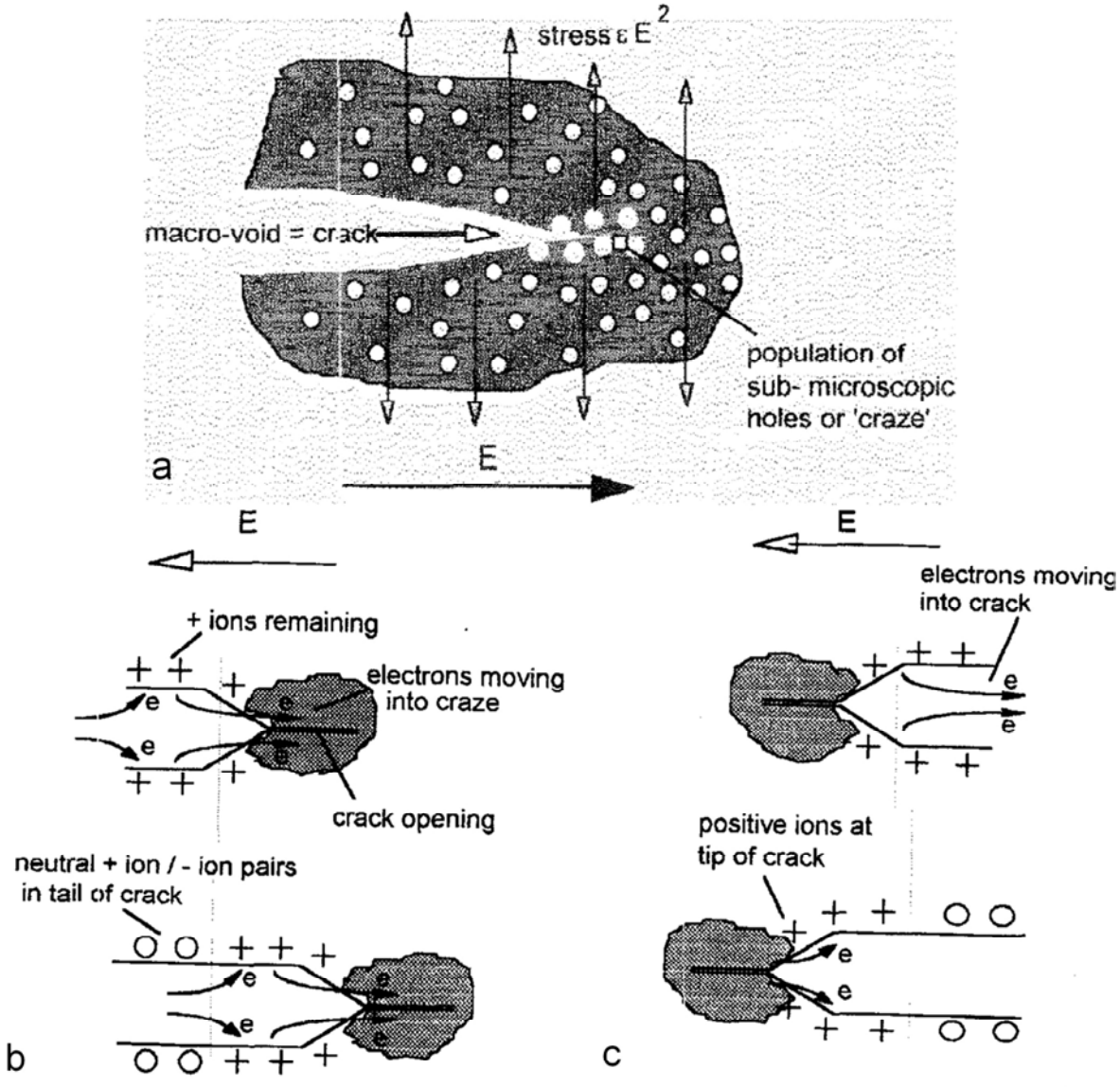

Figure 2.8 a) Generation of sub-micron voids and crack development under E2 stress, Crack guided propagation of b) positive and negative discharge. Taken from (Lewis 1998).

2.5.2 Negative discharge modes

Slow negative discharges are subsonic and characterized by step-wise propagation, associated with current spikes of several tens of nanoseconds. The average velocity of the discharge varies between tens to hundreds of meter per second. Additives with high electron affinity, like CCl_4, were shown to considerably increase up to several times the propagation velocity of the negative discharge (Beroual 1993).

Propagation of slow negative discharge could be almost inhibited by hydrostatic pressure of several MPa, in contrast to the initiation phase which, as we have seen above, is insensitive to hydrostatic pressure. It is stated that the negative discharge propagates by hydrodynamic expansion of gaseous cavity, formed by electronic avalanche in liquid. The delay between two successive steps of the discharge propagation is determined by time necessary to remove the negative charge, screening the applied field, from the interface. It explains the role of electron scavengers that are able to increase the average velocity reducing the time interval between consecutive avalanches (Devins *et al* 1981). Electrohydrodynamic (EHD) instability of the charged interface can explain the bushy morphology of slow negative discharge (Watson and Chadband 1988).

2.5.3 Slow positive discharge

Slow positive discharge in liquid hydrocarbons has similar bushy structure and Trichel–like current waveform with nanosecond current spikes as in slow negative mode (Gournay and Lesaint 1993). Propagation of slow mode is affected by hydrostatic pressure greater than 3 MPa and the discharge is believed to be confined inside gaseous cavity. However, low values of transient currents and hardly detectable emission indicate that the slow structures are weakly conductive. Slow mode is typically sub-sonic in hydrocarbons while supersonic velocities were found in water (An *et al* 2007). Depending on the duration and the amplitude of applied voltage a transition from slow positive mode to fast filamentary mode can occur (Gavrilov *et al* 1994). In water the transition from slow to fast mode occurs from one of the channels of primary structure, synchronized with current spike (Ceccato *et al* 2009).

2.5.4 Fast positive discharge

Fast positive mode consists of the separate channels. Their number and branching vary, depending on liquid and field distribution in the discharge gap (Lesaint and Jung 2000). The fast positive mode is essentially supersonic with the velocity strongly dependent on applied voltage. Propagation velocity does not change with hydrostatic pressure

at least up to the values of 7 MPa (Lesaint and Gournay 1994b). However, the discharge length and diameter of the channels are reduced at high hydrostatic pressure. Propagation of fast positive mode is associated with continuous transient current, which is correlated with the number of channels. In the case of water, the light emission and the discharge current increase with ionic conductivity, whereas the propagation velocity does not change (Ceccato *et al* 2009). However, it was found that in the case of liquid hydrocarbons and mineral oils, the propagation velocity increases with addition of low ionization potential compounds (Devins *et al* 1981). Propagation of the fast mode in water is step-wise with typical delay of 300 ps between two successive steps (Katsuki *et al* 2006). Each step of the discharge propagation initiates a spherical shock wave. For long gaps transition to leader mode bridging the gap can occur.

2.6 Properties of matter in the discharge channel

2.6.1 From metastable liquid to gas at high pressures

It is suggested that electron avalanche in liquid may bring it to the superheated metastable state that can occasionally turn in vapor. Pressure measurements inside the discharge channel of the fast mode, using optical interferometry, gives the values as high as 10^9 Pa (An *et al* 2007). Estimations of the energy dissipation inside the discharge channel demonstrate that no substantial heating of liquid inside the channel occurs and, hence, the dissociative mechanism of gas formation at high pressure is assumed. High pressure inside the discharge channel at inception explains insensitivity of fast positive mode to hydrostatic pressure. However, the hydrostatic pressure inhibits the expansion of the channel thus limiting the current and preventing initiation of new sections of the discharge channel.

2.6.2 Plasma parameters (ne,Te)

The main source of information on plasma parameters in liquid is nonintrusive optical emission spectroscopy (OES). OES has been

applied to study plasma density and chemical composition inside the discharge channels in a number of liquid dielectric including pure hydrocarbons (Sakamoto and Yamada 1980, Ingebrigtsen *et al* 2008), mineral oils (Bårmann *et al* 1997), liquefied gases (Hernandez-Avila *et al* 1994, Frayssines and Bonifaci 2002) and water (Sunka *et al* 1999, Nieto-Salazar *et al* 2005, Namihira and Sakai 2007, Bruggeman *et al* 2010). Typically emission spectra in visible and near UV region consisted of continuum emission and atomic lines corresponding to the electronically excited levels.

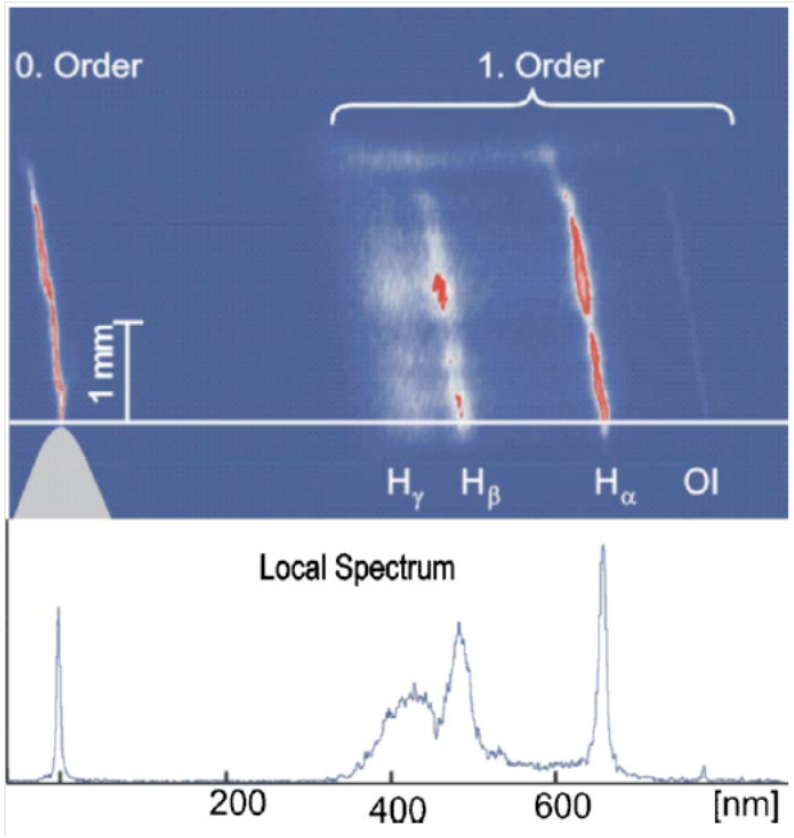

Figure 2.9 Spatially and time resolved OES of tree-like mode in water. Taken from (An *et al* 2007)

Figure 2.9 shows spatially resolved spectrum, emitted by one branch of tree-like discharge produced in water (An *et al* 2007). Horizontally dispersed spectral images of emitting filament were observed in the first diffraction order of the grating with a CCD camera. As one can see, the emission spectrum was dominated by Balmer series of atomic hydrogen and weak emission of the atomic oxygen IO line. The authors reported

that at the discharge ignition continuum emission was observed at the position of Balmer series. Separate line became apparent only several tens of nanoseconds after ignition. Continuum emission was also observed at the initial stage of discharge propagation in n-heptane before Balmer lines and C_2 Swan band became evident (Sakamoto and Yamada 1980). Authors attributed continuum emission to recombination of molecular fragments. In recent study, considering breakdown in water with bubbles, strong continuum emission was observed at the moment of the spark formation. Continuum was ascribed to black-body emission due to the strong Joule heating with typical blackbody temperatures in the range 6000 – 9000 K.

The main species observed from OES in water are atomic hydrogen and oxygen and OH radical. In some cases of saline solutions atomic lines corresponding to the elements constituting dissolved salts are present. For microsecond positive discharge in water it was found that a half width of atomic hydrogen Balmer alpha line was correlated with current signal of the positive discharge (Namihira and Sakai 2007). Emission spectra were registered starting from about 1 µs after discharge ignition over the decay of applied voltage pulse. The authors attributed the broadening to collisional Stark process which directly gives evolution of electronic density inside the discharge channels. It was found that spatially averaged plasma density varied between 10^{18} – 10^{19} cm^{-3} during the applied voltage pulse. Sputtering of the pin electrode made of Cu produced well defined atomic lines in emission spectra. Boltzmann temperature obtained from the atomic spectra of Cu, assuming thermal equilibrium, was found to be as high as 15000 K, although no spark occurred in this case. Spatially resolved measurements along the fast positive streamer in microsecond discharge in water were done in (An *et al* 2007). Similarly, only Stark collision broadening was taken into account. It was found that the electron density decreased from $5 \cdot 10^{19}$ to $2 \cdot 10^{18}$ along the channel from tip to the channel origin.

A two component profile of hydrogen alpha line was observed in positive discharge in transformer oil (Bårmann *et al* 1997) and in

discharge initiated in gaseous bubbles in water (Bruggeman *et al* 2010). In both cases the best fit was obtain as a sum of two Lorentzian profiles which were attributed to Stark broadening in regions with two different plasma densities. The authors proposed a model of the discharge channel with a dense plasma core and a sheath with lower plasma density in which recombination occurs predominantly. It was also shown that assuming Stark effect due to the macroscopic external fields H_α line profile could not reproduced (Bruggeman *et al* 2010).

In (Ingebrigtsen *et al* 2008) spectroscopic analysis of positive and negative microsecond pulsed discharge was performed in a series of chlorinated hydrocarbons. Broadening and red wing asymmetry of time averaged atomic chlorine lines was treated in assumption of simultaneous action of Stark and Van der Waals mechanisms. Deduced gas density inside the discharge channels was about 10% of critical density while degree of ionization varied between 0.1 – 1%. Average gas temperature calculated from C_2 Swan bands was of the order of $2 \cdot 10^3$ – $6 \cdot 10^3$ K.

The attempt to attribute rotational temperature of OH (A-X) band to gas temperature inside the discharge channels was done in several papers (Nieto-Salazar *et al* 2005, An *et al* 2007). The authors obtained 3000 – 5000 K from a comparison between experimental and simulated spectrum. However, as it was shown by Bruggeman with colleagues (Bruggeman *et al* 2009) the rotational temperature of OH band cannot be used as an accurate estimate for the gas temperature, since rotational distribution is influenced by production process, i.e. 'hot' OH radicals can be produced in some recombination process. Hence, the gas temperature calculated from OH band rotational structure seems to be overestimated.

Results presented above, demonstrate that the development of electrical discharge in liquid dielectrics is highly transient process, which implies that plasma density can strongly vary from the moment of discharge inception. Moreover, fast propagation on the nanosecond time scale brings into question the existence of local thermodynamic equilibrium,

although elevated electron and gas densities should induce strong interaction between the particles. In addition the complex discharge morphology induces spatial gradients of gas and plasma density. As it follows from mentioned above time and spatially resolved measurement are necessary for understanding of underlying physical phenomena.

3 Experimental setup

3.1 Nanosecond discharge in liquid dielectrics

The experimental techniques commonly applied for diagnostics of electrical discharges in liquid media are optical shadowgraphy, schlieren visualization, interferometry and broadband electrical measurements. Optical emission spectroscopy (OES) gained an increasing attention over the last years being a nonintrusive tool with a great potential to estimate plasma composition and parameters (n_e, T_e). However, the results obtained from the OES can hardly be used without information on discharge morphology and dynamics. As it was discussed in Chapter 2 electrical breakdown of liquid dielectrics occurs via formation of streamer-like structures propagating at velocities from 10^2 m/s up to 10^5 m/s depending on nature of liquid, electrode polarity and voltage rate. If we consider a fast positive streamer with a propagation velocity of 50 km/s, the simple estimate shows that the streamer covers the distance of 1 mm in just 20 ns, while typical streamer diameter is about 10 µm. It means that detailed information on streamer dynamics may be obtained only if nanosecond time resolution and microscopic spatial resolution are available. From the other hand, when microsecond and longer HV pulses are used to ignite the discharge the delay time prior to fast streamer formation may reach one microsecond whereas the jitter exceeds several tens of nanoseconds. Hence, the synchronization of detecting system with the discharge appearance becomes an important issue. One of possible solutions is to trigger the discharge ignition by HV pulses with a rise time of the order of streamer initiation time, i.e. by using nanosecond HV pulses.

Thus, we decided first to perform shadowgraph imaging of pulsed nanosecond discharge in water and several other dielectric liquids in order to characterize the conditions of the discharge initiation and discharge propagation dynamics. Afterwards, time-resolved

spectroscopic analysis of light emitted by the discharge was done. Figure 3.1 schematically summarizes the experimental approach that was used for time resolved diagnostics of pulsed nanosecond discharge. The setup consisted of generator, producing nanosecond pulses that were applied to the discharge device and electrical and optical diagnostics synchronized in time with HV pulse. Experimental technique was designed to achieve microscopic spatial and nanosecond temporal resolution of shadowgraph visualization synchronized within 1 ns with HV pulse. Below, each part of the experimental setup is discussed in details.

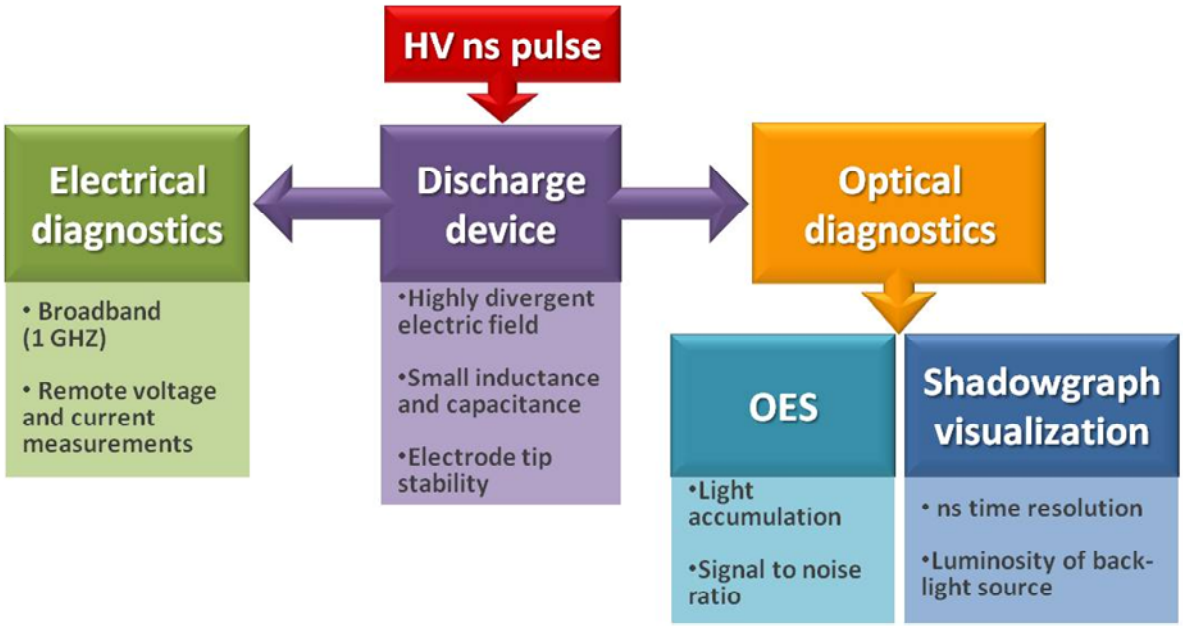

Figure 3.1 Schematic diagram of experimental setup.

3.2 Electrode configuration

Discharge initiation in liquid medium is a stochastic process which may be influenced by the presence of electrode asperities, dust particles or gaseous bubbles. For large spherical electrodes the discharge initiates randomly on the electrode surface and at arbitrary time instants, if low rate pulsed or DC voltage is used. In such non-reproducible conditions the study of discharge ignition and propagation becomes a tricky task. The use of asymmetric point-to-plate or point-to-wire electrode configuration allows producing highly nonuniform electric field at the

tip vicinity. High local Laplacian field enables to localize spatially the discharge initiation point. Depending on discharge configuration, liquid under study and applied voltage, pin electrodes with tip diameter in the range of several microns up to several hundreds of microns can be used. If 100 µm pin can be fabricated by simple mechanical polishing the pins of smaller diameter require special cutting or etching techniques. Being exposed to the extreme conditions of underwater discharge, electrode material should be both high melting and chemically inert. In present study, two point electrodes were used a commercial nickel plated pin with tip diameter of 65 µm and homemade nickel pin with diameter of the tip of 2 µm.

3.3 Production of pin electrodes

Electrochemical etching is the common technique applied to produce sub-micrometer size tips for scanning probe microscopy (STM, AFM). Nickel is known to have better oxidation resistance than widely used tungsten, however the latter shows greater refractoriness. We adopted a technique of Ni pins electrochemical etching developed by Albonetti and co-workers (Albonetti *et al* 2005). Nickel rod biased up to 1 V was inserted in the center of stainless steel ring connected to the negative polarity of a DC voltage source (Figure 3.2, a-b). The inner volume of the ring was filled with a film of 10% (v/v) HCl water solution sustained by surface tension. Etching process is driven by negative Cl^- ions bombarding positively polarized Ni rod (Figure 3.2, d). Consequently, etching profile is determined by Cl^- flux which reaches the maximum in direction orthogonal to pin axis where the electric field is the highest. A small sphere of plasticine of 8 mm in diameter was fixed at the lower end of the Ni rod (Figure 3.2, a). The plasticine ballast served to detach the lower pin when the etching process was completed. Normally, one etching procedure gave two upper and lower conical shape pins (Figure 3.2, c) with 40^o and 20^o apertures respectively. Lower pin had smaller tip diameter of about 2 ± 1 µm and it was used in experiments. Rather thick Ni rod of 1.2 mm in diameter was taken for ease of soldering in discharge device. The overall process of pin etching lasted about an hour.

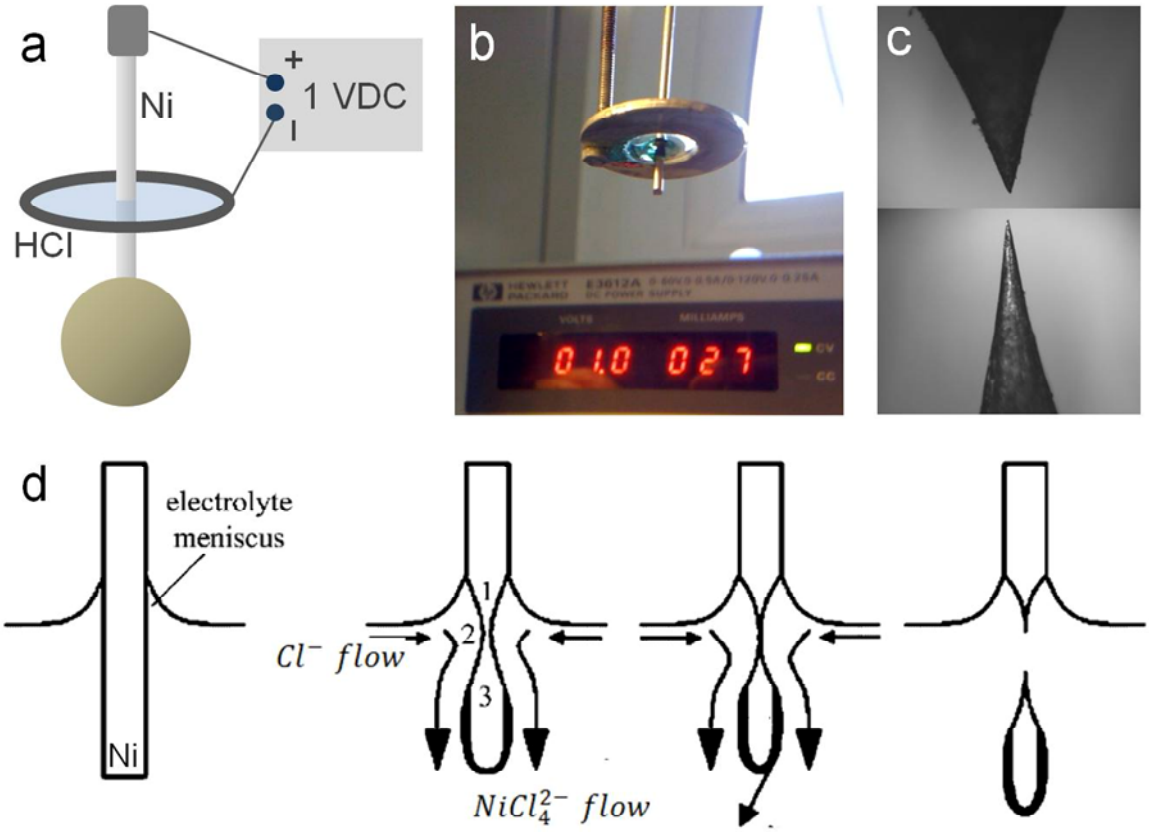

Figure 3.2 a) Schematic Ni pins etching device, b) Photograph of Ni pin etching, c) Micrographs representing upper and lower tips produced in a single etching process, d) Representation of chemical reactions occurring at anode during Ni pin etching in 10% HCl solution (modified from (Tahmasebipour *et al* 2009)*).*

3.4 Discharge device

Discharge device consisted of pin electrode, that was soldered to the core of a 50 Ω coaxial cable (RG213) and U-bent isolated wire soldered to the cable sheath like it is shown in Figure 3.6 . Electrode device was placed in discharge cell filled with the dielectric liquid. The discharge cell was made on the basis of a standard quartz photocolorimetric cuve (KFK) 50x25x40 mm (LxWxH) modified so that the upper cover of the quartz cell served as an electrode system holder. Homemade pin electrode had a parabolic profile with a tip diameter equal to (2 ± 1) µm. The pin was covered with an epoxy resin, leaving about 700 µm from the tip uncoated. Grounded electrode was oriented in such

a way, that its plane was parallel to the windows of cell, providing direct optical access to the discharge. Electrode configuration was close to point-to-wire geometry with the 2 mm minimal distance between the high-voltage pin and the insulation of the grounded. The coaxial geometry of the discharge device enabled to minimize the inductance and capacitance. However, because of small size of the discharge device the direct measurement of discharge voltage on the electrode was almost impossible. Instead, the current of HV pulse was measured in the coaxial cable using back current shunt (BCS) technique.

3.5 Electrical diagnostics of HV nanosecond pulses

Nanosecond pulses were applied through a 50 Ω HV coaxial cable (RG213). Temporal and spatial distribution of voltage and current in a two conductor transmission line are describe by telegraph equations given by (Metzger and Vabre 1969):

$$\frac{\partial^2 V}{\partial x^2} = RGV + (RC + LG)\frac{\partial V}{\partial t} + LC\frac{\partial^2 V}{\partial t^2} \qquad (3.\ 1)$$

$$\frac{\partial^2 I}{\partial x^2} = RGI + (RC + LG)\frac{\partial I}{\partial t} + LC\frac{\partial^2 I}{\partial t^2} \qquad (3.\ 2)$$

where *L, C, R, G* are respectively self-inductance, capacitance, resistance and transverse conductance per unit length. The physical meaning of this system of equations becomes evident assuming lossless line, i.e. zero resistance of the transmission line conductors and zero conductance of isolating material. If *R, G = 0* equations 3.1 and 3.2 become a second order differential equations describing propagation of a planar wave with the velocity $u = 1/\sqrt{LC}$. The solution of Equations 3.1 – 3.2 neglecting the losses can be found as a sum of propagating planar waves:

$$V(x,t) = g\left(x - \frac{t}{\sqrt{LC}}\right) + h\left(x + \frac{t}{\sqrt{LC}}\right) = V_i + V_r \qquad (3.\ 3)$$

$$I(x,t) = \frac{g}{Z}\left(x - \frac{t}{\sqrt{LC}}\right) - \frac{h}{Z}\left(x + \frac{t}{\sqrt{LC}}\right) = \frac{V_i}{Z} - \frac{V_r}{Z} = I_i + I_r \qquad (3.\ 4)$$

where g and h are arbitrary functions. Equation 3.4 is an equivalent of Ohm's law for transmission line relating voltage, current and wave impedance $Z = \sqrt{L/C}$. It worth noting, that the voltage in Equation 3.4 is the potential difference between two conductors of the transmission line and not the voltage drop across one of those conductors. The pairs of functions V_i, I_i and V_r, I_r represent two wave propagating with the same speed but in opposite directions. The second wave can occur in the line as a result of reflection at the load with impedance different from the cable impedance. Amplitude of the reflected wave from the load of impedance Z_l can be found as:

$$V_r = \frac{Z_l - Z_c}{Z_l + Z_c} V_i = \Gamma V_i \qquad (3.5)$$

$$I_r = -\frac{Z_l - Z_c}{Z_l + Z_c} I_i = -\Gamma I_i \qquad (3.6)$$

Hence, in the case of short circuit at one end of the line, e.g. the resistance and inductance of the load is zero, reflection coefficient Γ is equal to minus one. Consequently, in reflected wave the voltage has the same amplitude but inverse polarity, and the current has the same sign as in the incident wave. If we now consider an open end which can be approximated by a very high resistance $R_l \gg R_c$ and negligibly small capacitance the corresponding reflection coefficient Γ would be close to unity. Hence, the current in reflected wave changes the sign while the voltage remains invariable.

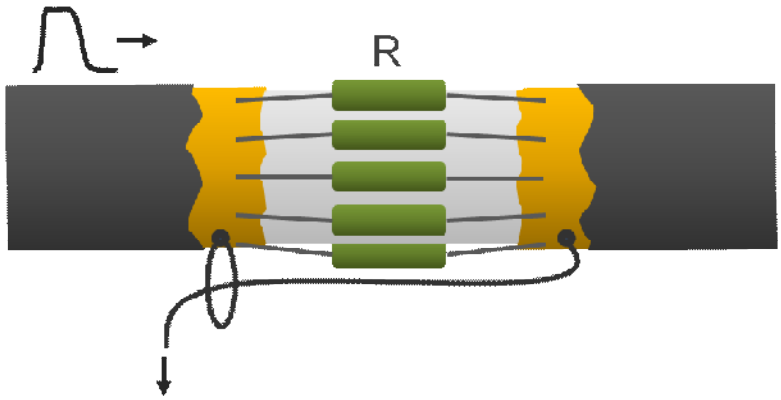

Figure 3.3 Schematic of back current shunt inserted in the sheath of coaxial cable and signal reading.

The current in the inner conductor of the coaxial pair has equal amplitude and inverse direction as compared to the current in the outer conductor sheath. Thereby, the current in the cable can be related to the voltage drop across a small shunt resistance integrated into the sheath of coaxial cable (Figure 3.3). Since the measured current differs in sign from the current of the propagating HV pulse, the divider is called back current shunt (BCS). In order to get a positive shunt signal corresponding to incident pulse of positive polarity, the core of signaling coaxial cable should be connected to far end of the BCS, while cable shielding is soldered to BCS forefront (Figure 3.3). BCS used in our experiments consisted of 13 low-inductance resistances of 2.2 Ω soldered in parallel in the break of cable shield like it is shown in Figure 3.3. In order to know the voltage amplitude in the cable it is necessary to multiply the shunt signal U_s by division coefficient k_s:

$$k_s = Z/R_s \qquad (3.7)$$

where R_s is the shunt resistance. Hence, the pulse energy can be obtained from BCS signal as

$$W = \int \frac{U^2}{Z} dt = \int \frac{U_s^2 Z}{R_s^2} dt \qquad (3.8)$$

In the case of partial discharge, which was the primary subject of the present work, no bridging of discharge gap by conductive streamers occurs and so the impedance of the gap can be considered infinite comparing to 50 Ω wave impedance of coaxial cable. As we have seen above, for HV pulse propagating in the cable, impedance mismatch at the open end induces the current inversion while the voltage polarity remains unchanged. Due to pulse reflection an identical voltage pulse propagates in the opposite direction. At the open end the incident and the reflected voltage pulses are superimposed which means that the voltage amplitude is doubled. For short-circuit or zero impedance conditions at the coaxial line end, the reflected pulse has opposite polarity as compared to incident pulse. If discharge ignites some fraction of pulse energy will be absorbed in plasma and reflected pulse will be smaller than initial one. Therefore, the energy dissipated in

plasma will be equal to the difference between integrated incident and reflected pulses, whereas discharge current will be found from respective incident and reflected currents. BCS allows discharge energy and current measurement at the condition that the incident and the reflected pulses are separated in time and do not superimpose at the shunt position. If the BCS is inserted in the middle of the cable the minimum cable length, necessary to measure separately incident and reflected pulses is given by

$$L = t\frac{c}{\sqrt{\varepsilon}} \qquad (3.9)$$

where t is the pulse duration and is dielectric permittivity of the cable isolating material. For example, in cables with polyethylene isolator (= 2.25) electromagnetic wave covers 1 m in 5 ns.

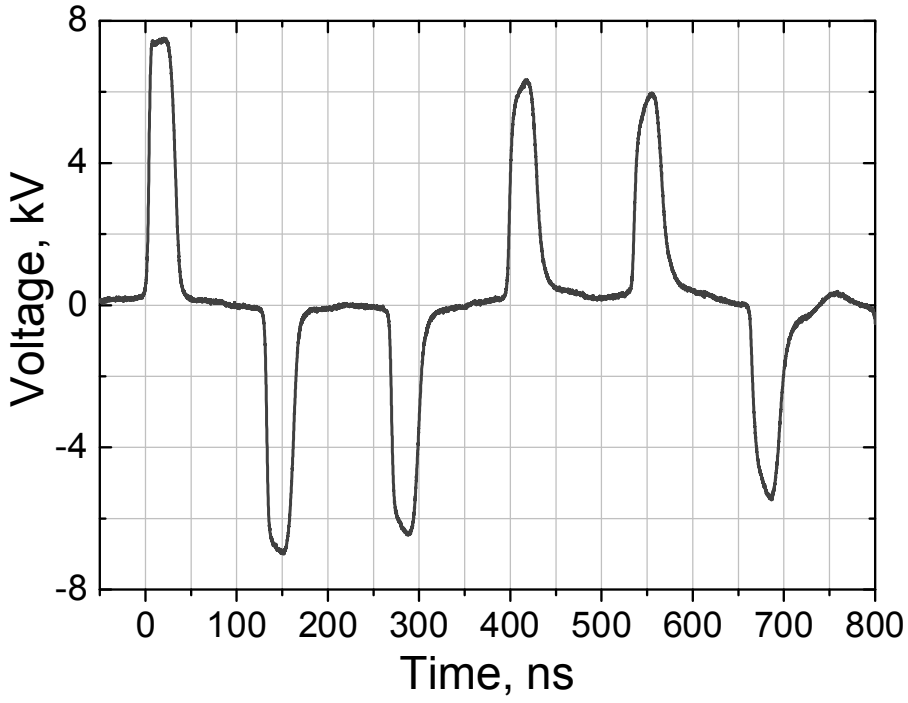

Figure 3.4 Waveform of HV pulses produced by nanosecond generator. BCS was inserted in the middle of 26 m long coaxial cable. Voltage was calculated from BCS signal using shunt division coefficient k_s = 295. Signal was collected on the 50 Ω input of LeCroy WaveSurfer (iX64) 600 MHz oscilloscope through 20 dB 50 Ω attenuator.

Cylindrical geometry of BCS allows minimizing of shunt inductance and thereby improving of bandwidth since the diffusion of magnetic field through the shunt material limits the frequency response. For BCS approximated by hollow cylinder of thickness d, the cut-off rising time τ of measurable signal is given by (Bluhm 2006):

$$\tau = 0.25 \frac{\mu_0 \mu d^2}{\rho}, \qquad (3.10)$$

where ρ and μ are shunt material resistivity and permeability respectively

Generator	Pulse amplitude kV	Rise time ns	Pulse width (FWHM) ns	Repetition rate, Hz
1	1 – 10	4.7	29	1000

Table 3.1 Parameters of three nanosecond generators (FID GmbH). Rise time was measured between 10% and 90% of maximum amplitude. Pulse width corresponds to FWHM of voltage pulse.

We apply a commercial nanosecond generators (FID GmbH) based on solid state switching with 50 Ω output impedance. Characteristic parameters of nanosecond generator are listed in Table 3.1. Custom made calibrated BCS iss applied for current and voltage measurements. Time response of electrical measurements is better than 1 ns and is practically limited by oscilloscope (LeCroy WaveSurfer iX64) bandwidth of 600 MHz. Voltage pulse registered with BCS is presented in Figure 3.4 Voltage amplitude in the cable is calculated from BCS signal multiplied by division coefficient $k_s = 295$. The rising slope of HV pulse is 4.6 ns measured between 10 and 90% of full maxima and amplitude varying from 1 to 10 kV. HV pulse shown in Figure 3.4 of 7.5 kV as measured in the cable results in 15 kV at pin electrode soldered to the open end. Cable length of 26 m induces delay of 130 ns between incident and reflected pulses of the same polarity measured in the center of the cable. As far as the sign of BCS signal depends on the current direction the reflected positive pulse produces negative shunt response as can be seen in Figure 3.4.

3.6 Shadowgraph visualization

The idea of shadowgraphy technique consists in detection of refractive index variation by visualization of deformed plane wave front after passing through a refracting slab Figure 3.5. Refraction of incident parallel beam leads to inhomogeneous deviation of rays in different parts of the beam resulting in certain intensity distribution in the detecting plane. The inhomogeneities with strong changes in refractive index produce well defined dark regions. Intensity variation can be calculated if spatial distribution of refractive index is a known function, from (Hutchinson 2002):

$$\frac{\Delta I_d}{I} = L\left[\frac{d^2}{dx^2} + \frac{d^2}{dy^2}\right]\int N dl \qquad (3.\ 11)$$

where I_d – detected intensity, I – incident beam intensity, L – distance to the detecting plane, x, y – directions orthogonal to the beam axis, N – refractive index. As one can see, the light intensity distribution in the shadowgraph depends on the second spatial derivative of the refractive index in contrast to the schlieren techniques which is sensitive to the first derivative. Consequently the shadowgraphy technique is less sensitive comparing to schlieren visualization, however higher phase shifts can be measured.

Discharges in liquids, as a general rule, are accompanied by phase transition and occurrence of gas cavities. Those low density regions induce large gradients of refraction and, hence, may be detected on the shadowgraph.

Illumination light sources

The choice of back-light source for shadowgraph imaging is an important issue, especially if micron resolution is required. In this case the light source should provide both high intensity and good uniformity. Laser sources have good brightness and produce parallel beams with very low divergence, however it is difficult to apply them for visualization of microscopic objects because of diffraction effects.

Although, one can use decoherent laser beam by passing it through the dye in order to overcome diffraction. Alternative solution would be to use broad spectrum light source based on spark discharge in inert gas (e.g., Ar, Xe, Kr), also called flashlamp. Flashlamps produce short of several microseconds pulses with spectral output expanding from vacuum ultraviolet to far infrared. Flashlamps are characterized by a considerably low jitter and high reproducibility even at operation in single shot regime.

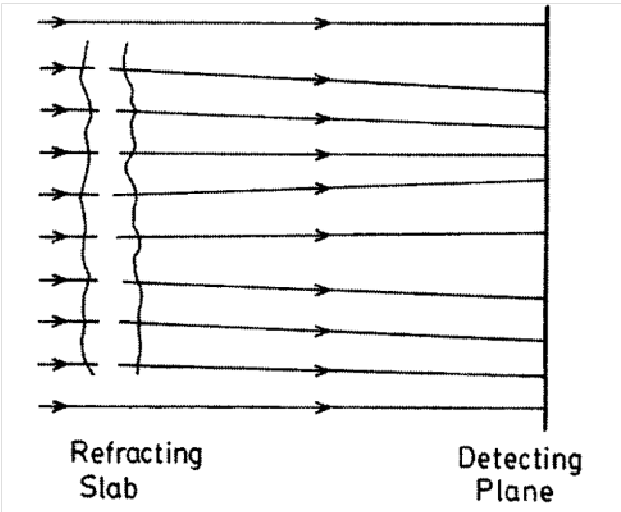

Figure 3.5 Principle of shadowgraph imaging (taken from (Hutchinson 2002)).

3.7 Experimental setup

For discharge visualization classical shadowgraphic technique scheme was applied. A xenon flash lamp (PAX – 10, PerkinElmer) with large spectral range (120-2000 nm) was used as a back-light illumination source. Flash lamp produced light pulses of 1.3 μs (FWHM) that were collected with a high focal ratio aspheric condenser lens (f/1) as shown in Figure 3.6. Condenser formed reduced real image of the xenon spark gap, which had several millimeters in length, on the pin hole adjusted to about 500 μm in diameter. Pin hole was placed in between the aspheric condenser L1 and achromatic doublet L2, in the focal point of the latter. Thus, condenser, pin hole and achromatic doublet formed an objective allowing the collimation of the light in almost parallel beam. Collimated beam was directed through the center of quartz cuve by two

aluminum mirrors. The cuve was aligned so that its optical windows were perpendicular to incident light beam. Quartz imaging lens (f/1.2) was used to form magnified shadow image of the tip on the 18 mm photocathode cathode of Andor iStrar DH734 ICDD camera.

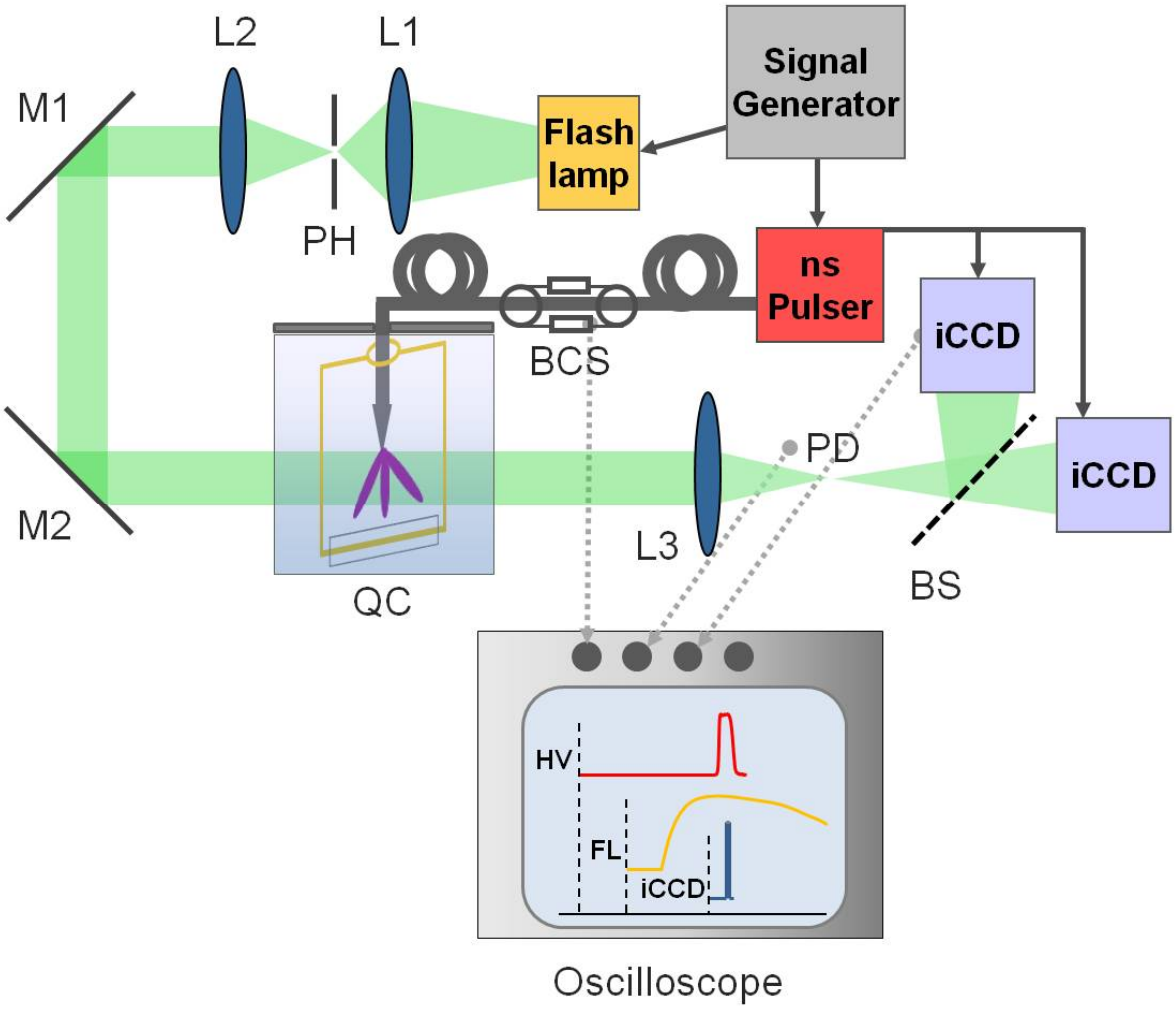

Figure 3.6 Experimental setup for nanosecond shadowgraphic visualization. L1 – f/1 aspheric condenser lens (Thorlabs), L2 – f/1.5 achromatic doublet (Thorlabs), PH – pin hole, M1 and M2 – high reflectivity aluminum mirrors (Thorlabs), QC – UV fused quartz cuvette of 50 ml, L3 – f60 UV quartz lens, BS – 50:50 Beam-splitter (Thorlabs), PD – biased photodiode with 1 ns rise time (Thorlabs), iCCD – Andor iStrar DH734 iCDD camera, BCS – custom-made back-current shunt, LeCroy (iX64) oscilloscope.

In some experiments two iCCD cameras were used for accurate temporal measurement. For this purpose a 50/50 beam splitter (BS) was placed at 15 cm from each camera (Figure 3.6). Spatial resolution of shadow visualization was calibrated with 50 µm tungsten wire fixed

on the pin electrode. Figure 3.7, a shows a typical shadowgraph of the pin electrode and Figure 3.7, b gives the shadow pattern of the 50 µm wire. The characteristic size of shadow structures was measured in pixel number with the help of Inkscape vector graphics software and then converted into microns using calibration procedure.

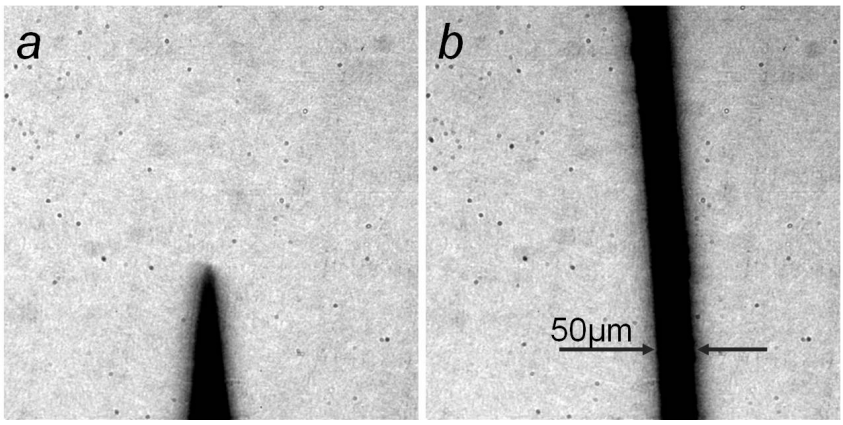

Figure 3.7 a) Shadow visualization of Ni pin electrode, b) Calibration with 50 µm tungsten wire.

Discharge visualization can be performed at the condition that HV pulse, flash lamp pulse and iCCD camera gate are synchronized in time. Taking into account the jitter of the nanosecond generator, which exceeded the HV pulse duration (Table 3.2) the iCCD camera was triggered using second BCS inserted in coaxial cable 1 m prior to generator. Cable length of 26 m resulted in time delay between HV pulse travelling in the cable and iCCD triggering signal enough for iCCD camera internal electronics to open the MCP (Multichannel plate). The flash lamp produced a light pulse of about 500 ns (FWHM), which was sufficiently long comparing to jitter of nanosecond generator and, hence, flash lamp was fired using the same trigger signal as pulser without detectable variation of shadowgraph luminosity. In summary, the synchronization scheme was organized as follows: nanosecond generator and flash lamp were triggered by two synchronized positive signals delivered by BNC 575 Pulse Generator (Berkeley Nucleonics Corp.). Time delay between nanosecond generator and flash lamp was adjusted accordingly to the moment of iCCD acquisition in order to obtain the maximal luminosity of the light beam. Signal from the first BCS triggered pulse generator (TTi TGP 10), which in turn produced a

positive TTL signal launching iCCD cameras. Time delay between two iCCD cameras was adjusted using ICCD acquisition delay function. The resulting jitter of iCCD camera gate was less than 1 ns.

Device	Operational time (FWHM) ns	Intrinsic delay ns	Jitter ns
Pulser	29	17300	40
Flash lamp	500	1700	<10
iCCD	2	~50	<1

Table 3.2 Characteristic time, intrinsic delay and jitter of the nanosecond pulser, flash lamp and iCCD camera.

3.8 Calibration of time delays of visualization scheme

The moment of discharge initiation can be determined with the precision of iCCD camera gate of 2 ns by scanning over HV pulse. In order to estimate the corresponding inception voltage the knowledge of the exact delay $\Delta\tau$ between arriving of HV pulse on the pin electrode (time moment corresponding to 10% of maxial amplitude) and iCCD camera opening is necessary. Since $\Delta\tau$ varies with the amplitude of applied voltage in the range of the order of rising slope of HV pulse a calibration should be done for each experimental value of HV pulse. To do this, the isolated ground electrode was replaced with a U-bent Cu stripe soldered to the cable sheath so that the distance between the tip of the pin electrode and the stripe was of the order of 100 µm. High voltage pulses were applied to the pin electrode while water was removed from the cuve which led to ignition of the spark discharge. Under such conditions a transition to spark should occur almost instantaneously once the discharge initiated (Pai *et al* 2010). Formation of conductive channel induced drastic change in boundary condition from infinite to almost zero impedance as seen by the incident pulse. It means that the voltage of the reflected pulse might change the sign at the moment of the spark formation. Consequently, the detection of the spark discharge simultaneously by appearance of plasma emission and

voltage flip in reflected pulse could be used as a reference time point allowing calculation of time delay $\Delta\tau$. Appearance of the discharge emission was controlled by iCCD camera with the same optical arrangement as in the shadowgraph experiments whereas flash lamp was switched off. The absence of time lag between camera gate monitor signal and opening of MCP was controlled with a fast photodiode (Thorlabs) placed at a focal distance of the UV imaging lens. A special attention was paid to take into account all the delays induced by optical and electrical paths resulting in 3.3 and 5 ns/m respectively. Photodiode, iCCD camera gate and BCS signals were collected with Lecroy (iX64) oscilloscope.

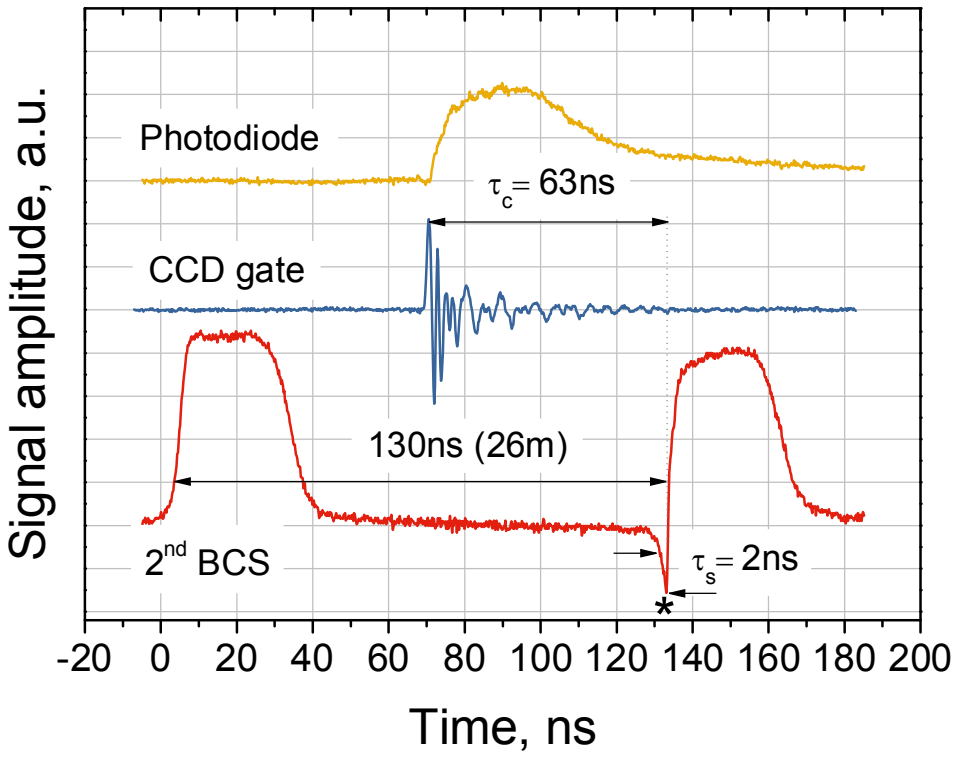

Figure 3.8 Calibration of time delay between iCCD camera gate and incident HV pulse by micro-spark discharge at 13 kV on the pin electrode. Asterisk denotes the moment of spark formation.

Figure 3.8 gives an example of the delay calibration between iCCD camera gate and incident HV pulse of 7.5 kV (13 kV on the pin

electrode). One should keep in mind that BCS and iCCD camera gate signals are measured at two different time instants separated by 2 x 13 m or 130 ns in time scale. The opening of camera gate in Figure 3.8 corresponds to the discharge initiation as it is detected by appearance of the light emission. The photodiode signal correlated within 1 ns with the iCCD gate monitor confirms the absence of the delay between the gate monitor and MCP opening. As one can see from the BCS signal of the reflected HV pulse (Figure 3.8) the spark discharge is ignited at 4.5 kV on the pin electrode with a transition time less than 0.6 ns (accuracy was limited by the sampling rate of the oscilloscope). A similar time lag for the spark formation was found from the emission images taken with a increasing delay of iCCD gate (Figure 3.9). It was found that bridging of the gap occurs over time interval of 0.5 ns. Finally, the delay $\Delta\tau$ can be calculated as

$$\Delta\tau = \tau_g + \tau_c - \tau_s \qquad (3.12)$$

where τ_g is iCCD camera gate delay (Figure 3.9), τ_c is delay between iCCD gate and BCS signal measured at the moment of spark ignition and τ_s is time lag of spark formation (Figure 3.8). Thereby, for HV pulse of 13 kV the delay $\Delta\tau$ is equal to 89 ns.

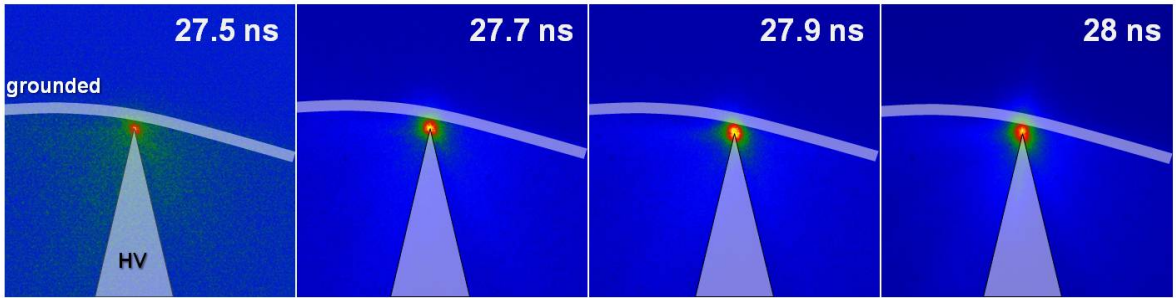

Figure 3.9 Formation of spark discharge in air. Discharge gap was about 100 μm and voltage amplitude on the tip was 13 kV. Time on emission images corresponds to specified delay of iCCD camera exposure gate (τ_g) in respect to triggering signal. Camera gate is 2 ns.

3.9 Optical emission spectroscopy

The experimental setup for spectroscopic diagnostics of the nanosecond discharge in dielectric liquids is presented in Figure 3.10. The light was collected with f=60 mm quartz lens placed at approximately double focal distance from the discharge in order to obtain slightly reduced image of the discharge on the entrance slit of monochromator. The spectrum was recorded with an iCCD camera mounted on the monochromator and triggered with the back current shunt (BCS) signal as it was done in shadowgraphic scheme. Typically the discharge was driven at frequency of 30 Hz slow enough for renewing of dielectric liquid in the discharge gap.

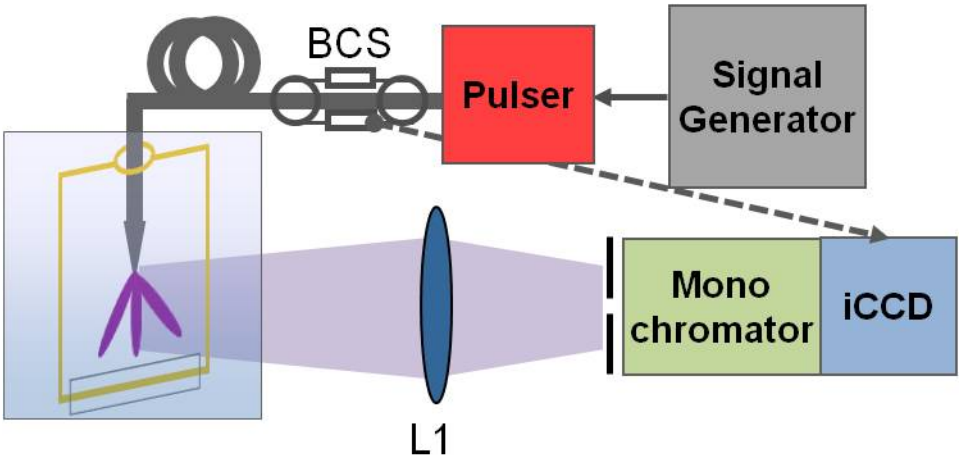

Figure 3.10 Schematic of setup for OES diagnostics of nanosecond discharge in dielectric liquids. L1 – f60 UV quartz lens.

Emission spectra were measured with a spectrometer consisting of the Andor Shamrock R–303i monochromator with mounted Andor iStar DH734-18U-03 iCCD camera as a detector. Monochromator was equipped with three gratings of 600, 1800 and 2400 lmm^{-1}. For full range spectrum measurements in the region 200 – 800 nm a 600 lmm^{-1} grating with maximal efficiency at 300 nm was used. Relative sensitivity of the spectra was corrected using calibration with a laser-driven broadband emission lamp (LDLS) EQ-99FC (Energetiq) providing a constant light intensity within a spectral range 170-2100 nm (Figure 3.11, a). A band pass filter at 300 nm was used in order to avoid the artefacts in the spectrum because of the second order

of diffraction. The correction procedure was as follows: all experimental spectra were divided by calibration spectrum (Figure 3.11, b) and then multiplied by the radiance function of calibration lamp (Figure 3.11, a). Time resolution of the spectral measurements was defined by a minimal iCCD gate. Because of low signal accumulation of light from the discharge, about 10^3 shots was needed for the gate duration between10 and 40 ns and entrance slit size of 100 µm.

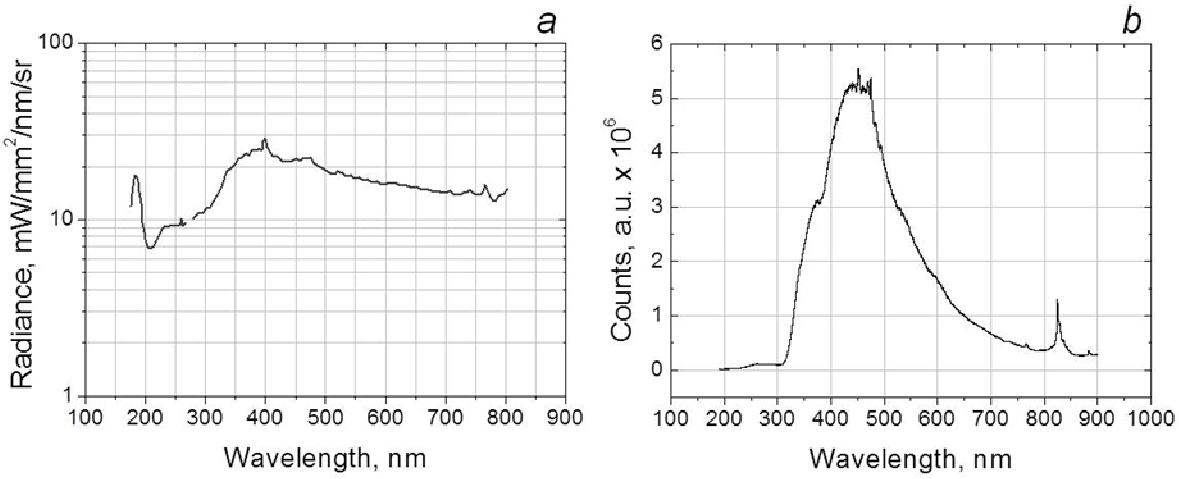

Figure 3.11 a) Radiance of EQ-99 calibration lamp, b) Calibration spectrum of Andor Shamrock R–303i spectrometer equipped with 600 lmm^{-1} grating.

3.10Dielectric liquids

The purity and dissolved gas content in liquid dielectric may have a drastic impact on the electrical strength. Before all the experiments the discharge cell was filled with 50 ml of fresh liquid through a special opening in the plastic cover. Three liquids were used in experiments deionized water, ethanol and n-pentane. Optionally several test were done in commercial carbonated water (Perrier). Deionized water was obtained from ELGA Elgastat Maxima purifier based on membrane filtering technology. The water conductivity was better than 5 µS/cm, pH neutral, TOC (total organic carbon) <50 ppb while all particles greater than 0.2 µm were eliminated by filtration. Reagent grade ethanol (0.997) and n-pentane (0.97) were purchased from Sigma Aldrich. Perrier carbonated water has neutral pH = 5.46 and TDS (total dissolved solids) = 475 mg l^{-1}.

3.11 DBD for biomedical applications

The second part of this thesis is devoted to the study of interaction between cold atmospheric plasma generated by dielectric barrier discharge (DBD) and living cells and tissues. The discharge device was rather similar to DBDs used by other groups (Fridman *et al* 2007, Vandamme *et al* 2010) with the difference that it was driven by nanosecond instead of microsecond high voltage pulses.

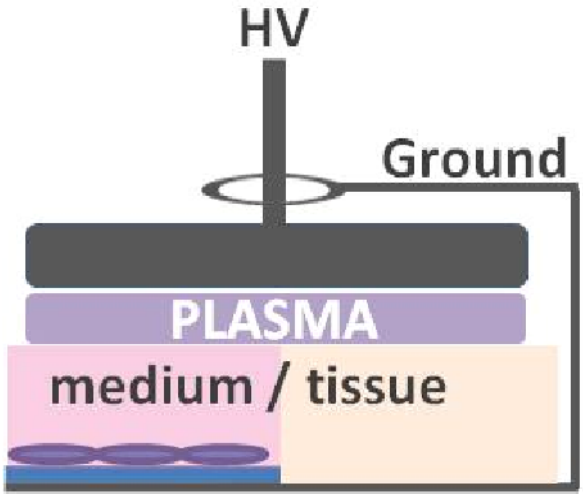

Figure 3.12 Schematic of DBD for biomedical applications.

The discharge was initiated in air gap of a few mm between the HV electrode and liquid in the plastic Petri dish or living tissue (Figure 3.12). The use of nanosecond pulsed voltage demands the coaxial electrode connection in order to avoid strong electromagnet tic noise. The solution was found as in the case of liquid discharge device by soldering the electrode directly to the core of coaxial cable (RG 213). Two cylindrical brass electrodes of 7 and 13 mm in diameter were used. Cable shielding was connected to a copper plate serving as the object stage. Smaller high voltage electrode had a glass cap isolation of 1.2 mm thickness. It was exclusively applied for mouse skin treatment and the isolation avoided the sticking of the skin to the electrode due to polarization. The larger electrode of Ø15 mm was used for living cells treatment in standard plastic Petri dishes with diameters of 16 and 35 mm. A powered electrode was fixed on the translation plate and the

gap between electrode and the object under treatment was adjusted using a micrometer screw.

A nanosecond pulse generator for biomedical DBD was chosen for several reasons. First of all, nanosecond pulsed electric field was shown to induce transient poration of cell membranes with typical pore size about 1 nm (Pakhomov *et al* 2009). However, very little is known about the role of pore formation under plasma exposure, while some authors argue that peroxidation of lipid bilayer may equally induce the partial loss of membrane integrity. Therefore, the study of nanosecond pulsed plasma is of great importance in order to get a deeper inside in this issue. Another, more technical, reason consisted in the possibility to use the same electrical and optical (OES and emission imaging) diagnostics for both liquid and DBD discharge in literally 'plug and play' mode. For electric measurements of voltage and discharge current a back current shunt technique was used. The method is described in details in Chapter 3.5. It allows precise measurement of the energy input in plasma for each HV pulse. Discharge was operated at the frequencies in the range 30 – 900 Hz that allowed a perfect flexibility in determination of treatment protocol.

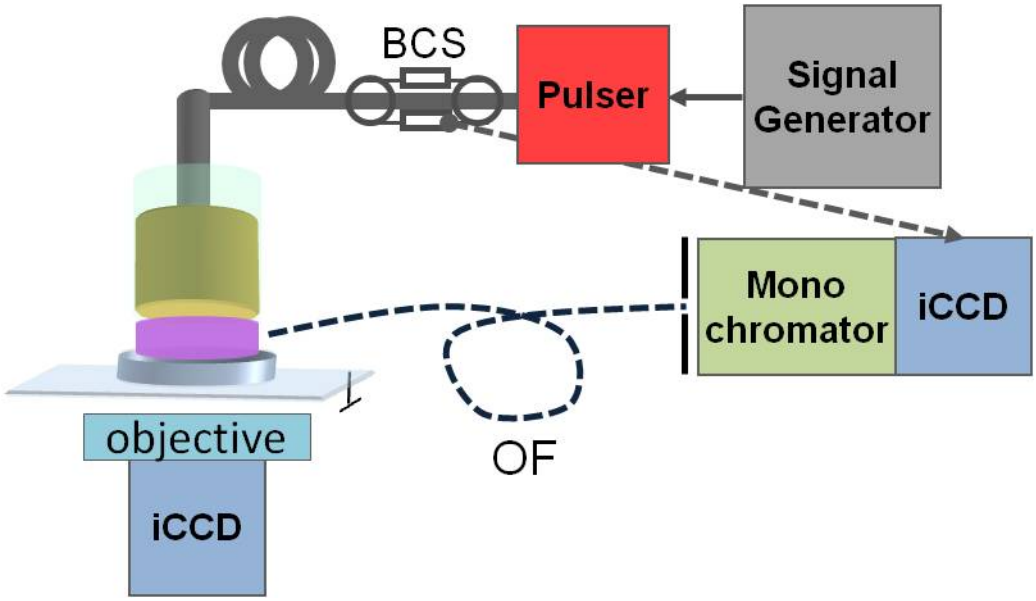

Figure 3.13 Schematic of iCCD imaging and spectroscopic analysis of DBD for biomedical applications. OF – optical fiber

3.11.1 Discharge characterization

Three main requirements that plasma devices for biomedical applications must strictly fulfill are the precise administration of the treatment dose, absence of substantial heating and uniformity of the treatment.

The term 'plasma dose' is widely accepted in literature and refers to the energy input in plasma per unit area of the treated object. The typical plasma doses capable to induce cytotoxic response in cells correspond to ~10 mJ/cm^2. For doses higher than 100 mJ/cm^2 the cells may occasionally lose their integrity. In contrast with radiotherapy and UV phototherapy, where the dose is defined as energy of radiation absorbed by unity of mass or unity of area respectively, the plasma dose is related to the energy required to generate plasma. Plasma dose defined as discharge power may be confusing since it does not provide an information about the energy transferred to the object. Moreover, the role of each type of energy produced by plasma (chemical, UV radiation, electric field, heat) remains unclear in overall effect. We propose to rely the plasma dose to the hydrogen peroxide production in culture medium as it was previously suggested in the experiments on E.coli deactivation (Dobrynin *et al* 2009). The detailed description of quantitative H_2O_2 measurements in water saline solution (PBS) will be given in Chapter 6.4 of this Thesis.

Discharge uniformity was controlled by iCCD imaging of plasma emission. Discharge visualization was performed through a transparent polymer film with deposited PtO/Au conductive coating connected to the ground. The iCCD camera was placed below the discharge like it is shown in Figure 3.13. Camera was triggered with BCS signal that ensured the synchronisation between exposure gate and HV pulse. Camera was mounted with optical objective in order to obtain a magnified image of the discharge.

Gas temperature in plasma zone was measured from rotational population in emission spectra of electronic transition of N_2 molecule ($C^3\Pi_u \longrightarrow B^3\Pi_g$). Time-resolved emission spectra were measured with

ANDOR Shamrock SR-303i spectrometer equipped with iCCD camera as a detector. A 600 l/mm grating having maximum at 350 nm was used for. Plasma emission was collected with an UV optical fiber placed at 1 cm from the discharge in the middle of the gap (Figure 3.13).

4 Initiation and development of nanosecond discharge in liquids

4.1 Initiation of nanosecond electrical discharge in water, ethanol and n-pentane.

As we have seen in Chapter 1 numerous experimental data on electrical breakdown of liquid dielectrics was accumulated over last 50 years. Extensive, generally, phenomenological description of the discharge morphology and propagation dynamics was done for pure hydrocarbons, mineral and silicon oils, cryogenic liquefied gases and water on the basis of shadowgraph or schlieren visualization and electrical diagnostics. It was found that the discharge morphology and propagation velocity are mostly defined by the applied electric field distribution and nature of liquid dielectric. However, no physical model adequately describing discharge propagation was formulated so far. The reason for that is not only the complexity of three-phase system consisting of liquid, gas/vapor and plasma, but to a considerable extent, rather limited number of diagnostics applicable in liquid phase.

Two distinct theories were proposed for the initiation phase of positive discharge, suggesting electron multiplication in extremely high electric field, occurring directly in the liquid phase and prerequisite formation of low density region or gaseous bubble (Qian *et al* 2005). Until recently no undoubted experimental evidence was found for either theory and it seems likely that the real phenomena is more complex and can probably combine both processes. Thus, it was suggested that under strong fields the proton current due to the Grotthuss mechanism may provide energy deposition high enough for cavity formation by Joule heating. The study of discharge initiation is complicated by small micron size of initial structures and necessity of nanosecond time resolution or even shorter due to the high propagation velocities. Multiple mechanisms

may be relevant in discharge ignition and propagation including evaporation at the discharge channel tip due to Joule heating (Lisitsyn *et al* 1999), phase transition in high divergent electric field (Kuskova 2001), cracking due to dielectrophoretic (Lewis 1998) or electrostrictive forces (Ushakov *et al* 2007).

The aim of this chapter is present the experimental results on ignition and propagation of electrical discharge over first nanoseconds after application of high voltage nanosecond pulse. The possibility of existence of the unique mechanism capable to explain experimental findings is discussed.

4.1.1 Three scenario under nanosecond positive HV pulse

The discharge was ignited by applying of the high positive pulse of 3 – 15 kV with rising slope shorter than 5 ns and 30 ns duration (FWHM) on the pin electrode with diameter of 2 μm. Figure 4.1, a-b shows typical shadow structures originating on the tip at voltage amplitude of 9 kV in deionized water. It was found that under such conditions, bush-like and tree-like discharges occurred stochastically. As it can be seen both discharge modes demonstrate filamentary pattern consisted of gaseous channels, however the typical length of discharge structures and, hence, the propagation velocity of 'bush-like' and 'tree-like' modes differ by one order of magnitude. In the following we will use the term bush-like discharge or slow mode and tree-like discharge or fast mode in order to designate two discharge types.

Propagation of the tree-like discharge was accompanied by the emission of successive spherical pressure waves (Figure 4.1, b) which indicates the strong energy release inside the discharge channels. When the bush-like discharge is ignited one spherical pressure wave can be seen. If the voltage on the pin electrode is decreased down to 4 kV, the bush-like discharge still can be observed in a statistical manner (Figure 4.1, d). The size of discharge structure and number of branches decreases for lower applied voltage while the spherical pressure wave can still be seen. The weaker contrast of pressure wave shadow at lower voltage

amplitude indicates that corresponding pressure gradient also attenuates.

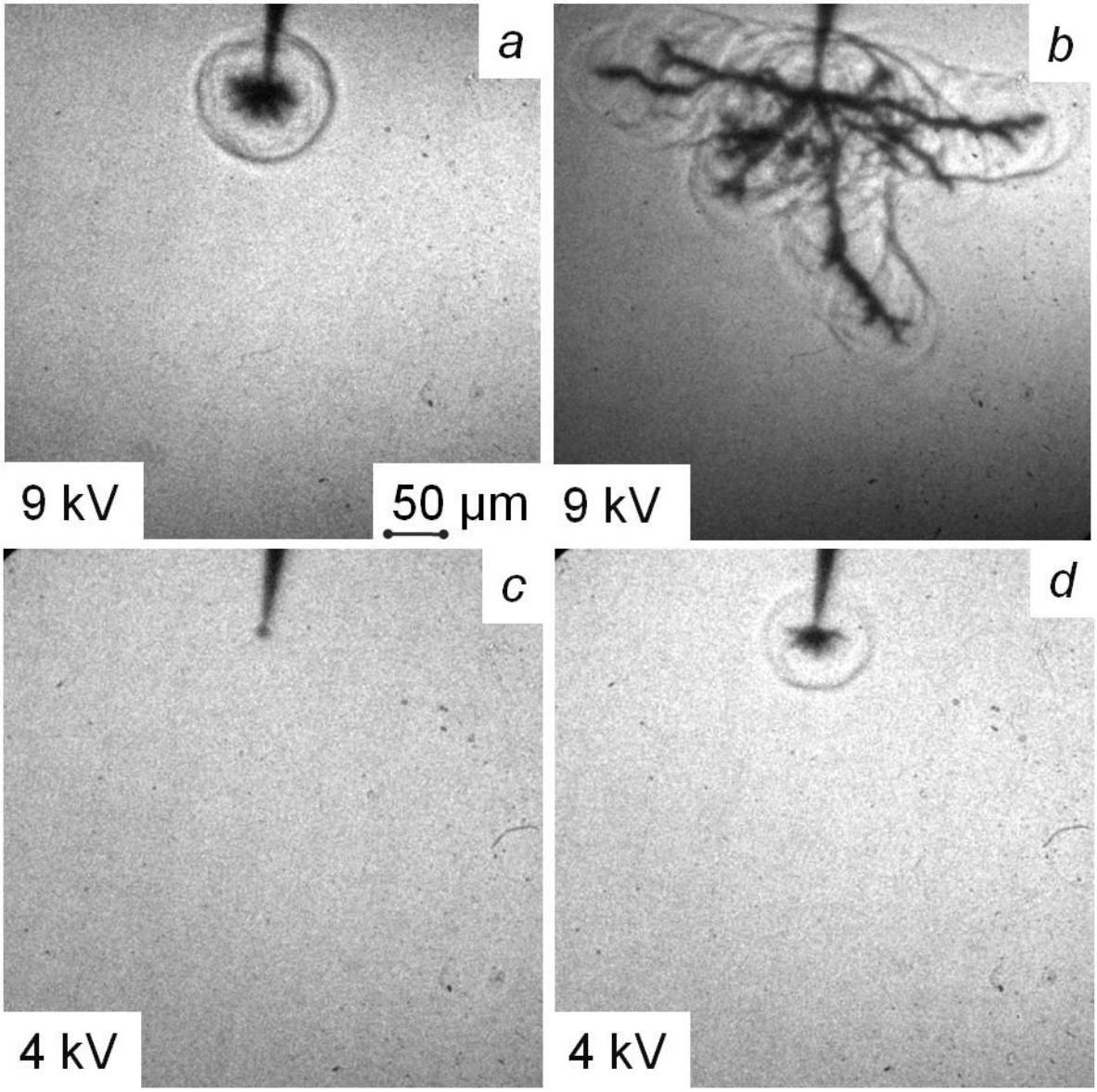

Figure 4.1 Shadowgraphs corresponding to a) slow (bush-like) and d) fast (tree-like) discharge at 9 kV, c) bubble and d) slow (bush-like) at 4 kV on the pin electrode and in deionized water (5 µS/cm) as measured 65 ns after application of HV pulse. Camera gate is 2 ns.

At voltage amplitude of 4 kV a spherical low density cavity, which is referred to as a 'bubble', is found on the pin electrode (Figure 4.1, c). No detectable hydrodynamic perturbations associated with bubble development have been observed in liquid. The difference in typical size and absence of pressure wave in the case of bubble initiation suggest

that processes underlying formation of bush-like and bubble mode should be energetically different. It is worth noting that the tree-like discharge was never ignited at such a low voltage. The comparative analysis of typical discharge structures appeared at point electrode under positive nanosecond pulse demonstrates that three different field dependent mechanisms may be realized in deionized water.

In the following chapters we will consider the initiation phase of each of three modes under varied voltage amplitude in three liquids with different dielectric constant.

4.1.2 Initiation of fast and slow modes in deionized water

Fast mode

As we have seen above, at the voltage amplitude of about 10 kV both tree-like and bush-like discharge may be ignited in a random way. These two modes have distinctly different propagation dynamics that was extensively described in literature (McKenny and McGrath 1984, Lesaint and Gournay 1994b, Gavrilov *et al* 1994), however little was known up to very recently about the initiation phase. By initiation phase we understand the first detectable evidence of the discharge formation within temporal and spatial resolution of the registration system. The originality of our experimental setup is that it provides the nanosecond time resolved micron scale detection synchronized with the high voltage pulse within 1 ns. The precise coupling between the registration system and the applied voltage allows one to study the phenomena in a single shot regime. Moreover, the accurate information on discharge ignition is necessary to answer the question whether the discharge initiation and propagation, e.g. initiation of each new step of discharge channel, can be described by the same mechanism.

As one can see in Figure 4.2, a-b weakly refracting structures of several tens of microns appear on the tip at the end of rising slope of applied voltage pulse of 9 kV. The zero time moment here and bellow corresponds to 10% of maximal pulse amplitude. The time instant of the discharge appearance on the shadowgraphs was quite reproducible

from shot to shot. The jitter in discharge ignition was about 0.5-1 ns depending on applied voltage. The time given in the frames corresponds to the closing of iCCD camera gate while the exposure time was always 2 ns. By shifting the iCCD camera gate with a step of 0.5 ns it was possible to scan over the HV pulse. The shadow pattern becomes visible abruptly between 6 and 6.5 ns, then the structure grows in size while induced density gradient increases. Note that at 6.5 ns the discharge pattern seems to be separated from the electrode tip. At 7 ns several filaments with diameter of less than 2 µm can be distinguished. Bright spot of emission is seen at the tip before the shadow pattern became observable (Figure 4.2, d). The initial size of the emitting spot was less than 2 µm and increased rapidly by a factor of 10 over 1 ns as can be seen in Figure 4.2, e-f. The intense light emission at the tip electrode can explain the apparent separation of discharge shadow from the pin. Thus, if plasma luminosity exceeds the brightness of the flash lamp beam, the shadow structures would be screened and appear like a bright field. Figure 4.2, c shows that the maximal length of the discharge shadow at 7 ns was about 40 µm, which gives a value of 20 km/s for the propagation velocity. It is worth noting that inaccuracy of 0.5 ns, a practical limit of synchronization between HV pulse and opening of iCCD camera, would result in 25% error in velocity calculation. Hence, obtained velocity should be taken as rough estimation. More accurate propagation velocity measurements, done with two synchronized iCCD cameras will be discussed in the following sections.

In order to investigate the effect of the field nonuniformity a pin electrode with larger diameter was used. The pin was a conical frustum with the diameter of smaller base equal to 65 µm. The intensity of the flash lamp was adjusted so it was possible to observe simultaneously the shadow of the pin and the light emitted from the discharge as demonstrated by Figure 4.2 g. Tree-like discharge initiation at 19 kV was accompanied by a strong light emission originating on the pin edge. Statistical analysis demonstrated that only one emitting spot appeared on the tip edge. Therefore, initiation of tree-like discharge was in accordance with maximal field strength taking into account that field

distribution was almost 2D confined in the plane of grounded electrode (for more details on filed distribution see Section 3.2). The emitting volume increased rapidly in size from 30 µm up to 100 µm in 2 ns which gives a propagation velocity of 35 km/s.

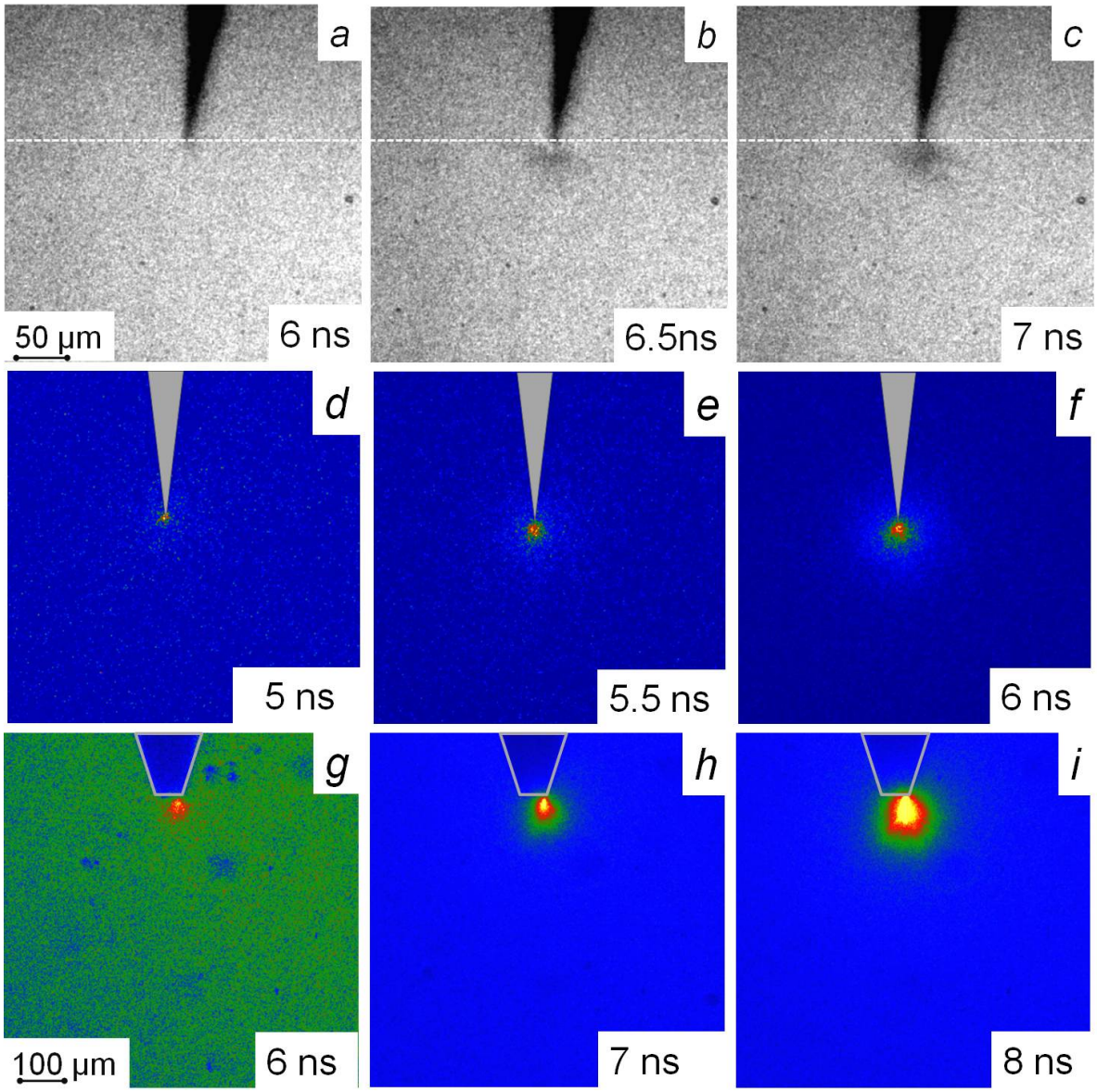

Figure 4.2 Initiation phase of fast (tree-like) mode. a) – c) shadowgraphs showing discharge initiation at 9 kV, e) – g) plasma emission images at 9 kV. Pin of Ø2 µm. g-i) shadowgraphs with plasma emission seen on electrode of Ø65 µm at 19 kV. Zero time moment corresponds to 10% of HV pulse amplitude at it rising slope. Camera gate of all frames is 2ns.

Obtained results demonstrate, within the resolution of the experimental setup that initiation of the tree-like discharge occurs by formation of a

micron size strongly emitting spot on the pin electrode over the rising slope of the applied voltage pulse (5 ns). Based on this finding, one can assume that the formation of low density region, at least at micron scale, is not prerequisite for the ignition of the tree-like discharge. The question of the nature of plasma emission will be addressed in the last part of this chapter.

Slow mode

Bush-like discharge observed under the same conditions as reported above for fast tree-like mode originated in 2π hemispherical form on the pin electrode (Figure 4.3, d-e). For longer time delay after ignition of slow mode (Figure 4.3, f) at 9 kV one could see that the shadow pattern is not uniform demonstrating an internal structure. When the voltage amplitude was decreased down to 4 kV the bush-like discharge still could be observed on the pin electrode. Figure 4.3, a-c shows that at lower applied voltage thin filaments radiating from spherical cavity can be distinguished already at 18 ns. The discharge structure is enveloped with a spherical pressure wave with the origin point close to the tip (Figure 4.3, f). Independently of the applied voltage, the discharge filaments were found to propagate synchronously with the expansion of spherical pressure wave. Note that at voltage amplitude of 4 kV tree-like discharge was never observed. At voltage amplitude of 9 kV the bush-like pattern increased by 20 µm over 5 ns that gives 4 km/s for the average propagation velocity. Note that the bush-like mode is also supersonic, however under the same conditions the tree-like mode had an order of magnitude higher velocity. Also, no light emission at ignition of bush-like discharge was detected. Consequently, one can suggest that the mechanisms describing the initiation of bush and tree-like modes can be different.

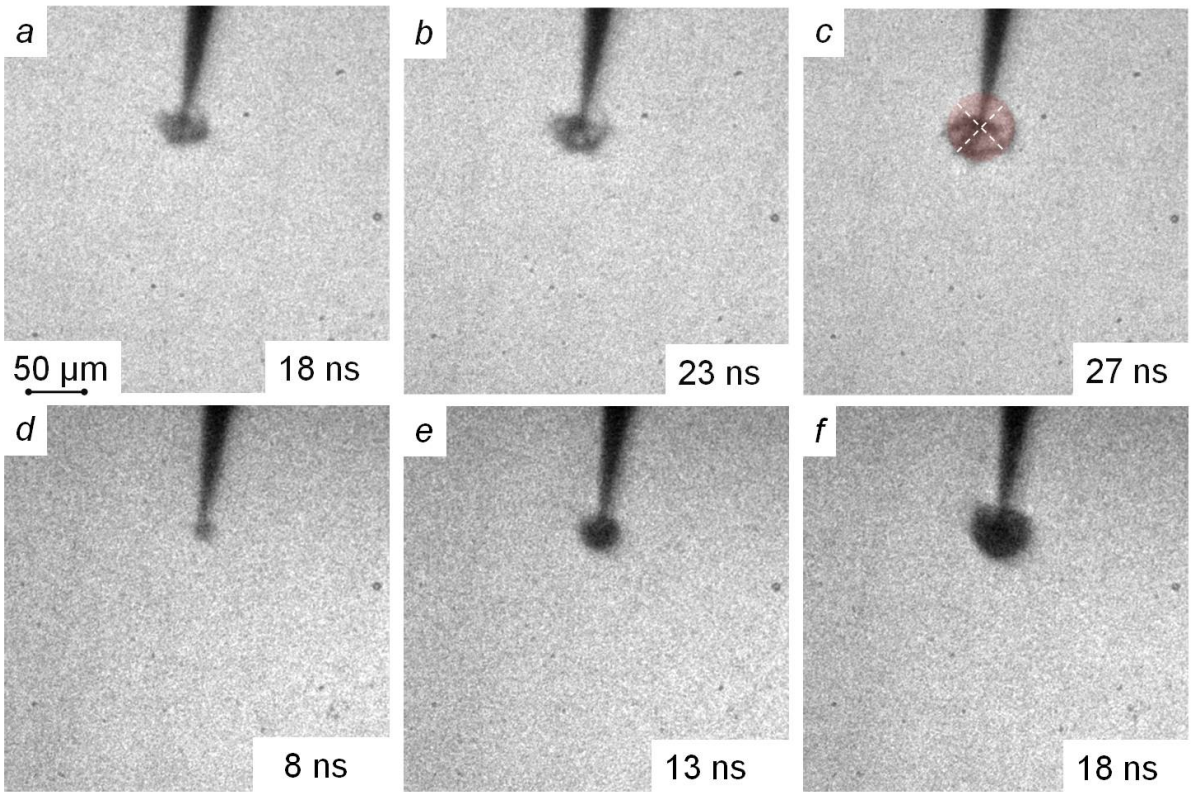

Figure 4.3 Initiation and development of slow 'bush-like' mode at a) – c) 4 kV, d) – f) 9 kV on the Ø2 µm pin electrode. Deionized water. Camera gate is 2 ns

Bush-like discharge was also observed on the pin electrode with larger diameter of the tip (Ø65 µm). Figure 4.4 demonstrates the formation and development of the bush-like discharge under the same condition as reported for the tree-like mode given by Figure 4.2, h-i. Slow mode originated in the form of two symmetrical hemispherical structures propagating synchronously from electrode edge. Shadow structures demonstrated a uniform pattern up to several tens of nanoseconds, when refractive channels and pressure wave became distinct (Figure 4.4, e). The pressure wave profile can be rather well approximated by superposition of two spherical waves (Figure 4.4, f). Interestingly, in Figure 4.4, f it can be seen that the origins of two spherical shock waves are situated about 15 µm away from the electrode surface. After the HV pulse end the bushy structures formed on the pin electrode demonstrated some expansion and coalescence suggesting on their gaseous nature (Figure 4.4, e-f). The whole shadow structure appeared in a hemispherical form with highly diffusive boundary. Discharge propagation velocity of each hemispherical structure derived from

Figure 4.4, b-c was found to be 4.5 km/s which is comparable with values found for the smaller pin electrode and voltage amplitude of 9 kv. Similarly no light emission was detected in this case within the exposure time of 2ns.

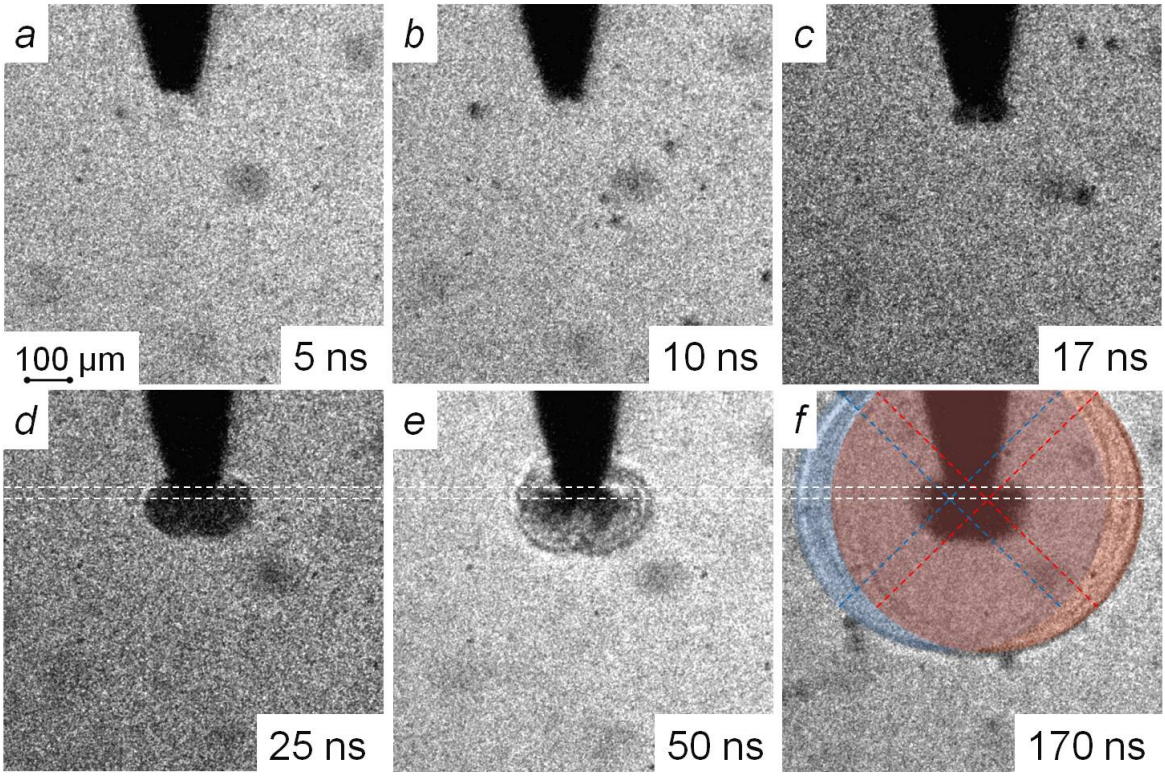

Figure 4.4 Initiation and development of slow 'bush-like' mode at 19 kV on Ø60 µm tip. Deionized water. Camera gate is 2 ns.

Under the lower voltage amplitude of 10 kV only a hydrodynamic perturbation could be seen during the HV pulse (Figure 4.5, a-c) while a small less than 10 µm in size hemispherical structures became apparent after the pulse end (Figure 4.5, d-f). Two low density structures had comparable size and originated at the tip edge. Two pressure waves produced by the discharge had lower velocity as can be seen from comparison of their size at the same time moments (Figure 4.4, e and Figure 4.5, e)

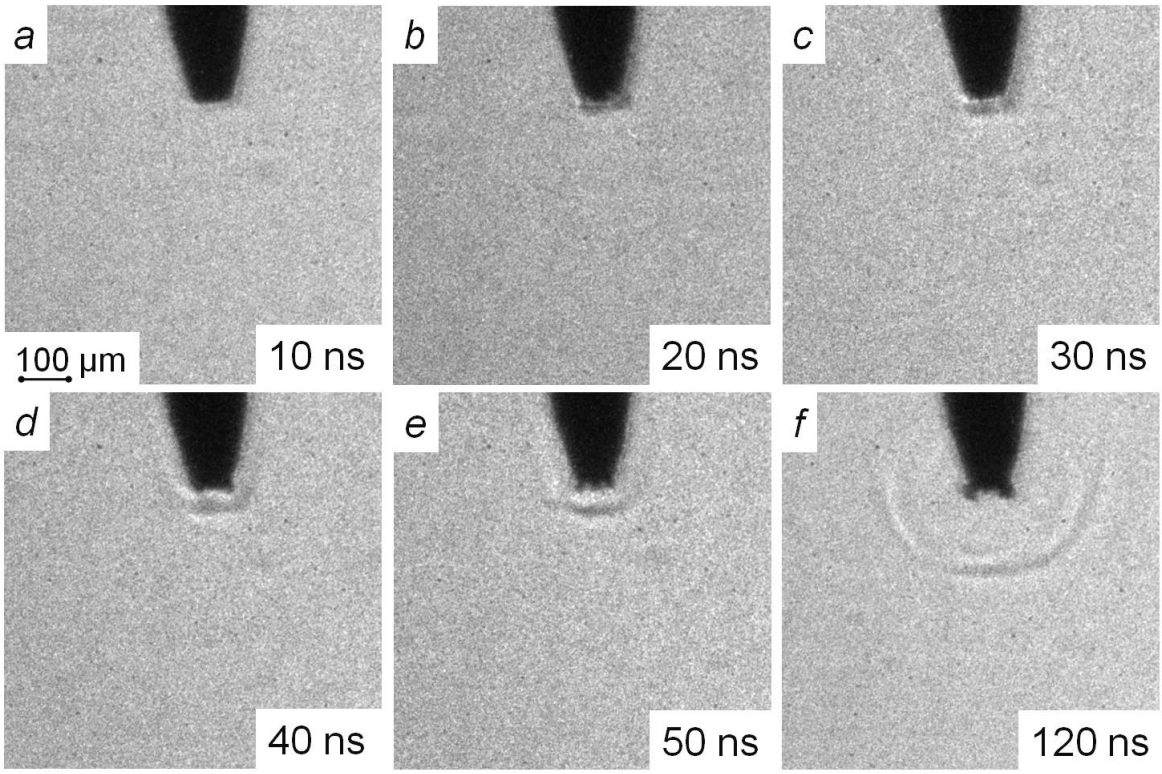

Figure 4.5 Initiation and development of slow 'bush-like' mode at 10 kV on Ø60 µm tip. Deionized water. Camera gate is 5 ns.

Shadowgraphic analysis shows that both tree-like and bush-like modes are supersonic and consist of thin gaseous channels. Strong light emission and formation of energetic shock wave suggest that both discharges modes are characterized by high local energy dissipation. As it was shown in the experiments with large pin electrode the initiation of the bush-like discharge is only governed by field distribution and cannot be attributed to some accidental presence of dissolved gas submicron bubbles. The fact that only one highly luminescent tree-like discharge is ignited under exactly the same conditions points to the fact that, in contrast with bush-like discharge, a high transient current should flow in tree-like discharge as supported by intense light emission. The fact that fast and slow modes could be ignited in random manner at 9 kV on 2 µm and 19 kV applied on 65 µm pin electrode points to the fact that two mechanisms could be realized under the same field strength. One can assume that some stochastic process should occur on submicron scale, i.e. cavitation or instability development.

We will now try to get better insight in initial processes occurring on the electrode by lowering further the applied voltage.

4.1.3 Dynamics of cavitation mode. Formation of gaseous cavity in the vicinity of pin electrode under prebreakdown voltage.

Figure 4.6, a shows that at voltage amplitude of 4 kV on Ø2 µm pin electrode a small, several microns in size, cavity is observed at the tip. It was found that the bubble reached the detectable size at the end of HV pulse becoming visible over the trailing slope of applied HV pulse (Figure 4.6, a). After the pulse end the bubble exhibited radial expansion reaching maximal diameter of 42 µm at 1.6 µs after ignition (Figure 4.6, b-d). Then the bubble collapsed (Figure 4.6, e-f) and a series of oscillations occurred. It was found that bubble the drifted downward along pin electrode axis in direction which was opposite to the buoyancy with a velocity about 5 m/s (Figure 4.6, e – h). Note that no light emission and no shock wave were detected during bubble formation or collapse.

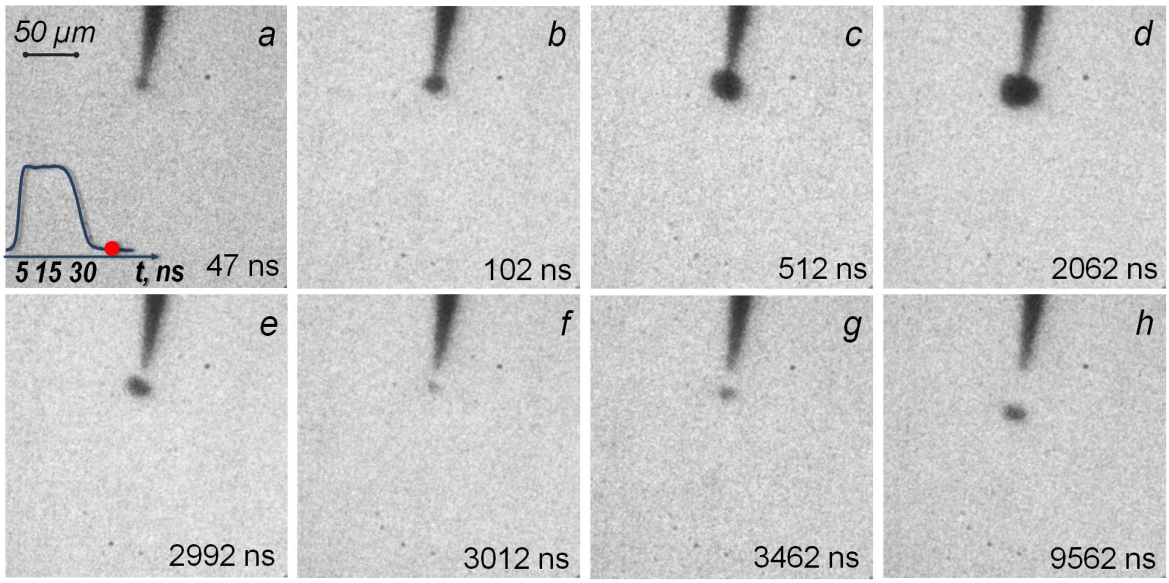

Figure 4.6 Dynamics of the cavitation mode in deionized water at 4 kV. Single-shot images, ICCD camera gate is 2 ns. Numbers in the frames correspond to the time instant from the voltage rise on the electrode.

It is worth noting that the bubble and the bush-like discharge occurred randomly under exactly the same conditions as it is demonstrated by Figure 4.3, a-c. At the applied voltage higher than 4 kV, the bush-like

discharge was preferentially ignited. For voltage amplitude of 3.5 kV no bush-like discharge was detected while microscopic bubble was always observed after the end of HV pulse. At 3.5 kV the bubble reached the maximal diameter of 16 µm at 1.1 µs. Figure 4.7 provides x-t diagram of the bubble expansion at 3.5 and 4 kV. The initial expansion velocity, deduced from x-t diagram, was about 80 m/s. As opposed to the bush-like and the tree-like discharges, the bubble mode is essentially subsonic. In the following we will use the term 'bubble mode' or 'cavitation mode' since there is no evidence supporting the discharge formation.

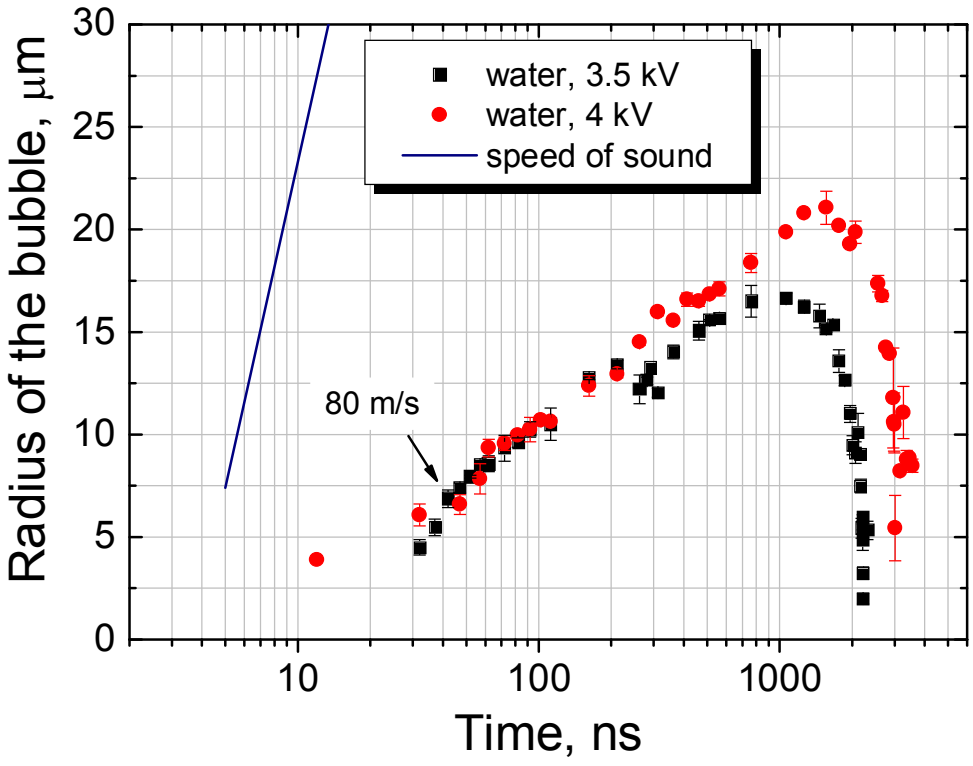

Figure 4.7 X-t diagram for radius of expanding bubble in deionized water at 3.5 and 4 kV. Speed of sound in water is 1.48 km/s.

As one can see, the bubble expansion dynamics is in rather good accordance with the close values of bubble radii at 3.5 kV and 4 kV over the first 200 ns after formation. At 4 kV two abrupt increases of bubble diameter occurred at about 300 ns and after 700 ns, which corresponds to the time instants of the reflected negative and positive

pulses arriving on the pin electrode. The analysis of the bubble expansion in terms of Rayleigh dynamics will be done in Section 4.1.5.1.

4.1.4 Effect of dielectric permittivity on the discharge ignition.

As it was mentioned in Section 2.4.7 under short nanosecond pulses mechanical stress produced by dielectrophoretic and electrostrictive forces acting on dielectric liquid placed in strong electric field, can produce local density lowering crucial for the discharge ignition. It is thought that rupture of liquid and cavitation may occur on the timescale of the electric field built-up (Shneider and Pekker 2013b). It is also suggested that field induced crack of liquid may precede electron multiplication and ionization process (Lewis 1998). The additional pressure stretching the liquid is proportional to E^2 and hence the effect is determined by liquid nature and applied electric field amplitude. Electrostrictive force occurring in dielectric under nonunifrom field pulls the liquid along the field gradient. Arising flow attempts to neutralize the mechanical stress and as it was shown by numerical modeling in the case of water (Shneider and Pekker 2013b), only for high voltage rate above 1.4 kV/ns, the conditions favorable for the rupture of liquid and cavitation induction can be attained. Another approach consists in considering of the dielectrophoretic force producing strong Lippmann effect at the interface (Lewis 1998).

In order to study the possible role of dielectric permittivity on the discharge ignition we used ethanol ($\varepsilon = 27$) and pentane ($\varepsilon = 1.84$) exposed to nanosecond positive voltage pulse of variable amplitude. The results obtained in deionized water ($\varepsilon = 80$) under similar conditions have been discussed in the previous paragraphs. Since the cavitation threshold in liquids strongly depends on amount of dissolved gas a carbonated water was also used in the tests.

4.1.4.1 Discharge initiation in ethanol

Cavitation mode

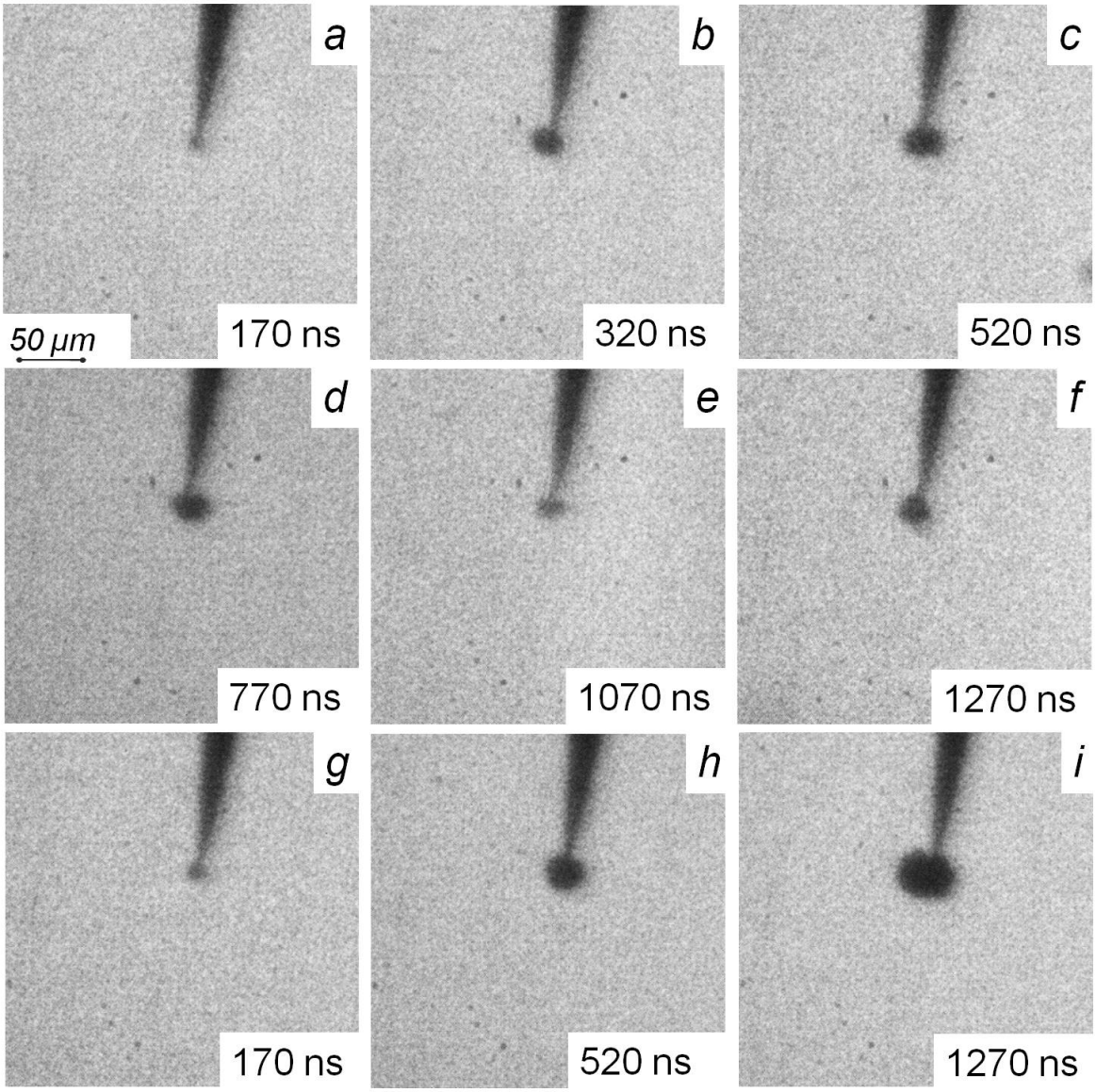

Figure 4.8 Bubble formation and collapse in ethanol a) – f) at 3.5 kV, g) – i) at 4.5 kV. Tip is Ø2µm. iCCD camera exposure gate is 2ns

In the case of ethanol no gaseous cavity or bubble formation has been detected on the pin electrode during applied voltage pulse of 3.5 – 4.5 kV. Only after the end of the HV pulse end a spherical shadow patterns of 4 – 7 µm in radius (Figure 4.8, a-g) became evident. The bubble increased in size reaching maximal radius of 15 µm at about 500 ns for 3.5 kV voltage pulse and 20 µm at 1270 ns for voltage amplitude of 4.5 kV (Figure 4.8, c-i). Then the bubble collapses and

rebound can be seen (Figure 4.8, e-f) according to well-known spherical cavity dynamics in liquid. At voltage amplitude of 3.5 kV the bubble radius was 15 – 20% smaller comparing to bubble observed in deionized water under the same conditions. Similarly to the case of deionized water no shock wave emission has been detected during the applied voltage pulse or during the collapse of the bubble in ethanol.

Slow and fast modes

At higher voltage amplitude of 5.5 kV two discharge modes were observed. Slower bush-like and faster tree-like modes, originated stochastically on the pin anode, were quite similar in form to two discharge modes observed in deionized water. For slow mode the refracting hemispherical structures with the radius of several microns became distinguishable at the end of rising slope of applied voltage pulse (Figure 4.9, a). When the discharge pattern radius reached 15 µm, a spherical pressure wave and the discharge channels became apparent (Figure 4.9, c). The pressure wave and the discharge filaments demonstrated radial expansion during the HV pulse. Several discharge channels originating from the tip are clearly seen (Figure 4.9, d).

For the given spatial resolution and sensitivity of the experimental setup the first detectable manifestation of the fast mode ignition was observed at about 8 ns after the application of HV pulse (Figure 4.9, e). Fast mode initiated in a form of thin weakly refracting filaments of several microns in diameter and about 10 µm in length. Several nanoseconds later two to three channels with stronger density gradient became visible (Figure 4.9, f-g). The channels were of 20 – 40 µm in length and average thickness of 5 µm. Starting from 17 ns one could distinguish the shock cone surrounding the discharge channels (Figure 4.9, h). It worth noting that the discharge channels originated directly on the tip while no intermediate bubbles or cavities have been observed.

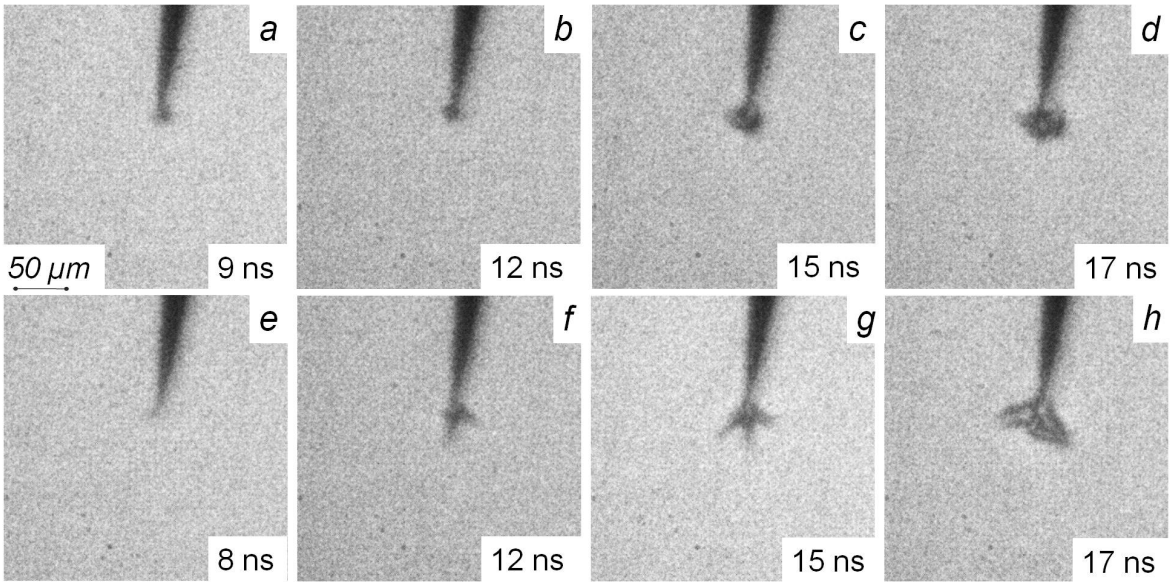

Figure 4.9 Two discharge modes observed in ethanol at 5.5 kV. a) – d) Development of slow discharge mode at 5.5 kV, a) – d) Development of fast mode at 5.5 kV. Tip is Ø2µm. iCCD camera exposure gate is 2ns

When voltage amplitude was raised up to 9 kV, still both modes could be seen on the pin electrode. The spherical pattern of slow mode slightly increased in size and appeared 'denser' on the shadowgraphs (Figure 4.10,a-b). At latter times the number of channels increased from 2 – 3 at 5.5 kV to 6 – 8 at 9 kV forming an almost symmetrical fan-like structure (Figure 4.10, c-d). Interestingly, at about 15 ns fast tree-like discharge always ignited from the tip of one of slow mode channels (Figure 4.10, b-c). As can be seen in Figure 4.10, b-d formation of fast mode did not affect the development of initial slow discharge and both modes continued to propagate in the discharge gap simultaneously. Transition from slow to fast mode was statistically observed in deionized water with big point electrode of 65 µm at 19 kV, i.e. under more uniform field. Moreover, the fast mode could be also initiated over the rising slope of applied voltage pulse as evidenced by formation of a thin channels of 10 – 15 µm in length already 6 ns after application of HV pulse (Figure 4.10, e). In several nanoseconds after fast mode ignition the discharge channels turned into uniform dark region adjacent to the electrode (Figure 4.10, f). The dark asymmetrical pattern rapidly increased in size and at about 18 ns strongly branched discharge channels and associated shock waves could be seen (Figure

4.10, h). The number of parent channels was 3 – 4 on average, while numerous daughter branches appeared during development of the fast mode.

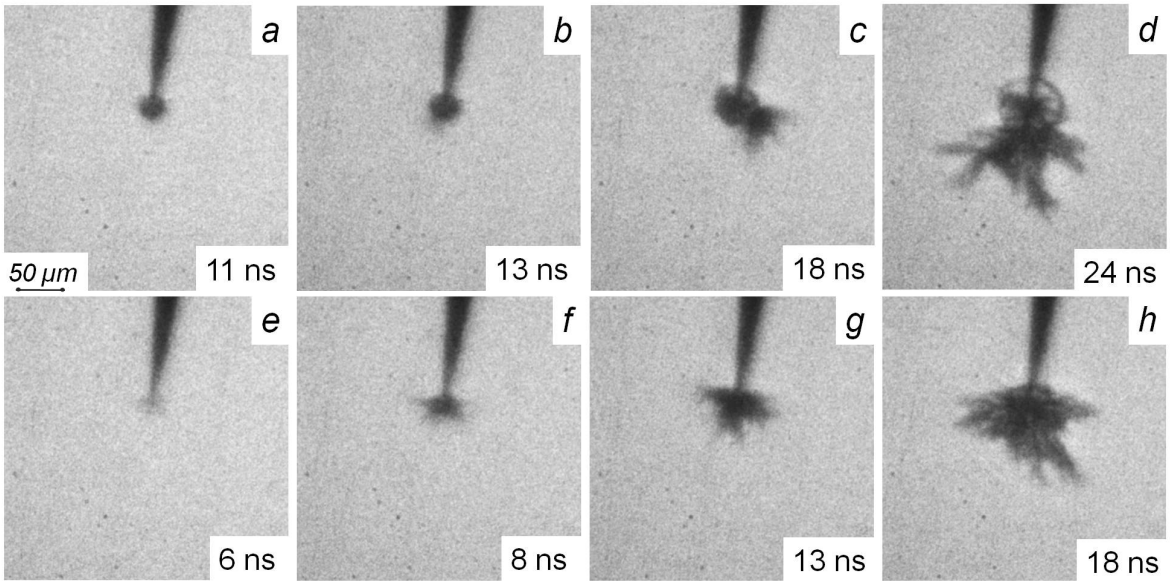

Figure 4.10 Initiation and development of slow and fast mode in ethanol at 9 kV. a,b) Formation of slow discharge, c,d) Transition to fast mode, e – h) Initiation and development of fast discharge. iCCD camera exposure gate is 2ns

Propagation velocity at discharge initiation, calculated from shadowgraphs given by Figure 4.10 was about 3 km/s for bush-like discharge and 4.8 km/s for tree-like discharge. As one can see in ethanol and deionized water, the size and propagation velocity of the bush-like discharge were comparable, while tree-like discharge was considerably slower in ethanol than in deionized water for the given voltage amplitude. Furthermore, in ethanol at 9 kV a transition from bush-like to three-like discharge always occurred during the plateau of HV pulse, whereas it was never observed in deionized water with small Ø2µm pin electrode. The transition from slow to fast mode are typical for microsecond discharges with voltage rising time longer than 20 ns (An *et al* 2007, Ceccato *et al* 2009). Similar phenomenon was observed in present study during successive reflected pulses and will be discussed in Section 4.4

4.1.4.2 Discharge initiation in n-pentane

Cavitation mode

In n-pentane, characterized by the lowest dielectric permittivity (1.84) among all tested liquids the shadow structures on the pin electrode appeared at the minimal voltage amplitude of 10 kV. Low density cavity with a radius of less than 5 µm could be seen 70 ns after application of the HV pulse (Figure 4.11,a). The size of the cavity increased reaching 13 µm at about 1.5 µs and collapse occurred at 4.5 µs (Figure 4.11, b – h). The maximal radius of the cavity observed in n-pentane was comparable with the maximal bubble expansion in deionized water and ethanol at 3.5 kV, however the collapse time was considerably longer. As in the case of deionized water and ethanol, we have not observed a shock wave emission that could indicate on the discharge initiation inside the bubble. At higher voltage amplitude of 12 kV, a spherical cavity with about 10% bigger radius still could be observed (Figure 4.12, a-d).

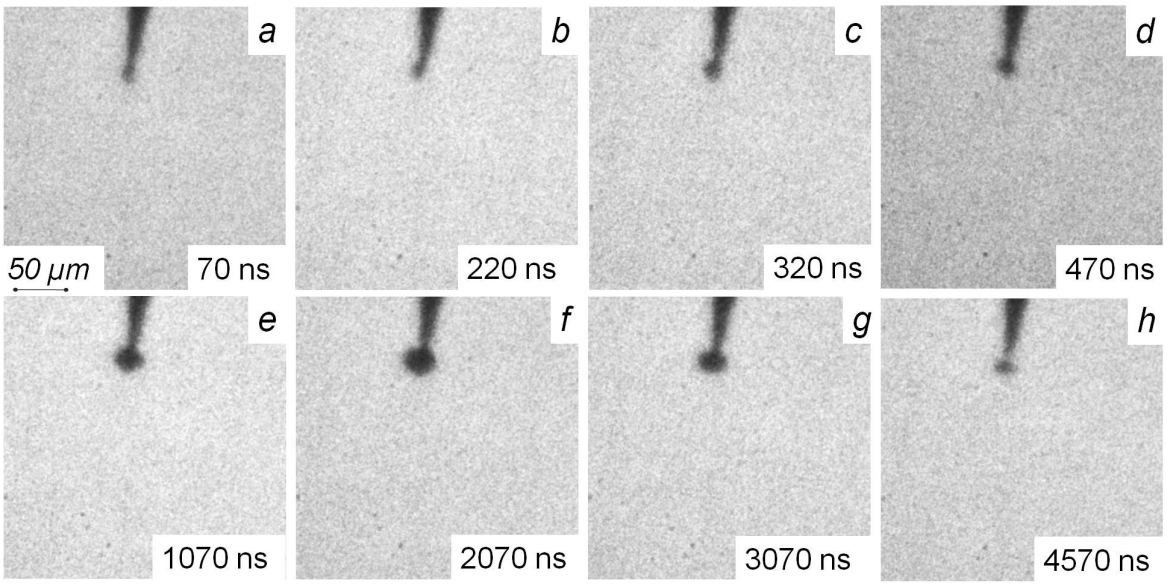

Figure 4.11 Bubble dynamics in pentane at 10 kV. Tip is Ø2µm. iCCD camera exposure gate is 2ns

Under the same conditions an occasional initiation of filamentary discharge was found. Discharge ignition could be detected by the appearance of a thin weakly refracting filament of 10 µm in length and about 3 µm in diameter that became visible at 13 ns (Figure 4.12, e). Discharge channel expanded during the HV pulse duration reaching

65 µm in length and 12 µm in diameter (Figure 4.12, f-h). A shock wave could be seen along the discharge channel.

The results obtained in n-pentane demonstrate that by applying a nanosecond pulse it was possible to produce a micron scale gaseous cavity, however the voltage threshold was about three times higher as compared to deionized water and ethanol. Filamentary discharge ignited at 12 kV was very similar in size and morphology to the tree-like discharge observed in ethanol at 5.5 – 6 kV. Discharge mode that was referred to as slow or bush-like discharge in deionized water and ethanol was never observed in n-pentane. In the literature, subsonic bush-like discharge was observed in n-pentane under the voltage pulses of several hundreds of nanoseconds with rising slope of 10 ns (Lesaint and Gournay 1994a). We cannot hence exclude that the bubble cavitating in n-pentane under our conditions is a first step of the bush-like discharge propagation. Sensitive current measurements would be helpful to clarify this issue because bush like must be accompanied by current while cavitation not.

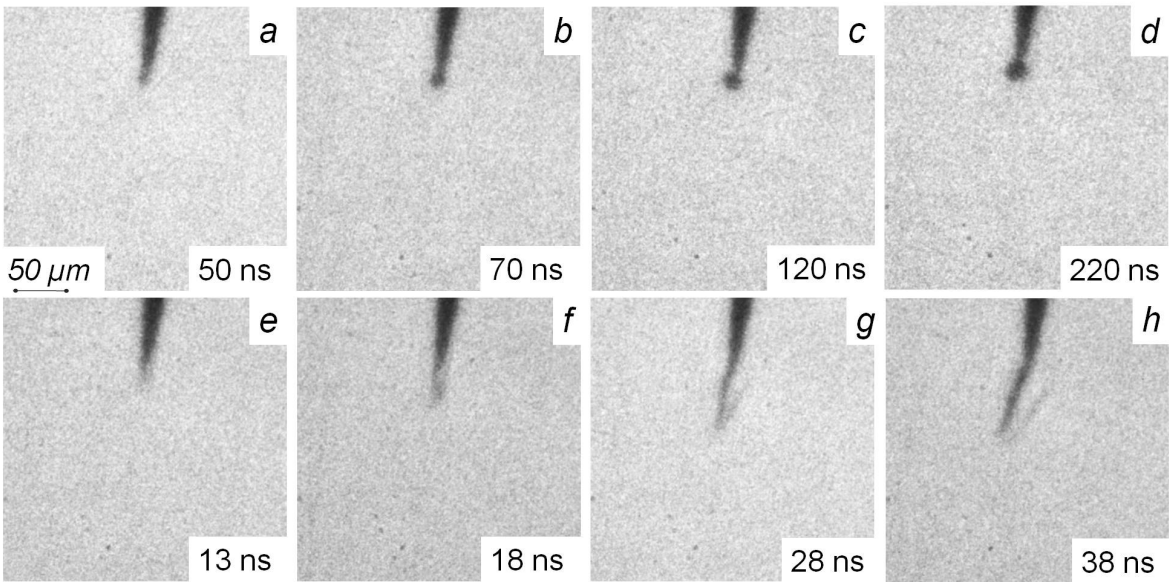

Figure 4.12 Bubble and filamentary mode observed under 12kV in pentane. a) – d) Cavitation of bubble, a) – d) Filamentary discharge formation. Tip is Ø2µm. iCCD camera exposure gate is 2ns

4.1.5 Initiation mechanisms of three modes

4.1.5.1 Mechanism of bubble formation

As we have seen above in all three liquids with highly different dielectric permittivity, below the threshold voltage for discharge initiation a spherical low density cavity of 5 – 10 µm in size could be formed. As one can see in Figure 4.13 the maximal radius of the bubble varied between 13 µm for n-pentane at 10 kV and 30 µm for carbonated water at 3.5 kV. In all tested liquids formation of a gaseous cavity or a bubble was observed after the first incident HV pulse of positive polarity. However, as was already mentioned Section 3.5, the reflections from open end on the electrode side of the coaxial cable and from the zero output impedance of generator (output resistance of pulse generator is zero when HV diode is closed) produced a series of pulses of alternate polarity split by 260 ns. The typical voltage signal of 3.5 kV maximal amplitude obtained with the help of back current shunt (BCS) is shown in Figure 4.13. The dynamics of the bubble expansion shows that the bubble radius before arriving of the first reflected pulse varied between 9 µm and 13 µm depending on liquid (Figure 4.13). As one can see a spike-like increase in bubble radius occurred during the negative pulse in deionized water at 4 kV. The third pulse that had positive polarity and amplitude about 25% smaller comparing to initial pulse did not seem to produce strong effect on bubble size at 3.5 kV in deionized water, while at 4 kV the dynamics of bubble expansion was affected as can be seen from linear increase of the radius after the third pulse. In the case of ethanol at 4.5 kV and carbonated water at 3.5 kV the radius of the bubble has significantly increased likewise after the second and third pulses. In n-pentane the bubble expansion phase appeared to be about 4 times shorter than the collapse phase suggesting that reflected pulses possibly affected bubble dynamics.

Below, we will use the well known Rayleigh-Plesset theory to describe the dynamics of the bubble expansion. The best coincidence within 20 – 25% was found between experimentally measured bubble lifetime, which is the time period between formation of the cavity and its first

collapse, in deionized water and ethanol at 3.5 kV and theoretically calculated values given by Rayleigh relation

$$t = 1.83 R_m \sqrt{\rho / P_0}, \qquad (4.1)$$

where R_m is maximal radius of the bubble, ρ is liquid density and P_0 is hydrostatic pressure.

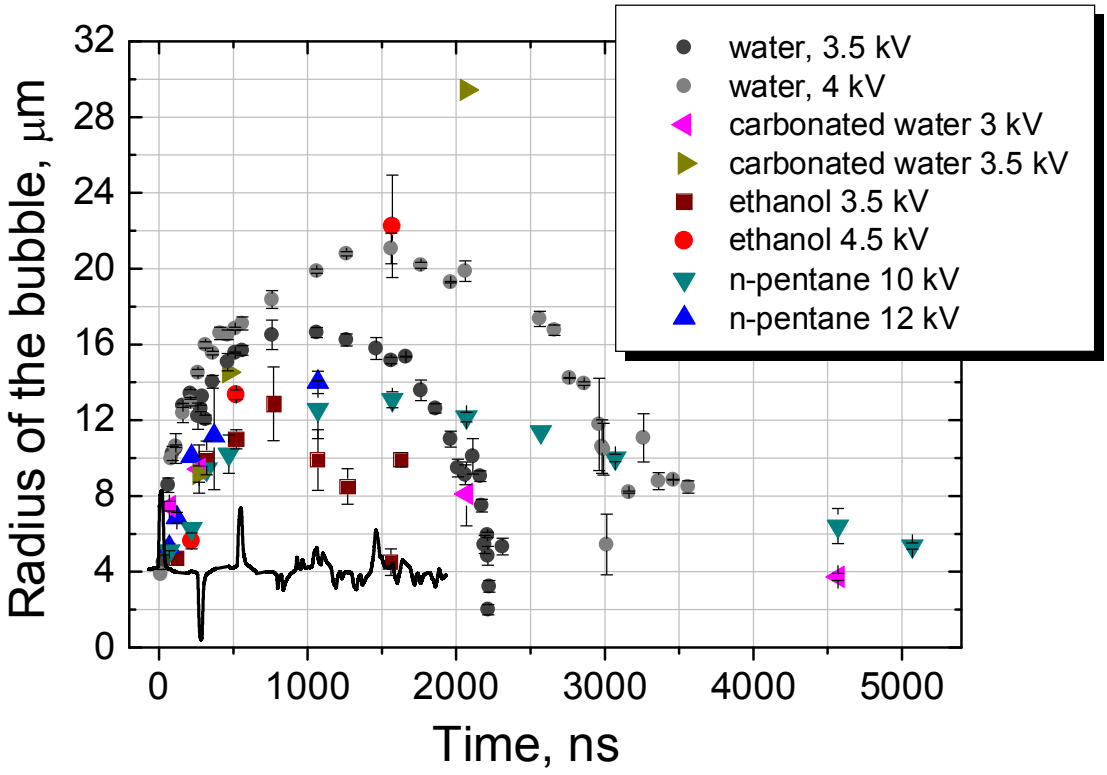

Figure 4.13 Bubble dynamics in deionized water, carbonated water, ethanol and n-pentane. Voltage amplitudes are given in the insertion. Typical voltage signal of 3.5 kV maximal amplitude is provided. The time x-axis scale of the voltage signal corresponds to the real time scale.

The measured lifetime was longer in both liquids comparing to the theoretical values presumably due to the additional pressure acting on the bubble surface during the reflected pulses as there was no evidence of partial discharge formation inside the bubbles. The initial pressure in the bubble can be approximately estimated assuming liquid inertia limited Rayleigh dynamics. The Rayleigh approximation is deliberately used for 'order of magnitude' estimation. It is worth to note that the value of the initial pressure is very sensitive to the precision in

measurements of the initial bubble radius and that the produced uncertainty far exceeds the effect of additional bubble expansion during successive HV pulses.

Expansion dynamics of spherical gaseous cavity at low Mach numbers (u/c < 0.3) in uncompressible liquid can be described by well known Rayleigh–Plesset equation:

$$R\ddot{R} + \frac{3}{2}\dot{R}^2 = \frac{1}{\rho}\left(P - P_0 - \frac{2\sigma}{R} - \frac{4\mu}{R}\dot{R}\right) \qquad (4.2)$$

We will assume adiabatic expansion of incondensable gas inside the cavity $P = P_1(R_1/R)^{3\gamma}$ and omit the effect of viscosity and surface tension which is justified for slow expansion velocities and big amplitudes of R. By integrating the Rayleigh–Plesset equation with respect to R one can obtain:

$$\dot{R}^2 = \frac{2P_1}{3\rho}\left\{\frac{1}{\gamma-1}\left(1 - \frac{R_1^{3\gamma-3}}{R^{3\gamma-3}}\right)\frac{R_1^3}{R^3} - \frac{P_0}{P_1}\left(1 - \frac{R_1^3}{R^3}\right)\right\}, \qquad (4.3)$$

where R_1 is initial bubble radius, P_1 is initial pressure and P_0 is hydrostatic pressure. At the moment when bubble radius reaches maximal value of R_m expansion velocity $\dot{R}$ becomes zero and one can estimate P_1 if P_0, ρ, R_m, R_1 are known. Assuming that the cavity is filled with vaporized liquid we take $\gamma = 1.32$ for the case of water and $\gamma = 1.13$ for gaseous ethanol. The smallest detected initial radius of the bubble in both liquids was about 4 µm. Resulting initial pressure P_1 was found to be 1 MPa in ethanol and 3 MPa in deionized water.

4.1.5.2 Electrostriction induced cavitation

As it was mentioned above, the negative pressure establishing in liquid due the strong electrostrictive effect in rapidly changing non-uniform electric field, can exceed the critical pressure P_c corresponding to the cavitation threshold (Shneider and Pekker 2013a). The size of area of the negative pressure, where the rupture of liquid may occur has a typical dimension of the order of the tip radius and is given by (Shneider *et al* 2012) :

$$R \approx r_0 \left(\varepsilon_0 \varepsilon \frac{V^2}{P_c r_0^2} \right)^{1/4} \qquad (4.4)$$

for polar dielectrics and by

$$R \approx r_0 \left(\frac{1}{6} \varepsilon_0 (\varepsilon - 1)(\varepsilon + 2) \frac{V^2}{P_c r_0^2} \right)^{1/4} \qquad (4.5)$$

for nonpolar dielectrics, where r_0 is the radius of the tip, V is the applied voltage and P_c is the cavitation threshold. The critical pressure is determined statistically from the number of nucleation sites appearing in unit volume of liquid over unit of time. Obviously the critical pressure depends on the method used for induction of cavitation, i.e. acoustic pulse, heat pulse, laser pulse etc. The typical values of critical pressure for deionized water and ethanol at 20 C are 30 MPa (Herbert *et al* 2006) and 20 MPa (Arvengas *et al* 2011) respectively. If we consider the point electrode radius of 1 μm relation (4.4) gives for the size of cavitation area the values of 3.5 and 4.1 μm for deionized water and ethanol respectively. Hence, the initial radius of the bubble can be estimated as 2 μm. The critical pressure for n-pentane is about three times lower than for the ethanol and the size of cavitation zone at 10 kV is about 3 μm. The negative pressure arising from stretching of dielectric in nonuniform electric field by ponderomotive forces can be found from (Shneider and Pekker 2013b)

$$p_e = -0.5 \alpha \varepsilon_0 \varepsilon E^2, \qquad (4.6)$$

where α is empirical constant relying density variation with change in dielectric constant of polar dielectric $\left(\alpha = \frac{\rho}{\varepsilon} \frac{\partial \varepsilon}{\partial \rho} \right)$. In the case of water α equals to 1.5 and for ethanol α can be taken equal to 1.2 (Ushakov *et al* 2007). For maximal electric field of $7.8 \cdot 10^8$ V/m calculated in point to plane approximation for 3.5 kV the electrostrictive negative pressure equals -322 and -87 MPa for deionized water and ethanol respectively. The pressure created by hydrodynamic flow of liquid attempts to equilibrate the electrostrictive pressure and the real pressure would be the sum of both. As it was shown by numerical calculations (Shneider

and Pekker 2013b) for voltage pulse of 7 kV with rising slope of 5 ns applied on point electrode of 5 µm the maximal total pressure is 4 times lower than the amplitude of electrostrictive pressure. The rough estimation gives a maximal negative pressure at the electrode axis of several tens of MPa in our experimental conditions. The negative pressure reaches its maximal value at the end of rising slope of the HV pulse. This estimation shows that in both liquids critical conditions for cavitation can be reached, whereas elevated initial pressure of several MPa points to some process with the energy input in the cavity.

Liquid	Density kg/m3	Relative permittivity	Surface tension N/m	Bulk modulus GPa	Speed of sound m/s	Vapor pressure kPa	Ionization potential eV
Water H_2O_2	998	80	7.1 10^{-2}	2.2	1480	2.3	12.6
Ethanol C_2H_5OH	789	27	2.2 10^{-2}	0.9	1160	5.8	10.6
n-Pentane C_5H_{12}	624	1.84	1.6 10^{-2}	0.5	1020	54.1	10.3

Table 4.1 Thermodynamic and dielectric properties of water, ethanol and n-pentane (Poling *et al* 2001, Lide 2005) *. All values are given for atmospheric pressure and 20 C. Ionization potential is given for gas phase.*

4.1.5.3 Mechanical crack

Another approach consists in considering of Griffith criterion of mechanical crack formation in liquid with high population of holes (absence of hydrogen bond) under strong electric field. The critical field for crack formation is given by (Lewis 1998)

$$E_c = \left(\frac{\gamma B}{l\varepsilon^2}\right)^{1/4}, \qquad (4.7)$$

where γ is the surface tension, B is the bulk modulus, l is the critical crack length (can be estimated as $10^{-5} - 10^{-8}$ m). An estimation of critical field for deionized water, ethanol and n-pentane gives close values for first two liquids of $6.5 \cdot 10^9$ V/m and two orders of magnitude higher value of $6\ 10^{11}$ V/m for n-pentane, l being 10^{-6} m. Since the absolute values of the critical field depend on the empirical parameter l, the relative critical fields of three liquids should be considered. The coincidence between the critical fields for deionized water and ethanol is in agreement with the experimental observations of the cavitation threshold voltage of 3.5 – 4 kV, however two orders of magnitude higher field predicted for n-pentane seems to be unrealistic since the cavitation in n-pentane was observed already under the fields three times higher than critical fields in deionized water and ethanol.

Therefore, the model assuming the presence of sub-microscopic holes in liquid with subsequent crack formation under the action of dielectrophoretic force acting on inhomogeneous dielectric does not seem to adequately describe experimentally observed bubble formation. On the contrary, the model based on electrostrictive rupture of liquid under highly nonuniform rapidly increasing electric fields is in good agreement with the experimental data. For all three tested liquids the product εE^2, which determines the maximal electrostrictive pressure, is proportional to the cavitation threshold values available in literature (Herbert *et al* 2006, Arvengas *et al* 2011).

4.1.5.4 Initiation of slow 'bush-like' mode

As we have seen above bush-like and tree-like modes are observed under the same conditions in deionized water and ethanol. Initiation of both discharge modes was characterized by formation of low density filamentary structures and by emission of shock waves. However, the morphology and typical dimensions of bush-like and tree-like discharges were rather different. Based on the experimental observation of the initiation of two discharge modes one may suggest that bush-like and tree-like discharge are described by distinct physical phenomena.

Since cavitation of bubble and formation of bush-like discharge was observed at the same value of applied voltage in polar deionized water and ethanol it is follows that bush-like discharge should ignite in the region saturated with sub-micron cavitation voids. Typical structure of bush-like discharge consists of a gaseous cavity and low density filaments propagating from the cavity. We, hence, suggest that the bush-like discharge ignites in the cavitation void formed under strong electrostrictive negative pressure in the vicinity of the tip. Discharge ignition induces a fast energy input in the small volume of the cavity, leading to the formation of a shock wave and rapid expansion of discharge structure. As it was shown, the center of the shock wave produced by the bush-like discharge is situated 15 μm away from the tip in the case of 65 μm tip. It means that the void should reach some critical size before the breakdown occurs. The filamentary structure of the bush-like mode can be explained by instability of the cavity interface in strongly divergent electric field (Aka-Ngnui and Beroual 2001). As it follows from numerical simulations, the area where cavitation may occur has the size of the order of tip radius and is separated from the tip by several microns of compressed liquid (Shneider and Pekker 2013b). This assumption shows that the current in the bush-like discharge is limited by the interface charging while the only current flowing in the circuit is a displacement current. Current spikes observed during formation of bush-like discharge under microsecond HV pulses (Ceccato *et al* 2009) support the idea of applied electric field screening by charge accumulation on the interface.

4.1.5.5 Initiation of 'tree-like' mode

The tree-like discharge ignites directly on the electrode surface as evidenced by appearance of the strong light emission. Thin discharge channels rapidly propagate from the pin electrode while no gaseous cavity can be observed. The tree-like discharge was observed in all three tested liquids with different dielectric permittivity. The critical field for the tree-like discharge initiation was found to decrease with increasing dielectric constant. Local density lowering due to the electrostrictive effect can probably facilitate the initiation of fast tree-like mode.

However, the role of electrostrictive force in initiation of tree-like discharge is uncertain. Especially because the dielectric permittivity is considerably lowered under the electric fields at which the tree-like mode is ignited, due to the saturated polarization (Suresh *et al* 2006). It is necessary to perform electrodynamic simulations in order to find the product of εE^2 which defines the maximal electrostrictive pressure. The saturation of dielectric polarization in the region of a strong electric field can induce local increase of the electric field. The field induced electron impact dissociation of liquid molecules in extremely high fields of the order of 10^9 V/m seems to play a role in initiation of tree-like discharge. The strong coupling between the hydrogen bonds and the dipole orientation in the case of water may explain considerably higher propagation velocity in the case of water as compared to other liquids. Electric field of the order of 10^9 V/m induces strengthening of the hydrogen bonds along the field axis while the hydrogen bonds, orthogonal to the field, are weakened (Vegiri 2004). Therefore, proton tunneling through the hydrogen bonding, known as Grotthuss mechanism, can also contribute in the development of the fast discharge mode.

4.1.6 Conclusion on initiation of three modes

We have shown that under nanosecond positive HV pulse three different phenomena occur depending on voltage amplitude.

- At low applied voltage of 3.5 kV – 4.5 kV (field of the order of $8 \cdot 10^8$ – 10^9 V/m) the cavitation process was observed in deionized water ($\varepsilon = 80$) and ethanol ($\varepsilon = 27$) presumably due to the strong electrostrictive effect. In n-pentane cavitation is observed at higher applied voltage of 10 kV-12 kV (2.4 – $2.9 \cdot 10^9$ V/m).
- The size of cavitation zone was found to be about 4 µm in all tested liquids which is in a good agreement with the predictions of electrostriction based mode proposed by other authors.
- Expansion of cavitation bubble can be approximated by Rayleigh dynamics in deionized water at 3.5 kV and in ethanol at 4 kV.

Calculated initial pressure in the case of deionized water and ethanol equals to 3 MPa and 1 MPa respectively.

- Slow bush-like mode seems to ignite in the gaseous void formed by cavitation process and separated from the point electrode by a layer of compressed liquid.
- Fast filamentary tree-like mode ignites on the point electrode as supported by occurrence of strong plasma emission.

In order to understand the different physical phenomena occurring in bush-like and tree-like discharge, we will consider the propagation dynamics of these two modes in the following section.

4.2 Propagation of bush-like and tree-like modes

In this section we will discuss the propagation dynamics of bush-like and tree-like modes in deionized water and ethanol, and propagation of filamentary discharge in n-pentane. The effect of the applied voltage on the discharge propagation will be demonstrated.

4.2.1 The effect of applied voltage on development of bush-like and tree-like modes in deionized water

As it was mentioned in previous section, the bush-like and the tree-like discharges can be ignited at the same value of applied voltage. Figure 4.14 demonstrates the typical shadowgraphs of two modes at 8 kV, 11 kV and 15 kV taken about 30 ns after the end of the applied voltage pulse. One can see that the bush-like mode in the post discharge phase shows nearly spherical pattern increasing in size with applied voltage amplitude. The radius of the bush-like discharge increases about 1.5 times when voltage is raised from 8 to 15 kV. The radius of the spherical shock wave also increases with voltage amplitude by about 20% between 8 and 15 kV.

The three-like discharge pattern in the post-discharge consisted of gaseous channels and a series of spherical shock waves along the discharge channels. The maximal discharge length and the number of

channels increased 4-5 times with increasing the voltage amplitude between 8 and 15 kV.

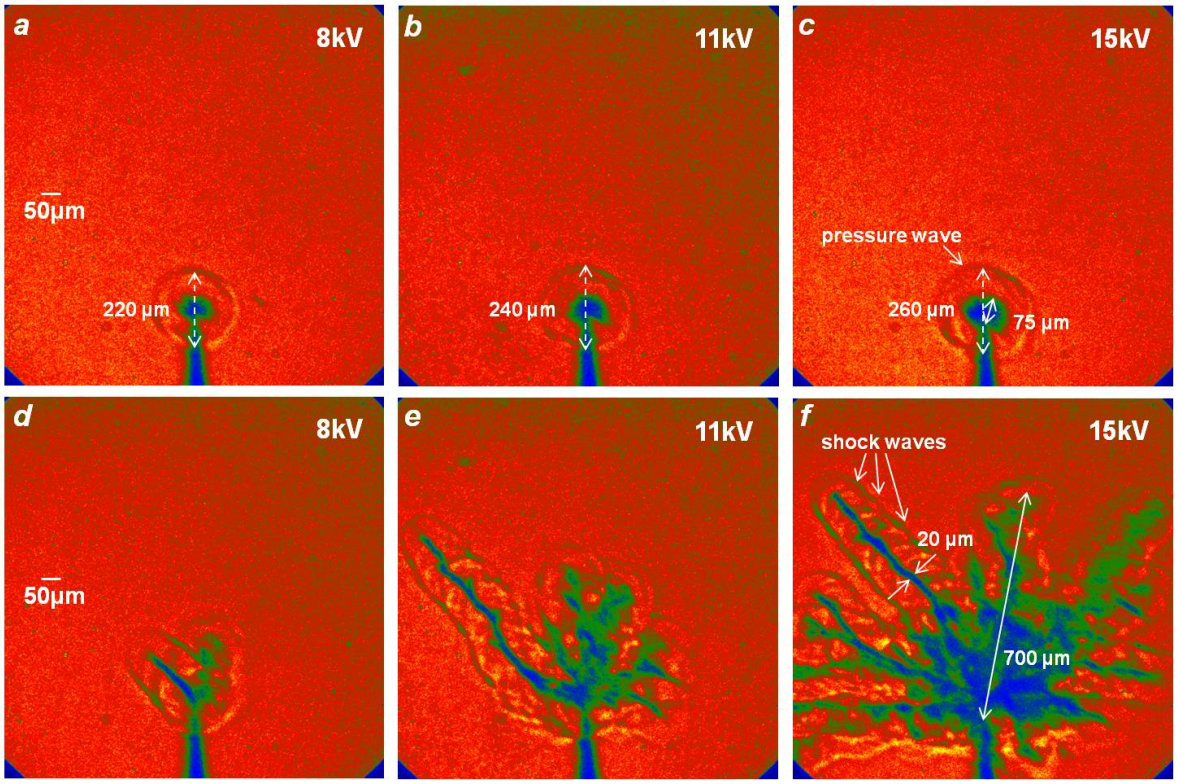

Figure 4.14 Shadowgraphs of (a)–(c) bush-like discharge pattern and (d)–(f) tree-like discharge. Post-discharge picture is taken at time instant 70 ns after the ignition. ICCD camera gate is 5 ns. False color.

Statistical analysis was applied in a series of 150 shots at voltage values between 8 and 15 kV with the step of 1 kV. Figure 4.15 demonstrates the number of bush and tree-like discharges ignited at given voltage amplitude and normalized by the total number of shots. As one can see, for voltage amplitudes below 8 kV (1.7×10^9 V/m) the bush-like discharge was preferentially ignited. Statistics for both modes in the range of the applied voltages between 8 kV and 15 kV demonstrates a well-pronounced dependence with almost equal probabilities at the voltage amplitude of 11 kV. At higher amplitudes the tree-like discharge was mainly observed. For voltages above 15 kV the bush-like discharge was not practically observed.

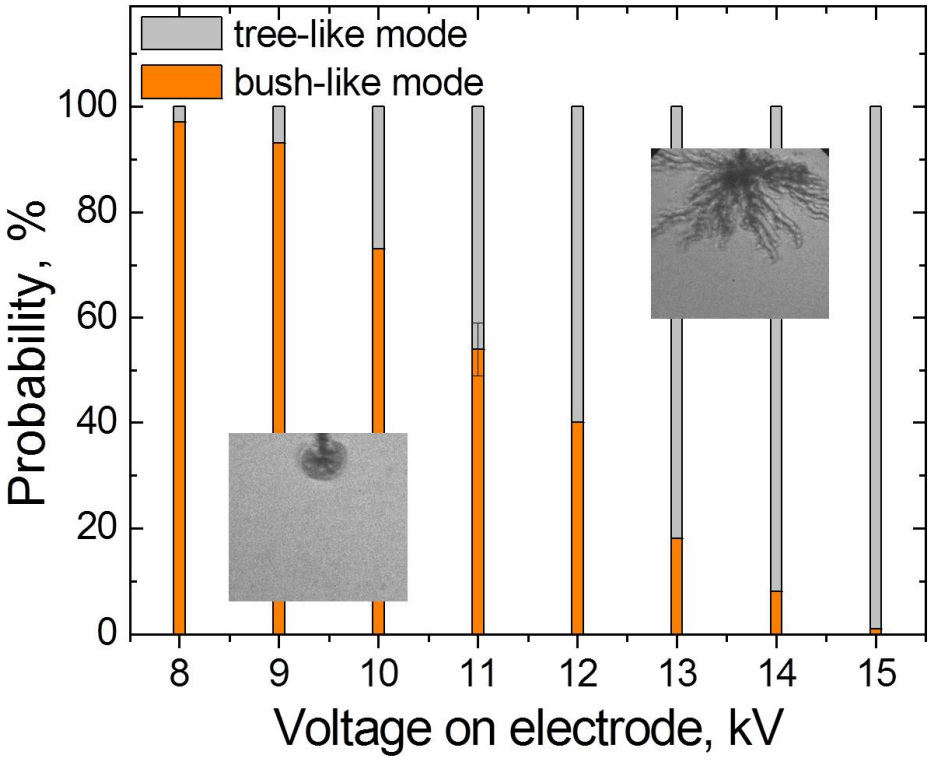

Figure 4.15 Probabilities of observation of tree-like and bush-like modes in deionized water as a function of applied voltage.

It is worth noting that the probabilities of the bush-like and the tree-like discharge appearance did not change with time in the course of the experiment neither if the repetition rate of applied HV pulses was increased from single shot to 10 Hz. It proves that the accumulation of discharge products (i.e. $^1O_2$, O_3, OH, H_2O_2) is not at the origin of one of the two modes. However the distribution of the tree-like and bush-like discharge was sensitive to the tip radius, for example when tip erosion occurred after about 10^4 shots the probability curve was shifted toward higher voltage amplitudes.

It was shown that

- Formation of the bush-like and the tree-like discharge depends on applied voltage. The probability to observe one of two discharge modes is a monotonous function of applied voltage. Bush-like

discharge is preferentially ignited at low voltage while the probability to observe the tree-like discharge increases with applied voltage.

- The increase in applied voltage from 8 kV to 15kV induced strong almost 4 times increase in the number and the length of the channels of the tree-like discharge.
- The diameter of bush-like discharge structure increases by only 30% - 40%
-

4.2.2 The effect of voltage amplitude on discharge development in ethanol and n-pentane

Ethanol

Figure 4.16, a-f shows the effect of the voltage amplitude on development of the bush-like and the tree-like discharge in ethanol. The amplitude of the HV pulse on the point electrode was varied between 5.5 and 9 kV. The shadowgraphs were taken at the time moment of 38 ns which corresponded to the end of HV pulse. As one can see from the comparison between Figure 4.16, a and b, the maximal length and the number of filaments of the bush-like discharge increases with applied voltage, that was already mentioned above for the discharge ignition phase (Chapter 4.1.4.1).

The bush-like discharge structure consisted of gaseous cavity of 20 – 30 µm in diameter and 3 – 5, in average, thin filaments characterized by the same distance between the filament tip and the point electrode. The maximal length of the structures was about 40 µm at 5.5 kV and 50 µm at 6 kV. The tree-like discharge under such low voltage demonstrated a filamentary structure with 1 to 2 channels of 3 – 6 µm in diameter as shown in Figure 4.16, d-e. The discharge channels had the maximal length of 65 µm; two spherical pressure waves were distinguished along the channel. The typical size of the bush-like and the tree-like discharge in ethanol were quite similar. However, the absence of the gaseous cavity in the case of the tree-like mode and only one shock wave observed for the bush-like discharge suggest that

mechanisms of discharge propagation should be different as in the case of deionized water. When voltage was raised up to the value of 9 kV, the typical patterns of two modes are drastically changed. Figure 4.16, c demonstrates the bush-like discharge structure at the end of 9 kV voltage pulse. One can still recognize the initial cavity of 45 µm in diameter on the pin electrode and a spherical shock wave around the discharge structures. The discharge channels were 100 µm long with diameter of 8 – 15 µm. At the extremity of two most extensive channels a new bush-like structure could be seen. Despite the overall complexity of the shadowgraph pattern one can notice a series of pressure waves along the discharge channels. A tree-like discharge at 9 kV, shown in Figure 4.16, f was formed by 2 – 3 parent channels with maximal length of 150 µm and diameter 15 µm. The parent channels demonstrated a dozen of thinner and shorter daughter branches that were also branched in turn. All the discharge filaments produced shock waves.

Pentane

In n-pentane filamentary tree-like discharges were observed at the voltage amplitude of 12 – 18 kV, whereas at lower voltages only bubble formation was detected. Figure 4.16, g-I provide typical shadowgraphs of tree-like discharge in n-pentane at 12 – 18 kV observed in post-discharge phase at 68 ns. As one can see the number of channels increased from 1 to 4, and the average discharge length from 70 to 100 µm with voltage amplitude. The diameter of the discharge channels did not show noticeable dependence on the applied voltage and was about 10 µm. Shock waves were observed along the discharge channels.

As it was shown that

- In ethanol the bush-like and the tree-like discharge demonstrate rather similar typical size at given applied voltage
- In n-pentane the number of channels increases gradually (4 – 5 times) with applied voltage between 12 kV and 18 kV, while the maximum discharge length increase only by 40%.

In the following sections the detailed time-resolved analysis of bush and tree-like discharge dynamics will be provided.

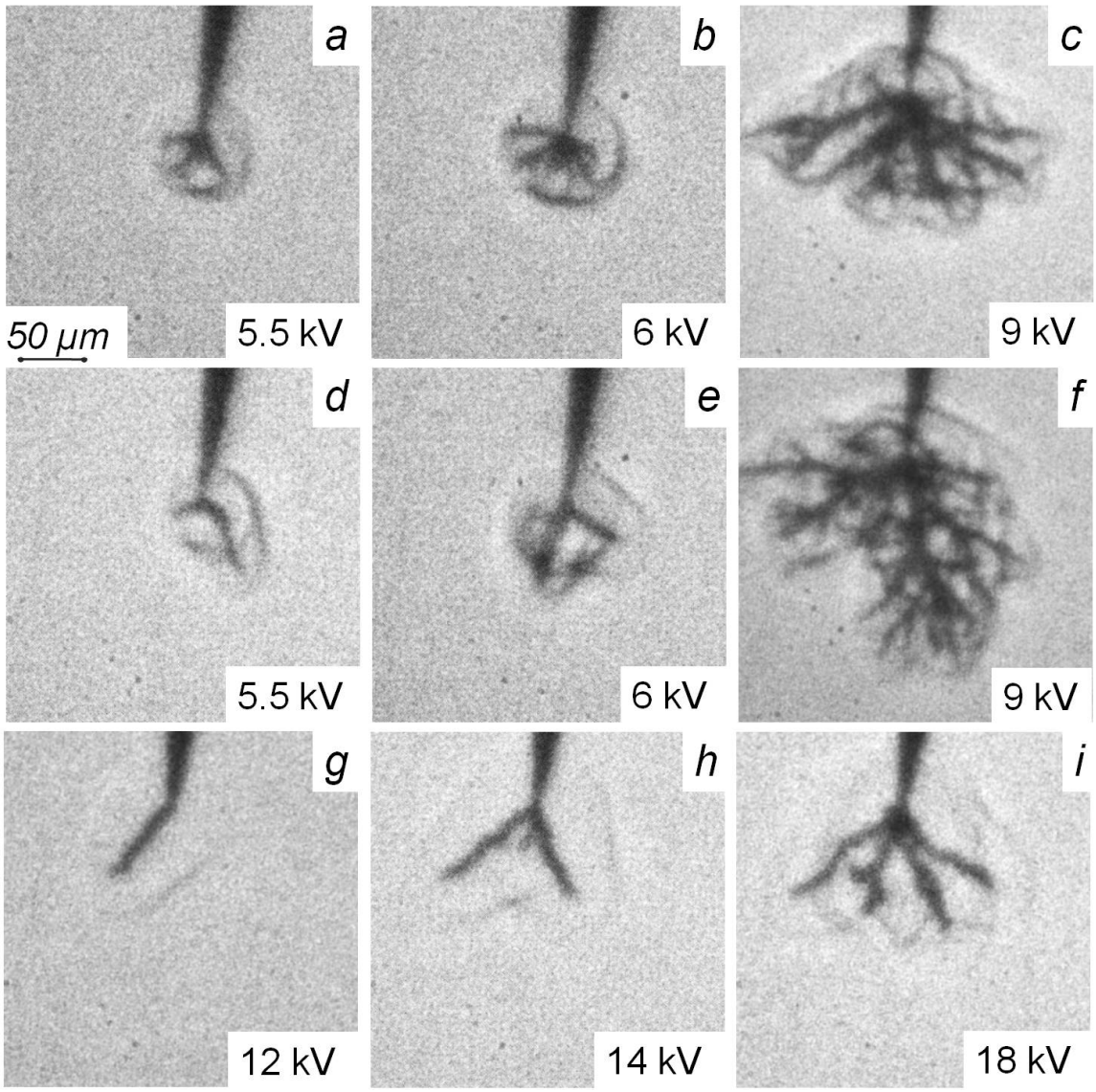

Figure 4.16 Effect of voltage amplitude on maximal size of slow mode at a) 5.5 kV, b) 6 kV, c) 9 kV and fast mode at d) 5.5 kV, e) 6 kV, f) 9 kV observed at 38 ns. Typical structures of filamentary discharge in n-pentane under g) 12 kV, h) 14 kV, i) 18 kV observed at 68 ns.

4.2.3 Propagation of bush-like discharge in deionized water and ethanol

The propagation dynamics of bush-like mode can be conventionally divided into two phases: discharge/electric field driven propagation and hydrodynamic expansion. During the first phase the discharge propagated in three forth pi spherical form consisted of the discharge channels and a spherical shock wave enveloping the discharge structures

as it is shown in Figure 4.17, a-d. The discharge pattern appeared uniform at the early stage of propagation due to the intensive light scattering on density gradients induced by discharge channels and strong shock wave. Discharge channels propagated in the trail of the shock wave till the end of the plateau of the applied voltage pulse (Figure 4.17, d).

Figure 4.18 shows X – t diagram of the bush-like discharge dynamics. As one can see the maximal velocity of the discharge structures and the shock wave front at ignition is about 4.3 km/s and decreases exponentially over 30 ns. Then the discharge channels almost stop to propagate in axial direction while pressure wave continue to propagate with acoustic velocity (1.48 km/s). At the end of the pulse one can distinguish 6 – 7 channels about 50 µm in length and 8 – 10 µm in diameter as shown in Figure 4.17, e. After the end of the HV pulse the discharge channels coalesce while the pressure waves propagate away from the channel tips (Figure 4.17, f-g). At about 200 ns after the ignition the discharge pattern demonstrates a hemispherical structure with a diffusive boundary, however several expanded channels that appear darker on the shadowgraph can still be distinguished (Figure 4.17, h). We have already mentioned in Chapter 3.5 that due to reflection from the coaxial line open end in the discharge device and from zero impedance of closed HV diode in pulse generator, a series of reflected pulses occurs for one generated pulse.

It was shown above that the reflected pulses can affect the bubble expansion dynamics by inducing the partial discharge in gaseous cavity, although no light or shock wave emission was detected. The detailed systematic analysis of the discharges produced by reflected pulses in the case when bush and tree-like mode are ignited over the first pulse will be provided in the Chapter 4.4. Here we will restrict ourselves by the consideration of the first reflected pulse of negative polarity arriving on the point electrode 260 ns after the initial positive pulse. As one can see in Figure 4.17 i the reflected negative pulse induces axial and radial expansion of the discharge channel accompanied by the emission of

shock waves. This fact indicates on the discharge initiation inside the existing bush-like structure.

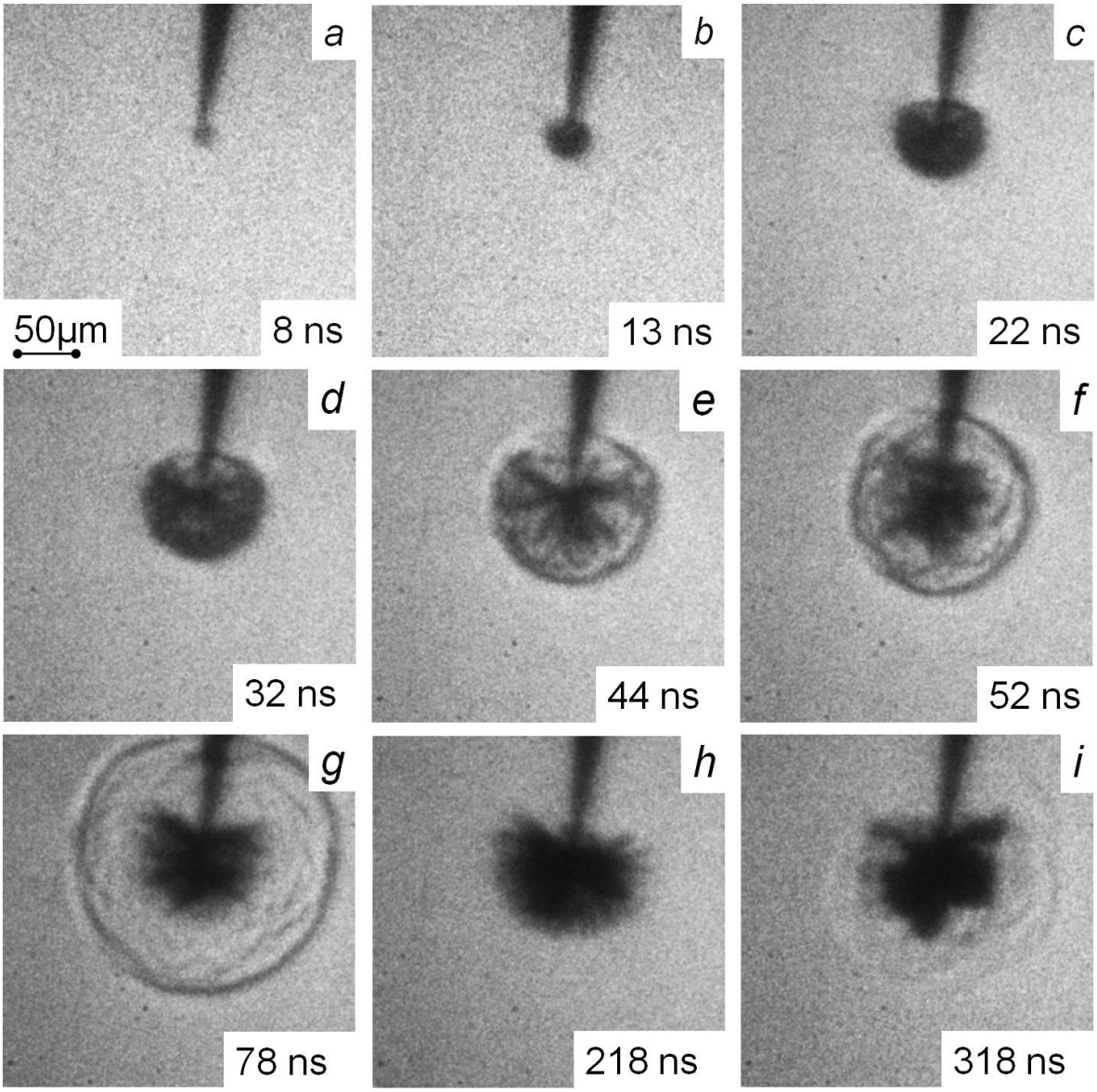

Figure 4.17 Propagation dynamics of bush-like discharge at 9kV in deionized water. Tip diameter is 2 μm. iCCD camera gate is 2 ns.

It should be noted that, the diffusive shell around the discharge channels disappears after the negative pulse. The nature of refracting medium cloaking the discharge structure is unclear. The shell appears after the pulse end, while its rather symmetrical hemispherical form follows the field distribution in the vicinity of the tip. It seems possible that the passage of the shock wave can induce the cavitation of submicron bubbles which then stick to the charged interface of

discharge channels. The strong electric field induced by the reflected pulse can possibly led to collapse of the bubbles.

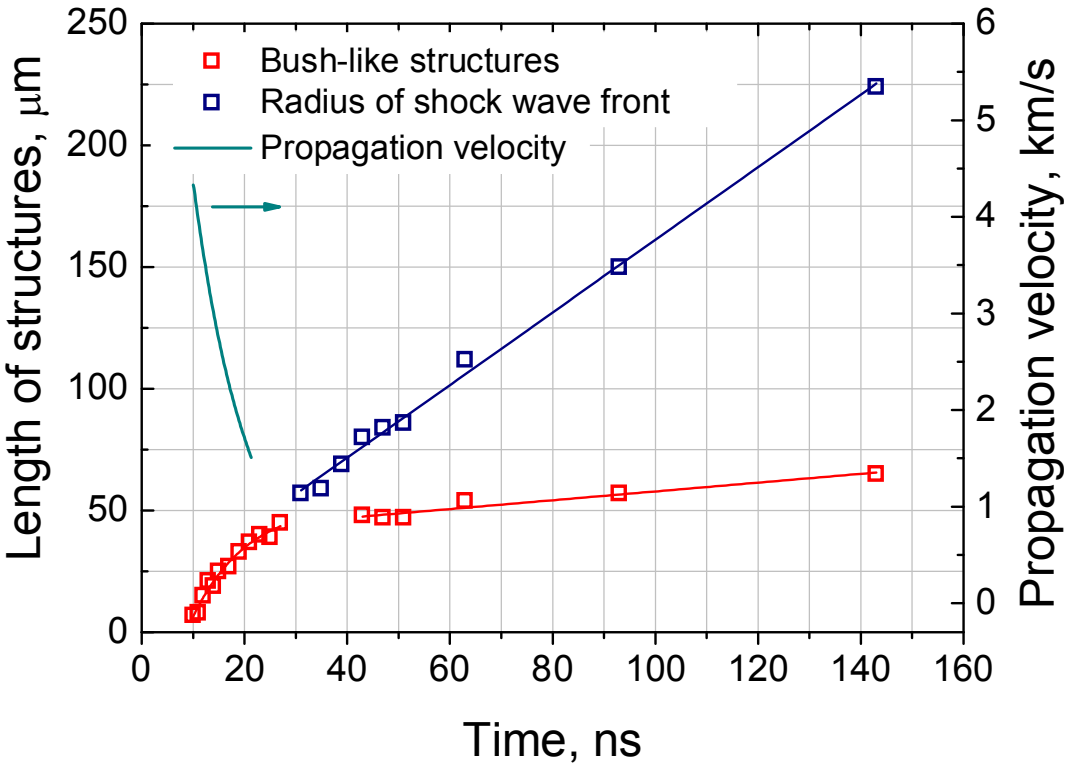

Figure 4.18 X-t diagram and derived velocity of bush-like discharge at 15 kV.

One can see that at lower voltage amplitude of 4 kV the discharge channels originate from the cavity on the point electrode while shock wave can be discerned already at 12 ns (Figure 4.19). Thin channels expansion in axial direction follows propagation of the shock front. At the end of the HV pulse plateau the discharge channels almost stop to propagate. Over the trailing slope of the voltage pulse the thinner extremities of discharge channels collapse and disappear (Figure 4.19). After the end of the HV pulse the discharge channels demonstrate lateral expansion and coalescence resulting in formation of a spherical cavity with diameter of 80 µm as observed 1.5 µs after the discharge ignition. As can be seen in Figure 4.19, h the cavity collapses at about 10 µs.

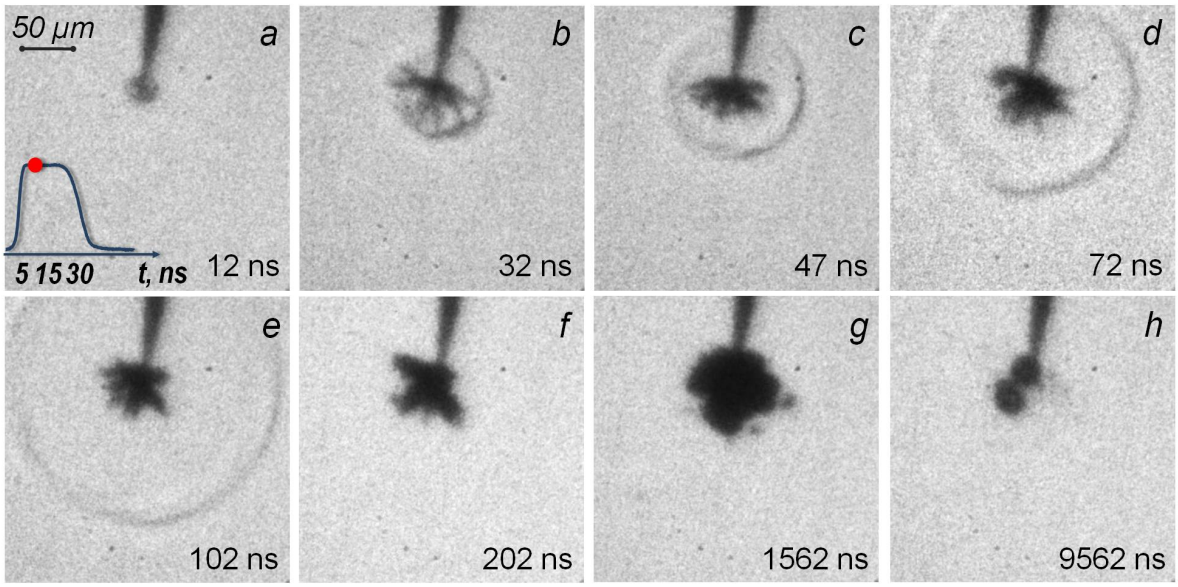

Figure 4.19 Ignition and dynamics of the bush-like mode in deionized water at 4 kV (the same conditions as for bubble formation).Single-shot images, ICCD camera gate is 2 ns.

Figure 4.20 gives an X-t diagram of the bush-like discharge at 4 and 9 kV of applied voltage. Since the discharge structures propagate simultaneously with the shock wave front, one can use the shock wave velocity as an estimate for discharge propagation velocity. Note that the spherical pressure wave produced by the bush-like discharge propagates with a supersonic velocity of 2.2 and 4.2 km/s for 4 and 9 kV respectively. Maximal shock wave velocity of 2.2 km/s gives for initial pressure the value of 1.2 GPa (see Section 4.3.1). The collapse of the discharge channels which occurs over the trailing edge of the voltage pulse possibly means that the pressure inside the channel is lower than the surface tension. Simple estimate considering the channel radius of 2 µm gives the excess pressure inside the discharge channels below $3 \cdot 10^4$ Pa. Apparent contradiction induced by 5 order of difference between the initial discharge pressure and the pressure inside the discharge channels at the end of the HV pulse can be due to the strong ponderomotive pressure stretching the channels along the electric field gradient. The total pressure inside the discharge structures is the sum of gas pressure, surface tension and ponderomotive pressure. When at the end of the HV pulse electric field decreases and ponderomotive

pressure drops with the field the surface tension exceeds the gas pressure inside the channels.

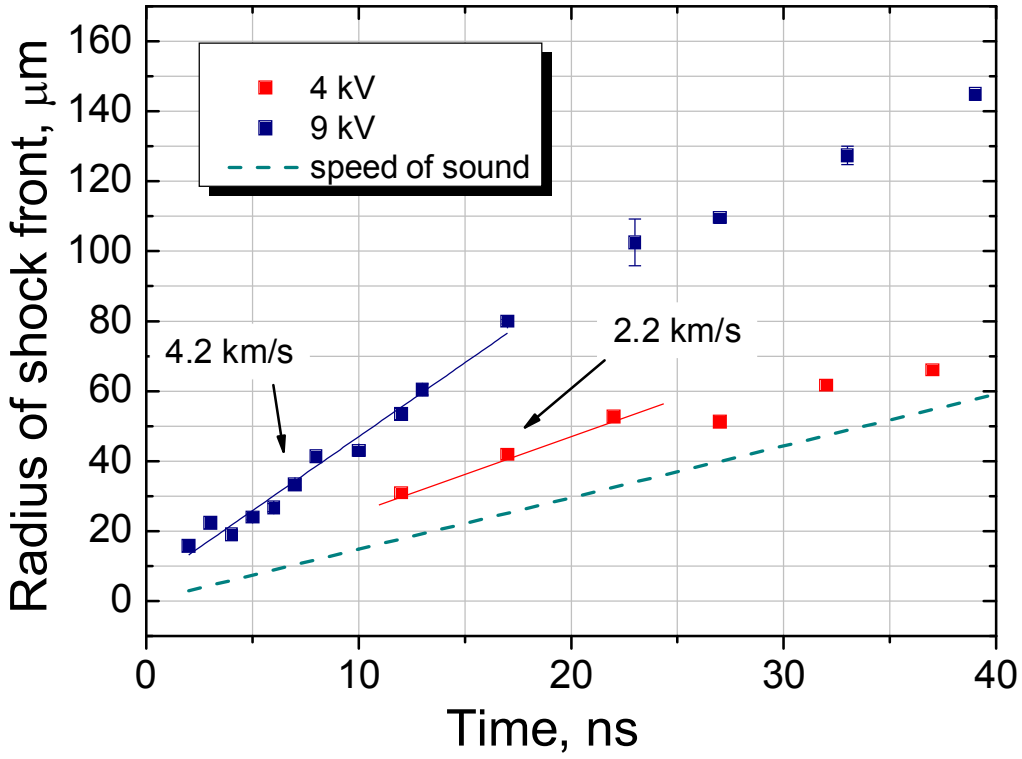

.

Figure 4.20 X-t diagram for radius of shock wave velocity produced by slow (bush-like) discharge in deionized water ignited at 4 and 9 kV on the pin electrode.

Quite similar bush-like discharge dynamics was observed in ethanol. Figure 4.21 demonstrated the variation of the discharge length at the ignition at 5.5 and 9 kV. Likewise the bush-like discharge in water, the discharge channels propagated synchronously with the shock wave during the constant voltage part of the pulse. The maximal propagation velocity was about 2 km/s at 5.5 kV and 3 km/s at 9 kV. The maximum velocities were about 30% lower comparing to the bush-like discharge propagating in water under the same conditions. The shock wave velocity decreases exponentially during the pulse and degenerates into acoustic wave at the trailing slope of the HV pulse as shown in Figure 4.22.

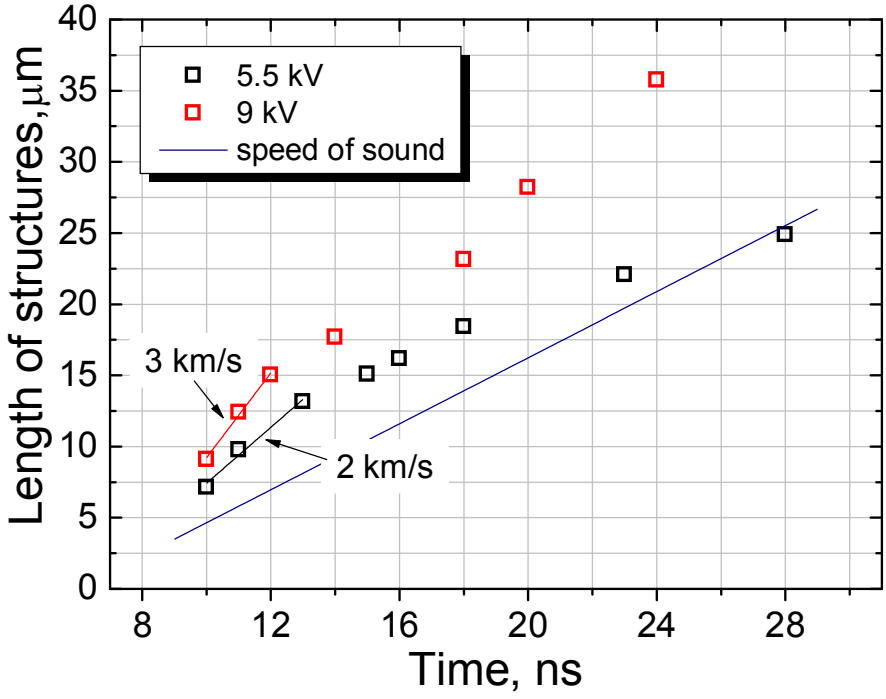

Figure 4.21 X-t diagram for slow mode formation in ethanol at 5.5 and 9 kV. Speed of sound in ethanol at 20 C equals 1160 m/s is given for the reference.

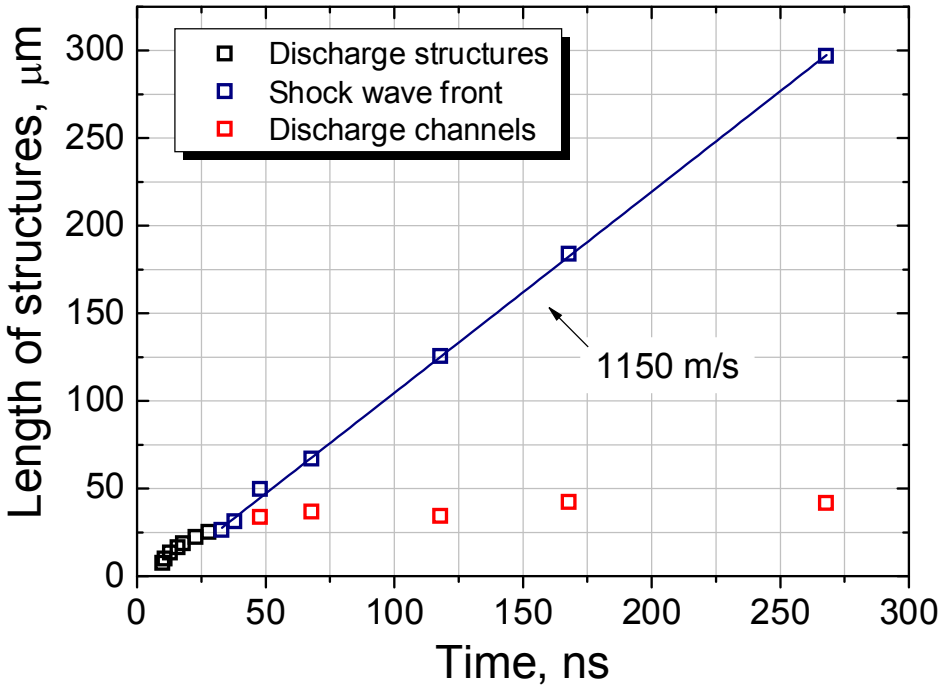

Figure 4.22 X-t diagram of bush-like discharge in ethanol at 5.5 kV.

4.2.3.1 **Conclusions on propagation of the bush-like mode**

As we have seen above, the propagation dynamics of the bush-like discharge is a rather complex phenomenon. The propagation starts with supersonic expansion of low density cavity accompanied by emission of a shock wave. Discharge channels expand from the cavity, presumably driven by ponderomotive and hydrodynamic forces, and propagate in the trail of the shock wave with the supersonic velocity. At high voltage amplitudes (9 kV and higher) a partial discharge ignites inside the channels leading to their radial expansion and emission of a shock waves. At lower voltage no discharge occurs in the channels, and they collapse at the end of the pulse due to the surface tension. In the post-discharge the channels coalesce producing a hemispherical gaseous cavity. At higher voltages the cavitation occurs after the passage of the shock wave. The submicron cavities collapse under the electric field of the reflected negative pulse. A very similar dynamics of bush-like discharge was observed in ethanol, whereas typical propagation velocities were 30% lower as compared to deionized water.

4.2.4 Propagation of tree-like mode

In this section we will demonstrate the results of time-resolved shadowgraph and emission visualization of the tree-like discharge in deionized water performed with two synchronized iCCD cameras. The application of two iCCD cameras with a controlled delay allows precise measurements of fast discharge mode propagation especially at the discharge ignition when the propagation velocity was the highest. Time resolved emission imaging and current measurements will be presented for the tree-like discharge in order to understand plasma evolution inside the discharge channels during the applied voltage pulse. Propagation velocities of tree-like mode in ethanol and n-pentane will be compared with the case of deionized water.

4.2.4.1 Tree-like discharge development in deionized water

As it was demonstrated in Section 4.1.2 the initiation of the tree-like discharge in deionized water is characterized by strong light emission and fast propagation of thin, about several microns in diameter,

discharge filaments. The average number of discharge channels and their length were reproducible at the given amplitude of HV pulse; however the size and number of branches of independent channels varied considerably. Taken into account a high propagation velocity and the complexity of discharge pattern two synchronized iCCD cameras were applied to study the discharge dynamics. Two shadow or emission images were obtained by placing a 50/50 beam splitter after the imaging lens L3 as shown in Figure 3.6.

Emission visualization was performed with the same optical arrangement by simple removing of back light beam. Two identical iCCD cameras were triggered using the same back current shunt signal (BCS). The time delay between two cameras due to the slightly different intrinsic delays was calibrated by appearance of the light emitting spot at initiation of the tree-like discharge and was found to be 4 ns. Figure 4.23 gives an overview of the discharge propagation registered in shadowgraph and emission visualization mode over the positive pulse of 15 kV. The provided figures correspond to two time instants of the same HV pulse, delayed by 1 ns at the beginning of the pulse and by 2 ns starting from 13 ns. The time in frames represent the real time during the HV pulse, where zero time instant was chosen as 10% of the maximal amplitude at the rising slope. Shadowgraphs and emission images reported for the same time delay correspond to two different shots, since the broadband emission of the flash lamp and broad spectrum of plasma emission, as will be shown below, could not be filtered.

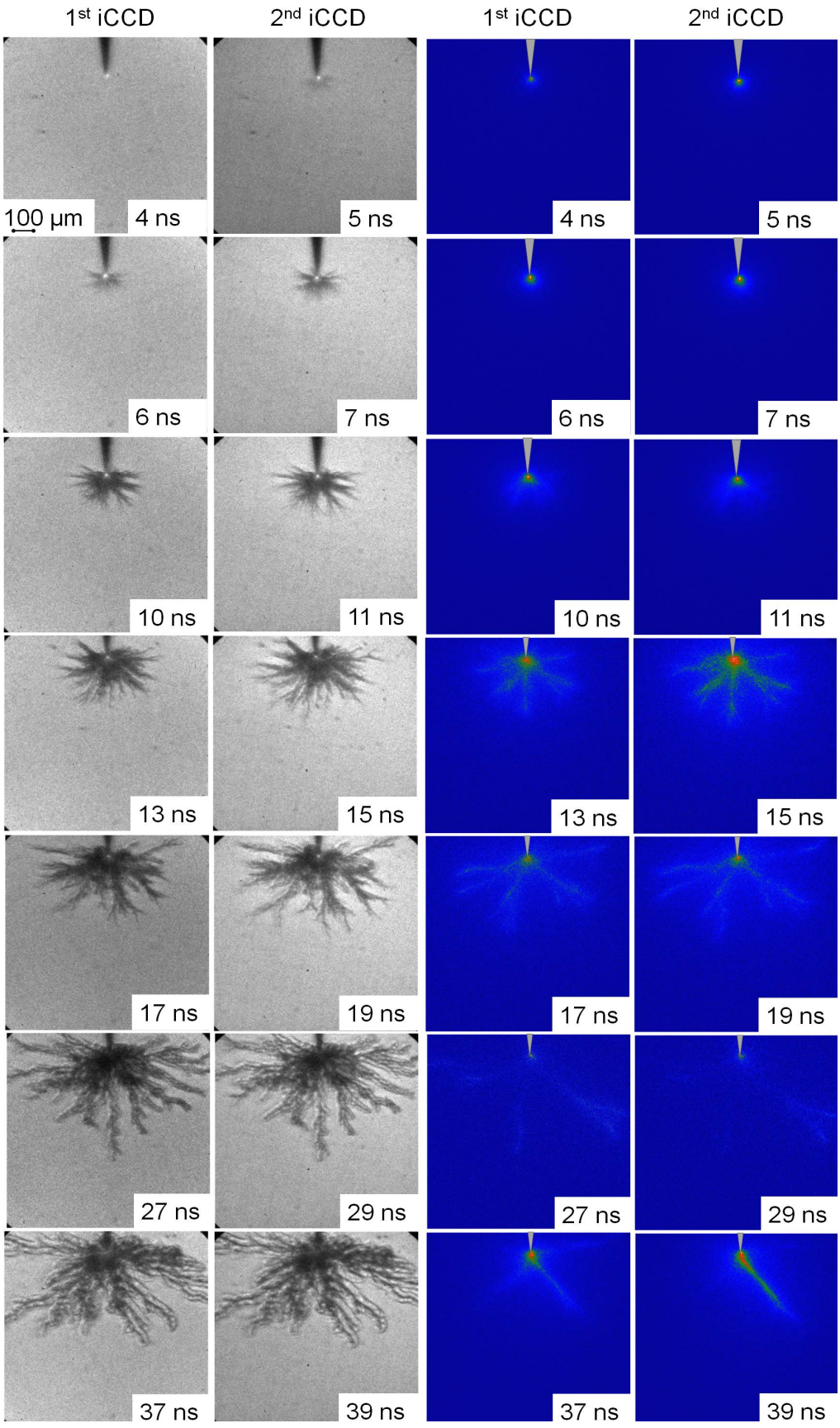

Figure 4.23 Shadowgraph and plasma emission visualization of tree-like discharge in deionized water under 15 kV positive pulse with two synchronized iCCD cameras.

As one can see the first manifestation of the discharge ignition consisted in appearance at 4 ns of the emitting spot with brightness, exceeding the intensity of back illumination. The light spot is clearly seen in shadowgraph and in emission images of the discharge. In 1 ns a set of weakly refracting channels with a maximal length of 60 µm became visible in the shadowgraph while nearly spherical emitting volume increased by more than two times. Note that due to the light scattering and strong intensity variation across the discharge pattern only rough estimation of the size of the emitting structures can be done. Nevertheless, the maximal length of the discharge shadow and characteristic size of emission pattern were in good agreement over first 30 ns of the discharge propagation.

At 6 – 7 ns low density, 5 µm in diameter channels and exceeding 100 µm in length became visible whereas the emission pattern still had a spherical shape. The discharge structure rapidly increased in size, demonstrating 8 – 10 branched parent channels at 10 – 11 ns distinguishable in the shadowgraphs and emission images. At 15 ns a series of shock waves along the discharge channels became apparent, while the emission intensity reached its maximum. Well defined filamentary emission pattern was clearly seen. The plasma emission intensity decreased gradually between 15 ns and 29 ns, however discharge channels continued to propagate reaching 700 µm in length.

Propagation of the discharge filaments initiated formation of a train of the spherical pressure waves with a step of about 40 µm, forming a conical wave front around the streamer. Starting from 30 ns which corresponds to the trailing slope of the applied HV pulse the discharge reignited in several parent channels as was evidenced by emission visualization, whereas no formation of new discharge channels was observed on the shadowgraphs. In Figure 4.23 one can clearly see the reillumination of one of the discharge channels, occurred between 37 ns and 39 ns.

In order to calculate the discharge propagation velocity the maximal length of the discharge channels was estimated as the radius of the

arch-line enveloping the discharge structure with the origin on the tip. The radius of the envelope was measured using vector graphic software (Inkscape) in pixel numbers and then converted into microns using a calibration with 50 µm tungsten wire. The x-t diagram and calculated velocity for the tree-like discharge are presented in Figure 4.24. The length of the discharge shadow structures detected with two iCCD cameras is approximated with the negative exponent curve. The propagation velocity was calculated as a difference in the discharge length detected by the 1st and 2nd iCCD cameras divided by the time delay between the gate opening of each camera. Maximum value of the discharge velocity was about 60 km/s at ignition and decreased exponentially during the voltage pulse.

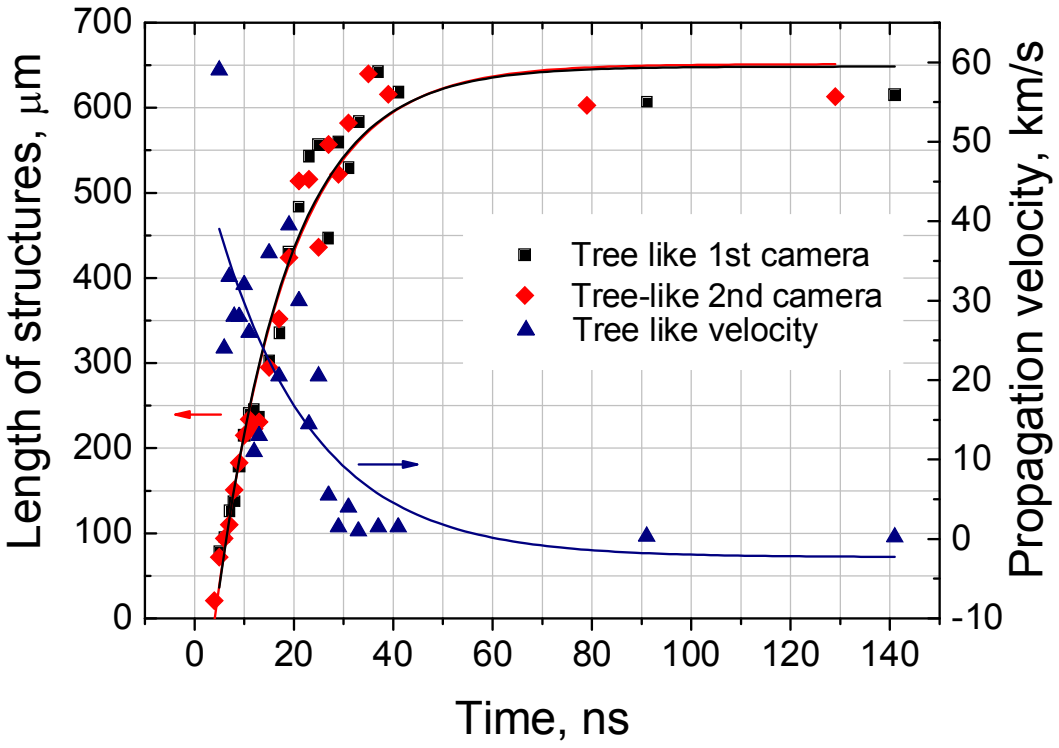

Figure 4.24 X-t diagram for tree-like discharge in deionized water at 15 kV.

It was found that the tree-like and the bush-like modes can be easily distinguished on the basis of emission pattern. Very weak, even being averaged over the entire HV pulse, glow-like emitting structure about 50 µm in size was typical for the bush mode (Figure 4.25, *). By comparing the emission with the shadow images one can easily see that

emission and shadow pattern of the bush-like discharge coincide, however, time resolved measurement are necessary to prove that light comes from the discharge volume and not from the track of a spherical shock wave. On the contrary, the tree-like mode was characterized by a strong light emission registered from the first nanosecond of the discharge propagation. As we have seen above, the filamentary discharge ignited as a bright emitting spot, preventing the shadowgraphic analysis during the first nanoseconds after ignition, before the plasma channels have appeared and became clear. Subsequent evolution of the emitting structure follows the propagation of the discharge filaments over the first 30 ns (Figure 4.23). We performed a detailed study of the evolution of the plasma emission intensity during applied voltage pulse. In order to avoid the variations of the intensity from pulse to pulse the discharge emission was averaged over 30 shots. Figure 4.25 shows time resolved evolution of the discharge emission at 12.5 kV. The emission pattern had a spherical structure over the first nanoseconds of propagation, turning in a fan-like structure starting from 8 ns. The emitting volume increased over first 22 ns and then decreased passing through its minimum at 25 ns and reignited during the trailing slope of the voltage pulse. Light emission completely extinguished when the voltage decreased to zero value.

The reillumination of the discharge channels at the voltage fall was reported for shorter nanosecond HV pulse of 10 ns (Starikovskiy *et al* 2011), for longer microsecond pulses with a relatively short voltage drop time of 20 ns (Nieto-Salazar *et al* 2005) and long voltage decay of several microseconds (Ceccato *et al* 2009). For short HV pulse of 10 ns the reillumination occurred during the plateau about 3 ns before the falling slope of the pulse. For longer pulses the discharge reignited at the trailing edge of the pulse. A series of light spikes, corresponding to successive reillumination were observed in the case of HV pulse with a long voltage decay. The reillumination spikes lasted about 20 ns and induced further propagation of the discharge channels in which the reillumination occurred (Ceccato *et al* 2009). In (Nieto-Salazar *et al*

2005) the authors observed a negative current spike which exceeded in amplitude the direct current signal during the discharge formation. Based on light emission and current measurements, it was suggested that a back-discharge due to the charge accumulation occurred in discharge channels. The idea of back discharge was supported by the absence of reillumination in saline solutions with high ionic conductivity (Ceccato *et al* 2009). At high ion concentration in water, efficient recombination at the interface between gaseous channel and bulk liquid prevents charge accumulation and no back discharge formation can be observed.

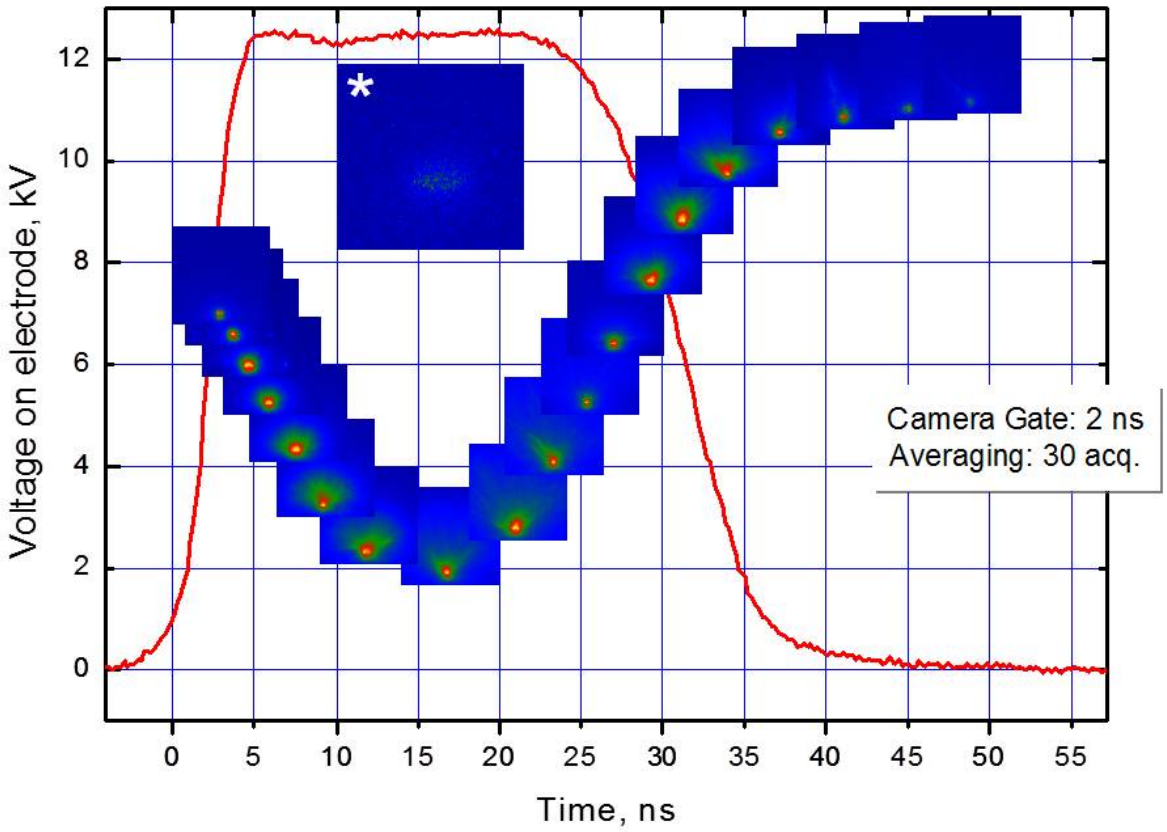

Figure 4.25 Time-resolved evolution of plasma emission averaged over 30 shots. iCCD camera gate is 2 ns. (*) Averaged optical emission from bush-like discharge in single shot. iCCD camera gate is 40 ns..

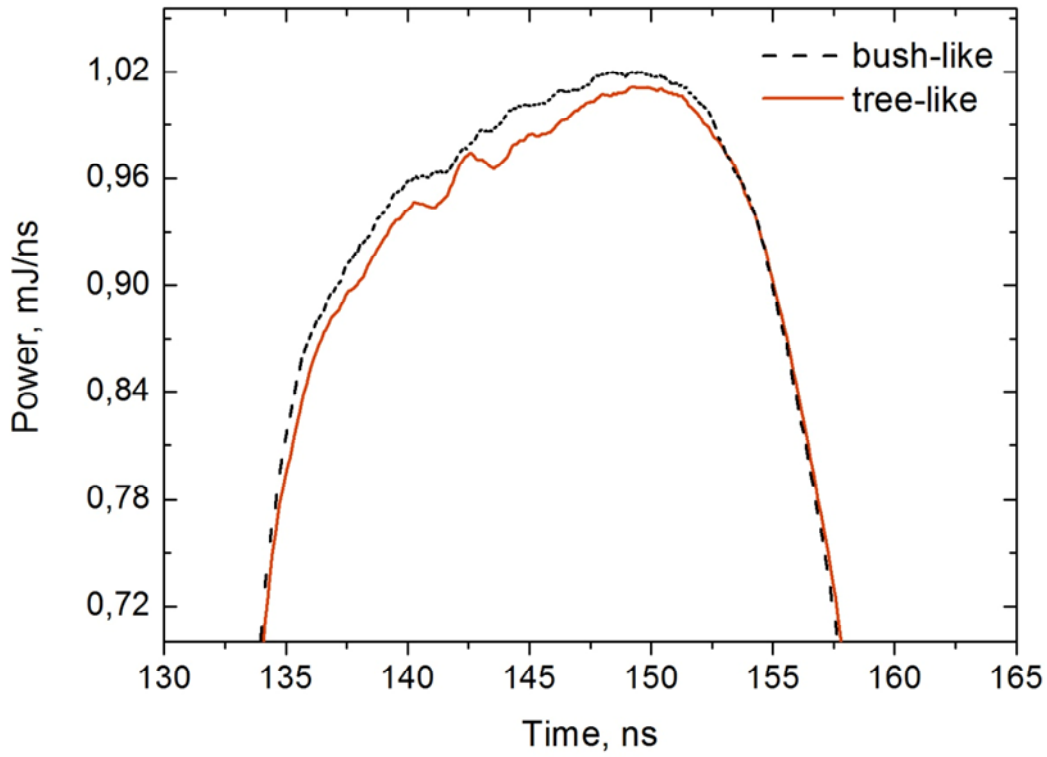

Figure 4.26 Electrical power calculated from BCS signals of pulses reflected on the electrode after ignition of bush-like and tree-like discharge at 15 kV. Total pulse energy is 30 mJ.

We attempted to measure the discharge current in order to check correlation between the light emission evolution and current signal. The discharge current and energy dissipation can be found from the difference between incident pulse, coming from generator and pulse, reflected from the open end in the discharge device, while pulse attenuation in cable should be taken into account. This difference gives the sum of the transient current associated with streamer propagation and the displacement current due to the charging of device capacity. The last one can be found in the case without plasma ignition by completely covering the pin with dielectric. It was found that transient current of the bush mode was less than the detection limit of the back current shunt (about 1 mA), and that the displacement current was dominating during the rising edge of the HV pulse. Therefore, for measurement of the discharge current in the tree-like mode it was possible to use the difference between the reflected pulses from tree-like and bush-like discharge ignited at the same voltage amplitude. Finally,

the energy absorbed in the tree-like mode can be calculated from the back current shunt signal using Equation 3.8. Back current shunt (BCS) gives the voltage signal induced across the shunt resistance ($R_s = 0.17$ Ohm) by current pulse passing in the coaxial cable. Therefore, the current can be obtained by dividing the BCS signal by the R_s. Figure 4.26 shows the zoom of the total power (the expression under the integral in Equation 3.8) of two averaged pulses reflected respectively after ignition of bush-like and tree-like discharge. Since bush-like and tree-like discharge ignited stochastically current signals were reordered with simultaneous optical control of the discharge. The difference in area under two signals gives the energy dissipated in the discharge over the rising slope and the plateau. It was found that at 15 kV the average energy dissipated in the tree-like discharge was about 0.2 mJ which corresponded to only 0.7% of total energy of the incident HV pulse.

Figure 4.27 shows maximal light emission intensity of the tree-like discharge and corresponding discharge current. As one can see the first maximum of the light emission coincides with the maximum of the current. Then the light intensity passes through the minimum and increases again at the trailing edge of the applied HV pulse. The current demonstrates a negative spike in this time period confirming that the back-discharge indeed occurred in the discharge channels. The duration of the current spike was equal to 5 ns and the amplitude was about 1.9 A. This was even higher than the current amplitude in forward discharge. The increase in maximal current of the back-discharge can be explained by partial pressure relaxation inside the discharge channels.

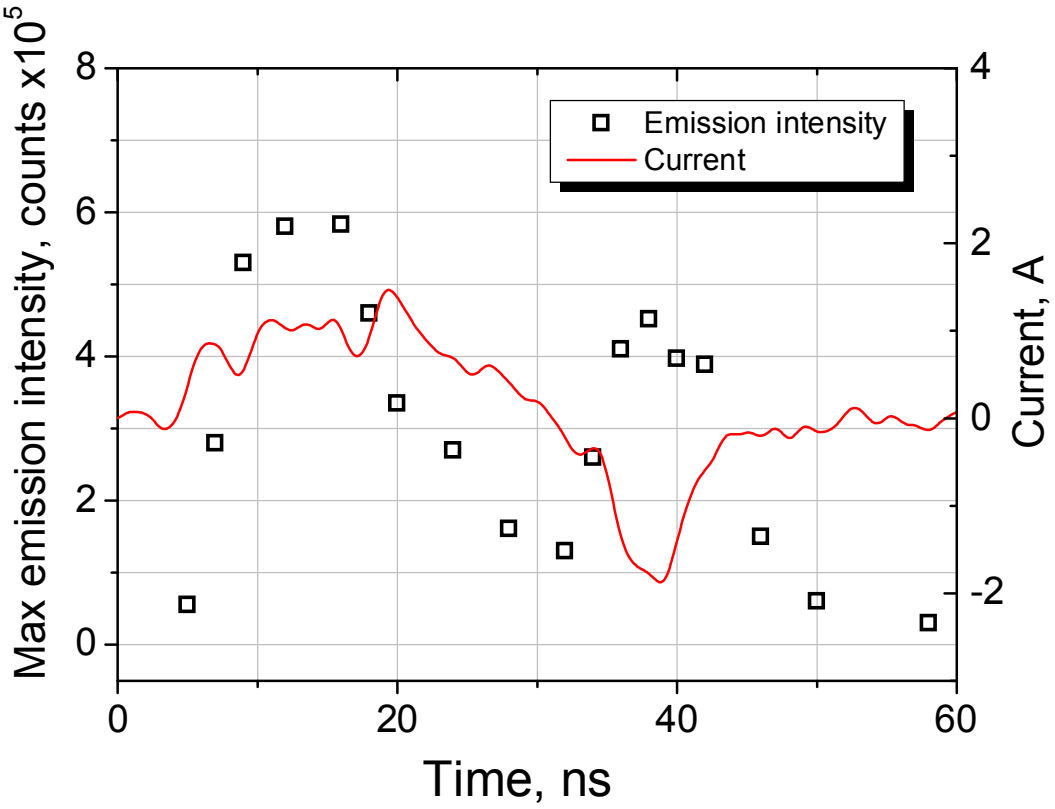

Figure 4.27 Evolution of plasma emission intensity and transient current of tree-like discharge in deionized water at15 kV.

4.2.4.2 Tree-like discharge development in ethanol

We have already mentioned that the filamentary tree-like discharge was also observed in ethanol at voltage amplitudes higher than 5.5 kV and in n-pentane starting from 12 kV. The discharge pattern was rather similar in ethanol at about 6 kV and in n-pentane at 12 kV with a few discharge channels originated on the pin electrode. At higher amplitudes of HV pulse strong branching of the discharge filaments was observed in ethanol while in n-pentane the number of unbranched channels increased gradually. Figure 4.28 gives an x-t diagram for the tree-like discharge propagation in ethanol at 5.5 kV and 9 kV. As one can see the length of the discharge channels increases linearly with time over first 20 ns. The discharge propagation velocity at this linear period is proportional to the HV pulse amplitude and is equal to 3.1 km/s at 5.5 kV and 4.8 km/s at 9 kV. At longer time delays the velocity

decreases exponentially. The maximal discharge length is equal to 70 µm and 150 µm respectively.

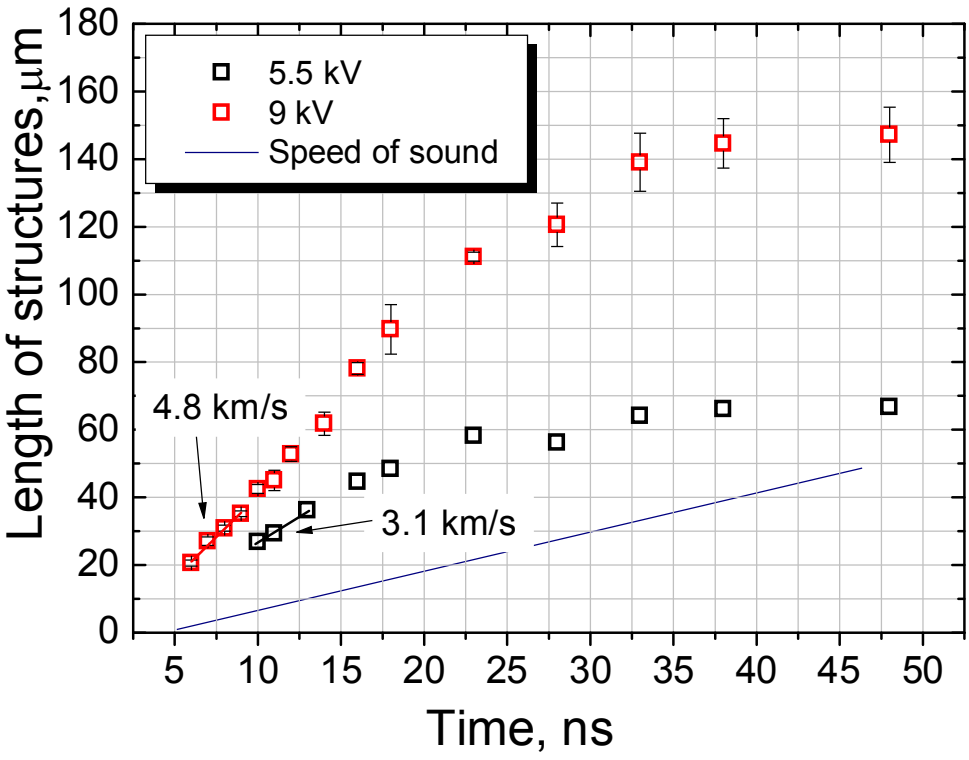

Figure 4.28 X-t diagram of tree-like discharge in ethanol at 5.5 and 9 kV.

4.2.4.3 Propagation of tree-like discharge in n-pentane

In n-pentane at 12 kV and 18 kV, as can been seen in Figure 4.29 the length of the discharge channels increases linearly during the plateau of the applied voltage pulse reaching 65 µm and 105 µm respectively. During the trailing slope of the pulse the discharge rapidly decelerateds and stops completely as voltage drops to zero. The maximal propagation velocity increase more than by a factor of two when voltage amplitude raised from 12 kV to 18 kV.

The linear growth of the tree-like discharge lasted about 10 ns in deionized water, 20 ns in ethanol and 27 ns in n-pentane. The discharge velocity was about 40 km/s in deionized water and about order of magnitude slower in ethanol and n-pentane. As we have seen from

optical emission and current measurements the charge deposition may be an important issue in the case of deionized water leading to field screening inside the discharge channels and, hence, can be responsible for velocity attenuation. In the case of water adsorbed charges can be stabilized by hydratation and polarization of liquid molecules. In ethanol, that is a polar liquid, charge accumulation seems to be relevant, however taken into account more than 10 times slower propagation velocity in ethanol as compared to deionized water, the charges have more time to recombine. No charge accumulation seems to occur in n-pentane under the conditions of a nanosecond pulse as follows from constant propagation velocity and which is in agreement with a nonpolar nature of n-pentane.

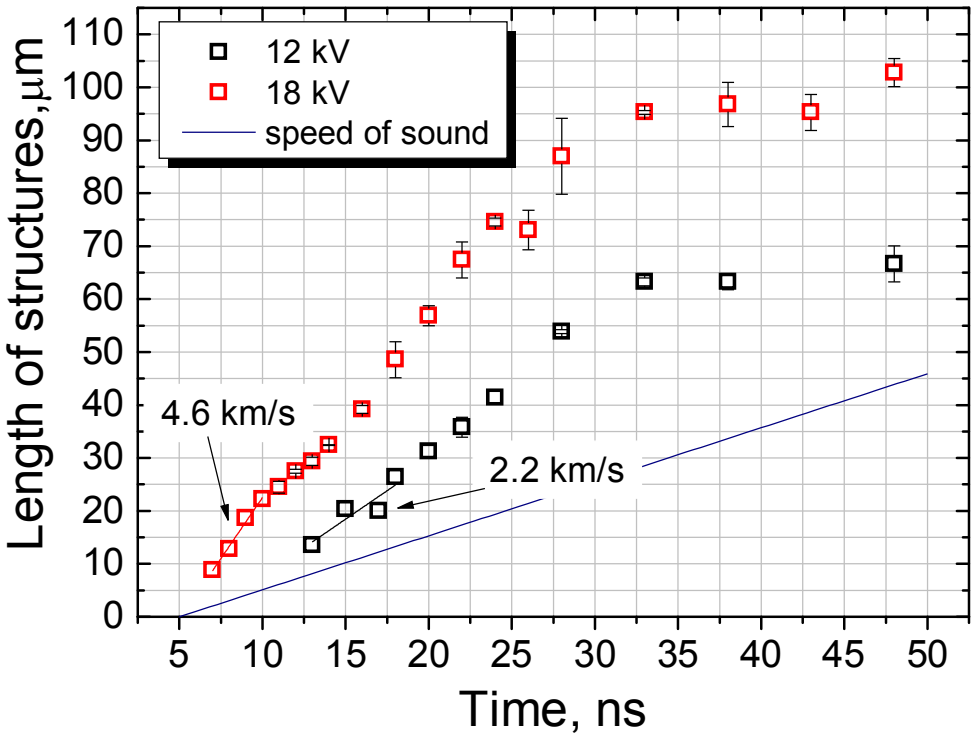

Figure 4.29 X-t diagram of filamentary discharge in n-pentane at 12 and 18 kV.

4.2.5 Conclusions on propagation dynamics of bush-like and tree-like modes

Time-resolved study of bush-like and tree-like discharge propagation in deionized water and ethanol and tree-like discharge in n-pentane was done.

The following peculiarities have been observed

- Bush-like and tree-like discharge in deionized water demonstrate rather different propagation dynamics. Bush-like discharge propagation is found to be less sensitive to the amplitude of the applied voltage, while a probability to observe the bush-like discharge decreases with the HV pulse amplitude. The bush-like discharge demonstrates an order of magnitude lower propagation velocity as compared to the tree-like discharge. Visualization of the discharge emission demonstrates three orders of magnitude lower plasma emission intensity in the case of bush-like discharge that is too weak to obtain time resolved evolution. Difference in propagation dynamics suggests that the mechanisms responsible for the propagation of the bush-like and the tree-like discharges are essentially different.
- Maximal velocity at ignition of the bush-like discharge varies between 2 km/s and 4.5 km/s at 4 – 15 kV of applied voltage. Propagation velocity decreases exponentially during the applied voltage pulse. A spherical shock wave produced at the ignition of the bus-like discharge degenerates to the acoustic wave during the applied voltage pulse. At high voltages (9 kV and higher) the propagation of the discharge filaments produces weaker shock waves. At voltage of 4 kV the discharge channels collapse at the trailing edge of HV pulse. Current of the bush-like discharge is much smaller than the detection limit.
- Tree-like discharge has maximal propagation velocity of 60 km/s at 15 kV. For the tree-like mode propagation of the discharge channels is accompanied by strong light emission and formation of a series of shock waves. Emission pattern demonstrates

filamentary structures starting from 10 ns that are similar in size and form with discharge shadow structures. Light emission intensity was found to have two maxima: about 15 ns during the plateau of applied HV pulse and at the voltage drop over the trailing edge. Light emission intensity is correlated with current signal demonstrating a negative current spike at the trailing edge of the applied HV pulse. It is suggested that the back-discharge due to the charge accumulation occurs in gaseous channels. Maximal direct discharge current is 1.5 A and back-discharge current has an amplitude of 2 A. The total discharge energy is about 0.2 mJ for one pulse.

- In ethanol the difference in propagation dynamic between bush and tree-like mode was less evident. Maximum propagation velocity of bush-like discharge was found to be 2 – 3 km/s that was only 30% lower than the tree-like discharge velocity at given voltage amplitude.
- In n-pentane propagation velocity of tree-like discharge at 12kV and 18kV was 2.2 km/s and 4.6 km/s which was comparable with the tree-like discharge velocity in ethanol at 5.5 kV and 9 kV respectively.

4.3 Pressure evolution in the discharge channel

Propagation of the tree-like discharge induces formation of the series of shock waves along the pass of the discharge filament. The rapid radial expansion of the discharge channels was observed already during the HV pulse and continued in the post discharge phase as can be seen in Figure 4.30. These observations suggest the elevated pressure inside the discharge channels. We will apply two methods in order to get the estimation of the gas pressure inside the discharge channel. The first method is based on measurement of the initial pressure of the shock wave and the second method considers discharge channel expansion dynamics

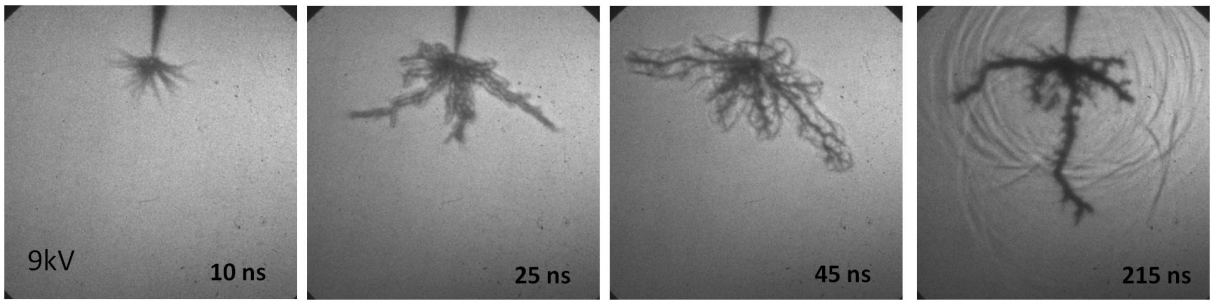

Figure 4.30 Propagation of tree-like discharge in deionized water at 9 kV

4.3.1 Shock wave velocity measurements

One can assume that the shock wave is emitted at the moment of channel formation and, hence the pressure of the shock wave is equal to the initial discharge pressure. The shock wave pressure is related to the shock wave velocity through the Hugoniot equations (Katsuki *et al* 2006):

$$P = \rho_0 u_s u_p \qquad (4.8)$$

$$u_s = A + B u_p, \qquad (4.9)$$

where ρ_0 is the water density, u_s is the shock wave velocity, u_p is the particle velocity, A (1.45 km/s) is the acoustic sound velocity in water and $B = 1.99$, which is experimentally derived parameter (Nagayama *et al* 2002). Therefore, P can be found as

$$P = \rho_0 u_s \frac{u_s - A}{B} \qquad (4.10)$$

The linearity of Hugoniot shock-particle velocity was experimentally demonstrated up to the pressure values of several GPa (Nagayama *et al* 2002)

4.3.2 Expansion dynamics of the discharge channel

We will consider the pressure acting on the cavity surface expanding in liquid. The liquid flow is assumed to be isentropic and is described by the momentum conservation (4.11), the continuity equations (4.12) and the equation of state (4.13) (Naugolnykh and Roy 1974):

$$\frac{\partial v}{\partial t} + \boldsymbol{v}\nabla\boldsymbol{v} = \frac{-\nabla P}{\rho} \tag{4.11}$$

$$\frac{\partial \rho}{\partial t} + \nabla \cdot (\rho \boldsymbol{v}) = 0 \tag{4.12}$$

$$P = A\left(\frac{\rho}{\rho_0}\right)^n - B, \tag{4.13}$$

where A, B and n are empirically defined parameters. In the case when liquid density varies slightly during the expansion process one can use the first integral of the Euler equation (4.12) in a form given by:

$$\frac{P}{\rho_0} + \frac{1}{2}v^2 + \frac{\partial \varphi}{\partial t} = const, \tag{4.14}$$

whereφ is velocity potential ($v = \boldsymbol{\nabla}\varphi$). For cylindrical cavity of length $l \gg R$ the velocity potential can be obtained in form

$$\varphi \approx -\frac{R'^2}{2} ln\left(\frac{2c_0 t}{R}\right) + \frac{R^2 t}{2} \tag{4.15}$$

Finally the pressure acting on cylinder surface is given by

$$P - P_0 = (\rho_0 R'^2 + RR'')ln(2c_0 t/R) - 1/2\,\rho_0 R'^2, \tag{4.16}$$

where P_0 is the hydrostatic pressure, ρ_0 is the density of liquid, c_o is the acoustic velocity and R is the radius of discharge channel. This formula (4.13) is valid for subsonic expansion of cylindrical cavity with length

$$l \gg c_0 \tau \gg R, \tag{4.17}$$

where τ is a typical time of channel formation.

4.3.3 Pressure evolution in discharge channel at low applied voltage

Figure 4.31 demonstrates successive shadowgraphs of the tree-like discharge propagation at 6 kV taken with two iCCD cameras. As one can see, the tree-like discharge in deionized water at 6 kV is characterized by 1 to 2 well separated discharge channels. Discharge energy measurements demonstrated that 80% of the total absorbed energy dissipates during first 15 ns after discharge ignition. Therefore, starting from 15 ns one can neglect the energy input in the channel expansion process. It is demonstrated that the discharge channels reach

their maximal length of 200 µm already at 10 ns. The initial radius of the channels is less than 5 µm. Therefore, the condition 4.14 seems to be satisfied for the tree-like discharge channel under given conditions.

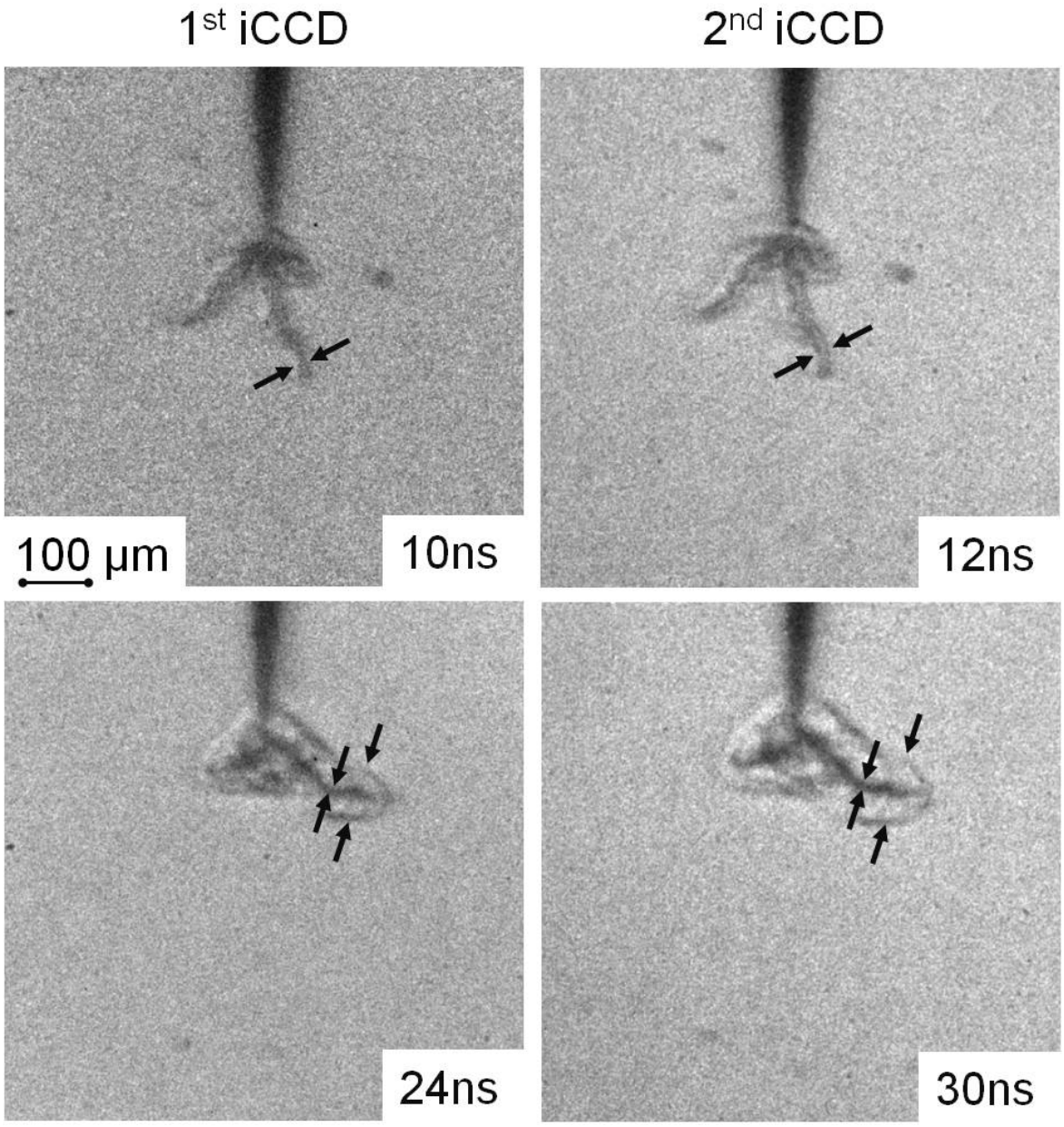

Figure 4.31 Expansion of tree-like discharge channels and shock propagation measured with two iCCD cameras. Deionized water at 6 kV. Camera gate is 2 ns.

From Equation 4.16 it follows that pressure inside cylindrical cavity can be found if the first and the second derivate of the radius R, in other words expansion velocity and acceleration, are known. Radius of the discharge channel and corresponding expansion velocity were measured using two iCCD cameras. Maximal expansion velocity was found to be

0.9 km/s at 11 ns as shown in Figure 4.32. Acceleration R'' was obtained by differentiating experimentally measured expansion velocity profile. Calculated pressure evolution is shown in Figure 4.32. The maximal pressure at 11 ns was found to be 0.28 GPa at 15 ns and decreased almost 4 times during the HV pulse duration.

From the shock wave velocity measurements we can estimate the initial pressure in the discharge channels. Initial pressure was found to be 0.4 GPa which corresponds to maximal measurable shock velocity of 1.9 km/s. As one can see two models give fairly consistent values of discharge pressure at channel formation. Note that the precision of the channel expansion velocity measurements was about 20-30%. It can be seen in Figure 4.32 that residual pressure inside the discharge channel drop to 10^6 Pa already at 200 ns after discharge ignition.

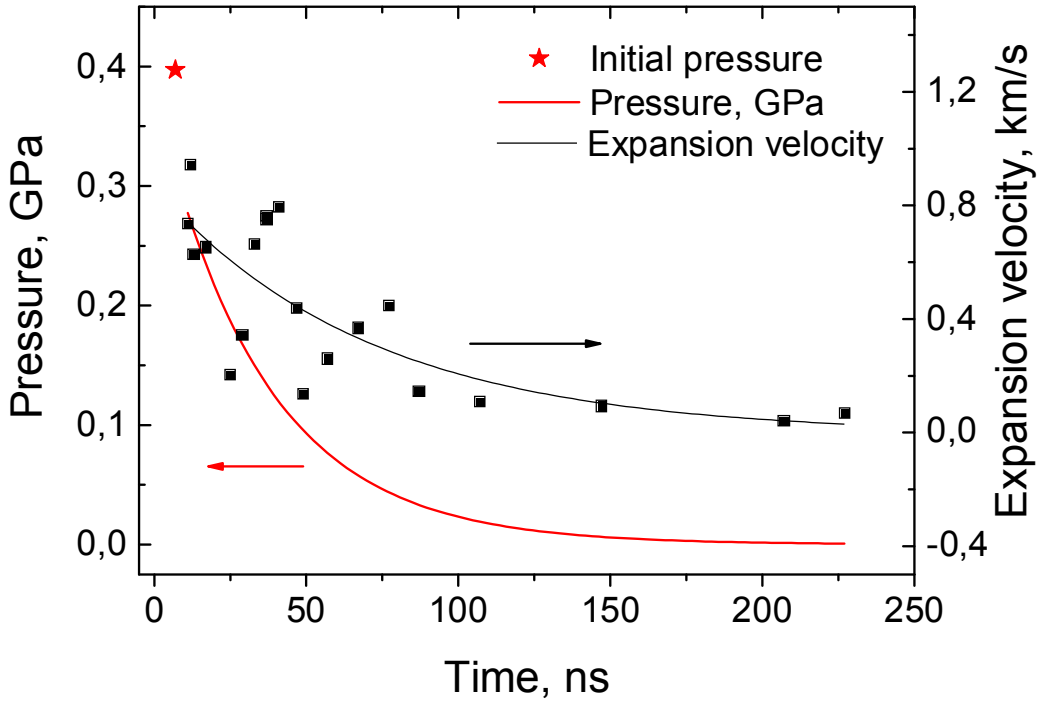

Figure 4.32 Gas pressure in tree-like discharge channels calculated from channel expansion and initial pressure calculated from shock velocity. Black scatter shows the experimental measurements and the black curve is a fit (~$t^{0.5}$). Deionized water, 6 kV.

4.3.4 Discharge pressure measurements at high voltage amplitude

At high applied voltages (15 kV) the discharge structure was rather complex with the diameter of the discharge channel which varied strongly between different channels and along given discharge filament. Given that, the analysis of the individual channel expansion at 15 kV did not allow to obtain a pressure value. Nevertheless, shock wave pressure measurements were performed under such conditions. Taking into account highly supersonic propagation of shock wave at the initial stage of the discharge formation the error in shock wave velocity measurements was far below the incertitude of the channel expansion velocity measurements. Figure 4.33 gives an x-t diagram for the shock wave propagation and corresponding velocity. As can be seen, the maximal detected shock wave velocity was about 4.2 km/s. The shock degenerated into an acoustic wave over the duration of the applied voltage pulse.

The maximal shock wave velocity of 4.2 km/s gives for the initial pressure inside the discharge channels a value of 5.8 GPa. Similar pressure values of 2 GP – 3 GPa were reported for the tree-like mode observed in the microsecond discharge and measured by optical interferometry (An *et al* 2007). Therefore, extremely high pressure in the discharge channel may explain the insensitivity of the tree-like discharge propagation velocity to the hydrostatic pressure up to the values of 10 MPa as was shown experimentally in (Lesaint and Gournay 1994a)

The gas pressure inside tree-like discharge channels demonstrated a strongly dependence on applied voltage decreasing by more than ten times when voltage was varied between 15 kV and 6 kV. It points to the fact that some field sensitive process should be responsible for the formation of gaseous phase in the tree-like mode. On the contrary, as we have seen in the case of bush-like discharge the maximal shock wave velocity at 15 kV and 4 kV varied only by a factor of 2. It supports the idea of bush-like discharge initiation in gaseous cavity and propagation

of tree-like discharge assisted by the field induced dissociation of bulk liquid.

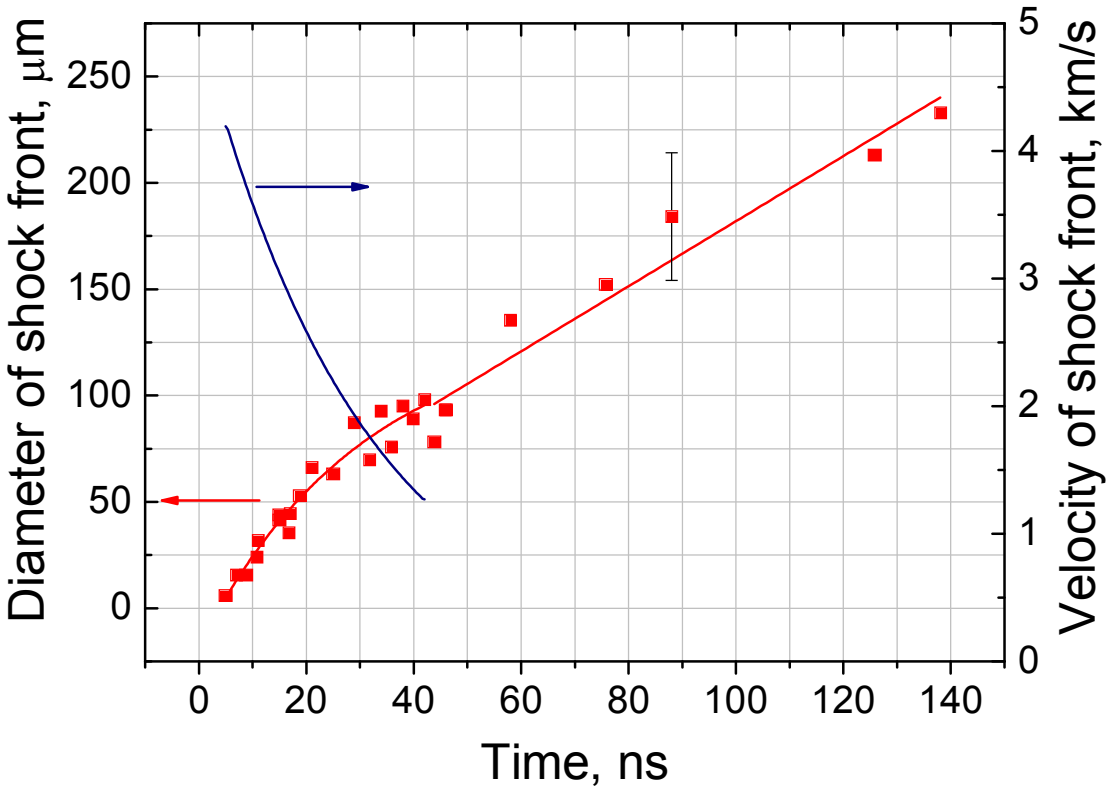

Figure 4.33 Pressure of shock wave calculated from shock front propagation velocity. Tree-like discharge at 15 kV in deionized water.

4.3.5 Conclusions on discharge pressure measurements

It was demonstrated that

- Two methods were applied to estimate the gas pressure inside the tree-like discharge channels in deionized water at 6 kV. Model based on shock wave pressure measurements and model describing the expansion of a long cylindrical cavity provided consistent values of the maximal pressure of 0.3 – 0.4 GPa.

- Pressure evolution during the HV pulse and in the postdischarge phase demonstrates rapid relaxation down to 10^6 Pa already at 200 ns.
- At higher voltage amplitude of 15 kV shock wave pressure measurements give 4.2 km/s for maximal velocity which corresponds to 5.8 GPa of initial pressure.
- Obtained results demonstrate a strong dependence of the discharge pressure in the tree-like mode on the amplitude of applied voltage.

4.4 Discharge development under successive HV pulses

As it was already mentioned in Section 3.5 one HV pulse produces a series of pulses of alternate polarity propagating in the coaxial cable back and forth between the generator and the discharge device. Mismatch of the impedance at the open end in the discharge device and zero impedance of closed HV diode in pulse generator lead to pulse reflection and appearance of successive pulses as can be seen in Figure 4.34. Time delay between the first pulse of positive polarity and the successive negative pulse is 260 ns which is defined by the length of a coaxial cable of 26 m. Reflected pulses allow one to study the electrical strength of water at high repetition rate (4 MHz) while problems typical for high-frequency discharges, like a complex impedance matching and significant water volume heating are completely avoided.

In this section we will consider the evolution of the bush-like and the tree-like discharges ignited at 15 kV under the second pulse of negative polarity and the third pulse of positive polarity. Discharge reignition during successive reflected pulses was detected by two synchronized iCCD cameras. In shadowgraph mode the first iCCD and the second iCCD cameras are triggered just before the beginning of the 2nd pulse and during the 3rd pulse in order to check the change in the overall discharge structure. For plasma emission visualization the first iCCD camera provided time averaged emission during the first HV pulse,

whereas the second camera detected the light emission over the second or the third HV pulses.

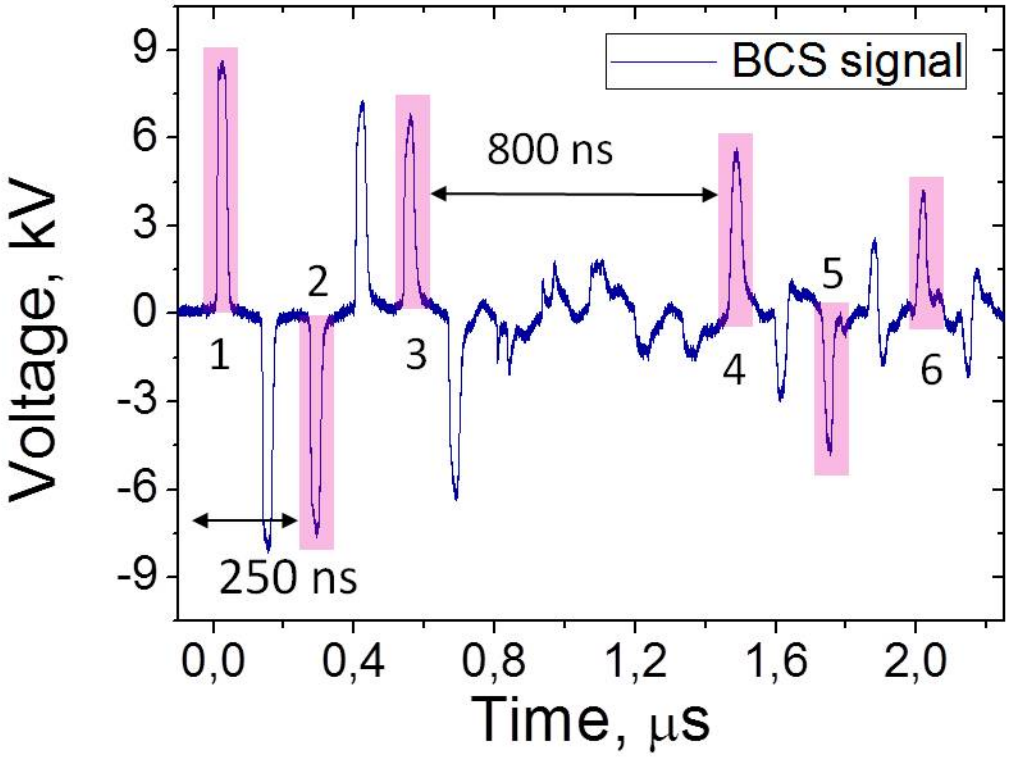

Figure 4.34 Typical BCS signal showing successive reflected pulses of alternate polarity at 9 kV.

4.4.1 Discharge development under the second (negative) pulse

We will first consider the case when the bush-like discharge is formed during the first applied voltage pulse. We are interested in the discharge evolution during successive negative pulses. As can be seen in Figure 4.35, a at the moment when the second (negative) pulse arrived on the tip electrode, channels, forming bush-like structure, have already exhibited some lateral expansion due to the pressure relaxation. So the separate channels cannot be clearly distinguished. Spherical acoustic wave from the first pulse is still can be seen at the distance of about 400 μm from the tip. Shadow image taken at 40 ns after the second discharge ignition (Figure 4.35, b) demonstrates both axial and radial increase of the bush-like discharge channels and formation of the pressure waves propagating from the channel extremities. No newly

formed discharge channels are observed. Figure 4.35, c shows that negative discharge in the bush-like structure is characterized by a very weak light emission. Maximal emission intensity observed under the negative HV pulse slightly exceeds the plasma emission intensity from the bush-like discharge during the first positive pulse.

If the tree-like discharge was ignited at the first positive HV pulse, during successive negative HV pulse a strong plasma emission are observed. Figure 4.36, a-b demonstrates integrated emission from two successive discharges corresponding to the first (positive) and the second (negative) HV pulses. From emission images (Figure 4.36, a-b) on can conclude that the negative discharge reignites close to the tip, in several already existing discharge channels. As can be seen in the shadowgraphs taken just before the second pulse (Figure 4.36, c) and 30 ns after ignition of the negative discharge (Figure 4.36, d), plasma reignition induces channel expansion and produces a pressure wave at the filament tip. (Figure 4.36, d). Similarly to the case of bush-like discharge no new structures are formed under negative HV pulse.

Obtained results demonstrate that under the negative HV pulse the discharge is confined in the pre-existing gaseous channels of the bush-like or the tree-like mode. No new discharge structures can be observed under the negative HV pulse. Surprisingly, emission intensity of the negative discharge is considerably lower in the case of the bush-like discharge as compared to the tree-like discharge. As it was shown in previous sections based on shock velocity measurements initial pressure in the bush-like and the tree-like discharges during the first pulse are comparable. One can, hence, expect that at the moment of the second negative discharge gas pressure inside bush-like structure is not exceeding the pressure in the tree-like discharge channels. So, it seems reasonable to suggest that due to the difference in formation mechanism the gas composition inside bush-like and tree-like mode may be rather different. However, further investigation is needed to clarify this observation.

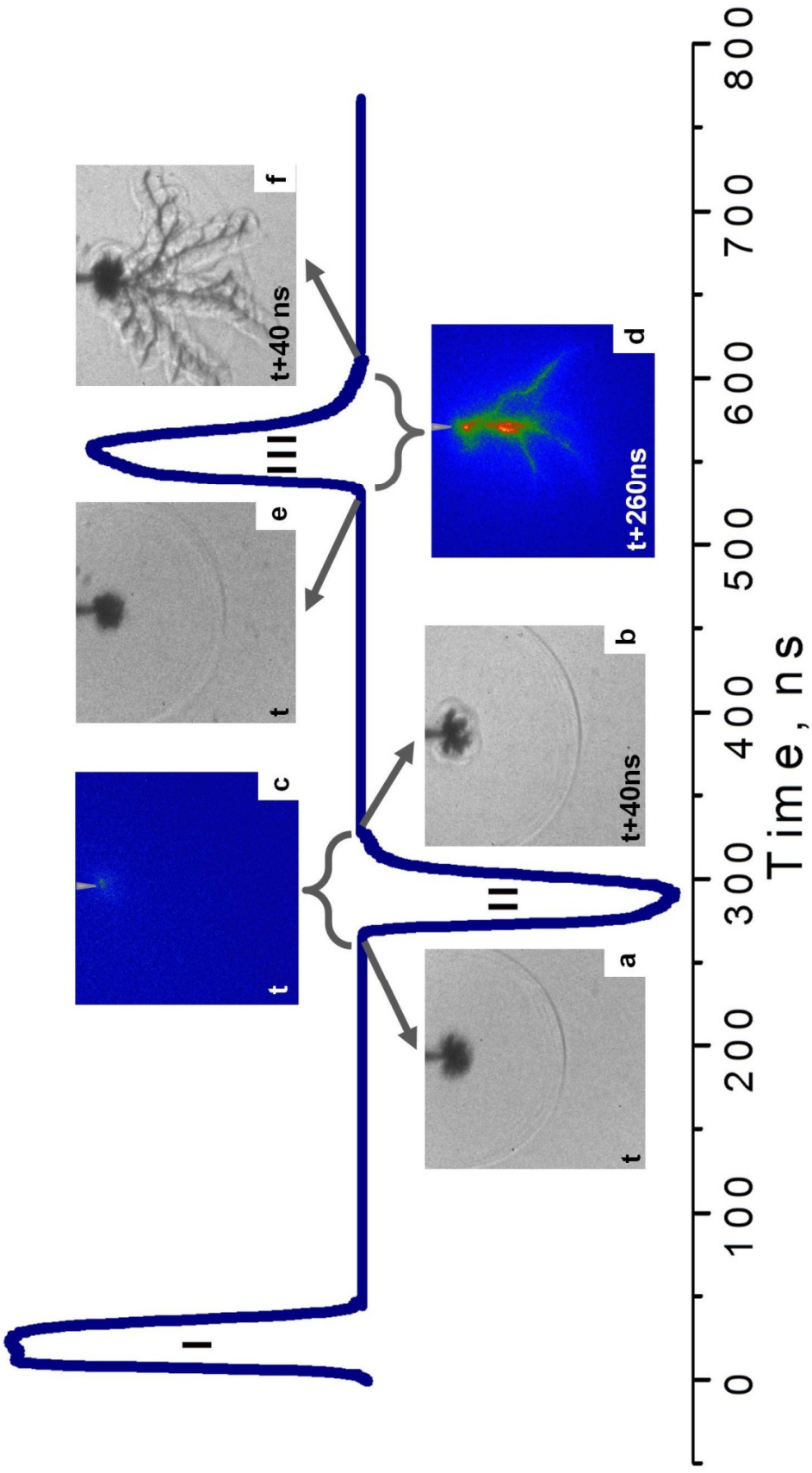

Figure 4.35 Evolution of bush-like discharge during successive reflected pulses at 15 kV.

4.4.2 Discharge development under third (positive) pulse

For the third pulse, as can be seen from the emission (Figure 4.35, c-d) and the shadow images (Figure 4.35, e-f) a transition from the bush structure to the tree-like discharge can occur. Emission images show that in the case of the bush-like to the tree-like discharge transition the discharge first ignites in one channels of the bush-like structure and then fast streamers emerge in the bulk water. Appearance of a filamentary discharge during the third pulse is stochastic and in some cases just only new bush-like structures are formed at the interface.

In the case of the tree-like discharge, formation of a new filamentary structures is also observed on the shadowgraphs (Figure 4.36, g-h) and was supported by formation of new emitting channel as shown by emission imaging (Figure 4.36, e-f). New tree-like structure could be ignited at the tips of existing channels. We have to stress that formation of new discharge channels during third pulse occurred in a random manner similarly to statistical appearance of bush and tree-like discharges ignited at the first HV pulse. For the third pulse bush structures could also be observed (Figure 4.36, g-h) at interface between filamentary channels and bulk water.

As one can see for discharge development under successive positive pulse was very similar to bush-like and tree-like discharge formation over first HV pulse. New bush-like and tree-like structure could be ignited in random manner, sometimes simultaneously, at the interface of gaseous cavities formed by initial tree-like and bush-like structures.

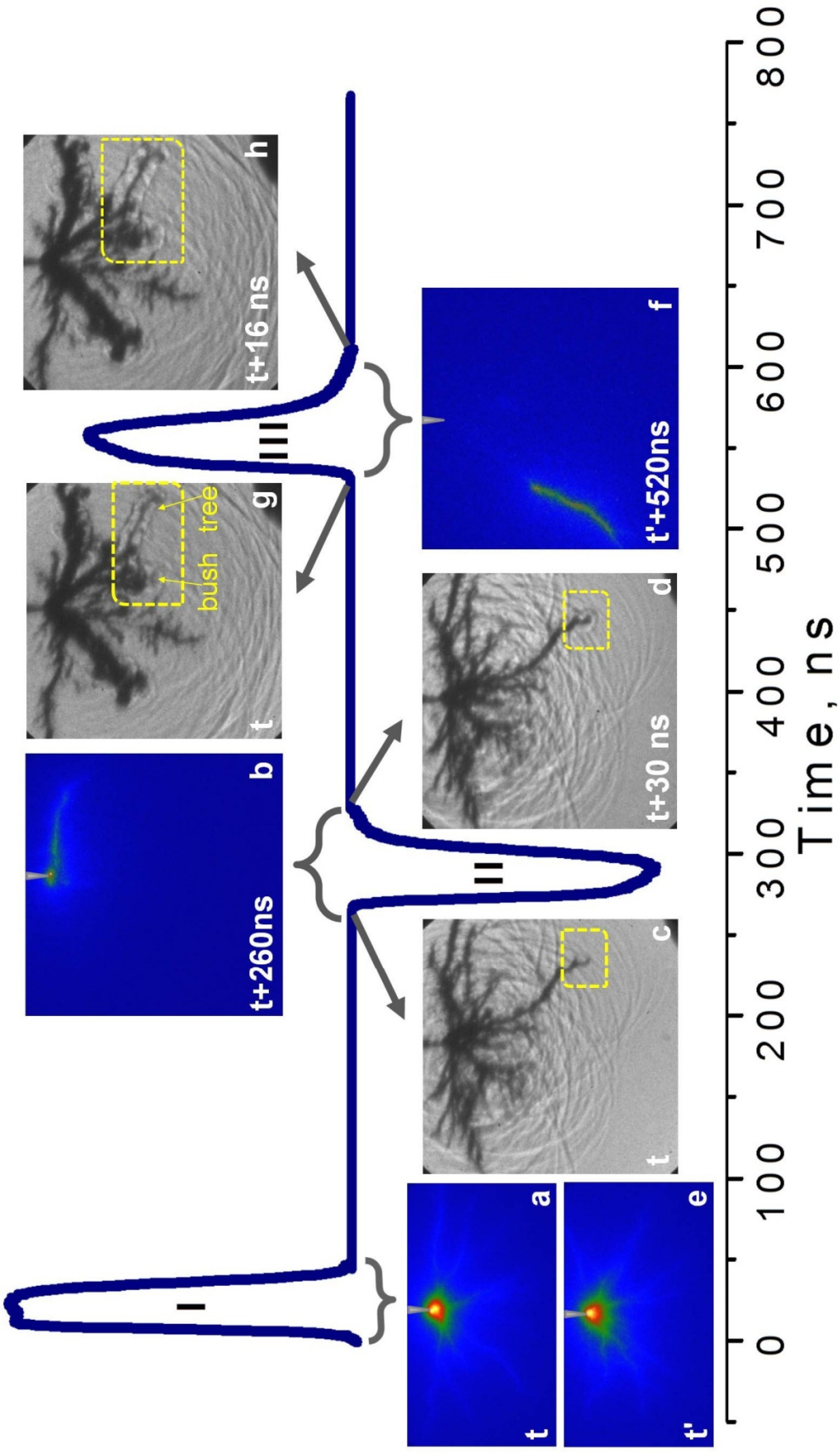

Figure 4.36 Development of tree-like discharge during successive reflected pulses at 15 kV.

4.4.3 Conclusion on discharge development under successive HV pulses

Shadowgraph and optical emission visualization of the successive discharges occurring under the reflected pulses of negative and positive polarity is done using two iCCD camera arrangement. Obtained results show that

- Negative discharge was confined in the channels of initial bush-like or tree-like structure. No formation of new structure or propagation of existed channels was observed. Formation of pressure waves at the extremities of all bush-like channels and at several tree-like filaments together with channel expansion was observed. Energy input was supported by strong light emission from several discharge channel in the case of tree-like discharge, while rather weak emission intensity was detected for bush-like discharge.
- Under the third pulse of the positive polarity new bush-like and tree-like discharges can be observed at the interface of gaseous cavity formed by the initial bush-like and tree-like structures.

4.5 Spectroscopic analysis of the fast mode (preliminary results)

4.5.1 Principle of measurements

Optical emission spectroscopy (OES) was applied to get an insight into plasma properties inside the discharge channel. As we have already seen nanosecond discharges in liquids demonstrate two important properties, namely, small sub-millimeter size and short duration. In such conditions accumulation of the signal becomes a challenging task. We have done an attempt to obtain a time resolved spectra at the expense of spatial averaging of the optical signal. As it was demonstrated by visualization of the discharge emission (Figure 4.25) the light intensity in the vicinity of the pin electrode and at the periphery of the discharge structure is

considerably different. One can argue that spectral features and, hence plasma parameters can be very different depending on the position along the discharge channel, as it was shown by advanced spatially resolved spectroscopic technique applied to the microsecond discharge (An *et al* 2007). The authors reported that electronic density increases almost ten times along the discharge channel away from the electrode tip.

The spectroscopic measurements in this Thesis were done using a commercial monochromator built on the basis of Czerny-Turner optical scheme (Andor Shamrock 303i) equipped with iCCD camera as a detector (Andor iStar). The use of the same iCCD camera for the shadowgraphic and the spectroscopic measurements enables us to avoid the recalibration of the time delays between the HV pulse and acquisition of the optical signal. The optical emission was collected with a quartz lens producing slightly reduced image of the discharge on the entrance slit of monochromator. The monochromator is supplied with three grating of 600, 1800 and 2400 l/mm centered respectively at 300, 500 and 600 nm. Grating of 600 l/mm was used in the most experiments as it allows covering of the greatest spectral range (30 nm) at the given grating position. Full spectrum in the range of 300 – 800 nm was recorded by successively turning the grating using a built-in 'step and glue' function in Andor Solis software. All spectra were corrected for the apparatus function using the calibration performed with a laser-driven broadband emission lamp (LDLS EQ-99FC Energetiq).

4.5.2 Van der Waals broadening

As it was demonstrated in Section 4.3 by shock velocity measurements and discharge channel expansion, initial pressure in the tree-like discharge can be as high as 6 GPa, depending upon the applied voltage. Such elevated pressure should entrain a strong broadening of the emission lines according to Van der Waals mechanism. Van der Waals mechanism arises from the induced dipole-dipole interactions between the neutral species and results in the line broadening and a red-shift.

The values of the line broadening and shift can be found in impact approximation by (Helbig and Kusch 1972)

$$\Delta\lambda_{VW} = 17.0 C_6^{2/5} \upsilon^{3/5} N_g \qquad (4.18)$$

$$\delta\lambda_{VW} = 6.16 C_6^{2/5} \upsilon^{3/5} N_g \,, \qquad (4.19)$$

where $\Delta\lambda$ is the FWHM of the line and $\delta\lambda$ is the corresponding red shift, C_6 is the difference in Van der Waals constants of the upper and the lower levels of emitting atom, ν is the mean relative velocity and N is the number density of perturbers. As one can see, the Van der Waals broadening and shift are proportional to the gas density and the temperature. Note that the impact approximation is valid for the gas densities

$$N_g \ll \left(\frac{3\pi C_6}{8\upsilon}\right)^{-0.6} \qquad (4.20)$$

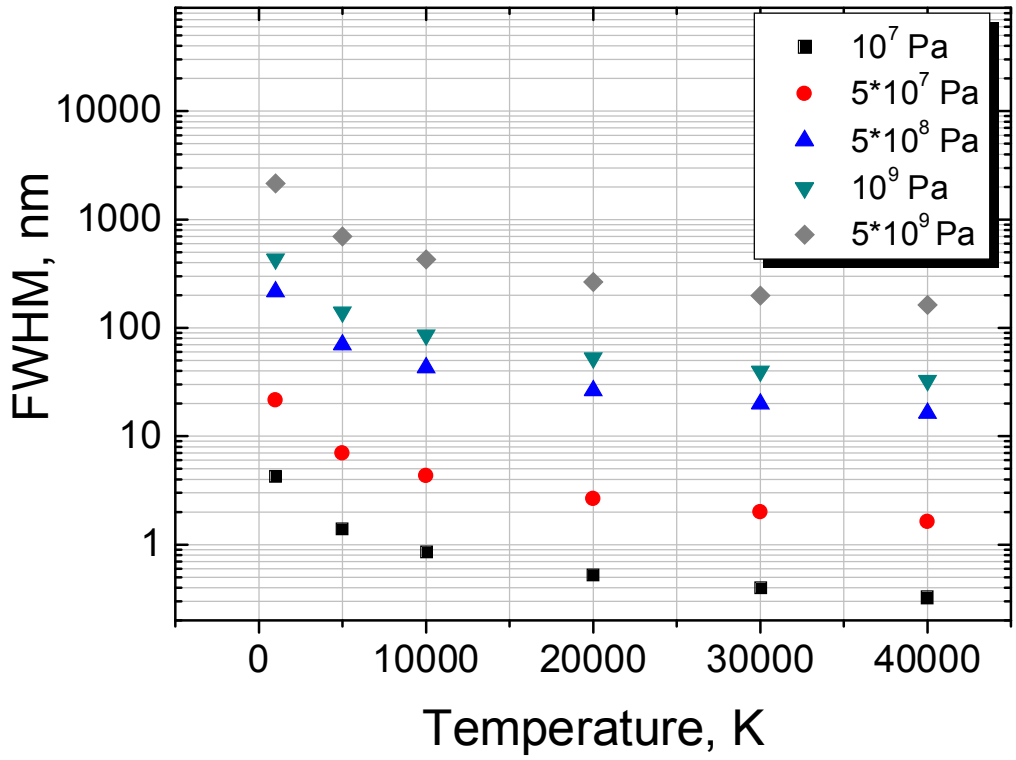

Figure 4.37 Van der Waals broadening of H_α line at different values of pressure and temperature.

For the hydrogen alpha line the Van der Waals contribution in the line broadening is given by

$$\Delta\lambda_{VW} = 6P/T_g^{0.7} \qquad (4.21)$$

In order to calculate the contribution of the Van der Waals process in overall line broadening one need to know the temperature of perturbers, i.e. the gas temperature inside the discharge channel. Figure 4.37 illustrates the resulting FWHM of H_α line for the pressure values between 10^7 and $5*10^9$ Pa and the temperature in the range of $10^3 - 4 \cdot 10^4$ K. As one can see at the initial phase of the discharge formation the width of H_α profile can attain several hundreds of nanometers for the pressure of 10^{10} Pa and the temperature of the order of $5*10^3 - 1.5*10^4$ K (Ingebrigtsen *et al* 2008, Namihira and Sakai 2007).

4.5.3 Stark broadening

Another important mechanism affecting H_α line width is a Stark broadening induced by microfields of the charged perturbers. Balmer series exhibits linear Stark effect resulting in symmetrical broadening with respect to the unperturbed wavelength, i.e. no shift of the line occurs. For the H_α line the Stark broadening is given by (van der Horst *et al* 2012)

$$\Delta\lambda_S = 8.33 \cdot 10^{-3} \left(\frac{n_e}{10^{20}}\right)^{2/3} \qquad (4.22)$$

As it directly follows, the knowledge of the Stark contribution to the overall line broadening allows calculating the electronic density. Electronic density as high as $6 \cdot 10^{25} m^{-3}$ was reported for the microsecond discharge in water (Namihira and Sakai 2007, An *et al* 2007). Electronic density of $10^{25} - 10^{26}$ m^{-3} can induce H_α broadening of the order of 4 – 18 nm (Figure 4.38). Therefore, under the conditions of the nanosecond discharge, Van der Waals and Stark mechanisms should be taken into account. Note that both broadening mechanisms have collisional nature and, thus produce a Lorentzian profile. Since two mechanisms act simultaneously the resulting profile would be a sum of two Lorentzian functions. It can be easily shown that the width

(FWHM) of the cumulative profile is the sum of the widths of two Lorentzian functions. As a result the contributions of Van der Waals and Stark broadening can be treated independently.

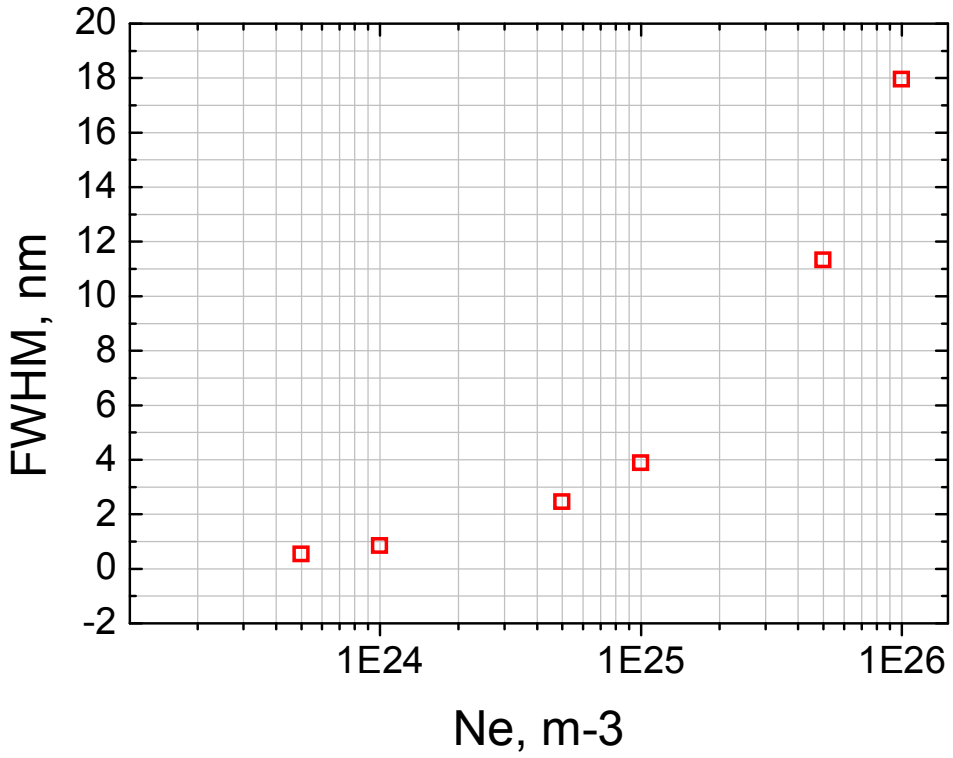

Figure 4.38 Stark broadening of H_α line as a function of electron density.

4.5.4 Continuum emission

If elevated temperatures of the order of $5*10^3$ K – $1.5*10^4$ K are attained in the discharge channel one can expect to observe a black body continuum emission assuming local thermodynamic equilibrium (LTE). Spectral power of black body emission is given by well known Planck's law

$$I_P(T) = \frac{2hc^2}{\lambda^5}\frac{1}{e^{hc/\lambda k_B T}-1}, \qquad (4.23)$$

where h is the Plank constant, k_B is the Boltzmann constant and c is the speed of light. Figure 4.39 gives an example of the spectral distribution of the black body emission for $5*10^3$ K and 10^4 K in the region of interest between 280 nm and 800 nm.

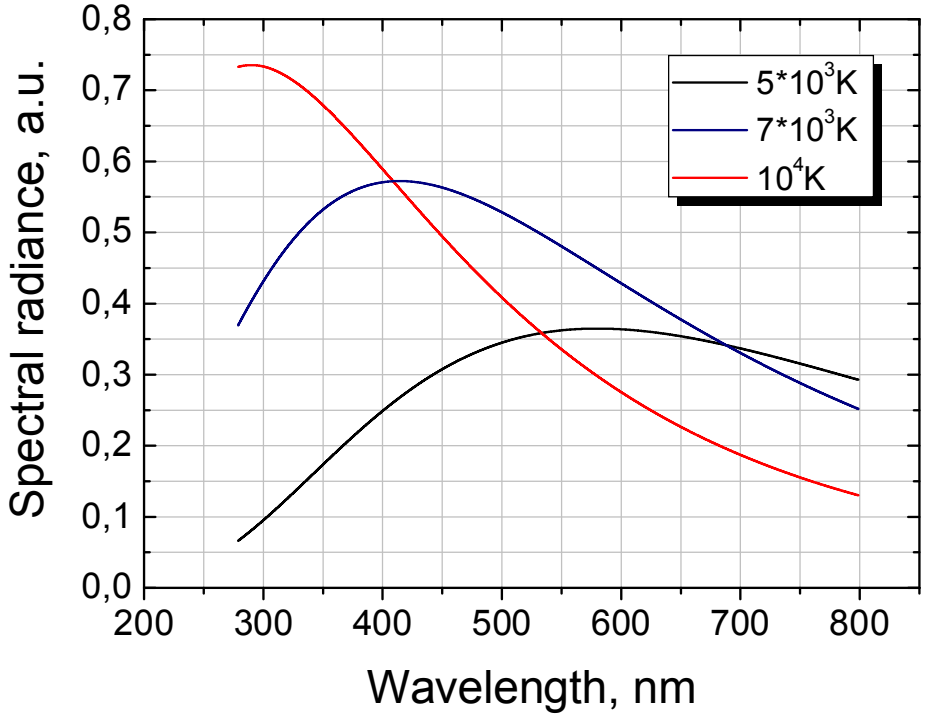

Figure 4.39 Spectral distribution of black body emission for $5*10^3$ K and 10^4 K.

Reported electronic densities of 10^{25} –10^{26} m^{-3} (An *et al* 2007) correspond to the degree of ionization of the order of 0.1 – 1%. Therefore, the continuum emission due to the electron-ion elastic collisions and recombination should be taken into account. Bremsstrahlung or free-free emission originates from the change of momentum of the unbound electrons interacting with the ions. Emissivity of corresponding continuum is given by (Ochkin 2009)

$$I_{ff} = g_{ff} C \frac{Z^2 n_i n_e}{\sqrt{T_e}} exp\left(-\frac{h\nu}{k_B T_e}\right), \qquad (4.24)$$

where g_{ff} is the Gaunt factor ($g_{ff} = 1$ in the case of hydrogen plasma), C is the ion-electron constant ($C = 1.08*10^{-51} J \cdot m^3 \cdot K^{0.5}$), Z is the charge number of the ion.

In the recombination or free-bound process free electron is captured by the ion into the bound state with a negative energy E_n. The spectral power of recombination process has similar to Bremsstrahlung emission form but decreases faster with increasing wavelength as given by

$$I_{fb} = g_{ff} C \frac{Z^2 n_i n_e}{\sqrt{T_e}} \left(\frac{2E_n}{n k_B T_e}\right) exp\left(\frac{E_n - h\nu}{k_B T_e}\right), \qquad (4.25)$$

where C is the same constant as in (4.17), n is the principal quantum number of the bound state. Note that formulae 4.24 and 4.25 were obtained in assumption of maxwellian distribution of the electrons. For both free-free and free-bound interactions the emission intensity depends on the electron density while spectral profile is defined by the electron temperature.

4.5.5 Experimental spectra and discussion

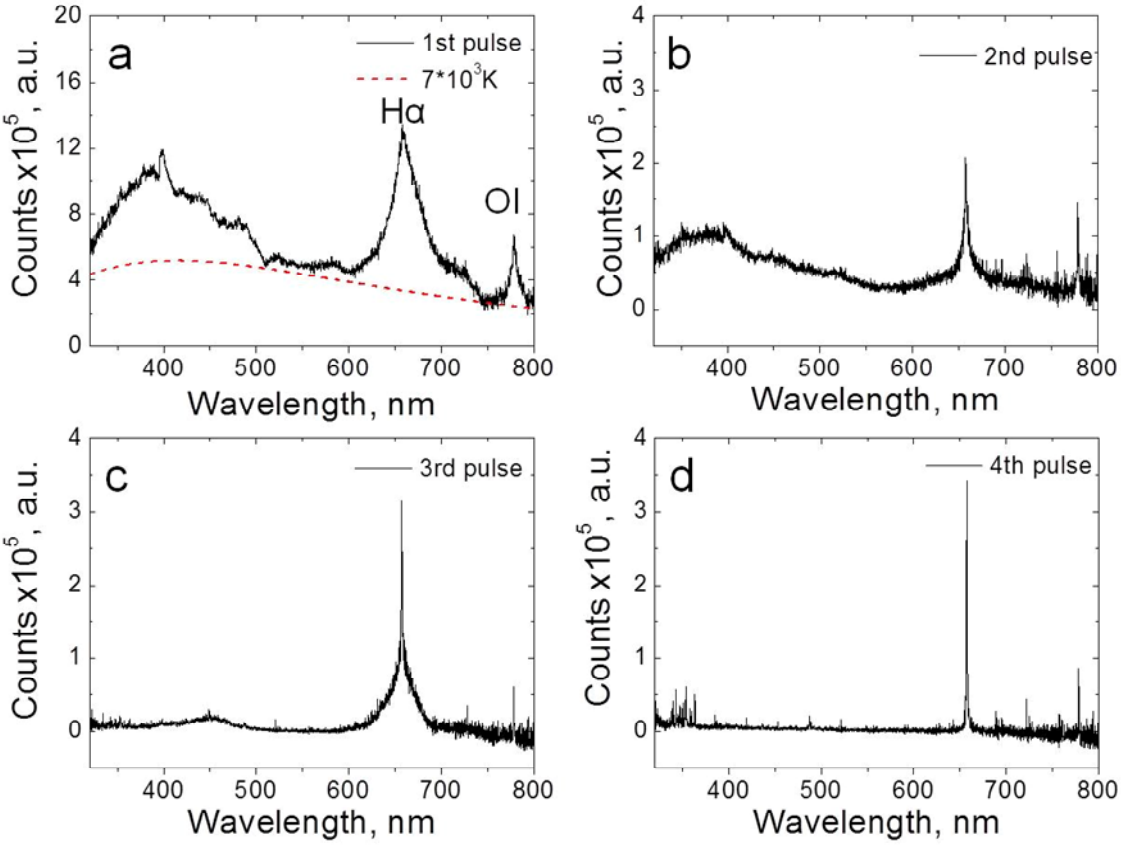

Figure 4.40 OES averaged over HV pulse duration corresponding to a) first (positive), b) second (negative), c) third (positive) and d) fourth (positive) pulses shown in Figure 4.34. Deionized water at 15 kV.

Figure 4.40 demonstrates the experimental spectra of the nanosecond discharge in deionized water averaged over the total duration of the first positive pulse and three reflected pulses of alternate polarity. In

order to obtain an acceptable signal to noise ration accumulation over 1000 shots was done. The spectra were corrected for the spectral response of the grating and apparatus function by using a continuum spectrum calibration light source (see Section 3.9 for more detail).

Dynamics of plasma emission under successive pulses

Emission spectrum corresponding to the first positive HV pulse (Figure 4.40, a) demonstrates continuum emission between 300 and 800 nm and strongly broadened atomic H_α and OI lines. As one can see, H_α line demonstrate asymmetric red wing with about 40 nm of FWHM. Spectrum recorded during the successive negative pulse coming 260 ns after the initial pulse demonstrates rather symmetrical profile with a FWHM of 12 nm superimposed on the continuum emission between 300 nm and 800 nm (Figure 4.40, b). The forth pulse having positive polarity and separated by about 1.5 µs from the first pulse produced narrow H_α line. The line profile can be rather well approximated with two Lorentzian profiles of 0.6 nm (FWHM), that was practically the resolution limit of spectrometer, and a broader one of 3.5 nm (FWHM).

If we consider exclusively the contribution of the Van der Waals broadening one can see that the time evolution of H_α profile observed between the first (positive), the second (negative) and the fourth (positive) pulses is consistent with the typical time of pressure relaxation inside the discharge channels. Under the initial HV pulse the discharge filaments are created with the initial pressure of about 6 GPa. At time instant when the negative discharge the pressure inside the discharge channels decreases by two orders of magnitude. Although, the energy input during the negative pulse can induce slight pressure increase as suggested by formation of a pressure wave (Figure 4.36) one can expect the discharge pressure to be far below during the second pulse as compared to the first pulse. The variation of the electron density with the gas pressure inside the discharge channel is less evident. However, assuming very fast ionization process at the discharge formation, initial plasma density should be extremely high. Therefore, we conclude that the large spread in the hydrogen alpha width between

the first and the second pulse is due to the strongly different plasma parameters at discharge initiation and during reillumination in relaxed discharge channel. Due to the attenuation of the applied voltage in the coaxial line no new structures can be observed during fourth HV pulse of positive polarity. We estimate the gas pressure inside the discharge channels at the time moment of the fourth pulse to be of the order of atmospheric pressure. Consequently, experimentally observed profiles of H_α line corresponding to first, second and fourth HV pulses are in agreement with pressure evolution inside the discharge channels.

Emission from newly-formed channels

At the third HV pulse that is delayed by 520 ns in respect to the first pulse, hydrogen alpha line profile can be fitted with two Lorentzian functions of 30 nm (FWHM) of 1 nm (FWHM). Practically no continuum emission is observed during the third pulse while broad emission feature at about 450 nm and very weak H_β line (486 nm) can be seen, as shown in (Figure 4.40 b).

As it was shown in previous section formation of a new discharge channels can occur under the third (positive) pulse. In this case plasma parameters in teh newly created channels and in the channels with already relaxed pressure should be rather different. This spatial inhomogeneity can explain the appearance of strongly and weakly broadened components of observed hydrogen alpha profile. However, the absence of continuum emission is quite surprising. One can assume that the pressure gradient between initial structures and the new channels can lead to faster pressure relaxation.

Continuum emission

Analysis of hydrogen alpha profile over the first and the second HV pulses is complicated by strong continuum emission as can be seen in Figure 4.40, a-b. The nature of continuum emission is unclear as it can be attributed to strongly broadened Balmer H_α, H_β and H_γ lines, recombination of excited radical species, free-free (Bremsstrahlung) and

free-bound (recombination) electron – ion inelastic collisions and black body emission.

In the following we will make a drastic approximation assuming LTE equilibrium inside the discharge channel. As will be discussed below, our preliminary results do not allow us to obtain the gas temperature and hence, the neutral density in the discharge. In order to estimate the contribution of black body emission one need to know the Plank temperature. We assume that the gas density is close to liquid density while channel expansion occurs in LTE. In fact, under such conditions the time of LTE establishment could be extremely short of the order of $1/\nu \approx 10^{-14}\ s$, where ν is frequency of collisions. Gas temperature and density are related to pressure through ideal gas equation

$$P = nkT_g \qquad (4.26)$$

As it was shown above fast filamentary discharge propagates on the sub-nanosecond time scale with a maximal velocity as high as 50 μm/ns. We can estimate the overall discharge volume assuming the instantaneous formation of the total length of all discharge channels. At 15 kV of applied voltage the statistical number of branches equals to 10 with the average length of 500 μm. If we take 1 μm for initial radius of the discharge channels at initial pressure of $5\ 10^9$ Pa, the total mechanical energy of compressed gas equals to 10^{-4} J, which is of the order of the energy dissipation measured by BCS ($2*10^{-4}$ J). Actually, one can expect rather high degree of dissociation and so the gas density can exceed the liquid density. If we take a number density of water under normal conditions of $3.3 \cdot 10^{28}$ m^{-3} the corresponding temperature would be 10^4 K. This value is comparable with the Boltzmann temperature of 15000 K obtained from emission Cu lines observed in the pulsed discharge in water with a copper pin electrode (Namihira and Sakai 2007).

As one can see in Figure 4.40, an attempt was done to approximate the baseline of emission spectrum with the theoretical curve of black body emission corresponding to T = 7000 K. Agreement within 30% between

the gas temperature obtained from the thermodynamic considerations and by fitting the baseline with black-body emission curve, seems to be conclusive taking into account the approximate nature of a two estimations.

Plasma density

Figure 4.41 demonstrates emission spectrum integrated over the first (positive) pulse and corrected for black body emission with T = 7000 K. As one can see, the spectrum consists of strongly broadened atomic hydrogen, oxygen and presumably Ni lines (NIST database), the last one occurring because of point electrode erosion. It is possible to identify two atomic oxygen OI triplets at 725 nm (3p – 5s) and 777 nm (3s – 3p). Balmer series is presented with clearly seen alpha line and overlapping beta, gamma and delta line. A narrow peak at 398 nm is ascribed to Ni I emission (4s – 4p), although the close position of H_ζ line of Balmer series complicates the analysis. The origin of continuum emission between 320nm and 390 nm is unclear. One can assume that the emission in this spectral region is due to the cumulative contribution of several atomic Ni I lines and, possibly molecular continuum.

Hydrogen alpha profile can be approximated with two Lorentzian functions as it is shown in Figure 4.41. The more intense and stronger broadened peak of 47 nm (FWHM) is observed at 664 nm. The second weaker peak and less broadened peak is observed at 568 nm with FWHM of 11 nm. As it was mentioned above (Figure 4.27), discharge emission intensity demonstrates two maxima during the first HV pulse at about 15 ns and 38 ns, which are correlated with the discharge current. During the time delay between the two emission maxima the discharge pressure decreases by several times as was shown by the discharge channel expansion measurements. Hence, one can ascribe two Lorentzian functions to the two maxima of discharge emission, or in other words to the direct discharge propagating at elevated pressure and to the back discharge taking place in already relaxed channels.

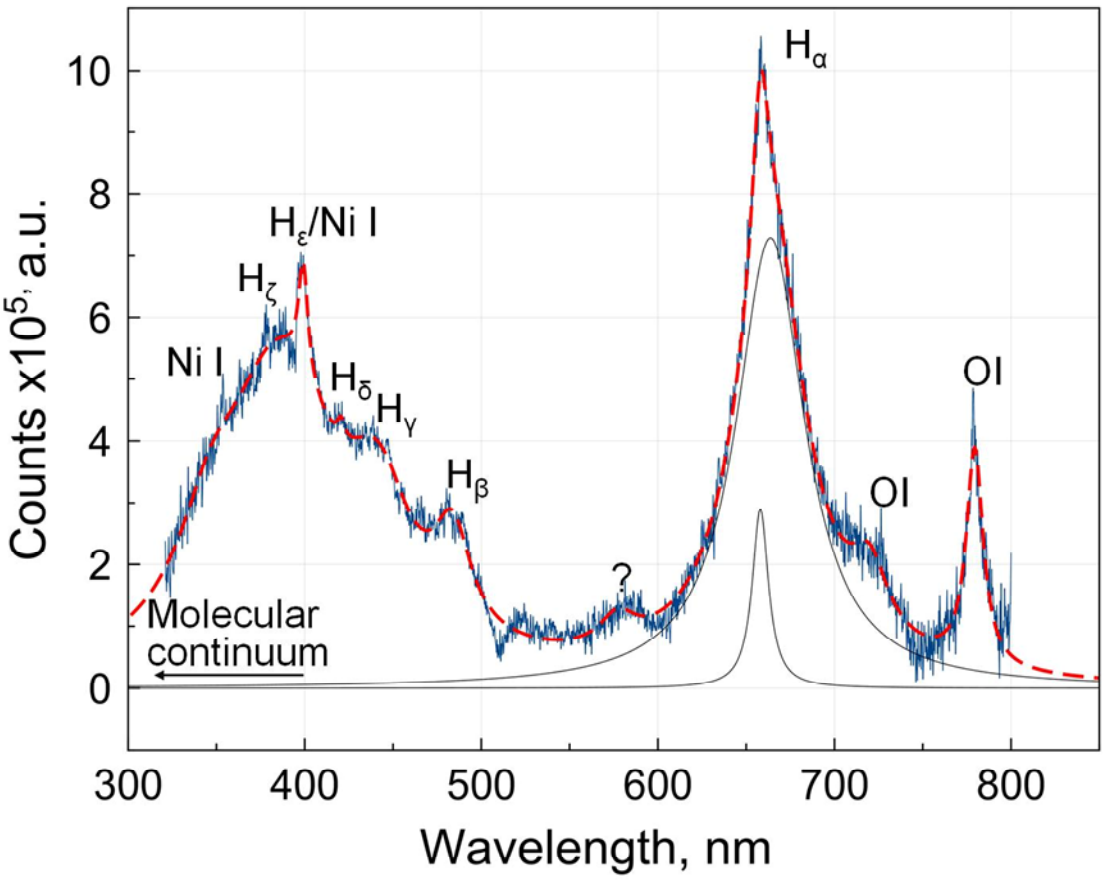

*Figure 4.41 OES of the first (positive) pulse corrected for the black body emission with T = 7*10³ K. Hydrogen Balmer series, atomic oxygen OI and possibly Ni I emission lines are identified (NIST database).*

Each Lorentzian profile should be seen as a result of combined Stark and Van der Waals broadening. Since the Balmer series exhibits linear Stark effect observed red shift can be exclusively attributed to the Van der Waals mechanism. In impact approximation the full width of Van der Waals broadening is related to the red shift by

$$\Delta\lambda = 0.28 \cdot \delta\lambda, \qquad (4.27)$$

where $\Delta\lambda$ is FWHM of the line and $\delta\lambda$ is the corresponding red shift. Given that we can estimate the contribution of the Van der Waals broadening in the total width of two Lorentzian profiles to be 21.5 nm and 5 nm respectively. As it was already mentioned for the sum of two Lorentzian functions (with the same maximal position) the width of resulting profile is the sum of the widths of two profiles. Therefore the Stark broadening can be found by subtracting the Van der Waals

contribution from the total profile width. It gives for the Stark width the values of 25.5 nm and 6 nm respectively. The corresponding electron densities are equal to $1.3*10^{26}\,m^{-3}$ and $2*10^{25}\,m^{-3}$ respectively. Obtained electron densities are in agreement with the values reported by other authors (An *et al* 2007). It is worth noting that in (An *et al* 2007) electron density was derived in a similar way from the Stark broadening of H_α line, however the Van der Waals broadening was completely neglected. Therefore, reported electron density can be overestimated.

Note that the black body temperature of 7000 K is, in fact, an average temperature and the maximal temperature at the discharge ignition can be somewhat higher.

As we have seen, the simple estimation, assuming LTE, gives for the discharge temperature the values of the order of 10^4 K, at the given pressure of 10^9 Pa and neutral density equal to $10^{28}m^{-3}$. Our actual knowledge about the plasma properties under such conditions is rather limited. The use of approximations developed for the low pressure plasmas is questionable and can be misleading. Plasma densities provided in this section are given with the only purpose to illustrate the complexity of observed phenomenon and should be considered as rather rough approximation.

Time resolved measurements would be helpful in understanding of the continuum emission and evolution of the atomic lines with the discharge pressure.

4.5.6 Conclusions on spectroscopic analysis of tree-like discharge

The attempt was done to apply the optical emission spectroscopy to study the evolution of plasma parameters, i.e. n_e, T, during the applied HV pulse and under the successive pulses.

Based on preliminary spectroscopic results it was shown that

- Emission spectra of first positive pulse consisted of intense continuum between 300 nm and 800 nm and strongly broadened lines of hydrogen Balmer series and atomic oxygen triplet bands OI at 725 nm and 777 nm. Baseline of spectrum can be approximated with the black body emission curve for T = 7000 K.
- The total width of hydrogen alpha line observed during second (negative) pulse demonstrated a more than three times decrease which is consistent with the pressure relaxation inside the discharge channel.
- H_α profile observed under the third (positive) HV pulse consists of a two Lorentzian components of 30 nm (FWHM) and 1 nm (FWHM). Two profiles can be attributed to emission from the spatially distinct denser high pressure plasma in newly created channels and the discharge in relaxed channels. No continuum emission is observed in this case.
- Weakly broadened (0.6 nm) hydrogen alpha profile detected under the fourth (positive) pulse is consistent with the pressure relaxation inside the discharge channel
- During the first (positive) discharge H_α profile demonstrates asymmetrical red wing and can be approximated with two shifted Lorentzian profiles. Two Lorentzian functions are ascribed to direct and back discharge inside the discharge channels. Each profile is assumed to be a sum of the combined action of the Stark and the Van der Waals broadening. Based on this assumption we obtained the electron density equal to $1.3*10^{26}\,m^{-3}$ for the direct discharge and $2*10^{25}\,m^{-3}$ for the back discharge.
- Because of long time of acquisition comparing to formative time of the discharge channel obtained electron densities seem to be rather approximative. Time resolved measurement have to be done in the future

4.6 Conclusions on initiation and propagation of nanosecond discharge in liquids

In this chapter initiation and propagation dynamics of the electric discharge in the liquid dielectrics was discussed. Time resolved optical shadowgraph visualization with spatial resolution of about 2 µm was developed and applied to study the nanosecond discharge in deionized water, ethanol and n-pentane. Three different scenarios can be observed in polar deionized water ($\varepsilon = 80$) and ethanol ($\varepsilon = 27$) depending on the applied voltage: i) formation of gaseous spherical cavity, ii) initiation of slower bush-like and iii) faster tree-like discharges on the point anode.

Cavitation mode: It is shown that for the voltage amplitude in the range of 3 – 4kV in deionized water and 3.5 – 4.5 kV in ethanol, a spherical gaseous cavity with a radius of about 4 µm is formed on the electrode tip after the end of the applied voltage pulse. For the lowest voltage values cavity expansion dynamics can be approximated by Rayleigh model. Deduced initial pressure in the cavity is found to be 3 MPa in water and 1 MPa in ethanol. In n-pentane ($\varepsilon = 1.8$) a spherical cavity of 5 µm was detected after the HV pulse of 10 – 12 kV. Experimentally observed cavitation in deionized water, ethanol and n-pentane under the nanosecond high voltage pulse with maximal electric field rate of $0.6 – 2{,}6 \cdot 10^9$ V/m · ns (3 – 12 kV, 5 ns rise time) is in good agreement with the recent theoretical predictions made by Shneider with coworkers (Shneider *et al* 2012, Shneider and Pekker 2013b). Electrostrictive negative pressure stretching the liquid in the direction of the electric field gradient can exceed the cavitation threshold for given liquid dielectric. For three tested liquids the product εE^2 which determines the maximal electrostrictive pressure is proportional to the cavitation threshold values available in literature (Herbert *et al* 2006, Arvengas *et al* 2011). Although, no light emission or shock wave formation was observed in the case of bubble cavitation, other mechanisms including evaporation under Joule heating and field induce dissociation cannot be completely discarded.

Slow plasma mode: It is demonstrated in deionized water and ethanol that if voltage amplitude on the point electrode is raised up to the values of 4 kV – 5.5 kV a bush-like discharge can be ignited. At the initial phase of the bush-like discharge development the propagation velocity is supersonic. The maximal velocity at ignition increases with the applied voltage from 2.2 km/s at 4 kV reaching 4.2 km/s at 9 kV in deionized water and from 2 km/s at 5.5 kV up to the 3 km/s at 9 kV in ethanol. Discharge propagation is accompanied by emission of a spherical shockwave. Initial discharge pressure in deionized water estimated from the maximal shock wave velocity gives 0.8 GPa and 5.7 GPa at 4 kV and 9 kV respectively. High initial pressure indicates that a strong energy release occurs at the discharge initiation. Field induced dissociation and autoionization of liquid molecules in the vicinity of the tip can be responsible for the formation of the bush-like discharge. The density lowering due to the electrostrictive force can provide local strengthening of reduced field promoting electron avalanche formation.

The bush-like discharge consists of a gaseous cavity and few filaments radiating from the cavity. The total structure is quite similar in deionized water and ethanol. The number of discharge filaments and their maximal length increase with the applied voltage. Discharge stops to propagate at the end of plateau of the applied voltage pulse. Excessive pressure inside the bush-like discharge filaments in the case of water does not exceed $3 \cdot 10^4$ Pa. We conclude that the propagation of bush-like discharge is governed by the expansion of the gaseous cavity and interface instability development in highly nonuniform electric field. Bush-like discharge is not observed in n-pentane.

Fast discharge mode: At voltage amplitude higher than 5.5 kV a fast filamentary tree-like discharge can be initiated on the point electrode. Statistically the probability to observe the fast mode increases with the applied voltage between 6 and 15kV. Light emission associated with the ignition of the tree-like discharge is detected during the rising slope of the applied voltage pulse before the shadow structures become visible.

The maximal discharge velocity is of the order of 20 – 50 km/s in water and an order of magnitude slower (3 – 5 km/s) in ethanol at 6 – 9 kV. Tree-like discharge is also observed in n-pentane at the voltage amplitude higher than 12 kV. The maximal propagation velocity in n-pentane varies between 2.2 and 4.6 km/s for voltage amplitude in the range of 12 – 18 kV.

The number and length of the discharge channels increase gradually with the applied voltage in all tested liquids. In deionized water energy dissipation in the tree-like discharge at 15 kV is about 0.2 mJ. The maximal discharge current is 1.5 A and the average charge transferred by each channel equals to 2 nC. Time evolution of the light emission from the discharge channels correlates with the total discharge current. A back discharge is observed over the trailing edge of the high voltage pulse as supported by negative current spike and reillumination of discharge channels.

Propagation of fast tree-like discharge is accompanied by formation of a series of the shock waves along the channel pass. The estimation of pressure in the discharge channel from the channel expansion dynamics and from the shock wave velocity gives 0.4 GPa at 6 kV and about 6 GPa at 15 kV.

Although the electrostrictive effect may facilitate the initiation of tree-like mode it does not seem capable of explaining the difference in the propagation velocity observed in deionized water, ethanol and n-pentane. Especially because under the electric fields at which the tree-like mode is ignited the dielectric permittivity is considerably lowered due to the saturated polarization (Suresh *et al* 2006). The latter effect can improve the nonuniformity and induce the local increase of the electric field. Field induced impact dissociation of liquid molecules in extremely high fields of the order of 10^9 V/m is believed to be responsible for the propagation of the tree-like mode. The strong coupling between hydrogen bonding and dipole orientation in the case of water can explain the higher propagation velocity as compared to ethanol. Electric field of the order of 10^9 V/m induces strengthening of

the hydrogen bonds along the field axis while hydrogen bonds orthogonal to the field are weakened (Vegiri 2004). Proton tunneling through the hydrogen bonds, known as Grotthuss mechanism, can contribute in the development of the fast discharge mode.

Obtained results demonstrate that depending on amplitude of applied nanosecond voltage pulse three different scenarios can be observed in polar dielectrics. Initiation of nanosecond discharge in liquid dielectrics is a complex phenomenon in which the electro-hydrodynamic and atomic mechanisms are strongly coupled. Hence the models taking into account hydrodynamic and electronic processes have to be developed in the future.

It is found that fast (tree-like) mode can be ignited occasionally during successive reflected pulse of the positive polarity coming about 520 ns after the initial HV pulse while it was never observed for the reflected pulse of the negative polarity. The polarity effect similar to the gas phase streamers (Briels *et al* 2008, Luque *et al* 2008) is due to the difference in mobility of the electrons and ions. A net negative charge is formed on the interface screening the applied field in the case of negative discharge.

Plasma parameters

We attempted to apply the optical emission spectroscopy (OES) in order to get insight into the plasma parameters. Spatially and time integrated over the HV pulse duration emission spectra demonstrate a continuum emission between 300 and 800 nm and strongly broadened atomic H_α (656 nm) and OI (777 nm) lines. Time evolution of hydrogen alpha profile measured in the successive reflected pulses is consistent with the typical time of pressure relaxation inside the discharge channels. During the first (positive) pulse the Hα line had asymmetric red wing and can be approximated with two shifted Lorentzian profiles. Two Lorentzian functions are ascribed to the direct and the back discharge inside the channels of the tree-like structure. Each profile is assumed to be a sum of combined action of the Stark and the Van der

Waals broadening. Based on this assumption we obtained an electron density of $1.3*10^{26}$ m^{-3} for the direct discharge and $2*10^{25}$ m^{-3} for the back discharge.

5 Biomedical applications of cold atmospheric plasma

5.1 Historical overview

Over the last ten years application of cold plasma for biomedical purposes has grown from a subdivision of the traditional plasma chemistry into an independent multidisciplinary field consolidating the efforts of plasma scientists, electrical engineers, biologists and medical doctors. The best example of fast growing interest in plasma medical application is the six fold increase in number of participants of a specialized biennial International conference on plasma medicine (ICPM) that has been held for already 4 times since its first issue in 2007. Almost all biggest international conferences on plasma applications have now the sections and workshops entirely devoted to plasma medicine while several special issues of best ranked plasma journals have recently seen the light of the day.

Although, the first attempt to use the therapeutic properties of electrical discharge in air has been done in the end of 19th century using a self-induction coil transformer (Tesla Coil) under the name of 'Violet Ray' (Weltmann *et al* 2012). However, it is only in the late 1960s that the first patent for the plasma based sterilization has been issued (Menashi 1968) and the first plasma coagulator has been introduced during the 1970s (Morrison 1977). It's not earlier than 2003 that the pioneering work on plasma treatment of living eukaryote cells has been done by Stoffels and coworkers (Stoffels *et al* 2003). Since that time a number of beneficial applications of cold plasmas have been proposed and first encouraging results are now being reported. Among the most notable examples of plasma use in bio-medicine are dentistry(Yu *et al* 2012) , dermatology (Heinlin *et al* 2011), plasma assisted hemostasis (Fridman *et al* 2008) and oncology (Kim *et al* 2011).

5.2 Applications of cold plasmas in biology and medicine

5.2.1 Plasma in dentistry

The potential of cold plasma for dental purposes is triple: it kills oral bacteria, improves adhesion of dental composites and enhances tooth bleaching. It has been shown that Ar DC discharge plasma effectively kills oral bacteria of Streptococcus mutans (S. mutans) and Lactobacillus acidophilus (L. acidophilus) (Yu *et al* 2012) two main pathogens in dental caries. Special plasma jet device operating in He/O2 mixture is able to ignite plasma directly inside the root canal (Lu *et al* 2009) and the inactivation experiments showed that it can efficiently eliminate enterococcus faecalis, one of the main types of bacterium causing failure of root-canal treatment. Pretreatment of the dentin surface with the Ar plasma (Yu *et al* 2012) leads to the formation of a peroxide functional groups on collagen fibrils that promotes the polymerization of the hydroxyethyl methacrylate (HEMA) monomer, a primary component in many commercial dentin adhesives. The overall increases in bonding strength at the dentin/composite interface can achieve 60%. Combined action of hydrogen peroxide and plasma microjet (Sun *et al* 2010) has shown better results in teeth bleaching comparing to H_2O_2 alone due to the efficient OH radical production by plasma. It is believed that the OH radical is the main agent of bleaching effect. Also, SEM analysis demonstrated slight improvement in smoothness of the enamel due to the effect of nitric and nitrate acids produced by plasma

5.2.2 Plasma in dermatology

Plasma usage in dermatology covers such areas as sterilization of the tissues, treatment of the skin diseases, cosmetic applications, blood coagulation and wound healing. It has been known for a long time that plasmas produce a biocide effect, however the exact mechanism of plasma disinfection is not yet fully understood. Plasma components that are believed to be relevant for the sterilization are charged particles (electrons and ions), UV (A,B and C) radiation, strong electric fields and reactive species (O_3, OH, H_2O_2, NO, OH) and excited sates of

molecules and atoms ($O_2(a^1\Delta_g)$, $N_2(A^3\Sigma_u)$). According to current knowledge the synergy between several plasma parameters is responsible for the unique disinfecting effect of plasma (Ehlbeck *et al* 2011). Thus, UV radiation and electric field can directly damage cellular macromolecules and affect membrane, while DNA proteins and lipids are irreparably harmed by oxidative stress. Successful plasma treatment of chronic skin diseases like dermatitis (Heinlin *et al* 2011), Hailey–Hailey disease (Isbary *et al* 2011) and eczema (Emmert *et al* 2013) shows that plasma efficiently eliminates bacterial supercolonisation, e.g. Staphylococcus aureus, by producing the reactive oxygen and nitrogen species on the treatment surface (O_3, NO etc.).

Additionally, exposure to plasma decreases the skin pH leading to the acidification by nitric and nitrate acids, which can positively affect the healing process. Another beneficial property of the cold plasmas to speed the blood coagulation has been found by applying DBD plasma directly on the open wound or in the blood samples (Fridman *et al* 2008). The authors suggest the effect is non-thermal and, presumably, is due to the selective plasma interaction with fibrinogen protein leading to fibrin formation and its successive polymerization.

Despite the radical action on the prokaryotic cells cold plasmas at doses several times higher than required for the effective inactivation of bacteria is proven to be safe for living intact and wounded skin (Wu *et al* 2013). Furthermore, histological analysis performed in this study demonstrated that plasma toxic effects like epidermal damage and tissue burn are mostly dependent on the dose rate and not only on the dose itself of plasma exposure. However, as it was demonstrated in (Kalghatgi *et al* 2010) low plasma doses not only innocuous for normal porcine aortic endothelial cells (PAEC) but can enhance cells proliferation by reactive oxygen species mediated release of fibroblast growth factor-2 (FGF2). Intra- and extracellular ROS scavengers N-Acetyl-L-cysteine (NAC) and sodium pyruvate have been used in this work to determine the principal role of plasma generated reactive oxygen species. Plasma ability to promote proliferation of endothelial

cells is used in skin regeneration technology for skin rejuvenation and for treatment of wrinkles (Foster *et al* 2008).

5.2.3 Plasma in cancer treatment

A recent study on plasma interaction with the melanoma cancer cells (A2058) revealed that the plasma has the potential to induce apoptosis, or programmed cell death, and necrosis, spontaneous cell death by loosing cell integrity, in a dose dependant manner (Fridman *et al* 2007). Authors characterized quantitatively the cell response to the plasma treatment and have found that the plasma dose of 20 J/cm2 induces necrosis, which is still below of the damaging threshold of a healthy tissue. Lower doses of plasma were shown to initiate massive apoptosis at 12-24 hours after the treatment. More recently, the same group performed a deep analysis of apoptotic activity in plasma treated melanoma cells by Trypan blue exclusion test, Annexin-V/PI staining, caspase-3 cleavage, and TUNEL analysis (Sensenig *et al* 2011a). The experiments were done by direct exposure of melanoma cells covered with 100 µl of complete medium to dielectric barrier discharge plasma. It was found that preincubation of the cells with an intracellular ROS scavenger NAC reduces number of apoptotic cells from 35% to 20% for dose of 15 J/cm^2 at H24 and completely protects the DNA against the damage as seen from phosphorylation of H2AX, one of the signals against double-strand break (DSB), at already 1 hour after the treatment. These observations bring authors to conclusion that plasma apoptotic effect originates from direct interaction between ROS and cell DNA.

Another work devoted to the plasma treatment of mouse melanoma cells (B16F10) with surface type DBD in similar conditions (Kim *et al* 2010a) demonstrated that together with DSB damage to DNA and respective accumulation of proapoptotic p53 tumor suppressor gene, plasma can affect the mitochondria as shown by cytochrome C release and change in mitochondrial membrane potential by using mitochondrial membrane-specific fluorescent dye. Another notable example of cancer cells treatment, RF plasma torch operating in He

applied in human metastatic melanoma line (G361) (Lee *et al* 2009). Authors reported on loss of adhesion capability of 90% cells already for 15 s treatment with 100 µl of the complete medium (DMEM). Plasma was found to inhibit the expression of adhesion proteins (integrin $\alpha 2$, $\alpha 4$ and FAK) that are known to play an important role in malignant transformation.

The selective killing of melanoma cancer cells (1205Lu) comparing to primary keratinocytes was done by Zirnheld an coworkers (Zirnheld *et al* 2010). Using low frequency plasma torch in He authors demonstrated that 10 s of plasma exposure leads to alterations in morphology of melanoma cells and decrease of cell population viability down to 40% while keratinocytes maintain their morphology and demonstrate viability greater than 90 %. In comparative study (Keidar *et al* 2011) plasma ability to selectively kill cancer cells was confirmed in vitro with murine melanoma cells (B16F10) and murine primary macrophages and in vivo experiments on nude mice bearing murine melanoma tumor. It was found that in vitro plasma effectively induces apoptosis in melanoma model without affecting macrophage for the same dose. In-vivo experiments demonstrated efficient ablation of the tumor decreasing its growth rate and improving survival in the treatment group.

We intentionally focused on melanoma cancer cells here for the reason of literature available on the subject and in order to give an idea of the effect that different plasma sources and treatment strategies produce in a given cell model (keeping in mind that different melanoma lines may have very different malignant behavior and metastatic phenotypes). It worth noting that plasma has been successfully applied for apoptosis induction in human colorectal cancer cells (Kim *et al* 2010a) and human hepatocellular carcinoma line (Zhang *et al* 2008) as well.

We have seen that interaction of cold plasmas with the living cells is a complex and includes direct plasma influence on cell membrane proteins, cell organelles and DNA by production of ROS. Indirect

plasma action consists in specific triggering of chemical or biological mediators produced in the cell culture medium or directly in the cell.

5.2.4 Plasma sources for bio-medicine

Following the commonly use terminology (Weltmann *et al* 2010) currently available atmospheric plasma sources for bio-medical applications can be divided in two groups depending on how plasma is delivered to the object to be treated.

5.2.5 Directly generated plasma sources

The first group unites devices in which plasma is directly generated between the object and powered electrode. In this case living tissue or cell culture is exposed to the action of charged particles (electrons and ions), electric field and UV radiation (if no arrangement is done to avoid it) and heat as well as to complex plasma chemistry producing ROS and RNS. The extensively used example of such devices is a dielectric barrier discharge that can be operated in a regime when treated object is kept at floating potential (Fridman *et al* 2007) or is grounded (Vandamme *et al* 2012). Typically this discharge type operates under low frequency (10^2-10^3 Hz) HV of several tens of kilovolts and maximum discharge gap of 5 mm. Plasma generated by DBD is filamentary at atmospheric conditions with rather uniform plasma filament distribution over treated surface due to the surface charging and electrical repulsion of the filaments. Chemical composition of DBD in air has been a subject of computer simulation (Sakiyama *et al* 2012) and experimental investigations (Bruggeman and Brandenburg 2013). Numerical modeling predicts down-regulation of NO, O and O_2* when switching from dry air to the 30 % humid air, while the concentrations of N_2O, NO_3, N_2O_5 and O_3 increase and new species like OH, HO_2, H_2O_2 and HNO_3 will be produced. The DBD operating at the frequencies of 100 Hz demonstrates a slight temperature increase by about 30C in the plasma zone and can be driven over tens of minutes without causing the injuries to living tissues (Vandamme *et al* 2010). UV emission of such plasmas is associated with excitation state of molecular nitrogen and OH radical in the range of 300-400 nm and

NO_γ emission between 200 and 300 nm (Vandamme *et al* 2012). Although emission intensity from such plasma seems to be rather weak comparing to the typically used UV doses in dermatology, it may be significantly increased if Ar is added to air due to efficient energy transfer between Ar excited states and molecular nitrogen. The electric field seen by the treated object is the sum of the applied electric field and a local electric field associated with the streamer propagation.

5.2.6 Remote plasma sources

Indirectly generated plasma devices vary on how plasma is generated and delivered to the treatment zone. We restrict ourselves by considering three types of indirectly generated plasma sources. The first type is based on surface dielectric barrier discharge in which 2D plasma discharge propagates over a dielectric surface (Kim *et al* 2010a). The physical phenomena and operation principles for devices of this type are similar to volume DBDs. The main difference for bio-medical application is that in those devices charged particles recombine before they reach the treated surface and electric field, in general, is considerably weaker than in volume DBD. The important advantage of SDBD is that they are easily scalable and large surface discharges are now developed for sterilization application (Oehmigen *et al* 2010). Another type of indirect plasma source is so-called plasma jet, in which plasma is confined in dielectric tube or capillary. Depending on excitation source electrode configuration may be DBD-like for pulsed and low frequency jets (Robert *et al* 2009) and corona–like for devices operated at radio frequency (Stoffels *et al* 2003). Plasma jets are commonly operated in noble gas flow (He, Ar, Ne etc) or in mixture of noble gas with air or oxygen admixture. Operation in pure air is a difficult task requiring a higher injected energy due to the electron attachment to the O_2 and important energy dissipation through vibration excitation of nitrogen molecules. The ability to modify gas mixture makes a big advantage to plasma jets since it allows tailoring of ROS and RNS production in plasma plume (Reuter *et al* 2012). The need of high flow rate in order to keep the jet temperature tolerable by biological substances can be an important issue if working with a liquid

sample as it will be blown away or dried rapidly. Plasma propagation through the jet capillary may be hydrodynamic determined by gas flow like in radiofrequency glow–like jets and electrodynamic due to formation of volume charge sufficient to create electric field capable to ionized the gas in front. Propagation of ionization front depends on HV amplitude and repetition rate and can be as fast as several km/s. If this ionization wave reaches the object under the treatment it will be exposed to high electric fields of the order of 10^3 V/cm (Sretenović *et al* 2011).

5.2.7 Plasma in liquid media

Direct generation of plasma in liquid medium is another way of plasma treatment that can be applied for the yeast (Sato 1996) and mammalian cells (Sunka *et al* 2007). Discharges in liquids are characterized by high ROS densities and, as a rule, formation of the shock waves. Exposure of melanoma cells to the shock wave demonstrate an efficient cell elimination by inducing a perforation of the cell membrane (Sunka *et al* 2007). Discharges in liquids require higher electric field comparing to the atmospheric pressure gas discharges and can be produced by applying of the pulsed high voltage on a sharp tip electrode immersed in liquid sample. As we have previously found (Marinov *et al* 2013) nanosecond discharge in water with the pin electrode being anode demonstrates several distinctive morphologies with a different discharge size and energy input. ROS production should also vary with the energy dissipated in plasma. Discharge formation is almost not sensitive to the temperature in the large range and does not influenced by the ambient humidity. All this makes nanosecond discharge in water solutions an interesting model in study of direct interaction of plasma and living cells.

5.3 Structure and functioning of eukaryotic cells

5.3.1 Cell membrane structure and transport

Cell membrane, also called plasma membrane, is a thin, 5-10 nm wide, lipid bilayer sheet which defines the boundary of the cells. Chemically,

plasma membranes are non-covalent assemblies of lipids and proteins, with protein/lipid ratio depending on cell type. The lipid bilayer consists of three main lipid classes: phosphoglycerides, sphingolipids (glycolipids), and cholesterol – all comprising hydrophilic and hydrophobic groups (amphipathic). The most abundant phosphoglycerides in cell membrane are the diglycerides which have two hydrophobic fatty acid chains and one hydrophilic phosphate group. The phosphate group, in turn, may be linked to one of several hydrophilic groups, e.g. choline (forming phosphatidylcholine, PC), ethanolamine (forming phosphatidylethanolamine, PE), serine (forming phosphatidylserine, PS), or inositol (forming phosphatidylinositol, PI). Head group of phosphoglyceride with its water soluble part is negatively charged at physiologic pH for PS and PI whereas those groups of PC and PE are neutral. The amphipathic property of phospholipids defines the structure of lipid bilayer and plasma membrane since they represent at least half of the membrane mass. Water affinity of head groups and lipophilicity of fatty acid chains lead to spontaneous phospholipid organization in two-layer sheet, with head groups (each 15 Å in size with the shell of adjacent water molecules) forming inner (cytosol side) and outer (exoplasmic) surface, while combined fatty acid chains form the inner structure of the membrane (about 30 Å wide). Two layers of plasma membrane have different lipid composition, known as phospholipid asymmetry. Thus, the exoplasmic leaflet is mostly formed by phosphatidylcholine (PC) and sphingomyelin (SM), whereas on cytosolic side phosphatidylserine (PS), phosphatidylethanolamine (PE) and phosphatidylinositol (PI) prevail. It's worth noting, that cholesterol demonstrates almost equal distribution in both membrane layers. At physiologic conditions lipid bilayer has a fluidic nature and phospholipids can easily diffuse within the same leaflet, however flip-flop migration to another layer, being thermodynamically unfavorable, is rather slow process. For the major phospholipids (PS, PE, PC, and PI) the formation occurs on the cytosolic face where the corresponding enzymes responsible for lipid synthesis are localized. The asymmetry in phospholipids distribution between two leaflets is maintained by two

selective transmembrane enzymes: flippase and floppase (Daleke 2003). The first is responsible for ATP-dependent transport of PS from exoplasmic to inner surface of plasma membrane, while floppase catalyses the transport of PC and cholesterol in opposite direction. Note, that flippase is inhibited by Ca^{2+} (Bitbol *et al* 1987) and, hence, its activity can be regulated in the cells.

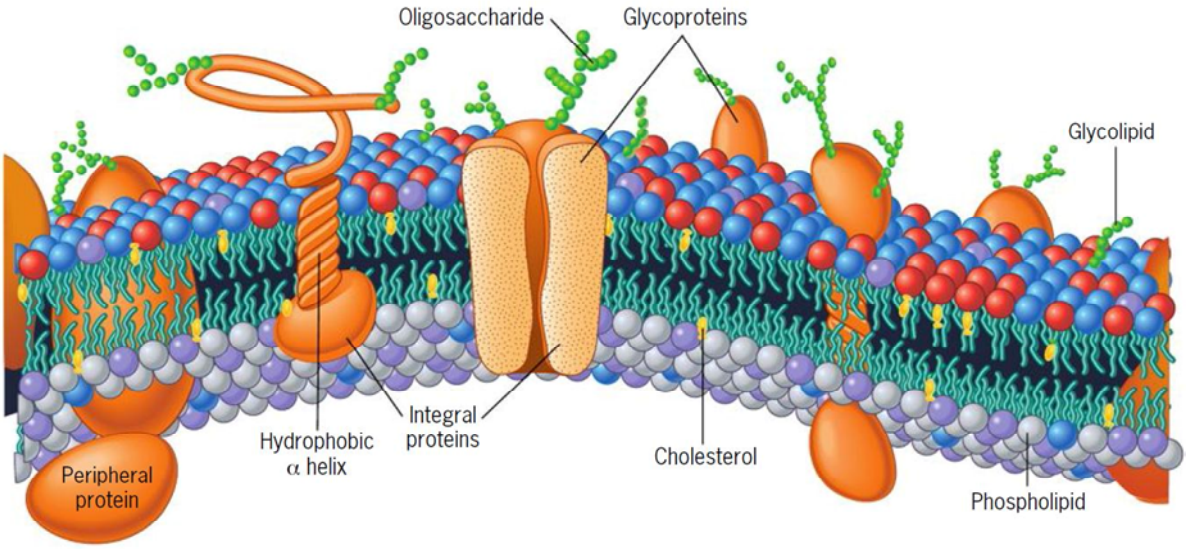

Figure 5. 1 The structure of plasma membrane (taken from Karp G., Cell and Molecular Biology, Wiley, 2009)

Another transmembrane transporter is a scramblase protein which is responsible for the nonspecific bidirectional transport of phospholipids under homeostatic conditions. Scramblase is Ca^{2+} activated and contributes to membrane reorganization and dissipation of transbilayer asymmetry (Daleke 2003).

The cell membrane proteins can be embedded in lipid bilayer (integral proteins), lay on it inner or outer surface (noncovalently bounded peripheral proteins) or covalently linked to bilayer lipid molecule (lipid anchored). Depending on protein function and whether it interacts with extracellular substances (e.g. other cells) or cytosol each protein has an orientation regarding the cytoplasm. Integral proteins as membrane lipids are amphipathic and fix in bilayer by Van der Waals bonding between amino acid residues and fatty acid groups of plasma lipids. Several groups of integral proteins have an inner aqueous channel that enables transport of water soluble substances through the lipid bilayer.

Peripheral proteins are fixed by a weak electrostatic bonding on cell membrane; sometimes a soluble part of a integral protein remaining on the surface can be considered as peripheral protein. Some of peripheral proteins of cytosolic surface contribute for mechanical strength of the membrane. The majority of exoplasmic receptors, enzymes and cell adhesion proteins (all correspond to lipid anchored proteins) bind to the membrane by oligosaccharide linked on other side to phosphatidylinositol (PI) of outer lipidic layer. One of the most important examples of lipid anchored protein, fibronectin regulates the cell interactions with the extracellular matrix and plays important role in cell adhesion, migration, growth and differentiation, while alteration in fibronectin expression may lead to cancer and fibrosis (Pankov and Yamada 2002).

Plasma membrane due to its compact lipidic structure is impermeable for small polar molecules, charged ions and macromolecules of biological interest like glucose, proteins and hormones. It implies, that cell membrane by some means regulates the fluxes of these compounds between cytosol and extracellular medium since all of them are vital for cell metabolism. The main mechanisms of membrane transport include diffusion through the aqueous channel of transmembrane proteins, selective diffusion assisted by specific integral protein and energy-driven protein "pump", all able to move the species against their concentration gradient.

5.3.2 Cytosol, extra and intracellular medium

The concept of extracellular environment and complexity of its composition was first suggested by Claude Bernard in his famous expression *milieu intérieur.* Later on, the role of ionic composition in regulation of many of the cellular processes was widely accepted. Extracellular medium can be seen as water salt solution of NaCl, KCl and $NaHCO_3$ containing organic constituents, e.g. amino acids, proteins, vitamins, hormones and glucose. Since the soluble salts present in water in a form of hydrated ions one should consider the ion transfer between the cell and cellular environment. As it is well known from the

thermodynamics the gradient of solute concentration across a partially permeable membrane will lead to movement of the solvent molecules in the direction of higher density of the solute molecules. This phenomenon, called osmosis, is driven by the tendency of a multinary system to minimize its free energy which decreases with the dilution. For cell membrane which is permeable for water and some other small molecules (e.g. O_2, CO_2, N_2, NO) ion transfer is regulated by specific ion channels and by special Na^+/K^+-ATPase membrane enzyme, also called sodium-potassium pump.

Ion	**Cytosol**	**Extracellular Medium**
Sodium Na^+	10 mmol liter^{-1}	150 mmol liter^{-1}
Potassium K^+	140 mmol liter^{-1}	5 mmol liter^{-1}
Calcium Ca^{2+}	100 nmol liter^{-1}	1 mmol liter^{-1}
Chloride Cl^-	5 mmol liter^{-1}	100 mmol liter^{-1}
Hydrogen ion H^+ (really H_3O^+)	63 nmol liter^{-1} or pH 7.2	40 nmol liter^{-1} or pH 7.4

Table 5.1Typical concentrations for five important ions in mammalian cytosol and extracellular medium. Taken from (Bolsover *et al* 2004).

This enzyme uses the energy of ATP hydrolysis to expel the sodium ions out of the cells and bring two potassium ions to the cytosol at the rate of 10^2 units/s for every three sodium ions ejected. Consequently, the density of K^+ in cytosol will exceed its concentration outside the cell and unbalanced electrical charge will induce the voltage across the membrane. Some of potassium ions are, however, able to escape from the cytosol through the specific potassium ion channel (it does not let, for instance, N^+ go out the cell, even though it has smaller size of 0.95 Å vs 1.33 Å for K^+, driven by the density gradient and with the maximum rate of about 10^6 units/s. The outcome of potassium ions from the cytosol is, therefore, limited by the space negative charge of the cell. Negative chloride ions are repelled by electric field of cytosol space charge and, so their concentration is about 20 times higher in extracellular medium. The equilibrium voltage across the cell membrane for which the density gradient of the ions is equilibrated by the electric field gradient is given by Nernst equation:

$$V_{eq} = \frac{RT}{zF}\ ln\frac{(I_{out})}{(I_{in})} \qquad (5.1)$$

where R is the gas constant ($8.315\ J/(mol \cdot K)$, T- temperature (K), z- ion charge (in elementary units, e.g. $z(K^+) = 1$), F- Faraday constant (96,485 C/mol) and I-ion concentration. Thereby, the equilibrium voltage across the membrane of normal animal cells is about -90 mV.

During the metabolic activity of the cell the glucose (one of three monosaccharides and the main source of energy) undergoes the breakdown in a series of reactions called glycolysis giving rise to the lactic acid concentrations and, hence, change in the pH ($pH = -log_{10}(H^+)$ where H^+ is measured in moles per liter). The pH of pure water which is said to be 'neutral' equals to 7, or in terms of proton concentration is $[H^+] = 100\ nM$.

5.3.3 Cell cycle and death

Most cells regenerate to replace dead or damaged cells or to grow. In order to grow, the cell doubles its DNA content. The DNA forms two sets of chromosomes, which line up on spindles within the cell before the cell divides into two equal halves. Just before the division, or mitosis, the cell will contain twice the normal amount of DNA. The normal amount of DNA is referred to as diploid. The cell cycle is generally split into three identifiable component parts. These are the G0/G1, S and G2/M phases of the cell cycle (Figure 5.2). More correctly, G0 is a phase where cells are quiescent and not taking part in cell division.G1 is the phase where cells are gearing up to move through cell division. As both of these components of the cell cycle have 2n DNA, these phases are not distinguishable from each other using solely a DNA probe. S phase is that part of the cell cycle where synthesis of DNA occurs and where DNA staining increases. G2 and M phases of the cell cycle are where 4n DNA is present, just prior to and during mitosis, respectively. Again, with just a DNA probe, these two phases are not distinguishable from each other by the flow cytometer.

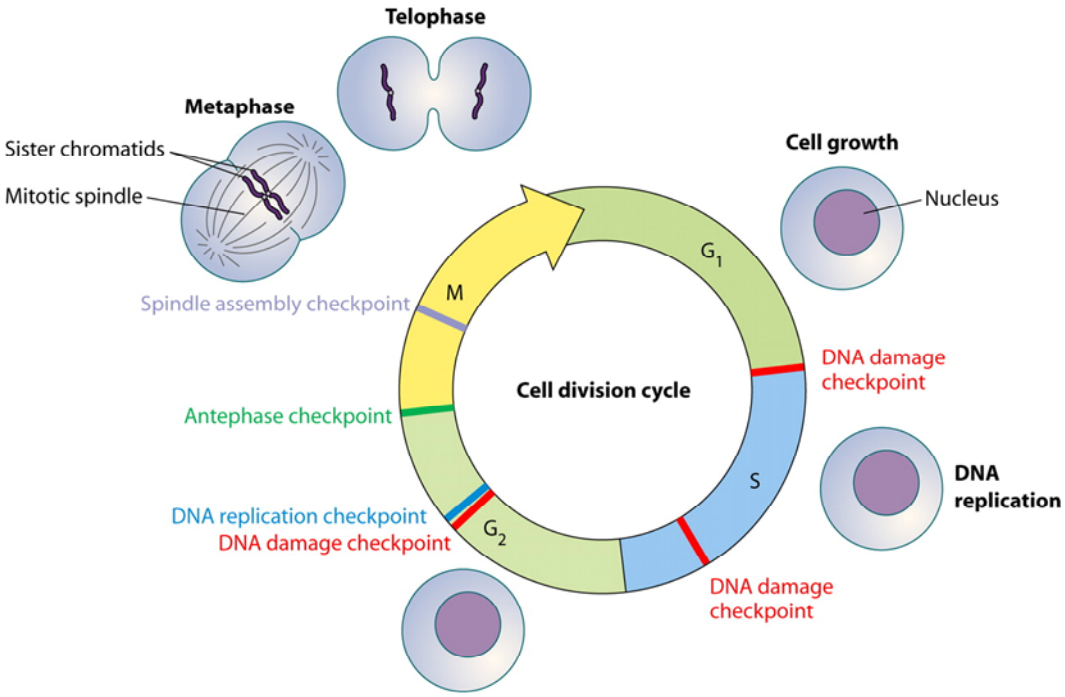

Figure 5.2 Cell cycle and checkpoints (taken from (Chin and Yeong 2010))

5.3.4 Culturing of mammalian cells in vitro

Experiments on living cells in-vitro which literally means 'in glass' (outside the body) are based on culturing of cell colonies on a substrate or in suspension depending on their nature at an abundance of appropriate culture medium. The first experiments on mammalian cells, dating to the beginning of 1950s, were carried out in Pyrex flasks and Petri dishes. However, the difficulty of handling with glass vessels and, more importantly, the low adherence of most the cells to the glass surface led to the wide spread of plastic polystyrene dishes already by the early 1960s. Polystyrene is generally chosen because of its good optical clarity and easy molding, but showing hydrophobic properties and, hence, low cell adherence it requires further treatment. Exposure to low-pressure glow discharge plasma can induce formation of carboxyl and hydroxyl groups on the polystyrene surface (Tamada and Ikada 1993), improving its wettability. Binding of cell attachment proteins, e.g. fibronectin, (Dekker *et al* 1991) to negatively charged hydroxyl groups favors the overall cell adherence to the surface. It's worth noting

that activity of integrins (attachment proteins) depends strictly on the presence of divalent Ca^{2+} and Mg^{2+} ions.

Culture medium (or growth medium) is liquid nutrient solution used for in vitro growth of living cells, therefore it must mimic as closely as possible the real in vivo environment for cell survival and proliferation. In other words, simply to keep the cells alive in artificial solution, four physicochemical conditions should be fulfilled: temperature (37°C for mammalian cells), concentration of dissolved oxygen (typical values in vivo may vary between 0.2 kPa for tissues up to 16 kPa for arteriolar capillaries) and carbon dioxide (5.6 kPa for mammalian cells), osmotic pressure of dissolved salts (NaCl, KCl and *pH* of the solution (7.4 for mammalian cells) (Silver 1975). The common solution for the first two requirements is to maintain the cells in a commercially available thermo stabilized incubators with typical relative humidity $> 95\%$ and controllable supply of oxygen and carbon dioxide. Practically it means that the time spent by the cells outside the incubator must be minimized to the time necessary for seeding, treatment, staining and analysis of the cells.

The culture medium for in vitro studies must provide the same concentration ratio of the most abundant ions found in cytosol and extracellular medium in vivo (Na^+, K^+, Cl^-, Ca^{2+} and H^+). In order to maintain the pH in vitro a $NaHCO_3/CO_2$ couple is often used. The concentration of sodium bicarbonate should be in equilibrium with 5 % of carbon dioxide in culture environment.

5.4 Apoptosis induced by cold atmospheric plasma

Recent study on plasma interaction with melanoma cancer cells (A2058) revealed that plasma has the potential to induce apoptosis, or programmed cell death, and necrosis, spontaneous cell death by loosing cell integrity, in dose dependant manner (Fridman *et al* 2007). Authors characterized quantitatively cell response to plasma treatment and found that the plasma dose needed to kill melanoma cells through

necrosis equals to 20 J/cm^2, which is still below of the damaging threshold of healthy tissue. Lower doses of plasma were shown to initiate massive apoptosis 12-24 hours after the treatment. More recently, the same group performed a deep analysis of apoptotic activity in plasma treated melanoma cells by Trypan blue exclusion test, Annexin-V/PI staining, caspase-3 cleavage, and TUNEL analysis (Sensenig *et al* 2011a). The experiments were done by direct exposure of melanoma cells covered with 100 µm of complete medium to dielectric barrier discharge plasma. It was found that preincubation of the cells with an intracellular ROS scavenger NAC reduces the number of apoptotic cells from 35% to 20% for dose of 15 J/cm2 at H24 and completely protects the DNA against the damage as seen from phosphorylation of H2AX, one of the signals against double-strand break (DSB), at already 1 hour after the treatment. These observations bring authors to conclusion that plasma apoptotic effect originates from direct interaction between ROS and cell DNA.

Another work devoted to plasma treatment of murine melanoma cells (B16F10) by surface type DBD in similar conditions (Kim *et al* 2010a) demonstrated that together with DSB damage to DNA and respective accumulation of proapoptotic p53 tumor suppressor gene, plasma can affect the mitochondria as shown by cytochrome C release and change in mitochondrial membrane potential by using mitochondrial membrane-specific fluorescent dye. In another notable work on cancer cells treatment, RF plasma torch operating in He was applied in human metastatic melanoma line (G361) (Lee *et al* 2009). Authors reported on loss of adhesion capability of 90% cells already 15 s after the treatment. Plasma was found to inhibit the expression of adhesion proteins (integrin α2, α4 and FAK) that are known to play an important role in malignant transformation.

The selective killing of melanoma cancer cells (1205Lu) comparing to primary keratinocytes was done in (Zirnheld *et al* 2010). Using low frequency plasma torch in He authors demonstrated that 10 s of exposure to plasma leads to alterations in morphology of melanoma

cells and decrease of cell population viability down to 40% whereas keratinocytes maintain their morphology and demonstrate viability greater than 90 %. In comparative study done in (Keidar *et al* 2011) plasma ability to selectively kill cancer cells was confirmed in vitro with murine melanoma cells (B16F10) and murine primary macrophages and in vivo experiments on nude mice bearing murine melanoma tumor. It was found that in vitro plasma effectively induces apoptosis in melanoma model without affecting macrophage for the same dose. In-vivo experiments demonstrated efficient ablation of the tumor decreasing its growth rate and improving survival in the treatment group.

We intentionally focused on melanoma cancer cells here for the reason of literature available on the subject and in order to give an idea of the effect that different plasma sources and treatment strategies produce in a given cell model (keeping in mind that different melanoma lines has different resistivity and can demonstrate quite different malignant behavior and metastatic phenotypes). It's worth noting that plasma has been successfully applied for apoptosis induction in human colorectal cancer cells (Kim *et al* 2010a) and human hepatocellular carcinoma line (Zhang *et al* 2008) as well.

We have seen that interaction of cold plasmas with living cells is rather complex process comprising direct plasma effect on cell membrane proteins, cell organelles and DNA by production of ROS. Indirect plasma action consists in specific triggering of chemical or biological mediators in the cell culture medium or directly in the cell.

5.4.1 The role of ROS

Much work has been done in an effort to understand the mechanisms of plasma action on living cells by GREMI-Orleans group. Note that the first in-vivo plasma treatment of the tumor xenografts in nude mice model (Vandamme *et al* 2010) has been performed in Orleans. In their study U87 malignant glioma cells transfected with firefly luciferase gene have been injected subcutaneously into flanks of nude mice. When tumor volume reached 150 mm^3 it was exposed to DBD plasma in

ambient air. Plasma treatment was repeated 3 times daily during 5 consecutive days and resulted in about 30% decrease in tumor volume measured by bioluminescence. Skin pH measurements revealed a drastic drop of pH from7.0 to 2.0 while subcutaneous pH slightly increased up to 8.5. Authors concluded that some reactive plasma species like NO may penetrate through the mouse skin causing the pH increase. Synergetic coupling of electric field and reactive species was suggested to explain the plasma induced cytotoxic effect.

Further in-vitro experiments performed on the same cell line (Vandamme *et al* 2012) showed a key role of ROS generated in cell medium. Transfected U87MG-Luc2 glioma cells were seeded in 24-well plates and treated with 500 µl of compete MEM (10% SFB, 1% Glu, 1% Pen-Streptomycin). Cell viability was measured by bioluminescence. It was shown that direct exposure to plasma of cells with medium and separate medium treatment give the same viability levels in experimental error limits. Thus, plasma dose of 20 J/cm^2 induced a 100% cell death in directly and indirectly treated cells as seen 24 hours after the treatment. Intracellular ROS scavenger (NAC) was shown to improve the cell viability even for highest doses of plasma. Oxidation sensitive fluorescent probes (H2DCFDA, DHE) were used to measure hydrogen peroxide (H_2O_2) and superoxide (O_2^-) concentrations in cell medium. Both probes give strong fluorescence intensity in treated medium suggesting on high production rates of corresponding species. However, since the H2DCFDA probe is equally sensitive to OH and ONOO radicals, the peroxide concentration was overestimated almost two times as compared to cells viability after the treatment with the equivalent concentration of H_2O_2.

Although, most authors suppose some synergy between ROS and plasma UV light or electric field no experimental evidence of its existence was shown so far. The experimental difficulty to measure properly ROS concentrations is one of the reasons. Another reason consists in necessity of development of the model system, since the use of multiple plasma devices and treatment protocols from one hand and

numerous cell cultures from another complicates comparison of the results obtained by different groups.

5.4.2 The role of pulsed electric field

It's known that exposure of living cell to short pulsed electric field induces cell membrane electroporation, also called electropermeabilization. This phenomenon was first discovered in the 1970s and is still used for gene transfection in vitro. More recently, electroporation was applied to enhance the efficiency of the antitumoral non-permeant chemotherapeutic drugs. Short nanosecond high voltage pulses was shown to produce a strong effect in living cells variant from those caused by conventional electroporation. Thus the cells exposed to nanosecond pulsed electric field of several tens of kilovolts per centimeter demonstrate membrane permeabilization with a pore size of about several nanometers, intracellular calcium release, DNA damage and triggering of apoptotic pathways (Breton and Mir 2012). The possible explanation of nanosecond pulsed electric field hypothesize that initial ns pulses release calcium from the endoplasmic reticulum, followed by calcium redistribution within the cytoplasm. With further EP pulses calcium penetrates mitochondrial membranes and causes changes that trigger release of cytochrome c and other death molecules. It was demonstrated that nanosecond electric pulse are able to reduce tumor growth in vivo (Nuccitelli *et al* 2009).

Recently Leduc and coworkers (Leduc *et al* 2009) reported on permeabilization of HeLa cells exposed to RF plasma jet operating in He. Cells were treated in presence of 130 µl of complete MEME, just covering the bottom of Petri dish, containing 80 µg/µl of 3, 10, 40 and 70 kDa dextrans. Size exclusion approach with non-permeable dextran molecules gave for the plasma induced pore the size of less than 6 nm. Since electric field does not seem to be of great importance in this case authors suggested that membrane permeabilization occurs due to the lipid peroxidation. It is stated that plasma produced ROS are able to

abstract a hydrogen atom from the methylene group. The hydroxyl radical (OH) is one of the most reactive species and, thus, a good candidate for lipid peroxidation since it is produced in abundance in discharge afterglow in ambient air. Consecutive lipid peroxidation may lead to the cross linking of the fatty acid side chains and eventual formation of transient pores.

Experimental results discussed above show that atmospheric plasma is able to permeabilize the cell membrane by different ways involving intense short electric field and chemical attack on membrane lipids. Special attention should be attributed to this specific aspect of cold plasma as simultaneous membrane permeabilization with high production of ROS and RNS in cell medium or tissue may be at the origin of synergetic enhancement of plasma action.

6 Materials, methods and protocols

6.1 Haemocytemeter. Trypan blue

Haemocytometer is a cell counting device, consisting of a glass microscope slide with a rectangular slot that creates a chamber. The bottom of this chamber is engraved with a grid of perpendicular lines with a typical spacing of 50 µm. The chamber is covered with a thin glass slip leaving 100 µm gap from the grid. The culture media with cells at the given dilution is introduced in the chamber by capillary forces. Visually counting the number of cells over the grid with an optical microscope and knowing the volume corresponding to the grid surface, on may easily find the overall cell concentration in the medium. In order to distinguish between viable and dead cells since they can appear similar within the optical resolution, Trypan blue cell viability dye is generally used. Trypan blue is a diazo dye molecule (960 Da) and being negatively charged it is excluded from the viable cells while it can penetrate trough the damaged membrane of dead cell. Thereby, the dead cells are stained blue and may be easily discerned.

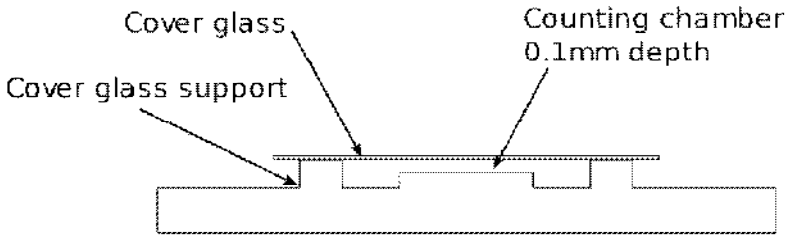

Figure 6.1The scheme of haemocytometer (taken from wikipedia).

6.2 Flowcytometry. Annexine V (AV) and Propidium iodide (PI) assay

Flowcytometry is a technique providing quantitative analysis of multiple physical characteristics of single particle or cell in a steam of fluid. Coulter counter is considered as the first prototype of modern flowcytometers. Its principle relies on measurement of current drop

associated with change in the impedance when a nonconductive particle (which may be a living cell) passes through the orifice separating two vessel filled with electrolyte. Coulter counter allows counting and sizing of cells and is widely used for blood analysis. Later on, the progress of laser technique and new fluorescent markers led to development of Fluorescence-activated cell sorting (FACS) in late 60s. In FACS device an isolated cell is flowing in hydrodynamically focused stream of liquid crossing the laser beam with axis perpendicular to the flow direction. Light scattered on the cell structures is then collected in forward and lateral direction in respect to the incident beam, filtered and analyzed. Modern flowcytometers are able to detect up to ten thousand particles per second with simultaneous analysis of more than thirteen fluorescent channels. The use of fluorescent dyes and specific fluorochrome conjugated monoclonal antibodies expands the scope of flowcytometry to determination of nucleic acid content, probing of intracellular pH change, concentration of ROS and Ca^{2+} fluxes , sensing of plasma membrane receptors and intracellular organelles, immunophenotyping and apoptosis detection.

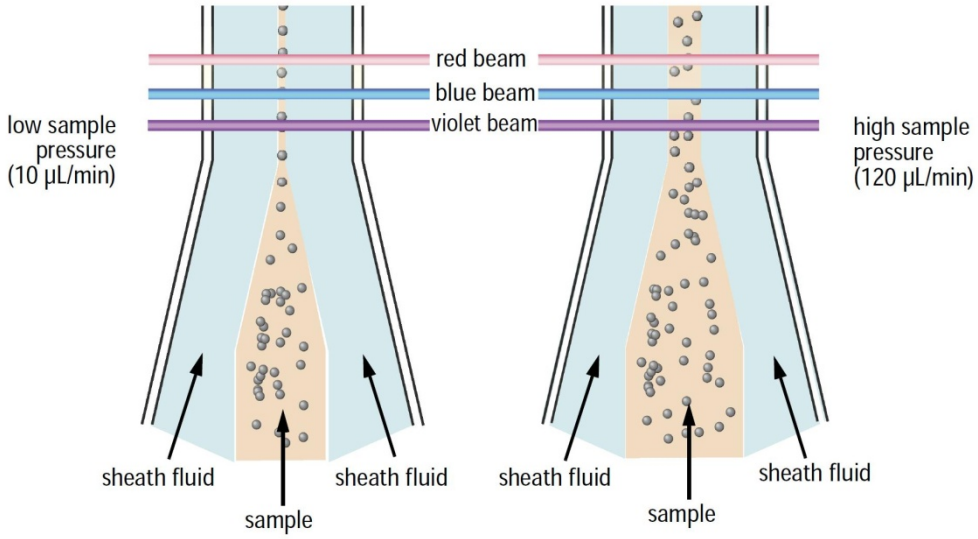

Figure 6.2 Hydrodynamic focusing of liquid flow with cells (taken from BD Canto II manual).

Operation of flowcytometer can be conventionally divided into three blocks: fluidic, optical and signal processing. We will start with the fluidic part. When the buffer solution with cells is injected in the flow cell ending with a nozzle of about 70 µm in diameter, the cells are randomly distributed in the whole volume of fluid (

Figure *6.2*). Thus, for their individual analysis the cells would need first to be ordered into a stream of single particles. It may be realized by means of hydrodynamic focusing of sample stream enclosed by sheath of faster flowing liquid (

Figure 6.2). Under laminar conditions the sampling flux will not mix with the sheath fluid, however the strong drag acting on the central flow results in its narrowing with parabolic velocity profile. The width of focused stream, and hence the sampling rate is determined by hydrostatic pressure in the sample tube.

After hydrodynamic focusing the stream of cells passes through the aligned laser beams focused in the flow cell. Typically, flowcytometers are equipped with two low power lasers emitting in blue and red parts of visible spectrum. To give an example, solid state Sapphire laser with maximum at 488 nm and HeNe laser emitting at 633 nm are commonly used in tandem (BD Biosciences 2006). The laser beam has elliptic geometry with very high aspect ratio about 1:9 (9:90 µm) allowing uniform cell illumination along the transverse axis and better resolution in the direction of the flow. Thus, the cell crossing the laser beam produces the flash of scattered light with typical duration in the range of microseconds. Scattered light of the lower wavelength laser (488 nm) is then used to estimate cell size and internal structure. Indeed, the intensity and angular distribution of scattered light can be approximated as a sum of Rayleigh scattering on small particles of the cell internal structure (e.g. proteins of units up to tens of nanometers in size) and anomalous diffraction (van de Hulst approximation) valid for large particles with relative refractive index close to unity (Latimer 1982). The last assumption is valid for living cells since the cytosol and the medium have just slight difference in

overall refractive index which, however, induces phase shift of transmitted light. The interference of diffracted beams with retarded phases leads to small angle scattering in forward direction proportional to the cell size (Figure 6.3 a). The scattering on the small particles has almost isotropic pattern with scatter intensity depending on number of small structures and their size. Side scatter as was shown for yeast cells (Latimer 1982 and references herein) represents less than 5% of total scattering.

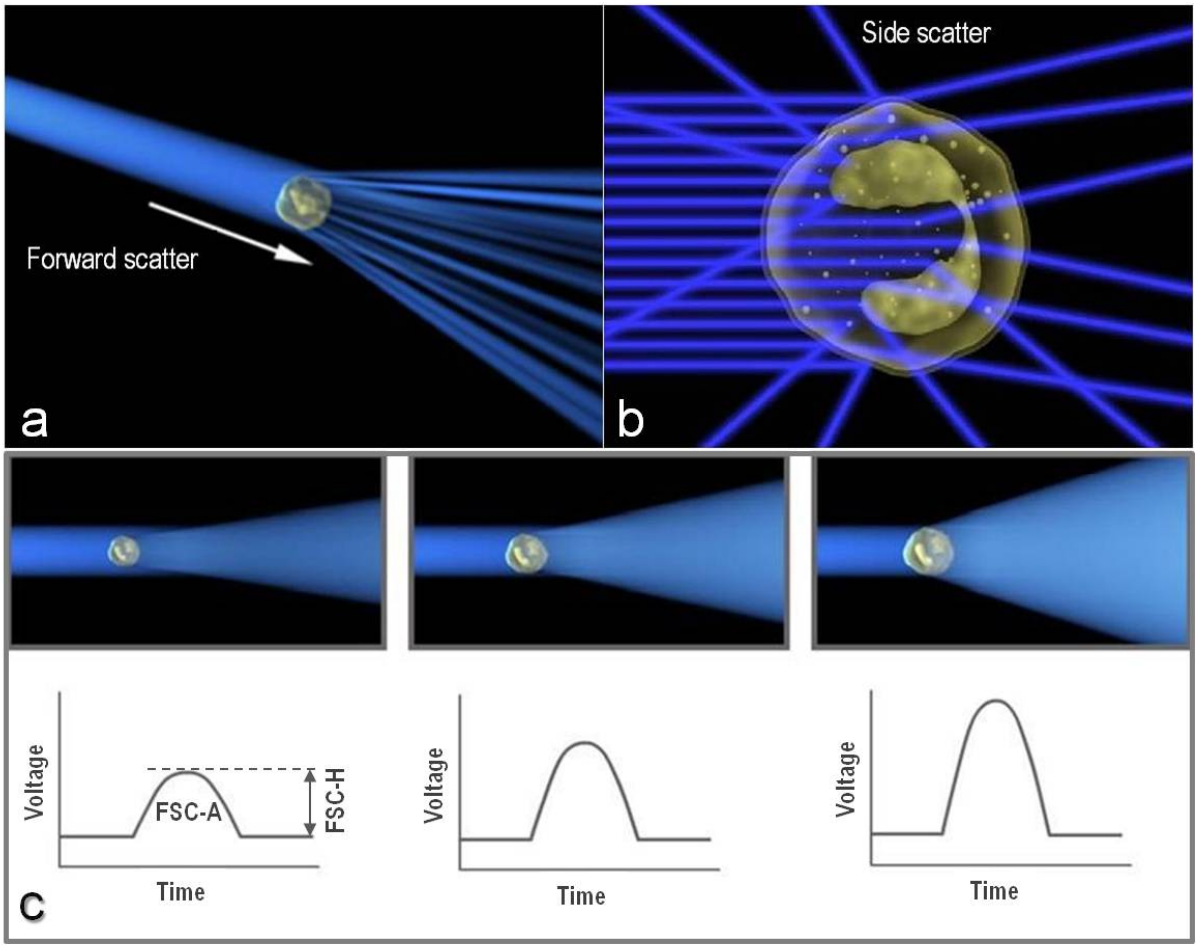

Figure 6.3 Forward and side light beam scatter on living cell. (Modified from media.invitrogen.com.edgesuite.net/tutorials)

In other words, by measuring the intensity of light scattered in forward direction one may get information on relative cell size whereas light intensity measured at right angle correlates with cell internal structure. As a rule, in modern flowcytometers forward light scatter (FSC) which is stronger comparing to side scatter (SSC) is detected with a

photodiode (PD) in 0.5-2° offset from laser axis, while light transmitted without scattering is blocked by obscuration bar. SSC signal is measured at about 90º to the laser beam axis with photomultiplier tube (PMT) which has better sensitivity. Both PD signal for forward scatter and PMT signal for side scatter have bell-shaped temporal profile with maximum corresponding to full laser beam intersection by the cell (Figure 6.3 c). Practically the height of the peak (FSC-H and SSC-H) is used for analysis, however in some cases the peak area (FSC-A and SSC-A) or its width (FSC-W and SSC-W) may be useful in the discrimination of clumping cells. Since the cell doublet profile has the same FSC-H signal, while the width of the signal is doubled. The last consideration is only valid in the case of axial orientation of the doublet in flow cell channel and does not take into account its possible rotation. Combination of FSC and SSC signals is thereby unique fingerprint of each cell and allows recognizing of morphologically distinct cells. Even if flowcytometry gives information on properties of a single cell, only statistical analysis over about 10^4 cells can characterize the state of the cell colony.

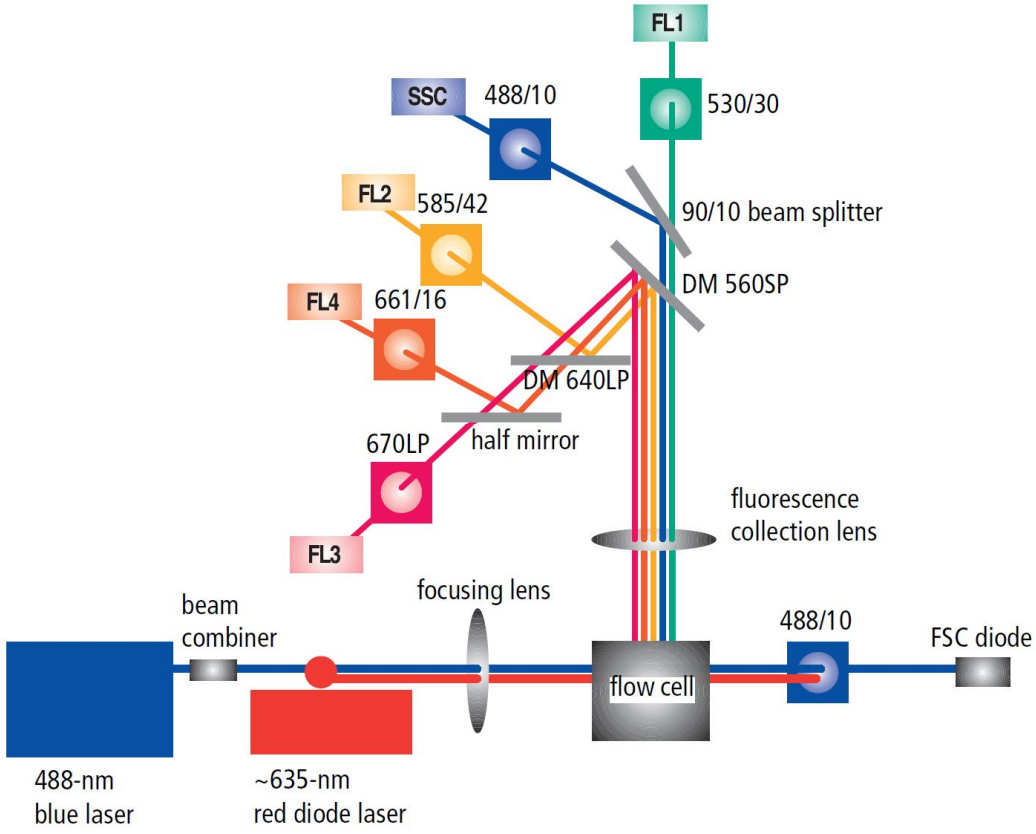

Figure 6.4 Optical scheme of BD Canto II flowcytometer (taken from the manual).

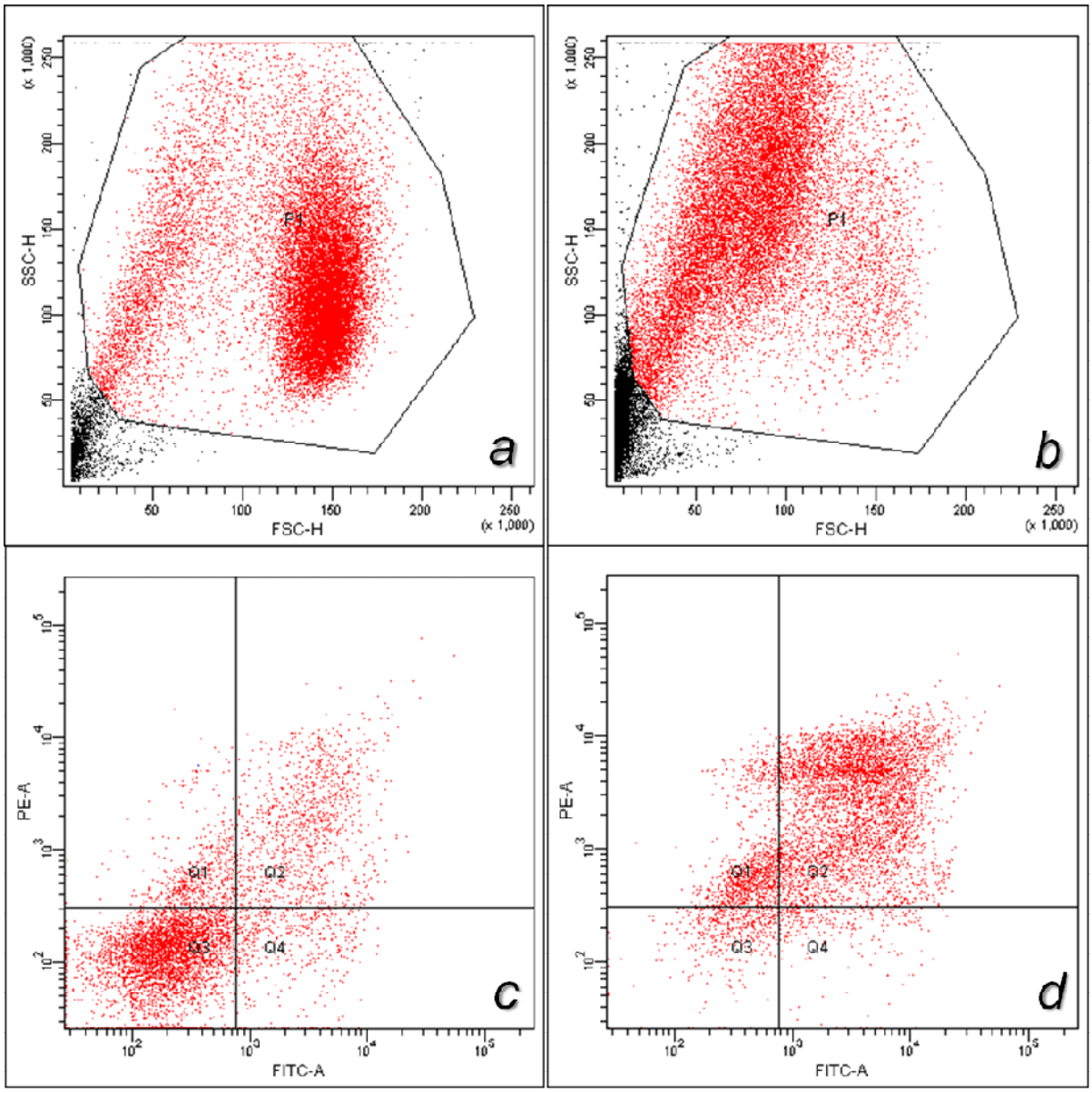

Figure 6.5 Cytograms for Jurkat cells a) untreated and b) treated with DBD plasma. c) Fluorescent 2d plot showing viable cells, d) apoptotic behavior shown with AnnexinV and PI.

Consequently, if we trace a SSC-H signal as a function of FSC-H on a 2d plot called cytogram each analyzed cell will be represented by a point. Figure 6.5 a demonstrates a cytogram corresponding to accumulation of 10^4 Jurkat cells on a BD Canto II flowcytometer. O-shaped zone with maximal data point density corresponds to the majority of viable cells proceeding from G1 to G2 through S phase since those cells prevailing at exponential growth. The characteristic form of

this pattern extended along the side scatter axis points to the overall increase in number of internal structures, which is virtually doubled before the cell will be able to enter the mytosis phase. The points occupying the lower cell size region of the cytogram should be attributed to shrinkage and disintegration of cells typical for apoptosis and occurring naturally in cell colony. Inducing the apoptosis in the cell colony by, for example, exposure to low temperature plasma (the detailed protocol of plasma treatment is given in Chapter 7.2) is characterized by shift of cell population to the upper left part of the cytogram suggesting the decrease in cells size, whereas their internal structure becomes denser. The condensation of chromatin in the cell nucleus –one of the characteristics of apoptosis seems to be in agreement with this flowcytometric observation. Moreover, in vitro conditions the apoptotic bodies and cell fragments are not recycled by phagocytes as it normally occurs in animals and humans (Krysko *et al* 2008), hence, they can been seen in the lower left corner of the cytogram (Figure 6.5 a,b). As one can see the cell debris are excluded from the analysis region, also called gating, as they do not posses any longer the characteristics of the cell as a whole. Note that the increase in the relative number of cell debris can be itself a sign of necrosis or late apoptosis.

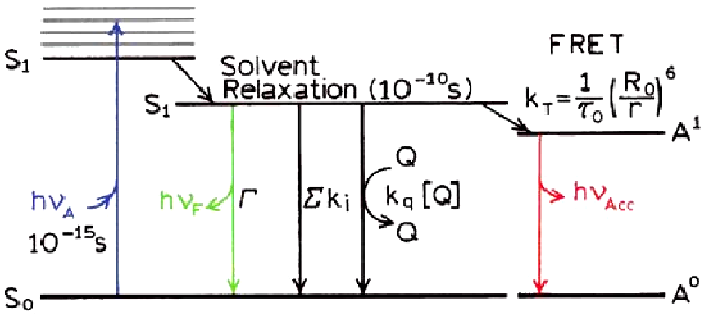

Figure 6.6 Jablonski diagram. Q –collision quenching, FRET– fluorescence resonant energy transfer, Σk_i – all other nonradiative transitions (Lakowicz 2006).

As it was stated above the staining of cells with specific fluorochrome can be useful for selective probing of cell compartments (e.g. membranes, cytosol, nuclei and mitochondria). Along with information on morphological changes obtained from forward and side light scatter,

fluorescent signal of some specific probes may be used as a hallmark of apoptosis and can provide its quantitative measure. It's worth noting that the reason for using fluorescent methods and not, for example, absorption technique consists in high sensitivity and special resolution of the former, allowing detection of a single fluorescing molecule (Lakowicz 2006).

The physical phenomenon underlying the fluorescence process may be described by well-known Jablonski diagram shown in Figure 6.6. Excitation of high vibrational level of the first S_1 or second S_2 electronic state is followed by rapid redistribution of the part of incident photon energy between the internal degrees of freedom leading to thermalisation of the excited state during 10^{-12} s. Transition from excited state with the lowest vibrational energy typically occurs to the high vibrational level of the ground state which then quickly relax to thermal equilibrium. Emission of the lower wavelength photon than the absorbed one is called Stokes shift. Nonradiative disexcitation of the S_1 state may also occur through the collisional quenching, resonant energy transfer to the neighboring molecules and some other processes. As in the stained cell the fluorochrome molecules have random orientation the fluorescence may be considered isotropic. It allows one to collect the fluorescent signal with the same optical arrangement as is normally used to detect the side scatter. The photons resulted from Rayleigh scattering, which naturally does not induce any wavelength change and the Stokes shifted photons produced by fluorescence may be easily separated by a dichroic mirror. If the cutoff of dichroic filter is situated between shifted and unshifted wavelengths the high energy photon will pass through while the Stokes photon will be reflected. Modern flowcytometers provide typically from 4 up to 13 independent detectors for simultaneous multicolor fluorescence studies. Consequently a series of dichroic filters must be used to successively filter fluorescent signals as it is shown for the case of 4 color flowcytometer (Figure 6.4). A band-pass filter centered at the wavelength of maximum fluorescence intensity and placed just before each detector eliminates lower wavelength light from other fluorochromes used and, hence, reduces the

overlap. Actually, the numerous fluochromes are available with wide range of excitation and emission properties making possible combined use of several fluochromes on a given flowcytometer. The fluochromes of biological interest must, however, selectively interact or be accumulated in cell compartments under study. Some fluorescent molecules demonstrate natural selectivity in respect to the nucleic acids contained in DNA and RNA, like for example propidium iodide (PI), phycoerythrin (PE), 4',6-diamidino-2-phenylindole (DAPI) and 7-Aminoactinomycin D (7-AAD) widely used for DNA content analysis (Darzynkiewicz *et al* 1997). Other may be conjugated with monoclonal antibodies able to recognize and selectively bind to the desired site within the cell. Among the latter we will cite FITC and the family of Alexa Fluor fluochromes conjugated with Annexin V. Another group of probes is the molecules which are not fluorescent under normal condition and that may become fluorescent if undergo a chemical transformation while being introduced to the intracellular medium. The DCF probe for intracellular ROS testing is activated by enzyme whereas the complex is fluorescent and cell membrane is no longer permeable.

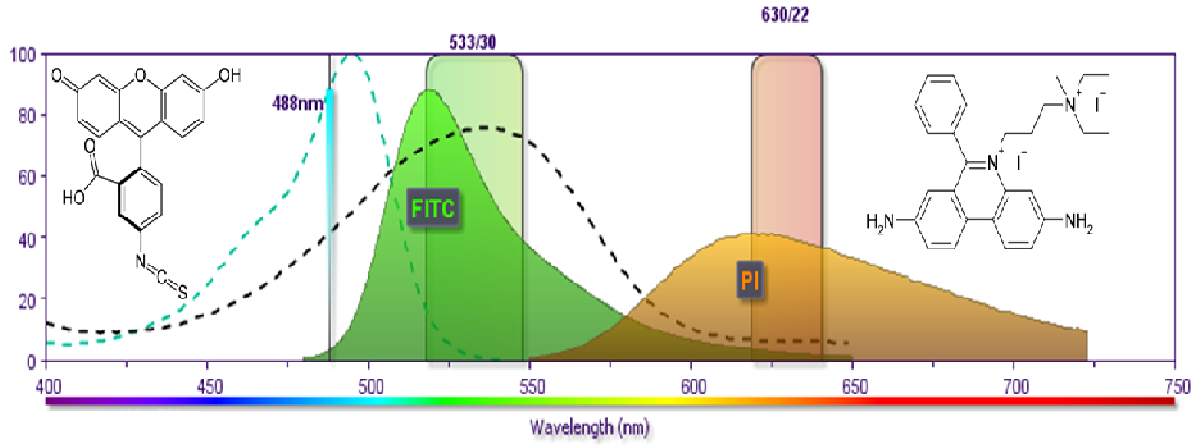

Figure 6.7 Fluorescence excitation and emission spectra of FITC and PI (BD Fluorescence Spectrum Viewer).

As it was previously mentioned, one of the earliest manifestations of apoptosis induction is the translocation of phosphatidylserine (PS) phospholipid to the outer leaflet of cell membrane. Apoptosis terminates by cell disintegration and formation of apoptotic bodies. The time

necessary for completion of the whole cycle depends on cell type, its environment and induction agent. An evident complexity in detection of apoptosis arises from the fact that the late stage of apoptosis rather often could be hardly distinguished from the necrotic collapse. It implies that only consecutive observation can provide quantitative measure of apoptosis. The common approach consists in using of two distinct markers for detection of early and late evidences of apoptosis while their respective intensities measured over a time indicate the state of apoptosis progression. Annexin V is a phospholipid-binding protein with high affinity for PS. Annexin V can be conjugated to one of commonly used fluorochromes, like FITC or Alexa Fluor, while it preserves its affinity for PS and, thus, it fits for flow cytometric detection of cells undergoing apoptosis. One of DNA staining dyes like PI or 7-AAD, normally excluded from viable cells and attaching to DNA fragments after the loss of cell integrity is generally chosen as a companion for Annexin V based probe.

From experimental point of view, the use of FITC-Annexin V together with PI has several notable advantages, as both fluorochromes may be excited with the same laser source (typically laser at 488 nm is used) and secondly, their emission profiles has just slight overlapping in the region between 550 and 650 nm. The spillover fluorescence may be consider negligible if the FITC signal is detected on the first fluorescent channel (FL1) at 530 nm while the PI fluorescence is measured with on the third channel (FL3) at 630 nm as it is shown in Figure 6.7.

Figure 6.5 c and d give an example of simultaneous staining of Jurkat B lymphocyte cells with FITC-Annexin V and PI and correspond respectively to the cells from the gate P1 on cytograms a and b (Figure 6.5 a and b). For ease of interpretation it is common to trace the fluorescence signals from both probes in a form of 2d plot, as it is done for forward and side scatter. The logarithmic scale is generally used for the reason of perceptivity. On the fluorescent cytogram each point, thus, represents a cell with respective intensity in two spectral regions at 530 nm for FITC and 630 nm for PI dye. As it can be clearly

seen from the fluorescence cytogram the majority of viable cells demonstrate a uniform pattern with comparatively low emission intensity measured in those spectral windows, originating mainly from cell auto-fluorescence (Monici 2005). By selecting on the scatter cytogram the cell population that is considered apoptotic, it can be seen that those cells occupying a diagonal sector on the fluorescence plot have higher fluorescence intensity comparing to viable cells (this gating is not shown on Figure 6.5). Since the fluorescence intensity varies smoothly while passing from viable to apoptotic cells the calibration by staining with single dye is needed in order to establish the threshold values separating viable, early and late apoptotic and necrotic cells. For calibration the apoptosis can be massively induced by exposing the cells to the UVB emission, starving the cells or by one of the commercially available apoptosis inducers, like Antimycin A.

Finally, as we have seen four quadrants Q_1, Q_2, Q_3, Q_4 should be empirically determined for each cell type and experimental conditions. The cells that are found in Q_3 sector are considered as viable, the cells in Q_4 sector demonstrating only FITC fluorescence and excluding PI are therefore early apoptotic cells, the cells occupying Q_2 sector show active fluorescence of both fluochromes and, hence, proceed through the late stage of apoptosis and, finally the particles from Q_1 sector which do not bind Annexin V are most likely to be the cell fragment occurring as a result of necrosis.

Obviously, only cells suspended in liquid solution may be analyzed by flowcytometer. This requirement seems to be easily fulfilled for circulating blood and lymphatic cells, although special attention must be paid to avoid sticking of the cells and agglomerate formation. It could be done by gentle vortexing of the sample just before the analysis or by adding EDTA Ca^{2+} chelator to the buffer solution. However, the adherent cells require a detachment procedure prior to flowcytometric analysis. The commonly used protocols for harvesting of adherent cells are proteolisys of integrins by trypsin, Ca^{2+} chelating by EDTA (EGTA).

6.3 WST-1 colorimetric proliferation assay

The WST-1 (Water soluble Tetrazolium salts) provides spectrophotometric quantification of cell proliferation, cell viability or cytotoxicity based on cell metabolic activity. The principle of the assay relies on the enzymatic cleavage of cell-impermeable tetrazolium salt WST-1 to insoluble formazan stainig the cell medium with purple color. Reduction of WST-1 reagent occurring due to the enzymatic activity can be related to the number of viable cells. The reeding are perforem directly in microtiter plate without any addition step.

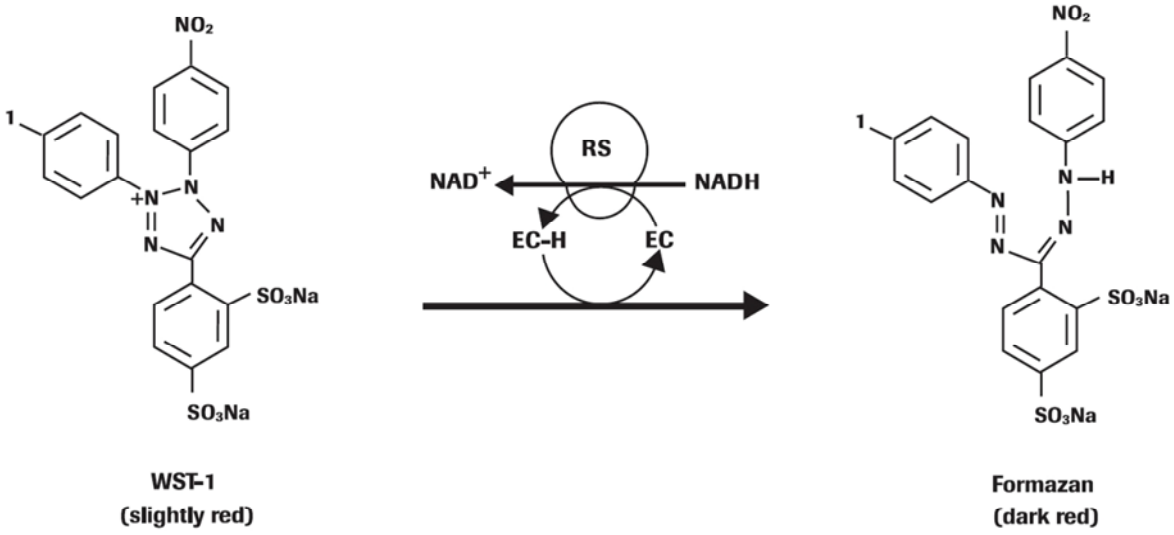

Figure 6.8 Enzymatic cleavage of WST-1 salt giving water insoluble formazan.

6.4 Amplex Red extracellular hydrogen peroxide (H2O2) fluorescent probe

Amplex Red reagent (10-acetyl-3,7-dihydroxyphenoxazine) in combination with horseradish peroxidase (HRP) allows one-step assay detection of hydrogen peroxide (H_2O_2) or peroxidase activity. In the presence of HRP Amplex Red reacts with hydrogen peroxide in a 1:1stoichiometry giving colored red-fluorescent resorufin. Horseradish peroxidase uses Amplex red as an electron donor during the reduction of hydrogen peroxide to water. Hydrogen peroxide concentration as low as 50 nM can be detected.

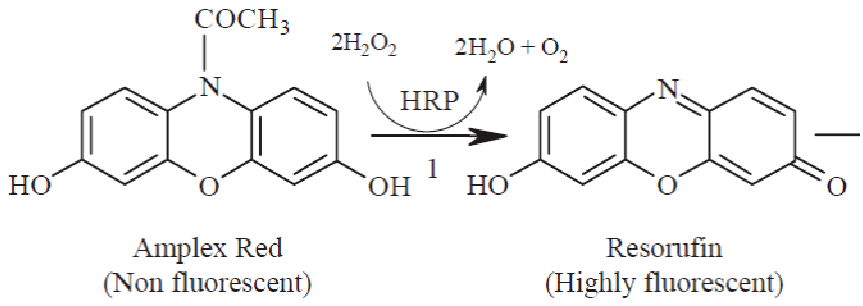

Figure 1 AmplexRed conversion to fluorescent resorufin.

7 Results on plasma treatment of living cells

7.1 DBD parameters

7.1.1 Absorbed energy measurements

Measurement of the energy input in plasma is a crucial issue for biomedical applications since the energy dissipation defines the term of 'plasma dose'. Although, the use of plasma dose makes sense only under the given conditions and for the same discharge type, it is commonly applied to characterise the plasma treatment procedure.

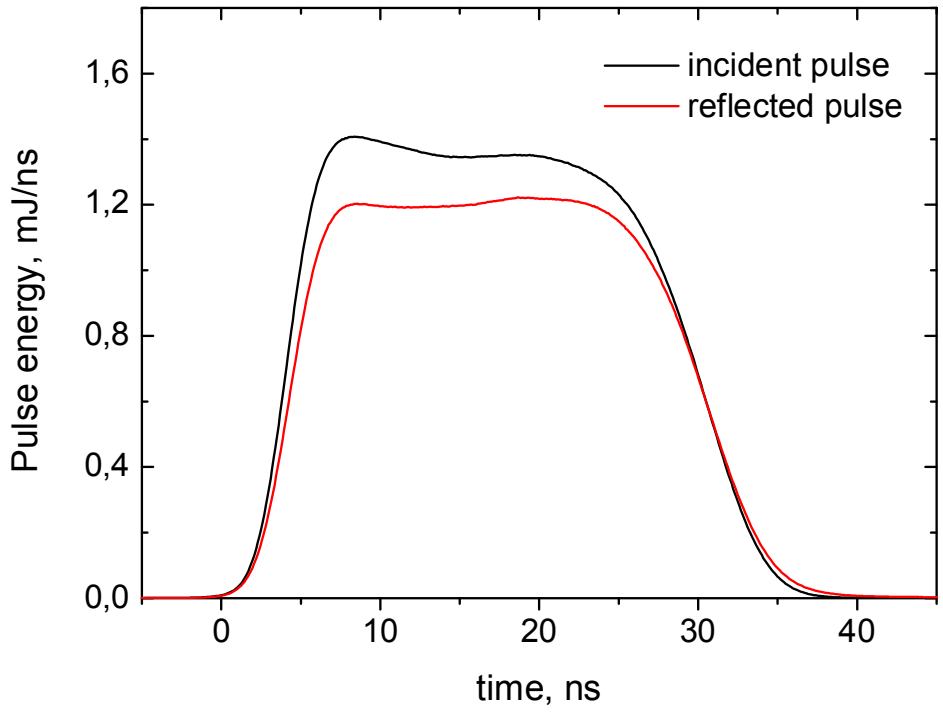

Figure 7.1 Power of incident and reflected HV pulses measured by BCS. 19 kV.

Applied technique is based on the discharge energy measurements from the back current shunt (BCS) signal as it was discussed in Chapter 3. The energy is calculated as a difference between HV pulse traveling from generator to discharge device and the same HV pulse reflected from the discharge gap (Figure 7.1). As we have seen above, a series of six HV pulses of alternate polarity occurs, because of reflections, for one pulse produced by generator. Energy dissipation under each of six

pulses is equal to 3.8 mJ, 3.2 mJ, 3.4 mJ, 2.8 mJ, 2.2 mJ and 2.4 mJ respectively. Therefore, the overall energy corresponding for one HV pulse applied is about 18 mJ, corresponding to 10 mJ/cm^2.

7.1.2 iCCD imaging

Uniform DBD

Electrical discharges produced at atmospheric pressure, in a general way, are filamentary. Streamers have a typical diameter of several hundreds of micrometers and their length in the case of DBDs is restricted by the gap size (Kogelschatz 2002). Streamer propagation velocity can achieve fraction of the speed of light which means that for a centimetre gap the characteristic propagation time is of the order of tens of nanoseconds. Each plasma filament is transferring a charge of about 100 nC and this charge being deposited on the dielectric surface tend to repulse other streamers leading to their uniform repartition over the dielectric. Two common techniques are used in order to obtain homogeneous discharge at atmospheric pressure. The first consists in using of the excitation source with a high repetition rate of about 100 KHz and higher (Massines *et al* 2009) in order to have the post-discharge phase shorter than typical recombination or de-excitation time at atmospheric pressure (1 µs - 100 µs). The charged and excited species remaining in the gap facilitate plasma reignition and due to their diffusion in the gap volume a homogeneous discharge may be obtained. One of the drawback for biomedical applications of this method is that high repetition rate can cause a substantial gas heating. Another approach is based on the use of short HV pulses with a sharp rising edge shorter than several tens of nanoseconds (Tao *et al* 2008). In this case discharge streamers are triggered simultaneously within the voltage rising time, whereas photo- and field-ionization contributes to formation of homogeneous discharge.

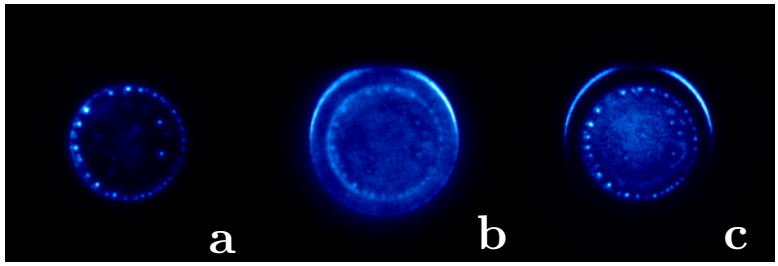

Figure 7.2 iCCD imaging of a discharge. a) First (positive) pulse, +19 kV on the electrode b)Second(negative) pulse -17 kV c) Third (positive) pulse +15 kV. Single shot. Camera gate is 40 ns.

The advantage of technique used in this work is a combination of the fast pulse rising slope of 5 ns and short delay between successive reflected pulses (260 ns). It means that for each series of pulses we have repetition rate in the series of 6 pulses of about 4 MHz, however initial pulses are applied with a low frequency of 100-900 Hz preventing gas heating. Figure 7.2 demonstrates a typical iCCD images illustrating plasma formation in single shot regime during three successive pulses of alternate polarity. So, under the first positive HV pulse one can see a homogeneous discharge pattern at the centre of electrode and a streamer discharge at the electrode edge. Successive negative discharge is quite homogeneous and fills entirely the gap. The third positive pulse produces a homogeneous discharge with simultaneous streamer discharge at the electrode edge.

7.1.3 Temperature measurements

Optical emission spectroscopy is powerful and widely used technique for non-intrusive measurements of atmospheric plasmas. Considering a direct electron excitation of nitrogen molecules and fast rotational-translational energy transfer at atmospheric pressure one can assume the equality of translational temperature and rotational temperatures in ground and exited state. This allows to measure gas temperature from rotational structure of emission nitrogen bands (Laux *et al* 2003).We determine plasma temperature from R-branch slope of 337 nm line ($C^3\Pi_u \longrightarrow B^3\Pi_g,\ 0-0$) comparing measured spectrum with

simulated one using Specair code Figure 7.3. The best fit between two spectral profiles gives temperature value within the error limits.

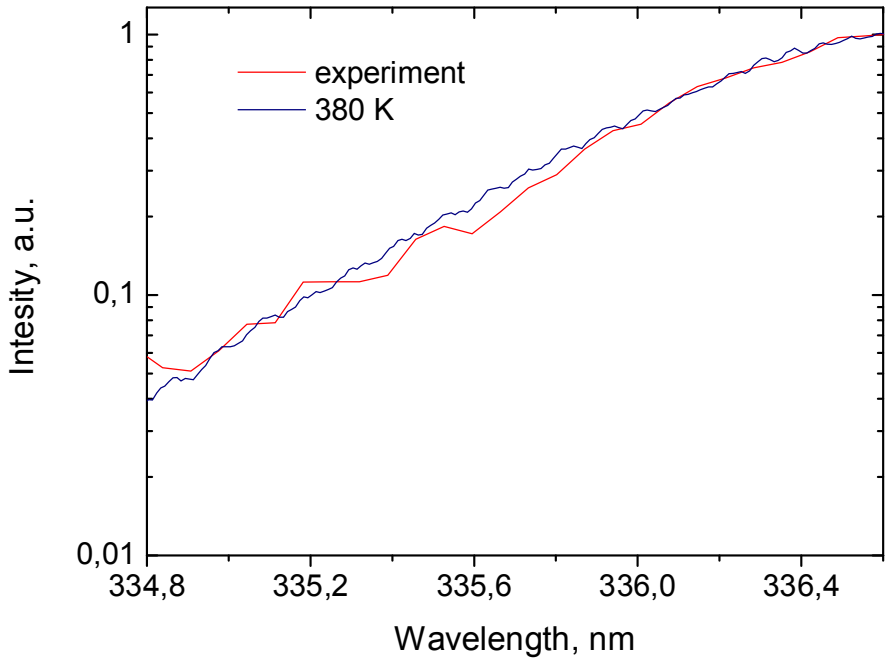

Figure 7.3 Experimental and calculated OES of $C^3\Pi_u \longrightarrow B^3\Pi_g$, $0-0$ *transition in* N_2.

The spectrum shown in Figure 7.3 is accumulated during entire first positive pulse and is averaged over 100 shots. It, hence, represents an average gas temperature in plasma during applied voltage pulse. Taking into account the short duration of HV pulses the heat transfer can be neglected and, therefore, deduced temperature is close to its possible maximal value. It's worth noting that the increase in gas temperature up to 380 K corresponds to very short time of a discharge and the overall energy going to heating is rather moderate. A raw estimation, assuming that all dissipated energy goes to substrate heating, gives less than 20 K temperature increase in 200 µl of culture medium treated during 30 s at 500 Hz. Hence, our DBD can be directly applied in cell cultures or on the living tissues.

7.1.4 Electric field measurements

High electric field is known to induce the pore formation in cell and intracellular membranes (Weaver *et al* 2012) and this fact is used in conventional electroporation for cell transfection or drug delivery. Short nanosecond high voltage pulses have been shown to affect the membrane of intracellular organelles resulting in membrane permeabilization (Silve *et al* 2012), intracellular calcium release(Vernier *et al* 2003), DNA damage(Stacey *et al* 2003) and apoptotic behavior(Beebe *et al* 2003).

Electroporation of cell membrane under nanosecond pulsed electric field can significantly improve the flux of plasma produced ROS into the cytosol. This peculiarity of nanosecond discharges make them very promising in cancer treatment. Therefore, the knowledge of electric field amplitude across the plasma zone is fundamental. In order to measure the electric field in the discharge we applied a nonintrusive spectroscopic method developed by Paris et al. (Paris *et al* 2005). The approach consists in measurement of intensity ratio of two nitrogen bands corresponding to electronic transitions in nitrogen molecular ion (N_2^+ B-X, 0-0) and neutral nitrogen molecule (N_2(C-B, 0-0). Obtained results are presented in Figure 7.4 demonstrate a narrow peak of the electric field, corresponding to rising slope of applied voltage pulse. Fast decrease of electric field in the discharge is due to the formation of volume charges that screen the applied electric field. The maximal amplitude of the electric field of $3.5 \cdot 10^5$V/m obtained in our conditions is two orders of magnitude higher than field necessary for nanopores formation as reported by, however electric field peak duration of about 2 ns is comparatively small. Moreover, the local electric field measured in plasma zone can be significantly different from the electric field acting on the cells in liquid medium. Spectroscopic measurements should be calibrated by using of D-dot field probe (Silve *et al* 2012) placed at the position of the cells.

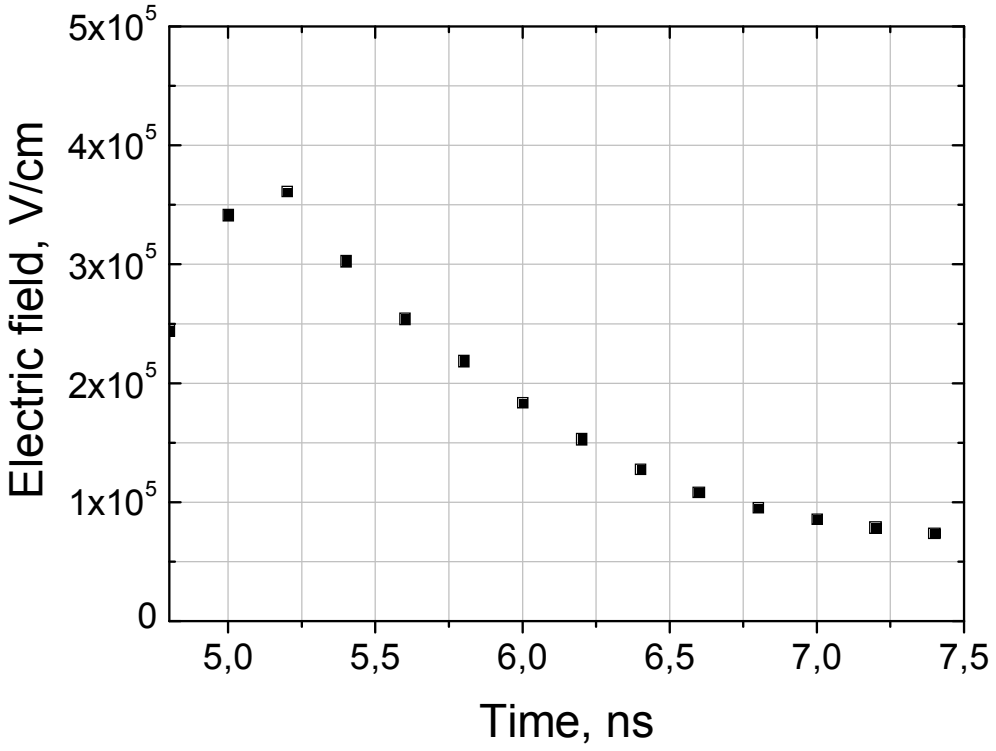

Figure 7.4 Electric field profile during rising slope of the first positive pulse.

7.1.5 pH change in culture medium under plasma treatment

For pH measurement of culture medium after plasma exposure pH indicator paper (Rota Prolab 35255) and pH probe (Hanna HI 98128) were used. To reduce the systematic error each plasma dose was applied in triplicate on 300 µl of fresh medium. pH readings were taken right after the treatment.

Figure 7.5 demonstrates the results of the pH measurement performed in triplicate in 300 µl of treated RPMI supplied with 20% of FCS. A pH of 7.2 was observed up to the highest dose of plasma corresponding to 450 J/cm^2 used in treatment of Jurkat cells. As a positive test, a three times higher dose of 1350 J/cm^2 resulted in pH drop to 6.1. As one can see, DBD plasma treatment of the complete medium for doses up to the 500 J/cm^2 does not induced the change of the pH, at higher doses acidic pH is observed.

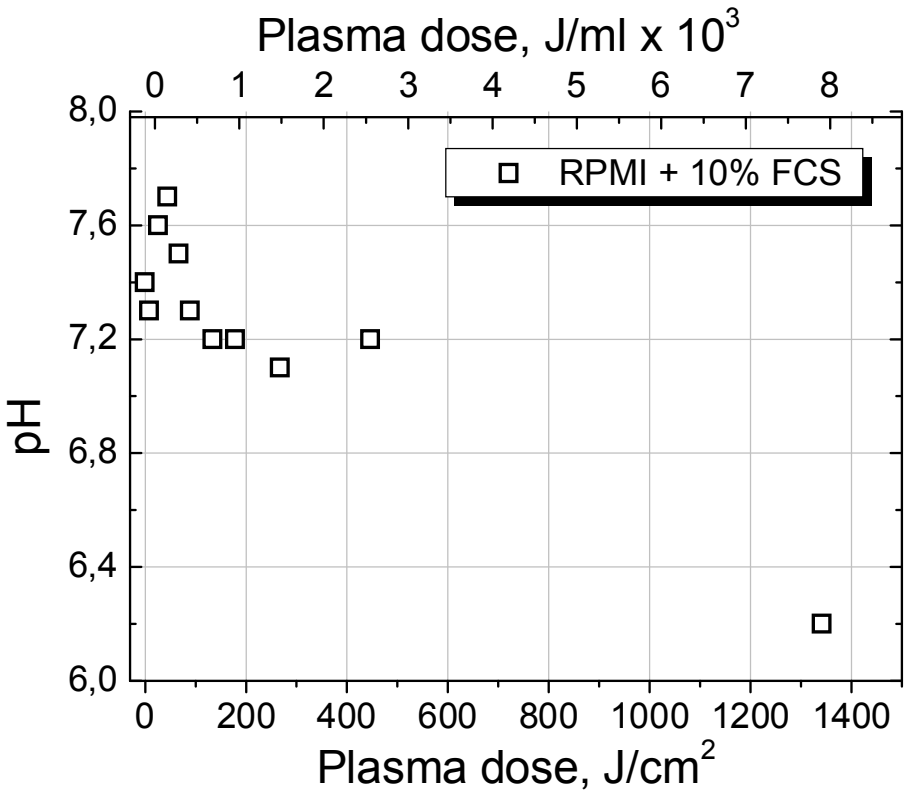

Figure 7.5 pH change in RPMI culture medium treated by DBD plasma. Treated volume is 300 µl.

7.2 Cell death induced by nanosecond DBD plasma (in collaboration with l'Hopital St Louis group)

7.2.1 In-vitro treatment of Jurkat and HMEC cells

7.2.1.1 Materials, methods and treatment protocol

Reagents

Fluorescein isothiocyanate (FITC)-conjugated Annexin V, Propidium iodide (PI), Cellrox Red® (fluorescent marker of intracytoplasmic oxidative stress), and Sytox Green® (marker for impaired plasmic membrane) were obtained from Invitrogen/Paisley/UK; Menadione (oxidative stress inducer) from Sigma-Aldrich/St.Louis/USA. Trypsin-EthylenDiamineTetrAcétic (0.05%/0.02%) from PAA/Piscataway/USA and Trypsin-Neutralizing-solution from CELL/SanDiego/USA.

Cell cultures

Jurkat cells and HMEC were obtained from ATCC/Virginia/USA. Cells were grown in uncoated T25 culture flasks. The culture medium was made up of RPMI with 10% foetal-calfserum for Jurkat cells, and of MCDB131 with 10% foetal-calf-serum, 10ng/mL epidermalgrowth-factor and 1Ng/mL hydrocortisone for HMEC. Experiments were performed in 24-well plates seeded with 60000 cells 48 hours previously.

Plasma treatment

The medium in each well was partly removed so that only 200µl remained. For Jurkat cells, attention was paid to avoiding removing the cells that had precipitated in the bottom of the well. The electrode was placed 2 mm above the medium surface. The presence of the discharge was confirmed by the emission of a particular sound and a blue light in the dark. After treatment, the medium removed was returned. Experiments were repeated at least three times.

Flowcytometry

The cells were labelled 8 hours or 24 hours after treatment. Jurkat cells were directly collected. HMEC cells were rapidly detached (less than 60 seconds) by Trypsin-EDTA at room temperature. A neutralising solution was added and the cell solutions were collected in cytometry tubes. Cells were counted, washed in Phosphate Buffered Saline solution (PBS) and then re-suspended in 100 µl of Annexin-V-buffer-solution (AVBS) with 0.3 µl of FITC Annexin-V solution and 1 µl of PI solution (100 Ng/ml). The cells were incubated in the dark for 15 minutes at room temperature. 400 µl of AVBS were added and cytometry analysis was performed. Cell suspensions were analysed on a Canto II cytometer from Becton Dickinson. Light scatters and fluorescence channels were set at linear and logarithmic gain, respectively. Analyses were performed on a Forward light scatter (FSC)/Side angle light scatter (SSC) dot plot, on a region containing cells and apoptotic bodies. Apoptosis was analysed on a FITC Annexin-V/PI dot plot.

7.2.1.2 Results on in-vitro plasma treatment

Flowcytometry data were analyzed on a four-quadrant dot-plot gated on a region including cells and debris. A propidium iodide (PI) signal was detected in the Phycoerythrine channel, on the Y axis. A FITC-labeled Annexin V signal was observed on the X axis. Non-apoptotic, non-necrotic, living cells were located in the lower left quadrant. The apoptotic pattern is defined as follows: in early-stage apoptosis, cells are labeled with Annexin V only. Later, since the plasmic membrane integrity is altered, they become positive for both Annexin V and PI. The necrotic pattern is defined as follows: c ells become positive for both Annexin V and PI at the same time because of the alteration of the plasmic membrane.

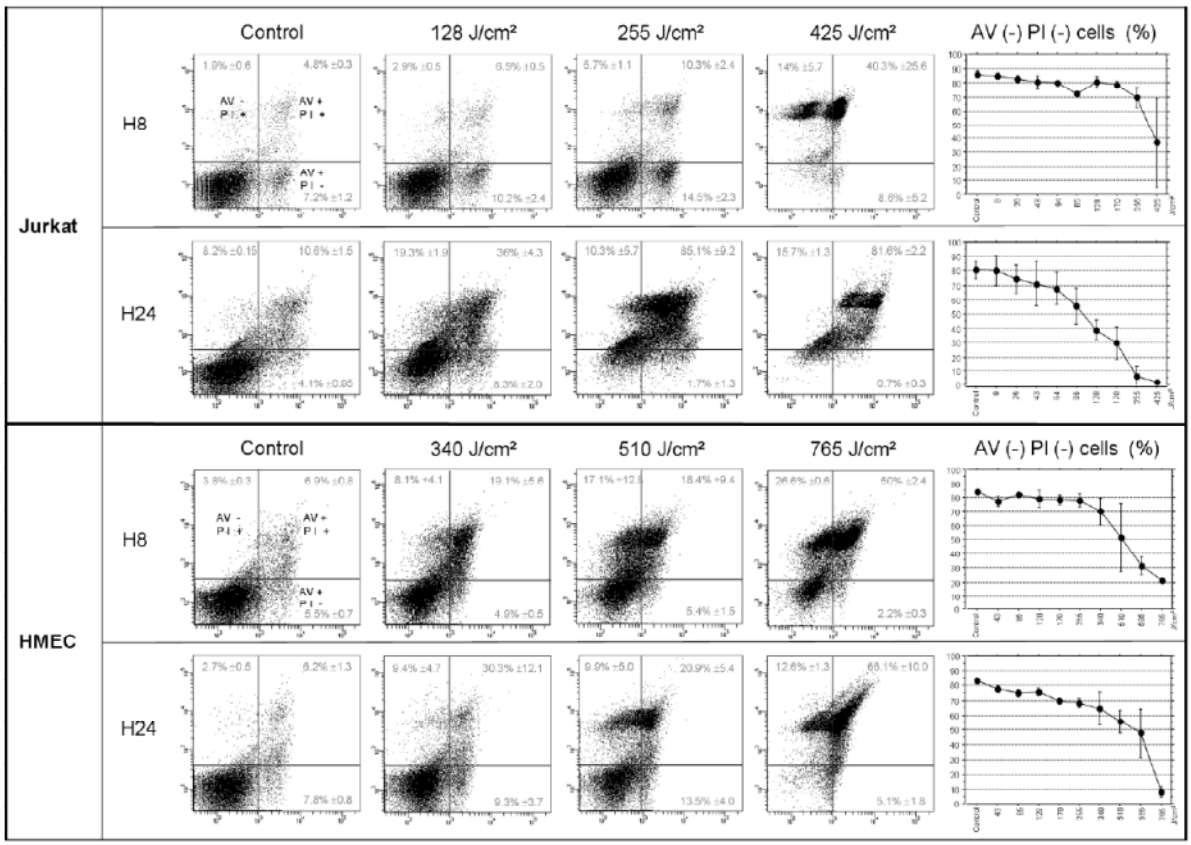

Figure 7.6 Annexin V/ I assay on HMEC and Jurkat cells 8 and 24 Hours after plasma treatment.

Obtained results are shown in Figure 7.6. On Jurkat cells, 8 hours after the treatment, the pattern is mainly apoptotic up to 255 J/cm^2. For higher doses, the pattern is necrotic. At H24, the pattern is non-specific,

consistent with late apoptosis or necrosis. For HMEC, 8 hours after the treatment, the pattern is not specific consistent with late apoptosis or necrosis for doses higher than 340 J/cm^2. At 24 hours after the treatment, the pattern is apoptotic up to 510 J/cm^2 and necrotic above. On HMEC and Jurkat, a dose dependent effect is observed. To reach a given percentage of cells mortality, HMEC need higher doses than Jurkat cells.

For intracellular oxidative stress and membrane permeabilization test, nucleuses were labeled with NucBlue, images were taken with the same parameters as for the negative control. Results are demonstrated in Figure 7.7. Oxidative stress assay: Cells were incubated one hour after treatment by plasma or menadione 100 µM with Cellrox deep green, an intracellular fluorescent marker for oxidative stress measurements. A, negative control, almost no fluorescence is apparent. B, Menadione, a strong cytoplasmic red fluorescence is present. C and D, medium and intense fluorescence depending on the plasma dose, 169 and 508 J/cm^2 respectively. Electroporation assay: Cells were incubated just before plasma treatment with Sytox green, a fluorescent marker of membrane impairment. E, negative control, almost no fluorescence is visible. F, high-dose plasma treatment (506 J/cm^2), a strong green fluorescence is present.

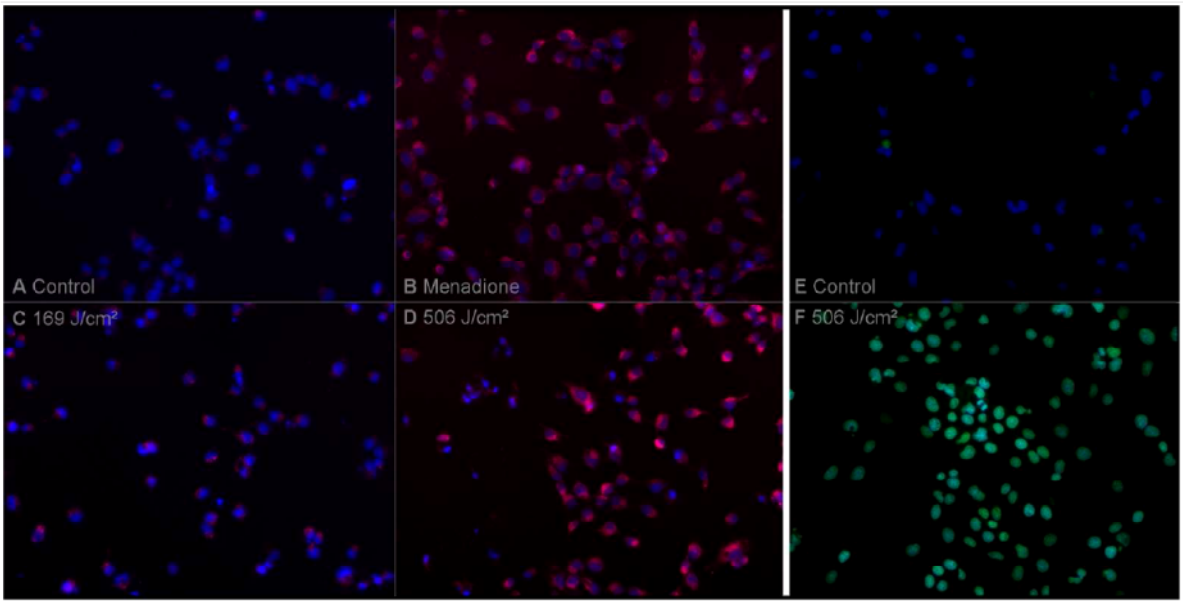

Figure 7.7 HMEC. Oxidative stress assay (A-D), Electroporation assay (E-F)

7.2.1.3 Conclusions on in-vitro plasma treatment of HMEC and Jurkat cells

- For in-vitro tests flowcytometry based cell viability assay with two markers AnnexinV and Propidium iodide (PI) was applied 5 and 24 h after exposure to plasma. In-vitro treatment of cultured Jurkat and HMEC cells demonstrated a dose dependent induction of apoptosis at doses up to 250 J/cm for circulating Jurkat cells and 340 J/cm for adherent HMEC. At higher doses a pattern was mostly necrotic.
- Intracellular oxidative stress was evaluated on HMEC with an intracytoplasmic fluorescent marker (Cellrox® Red). Red fluorescence appeared for doses above 169 J/cm² and increased up to the maximum dose of 506 J/cm².
- Electroporation was tested on HMEC with a fluorescent DNA stain (Sytox green®) which penetrates in the cells with membrane damage. Strong fluorescence appeared for high doses, 506 J/cm². No fluorescence could be seen for lower doses.

7.2.2 Nude mouse skin treatment

7.2.2.1 Protocol

Animal model

Sixteen seven-week-old nude mice were obtained from Iffa Credo (L'Arbresle, France). All mice were allowed to rest for 1 week before the treatment. All test on mice reported here have been approved by the Animal Housing and Experiment Board of the French government. The DBD plasma was applied to each mouse. Prior to the treatment all mice were anaesthetized with xylazine (10 mg/kg) and ketamine (100 mg/kg) by intra-peritoneal injection. Each mouse received six treatments at increasing plasma dose. Mice were euthanized 5 or 24 hours after the treatment.

Histological analysis

Euthanised mice were immediately dissected, and skin specimens were fixed in 10% formalin and further processed for paraffin embedding. 3 mm–thick paraffin sections were stained with hematoxylin and eosin. Some of the specimens were split, one part being fixed in 2% glutaraldehyde in cacodylate buffer and further processed for electron microscopy.

7.2.2.2 Results on nude mice treatment

A dose-effect was found clinically and microscopically. 24 hours after treatment, clinical abnormalities were present for doses higher than 300 Hz lasting 30 seconds (169 J/cm^2) and increased gradually with the dose. For high doses, above 394 J/cm^2, the skin was necrotic and subcutaneous tissues were damaged. Microscope observation of HES sections of nude mouse skin 24 hours after treatment showed similar abnormalities for the given product of the treatment time and the frequency of applied HV pulses. No abnormality has been observed for doses below 113 J/cm^2. At 113 J/cm^2 significant epidermal abnormalities were present. The delineation of individual cells was partly lost, the cytoplasms were strongly eosinophilic and the nucleuses were often picnotic. There was no visible abnormality below the epidermis. At 281 J/cm^2, the epidermis was severely damaged and considerable cell detachment was present. The dermis was oedematous. At 394 J/cm^2, the epidermis and the dermis were severely affected with no identifiable collagen fiber. The hypodermis and the muscle had oedema and vasodilatation. At 563 J/cm^2, the hypodermis and the muscle layer were severely damaged.

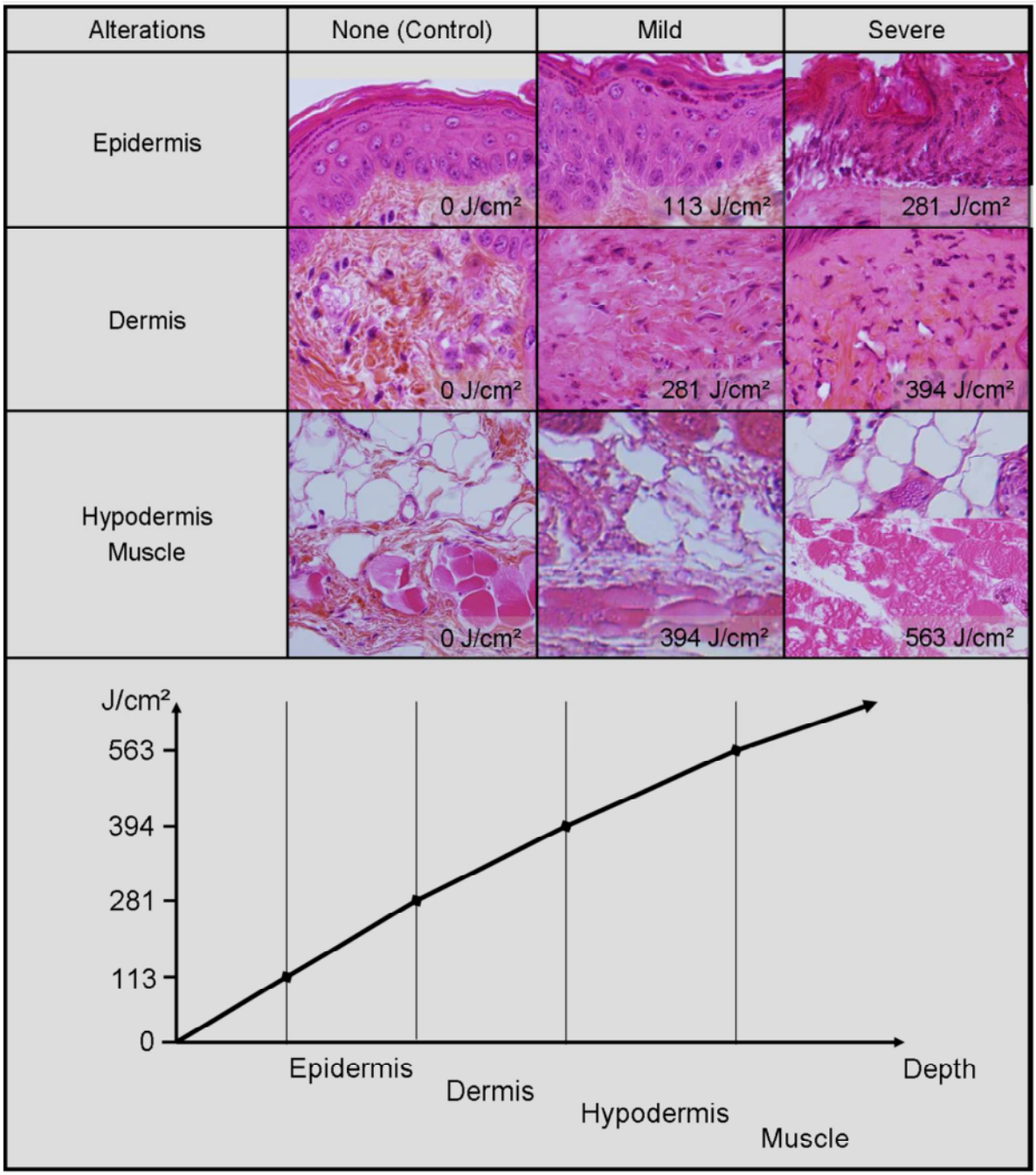

Figure 7.8 HES sections of nude mouse skin after plasma treatment.

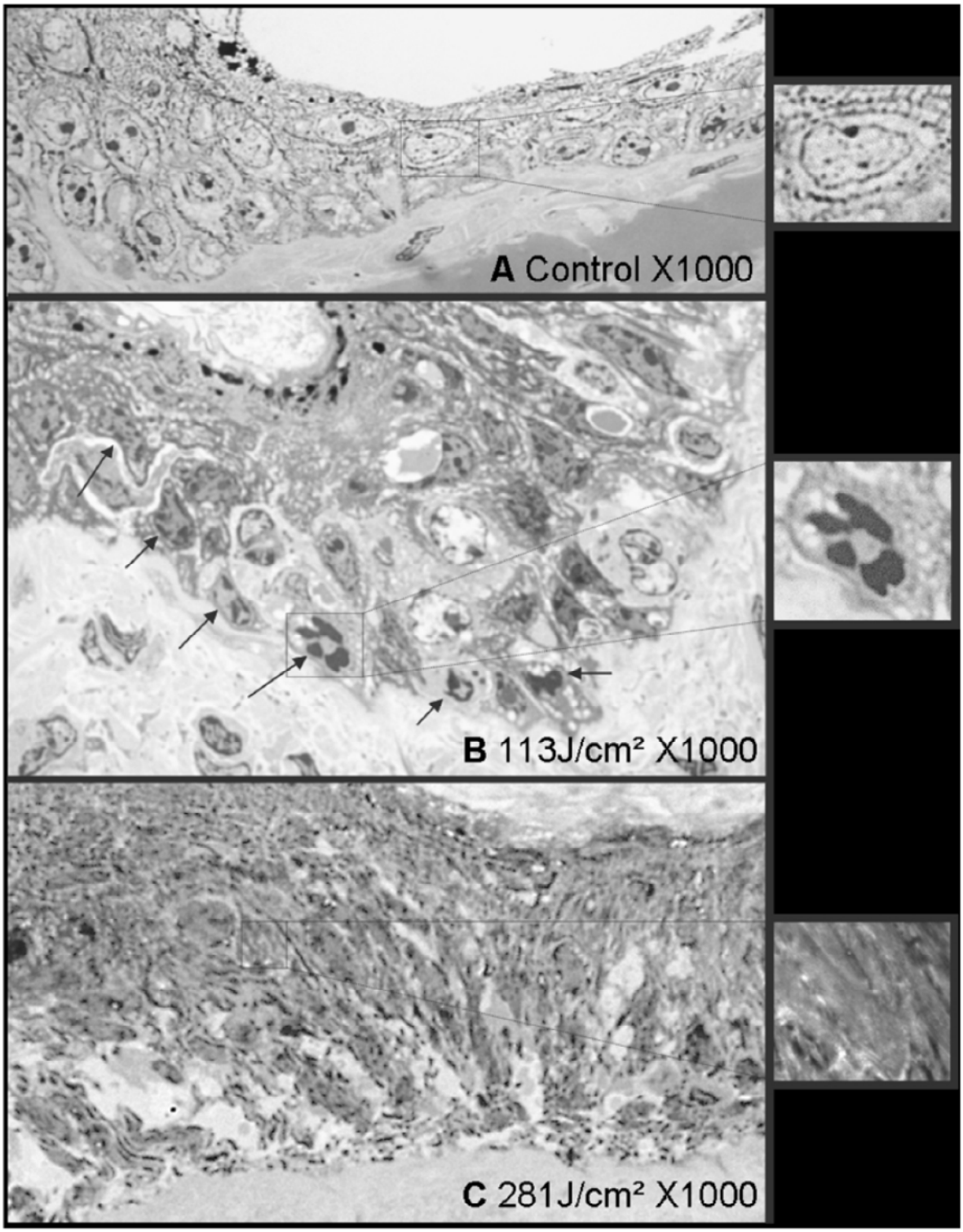

Figure 7.9 Electron microscopy of nude mouse epidermis after plasma treatment.

7.2.2.3 Conclusions on plasma treatment of nude mice skin

It was found that

- On hematoxylin-eosin sections, significant lesions appeared for doses above 113 J/cm² for the epidermis, 281 J/cm² for the dermis, and 394 J/cm² for the hypodermis and muscle. Thus, the higher the dose, the deeper is the effect in the tissue. On the epidermis, pathological analysis on ultra-thin sections was consistent with apoptosis for medium doses (113 J/cm²) and necrosis for higher doses (281 J/cm²).

7.3 Mechanisms of DBD plasma action

As we have seen in previous chapter exposure of normal mammary epithelial (HMEC) and cancer T lymphocyte cells (Jurkat) in vitro to nanosecond DBD plasma affects cells viability and is able to induce apoptosis in dose dependent manner. Plasma treatment of nude mouse skin results in very reproducible effect reaching muscular tissue for the highest plasma doses. It was shown that neither temperature increase nor suberythemal UV A, B and C emitted by plasma can explain the massive cells mortality. Recent studies undertaken by other groups point to the primary role of reactive oxygen species (ROS) as was shown by cells pretreatment with N-acetyl-L-cysteine (NAC intracellular ROS scavenger) (Sensenig *et al* 2011a, Vandamme *et al* 2012). However, it remains unclear whether plasma produced short-lived radical and nonradical species (O_3, $^1O_2$, OH, O_2^-) can diffuse through the medium layer and directly interact with cells. For highly reactive singlet oxygen ($^1O_2$) and hydroxyl radical (OH) the half-life time in water solutions is 10^{-6} s and 10^{-9} s respectively (Pryor 1986). Consequently, those species produced in the gas phase or at the gas/liquid interface could hardly reach the cells covered by several millimeters of the medium. Nevertheless, hydroxyl and singlet oxygen may be produced locally in Haber-Weiss process (Khan and Kasha 1994):

$$O_2^- + H_2O_2 \rightarrow {}^1O_2\left({}^1\Delta_g\right) + OH + OH^-$$

as super oxide (O_2^-) is more stable due to low constant of spontaneous dismutation if its concentration is weak (Fridovich 1983) .The main

stable product of O_2^- dismutation and OH recombination is, therefore, nonradical hydrogen peroxide (H_2O_2).

The quantitative measurement of short-lived ROS is a complicated task and practically each species requires a particular technique. For in situ or post-discharge measurements in the gas phase a number of absorption (UV, FTIR) and fluorescent techniques (LIF, TALIF) have been developed. They allow a precise and, as a rule time-resolved, probing of main chemical species. The knowledge on evolution of the main components generally suffice to calibrate global discharge models able to predict the discharge chemical kinetics and, hence, concentration of all species taken into account (Sakiyama *et al* 2012). However, at atmospheric conditions the discharge chemistry is strongly influenced by relative humidity and, hence, hardly controllable. Dry air purging may be used to minimize the impact of atmospheric humidity, but it does not permit to avoid completely the water desorbing from the treated sample, which could be a culture medium or living tissue. This important issue that complicates the quantitative gas phase measurements on one hand, and may affect the reproducibility of plasma treatment on the other hand must be solved before the first clinical tests could be done providing accurate administration of the plasma cure.

Cells response to plasma exposure in vitro, thus, should be related to ROS concentrations measured directly in culture medium as a more reliable parameter. Although, one should be careful when attempts to extrapolate the results obtained by in vitro test to the real model, it allows, nevertheless, identification of the main mechanisms.

In order to define the role of hydrogen peroxide as a possible mediator of apoptosis we have undertaken a quantitative measurement of plasma produced H_2O_2 concentration in extracellular medium. In parallel, we studied how H_2O_2 produced in extracellular medium affects cell viability.

These tests were done in "Reactive oxygen species and radiocarcinogenesis" group (UMR 8200) at Gustave Roussy Institute headed by Dr. Corinne Dupuy.

7.3.1 Dosage of hydrogen peroxide in culture medium

As it was discussed above (see Chapter 4.4) AmplexRed probe may be applied for quantitative and selective fluorescent measurement of hydrogen peroxide concentration in aqueous solution. We have chosen AmplexRed to measure production of hydrogen peroxide in culture medium treated with nanosecond DBD plasma in standard polystyrene 6 and 24 well plates (BD Biosciences). The first attempt aimed at feasibility analysis and choice of medium that would be compatible with plasma treatment and H_2O_2 dosage. The majority of literature describing the effect of cold plasma on mammalian cells deals with in vitro treatment performed in the presence of complete culture medium (Fridman *et al* 2007a, Kim *et al* 2010b, Vandamme *et al* 2012, Volotskova *et al* 2012, Zucker *et al* 2012, Hoentsch *et al* 2012). Although, those media most closely mimic the endogenic conditions they are strongly buffered to suppress oxidizing species for protection of the cells. The use of complete medium would lead to underestimation of hydrogen peroxide production while peroxidized byproducts resulted from reaction with proteins contained in complete medium may affect cells viability. Consequently, for the first tests phosphate buffer solution with $MgCO_3$ and $CaCO_3$ salts (PBS Mg^{2+} Ca^{2+}) has been chosen as having the simplest chemical composition (see Annex) and allowing cells incubation over at least several hours without visible effect on their viability.

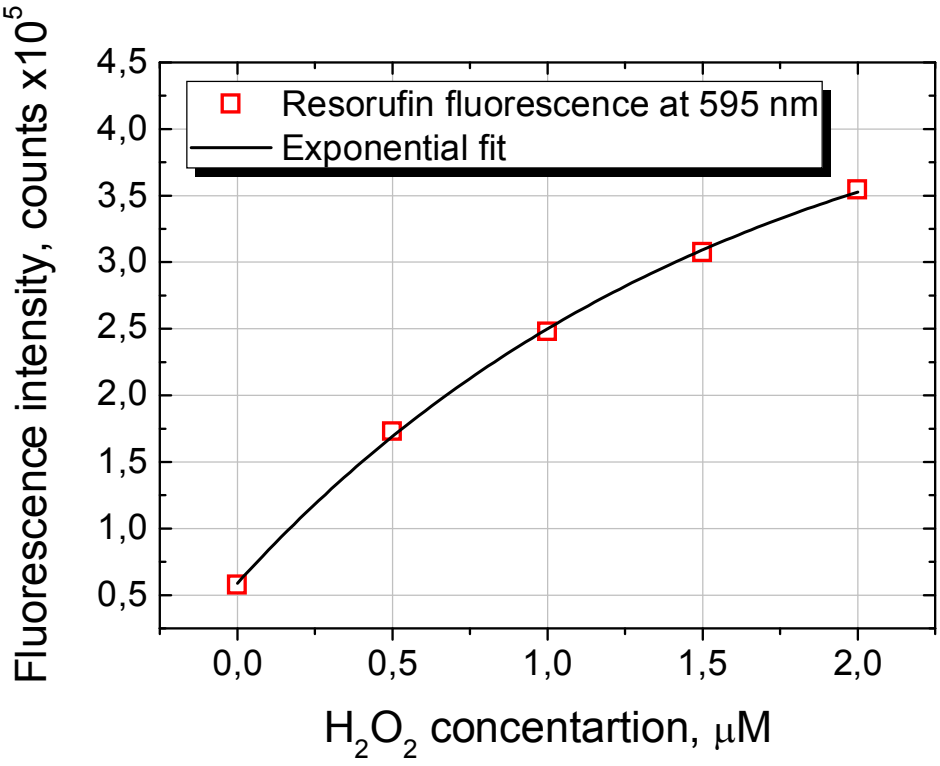

Figure 2 Calibration of resorufin fluorescent signal with standard concentrations of H_2O_2

The PBS $Mg^{2+}Ca^{2+}$ was treated by plasma in standard polystyrene 6 and 24 well plates (BD Biosciences) with typical diameter of the well equal to 35 mm and 16 mm respectively. The uncoated brass electrode of 13 mm in diameter was placed right in the center of the well and adjusted with micrometer screw at 2 mm above the liquid level. The cable sheath was connected to the aluminum plate placed under the plate in contact with the bottom of the wells. It was done to ensure the absence of parasite discharge underneath the well bottom. Nanosecond pulses of 19 kV in amplitude on the electrode were applied with repetition rate between 33 and 300 Hz. Practically the minimum volume of liquid needed to cover the bottom of well is about 200 µl for 16 mm well and 1 ml for 35 mm well. By filling the wells respectively with 300 µl and 2 ml of medium we ensured that the bas-fond of each well is entirely covered with liquid during the treatment.

As we have seen above (see Chapter 4.4) horseradish peroxidase uses 10-acetyl-3,7-dihydroxyphenoxazine (Amplex Red) as electron donor in

stochiometric reduction of hydrogen peroxide to water. The reaction product resorufin has the maximum absorption at 570 nm and maximal fluorescence intensity at 585 nm. Perkin Elmer Victor 3 fluorimeter was used to measure resorufin fluorescence at 595 nm where self-absorption self absorption could be neglected. For quantitative analysis the calibration of fluorescent signal was done using four H_2O_2 solutions prepared by dilution of 8.8 M H_2O_2 standard solution and giving final concentrations of 0.5, 1, 1.5 and 2 µM (Figure 2). The calibration concentrations were chosen to satisfy the optimal condition of enzymatic oxidation of AmplexRed ($K_M = 1.55$ µM of H_2O_2) and at the same time to avoid saturation or low signal to noise ratio of the fluorimeter. The volume of 100 µl of calibration solution was mixed with 100 µl of 1 mM AmplexRed containing 0.5 U/ml of HRP in opaque 96-well microtiter plate (OptiPlate 96). The resorufin fluorescence intensity at 595 nm was then measured using Victor 3 fluorimeter. As one may see (Figure 2) for H_2O_2 concentration between 0.5 and 2 µM the fluorescence signal exceeded the baseline by almost one order of magnitude while the signal saturates only slightly. The calibration curve may be rather well approximated with an exponent function which was then used to calculate plasma produced H_2O_2 concentrations. The calibration procedure was repeated each time as the sample analysis for correction of atmospheric conditions and response of the fluorimeter.

Since the working range of H_2O_2 concentration lies between 0.5 and 2 µM all plasma treated samples were diluted in fresh PBS $Mg^{2+}Ca^{2+}$ till the measurable scale. One should keep in mind that dilution can induce a significant error if final concentration occurs to be too close to the range limits. For example, the control point should not be diluted since the resulting signal would scale with the degree of dilution.

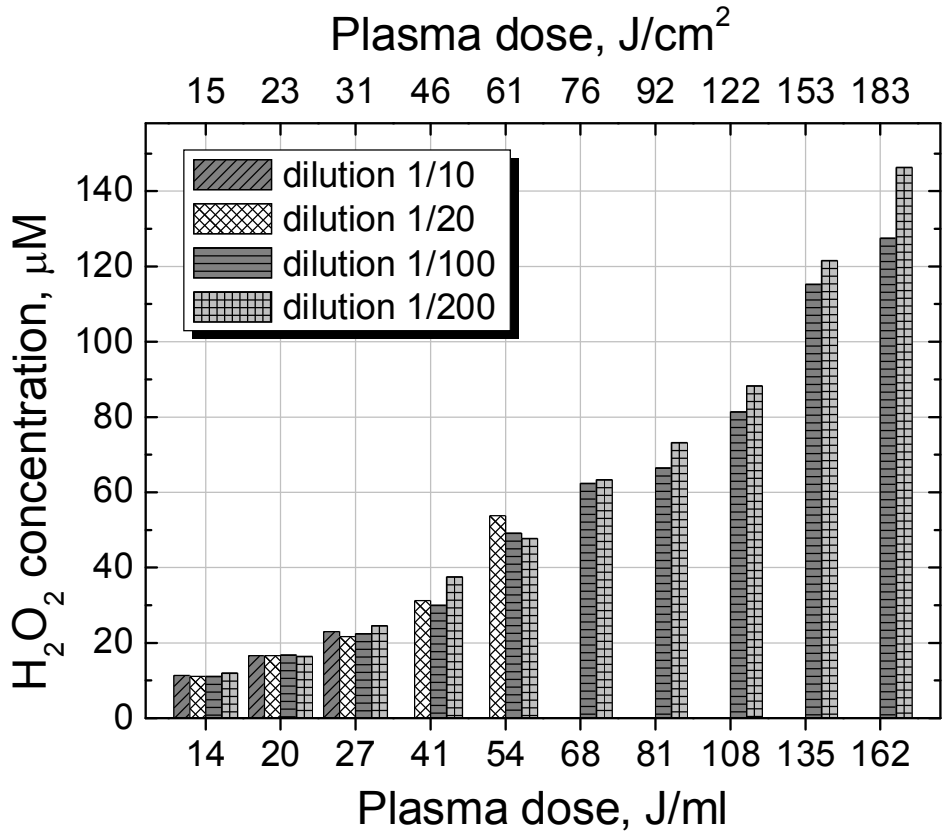

Figure 3 Production of H_2O_2 in 2 ml of PBS $Mg^{2+}Ca^{2+}$ treated by DBD plasma at 150 Hz. Plasma doses in Joule per milliliter and square centimeter are given. Several dilutions were used in order to avoid saturation of the fluorescent signal.

We found that hydrogen peroxide production weakly depends on repetition rate of HV pulses for the given absorbed energy. Slight increase in H_2O_2 concentration with frequency may be due to the better mixing at the gas/liquid interface as discharge induced surface modes may improve the effective surface. Thereby, the hydrogen peroxide production in our conditions can be determined by the product of pulse frequency and treatment time related to the volume of medium. Resulting plasma dose defined as energy dissipated in plasma per milliliter of treated medium was calculated from current signal measured in the cable (for more details see Chapter 2.1). The volumetric definition of plasma dose when working with liquid substrate seems to be more reliable and provide more physical significance if speaking about ROS production in the medium. In the majority of works dealing with plasma treatment of living cells and tissues authors use surface power density for plasma dose calculations. Historically, the

first tests on bacteria killing and deactivation of biofilms were done without liquid substrate and, as a rule, extended DBD and radiofrequency (RF) sources allowing uniform treatment were used. Nowadays, the so called plasma-jets with active plasma size from hundreds of microns up to several centimeters are as widely applied as direct DBD devices. Some ambiguity can, thus, arise with definition of real treated area when using a plasma jet device. In reality the plasma size can be only very roughly approximated with the well size if plasma is spread over its surface. In the case when plasma plume remains constricted, depending on jet construction and operation, the diameter of the jet orifice may serve as plasma size estimate. Of course, imaging techniques would allow precise measurement of plasma area in contact with sample under treatment. However, such techniques are expensive, complex and could hardly suit for clinical trials.

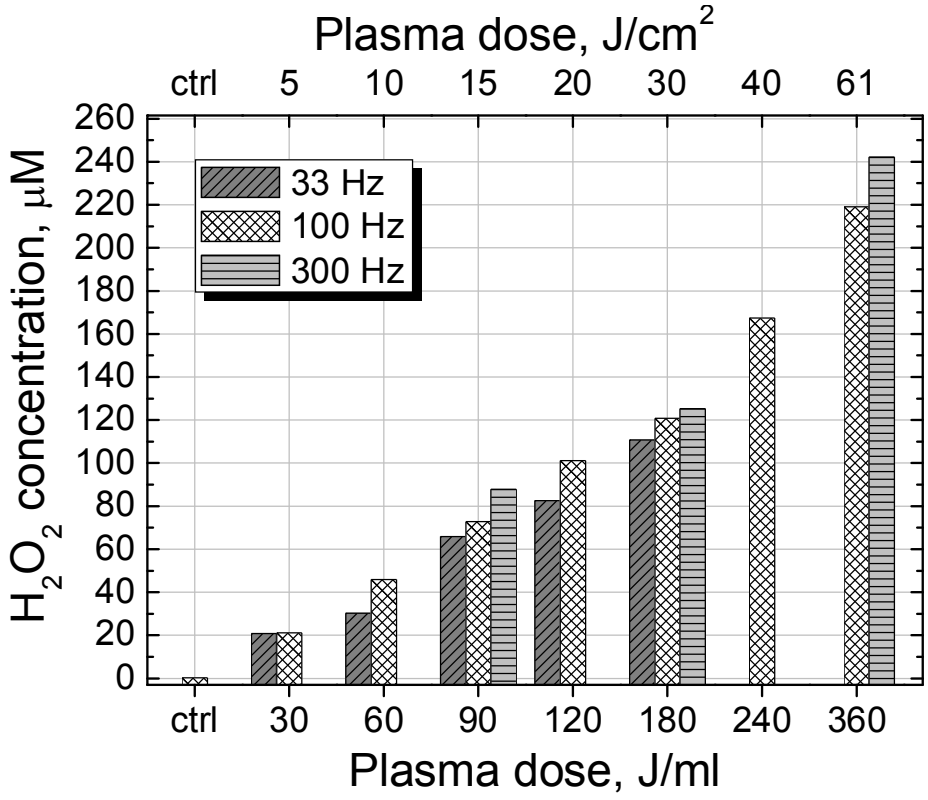

Figure 4 Production of H2O2 in 300 µl of PBS Mg2+Ca2+ treated by DBD plasma at 33, 100 and 300 Hz.

For ease of comparison with other works plasma dose values in Joule per square centimeter are also provided. The electrode area was taken for assessment of treated surface.

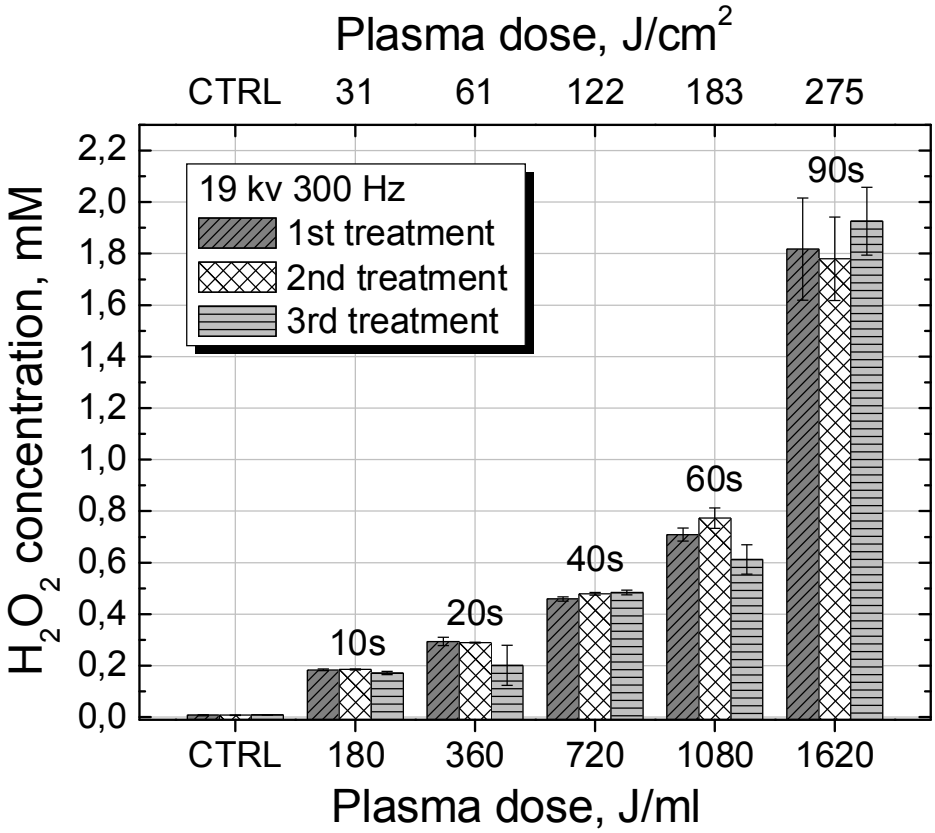

Figure 5 Production of H_2O_2 in 300 µl of PBS $Mg^{2+}Ca^{2+}$ treated in triplicate by DBD plasma at 300 Hz. H_2O_2 concentrations are presented as means ± SD of three assays.

To check the reproducibility of plasma treatment, dilution and dosage procedures 300 µl/well of PBS $Mg^{2+}Ca^{2+}$ were treated in 24 well plate in triplicate at 300 Hz over 10, 20, 40, 60 and 90 s. Right after plasma exposure 5 µl of treated PBS $Mg^{2+}Ca^{2+}$ was pipetted off and diluted to 1/500 in fresh PBS $Mg^{2+}Ca^{2+}$ kept on ice. The dilution was also done in triplicate to study the possible error due to handling with small volumes and nonhomogeneity of hydrogen peroxide distribution in the volume of well. Figure 5 summarizes the results of reproducibility test showing H_2O_2 concentration versus plasma dose expressed in Joules per milliliter of medium or per surface unity corresponding to the electrode area. The hydrogen peroxide concentrations for each treatment are

presented as means and error bars show the standard deviation (±SD) of three dilution assays. As one can see plasma treatment demonstrated good reproducibility in terms of H_2O_2 production with spread of measured values of about 5 % with the exception of two points. Two plasma doses of 360 J/ml and 1080 J/ml corresponding to the third treatment in triplicate resulted in 15-30 % lower H_2O_2 concentration comparing to rather reproducible first and second treatment. At the same time these two points had bigger scatter of three equivalent dilutions which suggested that the discrepancy was due to the dilution accuracy and not reproducibility of plasma treatment.

7.3.1.1 **Conclusions on H_2O_2 dosage**

To summarize the experiments on plasma produced hydrogen peroxide, we have shown:

- The feasibility of quantitative dosage of H_2O_2 using Amplex Red and Horseradish peroxidase in phosphate buffered saline with $MgCO_3$ and $CaCO_3$ (PBS $Mg^{2+}Ca^{2+}$) directly exposed to nanosecond DBD plasma.
- Plasma treatment resulted in reproducible and dose dependent production of hydrogen peroxide in the range 10 – 2000 µM for plasma doses between 14 and 1600 J/ml
- For standard 6 and 24 well plates with respectively 2 ml and 300 µl of medium H_2O_2 production was determined mainly by volumetric power density.

7.3.2 Treatment of thyroid HTori-3 cell line

Normal thyroid epithelial cell line (HTori-3) with high sensitivity to ROS (Ameziane-El-Hassani *et al* 2010) was selected for the first trial. HTori-3 cell line was obtained from normal thyroid tissue of an adult and then was immortalized by transfection with a plasmid containing origin-defective SV40 genome (SV-ori). As it was shown the exposure of thyroid cells to low sublethal concentrations of hydrogen peroxide induced chromosomal aberrations and could be at the origin of papillary

thyroid carcinoma (Ameziane-El-Hassani *et al* 2010). We took HTori- 3 line as a noncancerous model to study the effect of plasma exposure upon normal epithelial cells with low tolerance for hydrogen peroxide.

Two days before the treatment 10^5 cells were plated in 6 well plate and were grown in phenol–red free RPMI 1640 (Invitrogen, Inc.) supplemented with 1% (v/v) antibiotics/antimycotics (Invitrogen), 2 mmol/L of L-glutamine (Invitrogen), and 10% (v/v) FCS (fetal calf serum) (PAA Laboratories). Prior to plasma treatment culture medium was removed, cells were washed twice with PBS $Mg^{2+}Ca^{2+}$ at 37° and then supplied with 2 ml of PBS $Mg^{2+}Ca^{2+}$. The cells were placed at 37° over 15 min for equilibration and then exposed to DBD plasma according to above described protocol. Phosphate buffer solution with cells was treated during 10, 15, 20 and 30 s at 100 Hz (Figure 6). The same plasma doses were applied on wells containing even volume of PBS without cells. The sampling of hydrogen peroxide in treated medium with and without cells was done 5, 15 and 30 min after the treatment.

Figure *6* shows evolution of plasma produced H_2O_2 concentration over 30 min post treatment. It can be easily seen that in the case of PBS treatment without cells H_2O_2 concentration in the range 10-30 µM remained stable during 30 min at room temperature. Interestingly, the presence of HTori-3 cells in treated PBS led to visible decrease in hydrogen peroxide concentration with more than 80% loss over 30 min after the treatment even for the highest plasma dose of 27 J/ml (Figure 6). Evolution of H_2O_2 concentration normalized to initial concentration for each plasma dose is shown in Figure 7. As one can see the decrease in hydrogen peroxide is characterized by the same reaction rate for all plasma doses if first order kinetics is assumed. Observed behavior of H_2O_2 concentration indicates that hydrogen peroxide should be destructed in some specific reaction by the cells.

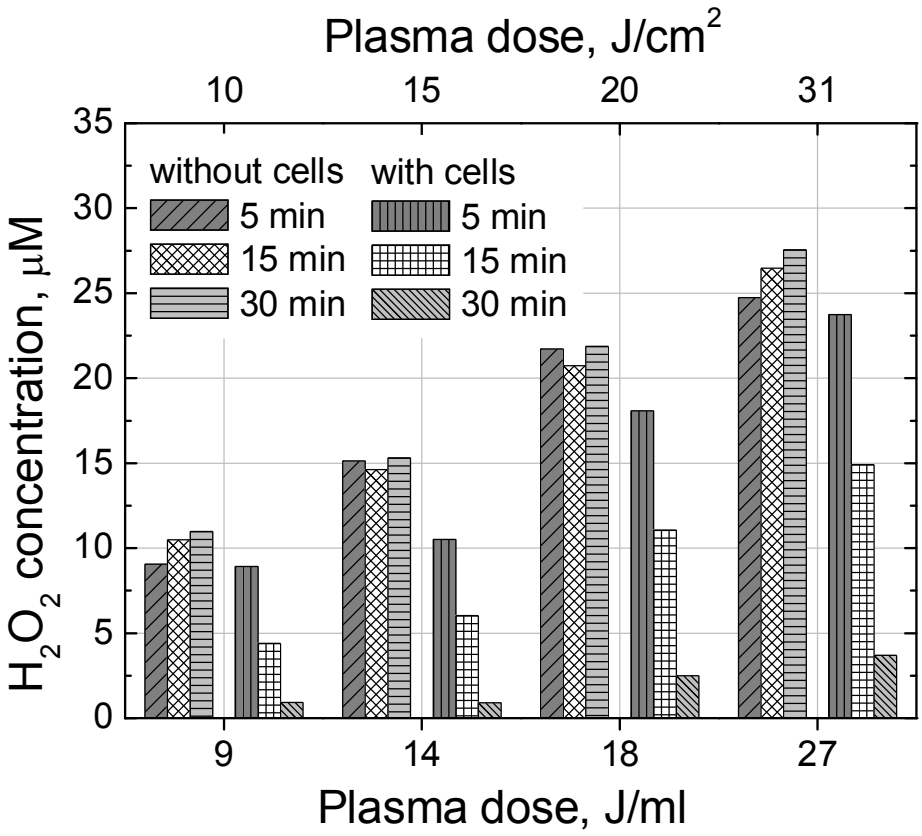

Figure 6 Time evolution of hydrogen peroxide concentration in 2 ml of PBS $Mg^{2+}Ca^{2+}$ produced under DBD plasma exposure with and without HTori-3 cells. Cells were seeded at a density of 10^5 cells/well in 6 well plates 2 days before the treatment.

Hydrogen peroxide may be lost at the cell membrane in the process of lipid peroxidation (Kellogg and Fridovich 1975) or reduced to H_2O in reaction with antioxidant enzymes catalase and glutathione peroxidase inside the cell (Thannickal and Fanburg 2000). Lipid peroxidation is rather slow process and may eventually induce the loss of membrane integrity and cell death at high concentrations of H_2O_2. In spite of small size of about 0.25 nm H_2O_2 molecules practically cannot cross the lipid bilayer of plasma membrane because of their high dipole moment (2.26 D higher than that of H_2O 1.85 D). However, since H_2O_2 has comparable size and similar dielectric properties as water molecule it can diffuse through specific water channels formed by integral membrane proteins aquaporins (Bienert *et al* 2006 and ref. herein). Among all aquaporins only two hAQP8 and AtTIP1 shows specificity regarding H_2O_2 transport (Bienert *et al* 2006). Consequently, the

destruction of exogeneously produced hydrogen peroxide is limited by diffusion time through the specific membrane channels. It may explain the linearity of H_2O_2 concentration evolution with time (Figure 7). Moreover, it was shown that sub-microsecond pulsed electric field of about 5 kV/cm was able to create a stable less than 1 nm in diameter pores in plasma membrane (Pakhomov *et al* 2009). Although, membrane permeabilization induced by short electric pulses was reversible the pores could exist over 10 min. We cannot exclude occurrence of pores under nanosecond pulse electric field in our experimental conditions. As it was shown electroporation triggers water influx through the cell membrane to neutralize osmotic gradients induced by intracellular Ca^{2+} bursts and leads to cell swelling (Pakhomov *et al* 2009). We observed slight increase in cell volume and swelling by optical microscopy just after plasma treatment, however one should keep in mind that partial loss of adherence would give the similar effect.

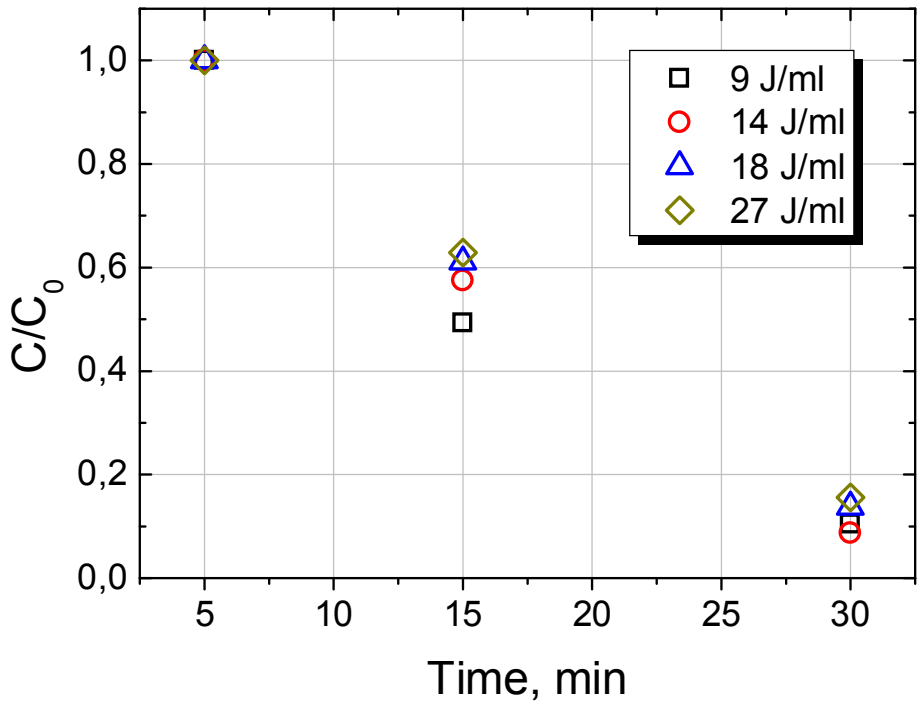

Figure 7 Kinetics of H_2O_2 decrement in extracellular medium for four plasma doses of 9, 14, 18 and 27 J/ml (the same as Figure 6).

Slightly higher plasma doses were selected to check cell viability using WST-1 (Water soluble tetrazolium salt) proliferation assay. The treatment was repeated three times on normally cultured cells, on cells preincubated the day before the treatment with 5 µM of DPI (diphenyleneiodonium inhibitor of intracellular ROS production) and with 400 U/ml of catalase at the moment of treatment (enzyme, extracellular ROS scavenger if added exogenously). In each case the dosage of H_2O_2 was done 5 min after the treatment. As it is demonstrated by Figure 8, 400 U/ml of catalase were able to suppress completely 100 µM of extracellular hydrogen peroxide already 5 min after the treatment. The negative values of H_2O_2 concentration simply mean that background signal decreased due to more intensive light absorption or scattering.

Preincubation of cells with intracellular ROS inhibitor DPI resulted in 10 – 20 % decrease in H_2O_2 concentration as compared to normally treated cells (Figure 8). DPI is known to inhibit the superoxide (O_2^-) production by mitochondria and NADPH oxidases (nicotinamide adenosine dinucleotide phosphate oxidases) (Li and Trush 1998). NADPH oxidases form a family of membrane bond flavoenzymes which play a key role in cellular ROS production along with mitochondria. NADPH oxidases produce superoxide from molecular oxygen in extracellular medium by transferring an electron through plasma membrane. Superoxide is then dismutes to H_2O_2 or can cross the membrane in the direction of cytosol through anion channels (Fisher 2009). Under normal conditions, NADPH oxidases help to maintain the intracellular redox state (Clément *et al* 1998). However, it was suggested that upregulation of ROS produced by NADPH oxidases may be at the origin of genomic instability and carcinogenesis (Weyemi and Dupuy 2012). Hereby, the incubation of cells with DPI allows discerning the role of exogenously ROS and ROS produced by the cell.

One can assume that the difference between H_2O_2 concentrations measured with normally treated cells and cells containing DPI corresponds to ROS produced by the cells themselves (Figure 8). If it is

so, the amount of H_2O_2 produced by the cells depends on plasma dose. This fact correlates with activation of NADPH oxidases in response to oxidative stress as was shown by exposure to γ-radiation (Collins-Underwood *et al* 2008).

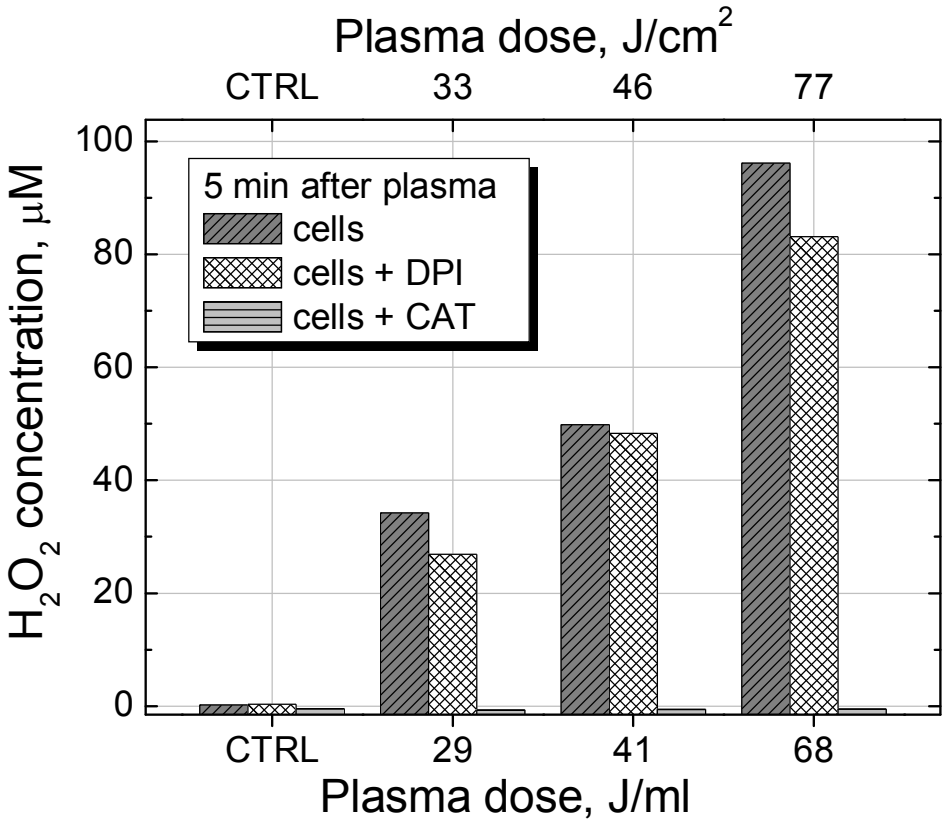

Figure 8 Dosage of H_2O_2 5 min after the treatment. HTori-3 cells in 2 ml of PBS, HTori-3 cells incubated with DPI and HTori-3 cells with 400 U/ml of catalase.

The influence of plasma treatment on cell viability was analyzed with WST-1 proliferation assay. After plasma exposure the cells were incubated over 30 min in treated PBS $Mg^{2+}Ca^{2+}$ at 37º C, then the cells were twice washed with PBS without $Mg^{2+}Ca^{2+}$, while the supernatant was collected in 15 ml tubes (BD Falcon). The cells were detached by trypsinization over 3 min, resuspended with supernatant in 5 ml of fresh RPMI with 10 % FCS and centrifugated at 1500 rpm. Then the cells were resuspended in 500 µl of fresh medium and gently vortexed. Cells were counted on hemocytometer using Trypan Blue staining of dead cells. For this reason 10 µl of medium with cells were diluted in

90 µl of Trypan Blue. Afterwards, 10^4 of viable cells that exclude Trypan Blue were seeded in 96 well microtiter about 1 hour after the treatment and grown with 200 µL of fresh medium at 37 C. The day of analysis the medium was replaced with 100 µL of fresh one supplied with 10 µL/well of WST-1 proliferation reagent (Roche). Cells were incubated for 2 H at 37º C and then the absorbance of formazan produced by the enzymatic cleavage of WST-1 was measured at 450 nm on Perkin Elmer Victor 3 microplate reader (photometer/fluorimeter). Only metabolically active cells could reduce WST-1 and, hence, absorption at the 450 nm was related to the number of viable cells.

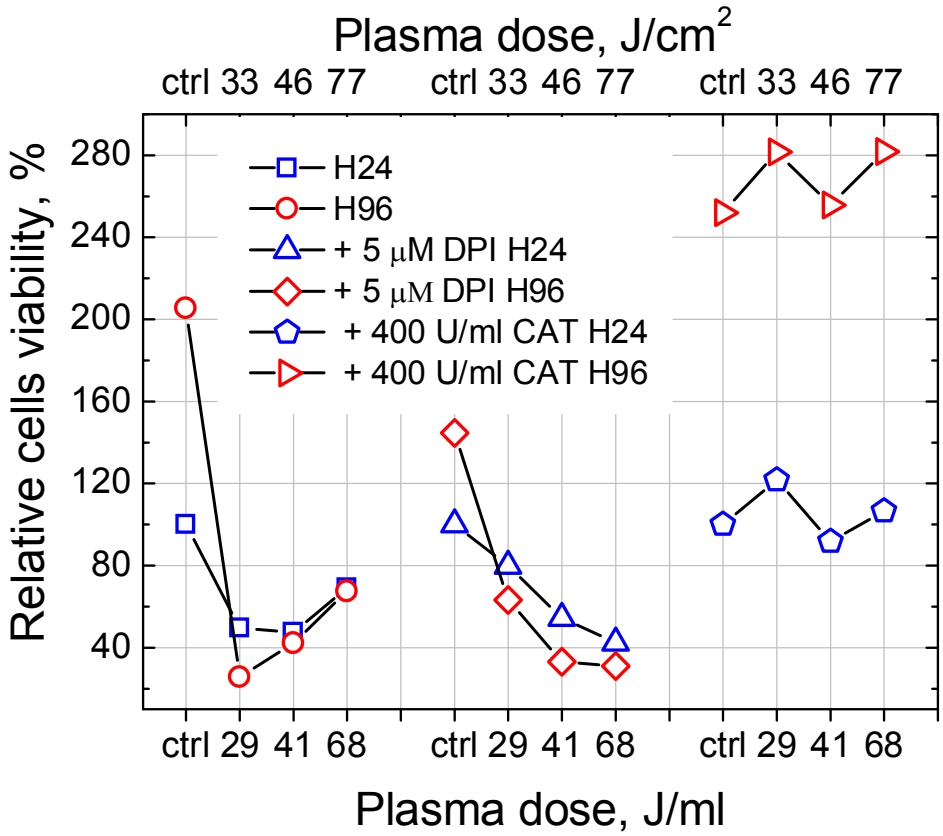

Figure 9 Viability of HTori-3 cells related to the untreated control after DBD plasma exposure determined by WST-1 assay 24 and 96 hours after the treatment. Normally treated cells, cells preincubated with 5 µM of DPI before treatment and cells treated with 400 U/ml of catalase.

The results of cells proliferation measurement 24 and 96 hours after the treatment (H24 and H96) are shown in Figure 9. The signal was

normalized for absorbance of untreated control measured 24 hours after the treatment and expressed as a percentage of number of viable cells. Remarkably, for normally treated cells viability curve demonstrated nonmonotonous dependence on plasma dose with equal drop in number of survived cells for two plasma doses of 29 J/ml (35 µM of H_2O_2) and 41 J/ml (50 µM of H_2O_2). Unexpectedly, slight improvement in cells viability was observed for the highest dose of 68 J/ml (96 µM of H_2O_2) as analyzed 24 hours after the treatment (Figure 9). WST-1 test performed at H96 demonstrated continuous decrease in number of viable cells for the lowest plasma dose while the number of cells treated with higher plasma doses remained almost unchanged.

Addition of 400 U/ml of catalase at the moment of treatment demonstrated complete suppression of H_2O_2 in the extracellular medium (Figure 8). WST-1 analysis of cells treated in the presence of catalase showed perfect protection of the cells for all three plasma doses and even slight improvement in proliferation (Figure 9). Although, there is no evidence that catalase having 250 kD of molecular weight can diffuse through the plasma membrane. The fact that catalase protects the cells by suppressing extracellular H_2O_2 points out the primary role of hydrogen peroxide as the main mediator of plasma cytotoxic effect.

As one can see, plasma produced hydrogen peroxide at concentrations below 50 µM induced cells death in about 50 % of cells already at H24 whereas higher concentrations of H_2O_2 resulted in delayed effect leading to cellular senescence (arrest of cell division). This result agrees with reported caspases (cysteinyl-aspartate-cleaving proteases, effectors of apoptosis) activation in Jurkat cells regulated by extracellular hydrogen peroxide (Hampton and Orrenius 1997). It was found that H_2O_2 concentrations of 30 – 50 µM induced caspases activation at H3 and manifestation of apoptosis already 6 hours after the treatment. Meanwhile, higher doses of H_2O_2 induced oxidative inactivation of caspases leading to delay or complete inhibition of apoptosis. In the last case authors suggested the cells death by necrosis. In the light of findings made in (Hampton and Orrenius 1997) it seems plausible that

plasma produced hydrogen peroxide can in similar manner induce and then inhibit caspase activation depending on plasma dose.

The treatment of cells preincubated with 5 µM of DPI (Diphenyleneiodonium, inhibitor of intracellular ROS production) demonstrated a considerable enhancement in number of viable cells corresponding to the lowest plasma dose while for the highest dose viability became poorer (Figure 9). Viability curve became monotonously decreasing with plasma dose as seen at H24 and H96. It's worth noting, that the two highest plasma doses of 41 and 68 J/ml resulted in very similar cell mortality as the lowest plasma dose applied on cells without DPI. Since DPI blocks ROS production by the cells the local decrease in hydrogen peroxide concentration in cell vicinity should be somewhat stronger than change in total H_2O_2 averaged over the entire volume of medium. In this case, cell viability could be affected by the cumulative effect of both plasma and cellular produced hydrogen peroxide. Consequently, the effect of DPI consisted in shifting of viability curve to the region of lower H_2O_2 concentrations. Interestingly, DPI affected the proliferation rate of untreated cells as can be seen from the comparison of untreated control cells without DPI and control cells which were incubated with DPI. It possibly means that DPI remained in cells after the treatment, wash, detachment and several changes of culture medium. It is known that activation of multiple cellular processes including proliferation is mediated by low concentrations of hydrogen peroxide (Gamaley and Klyubin 1999). It seems likely that DPI can inhibit activation pathways reducing cells proliferation.

7.3.2.1 **Conclusions on plasma treatment of HTori cells**

The experiments with enzymatic reduction of exogenously produced H_2O_2 by catalase and DPI induced inhibition of ROS production by the cells bring us to two main conclusions of this chapter:

- Plasma induced cell death is mediated by extracellularly produced hydrogen peroxide.

- Metabolically produced ROS or ROS released in response to oxidative stress contribute additively with plasma induced H_2O_2 in the overall cytotoxic effect.

7.3.3 Treatment of melanoma 1205Lu line

Melanoma 1205Lu line was taken as a cancerous model able to withstand high concentrations of exogenic hydrogen peroxide. Melanin being a ROS scavenger allows for melanocytes to support elevated concentration of hydrogen peroxide produced for example by UV B radiation. The natural role of melanocytes is the protection of keratinocytes from oxidative stress by supplying them with antioxidant melanin. In melanoma cells the melanosomes (melanin containing organelles) are disorganized and demonstrate a pro-oxidant state. Melanosomes together with upregulated NADPH activity contribute to abnormal ROS production in melanoma cells associated with disruption of redox regulation (Melo *et al* 2013). Finally, elevated concentration of intracellular ROS altering proliferation and apoptotic signaling pathways makes melanoma cells very resistive to chemotherapy. Singularity of melanoma redox state makes them interesting from fundamental point of view, while cutaneous cancers, in general, seem to be a practicable model for prospective clinical trials of DBD plasma treatment.

For the first test we chose 1205Lu (ATCC CRL-2812) cell line derived from lung metastases of WM793B cells (ATCC CRL-2806) after subcutaneous injection into immunodeficient mice. 1205Lu cells are highly invasive and exhibit spontaneous metastasis to lung and liver. One day before the treatment $2 \bullet 10^5$/well of melanoma 1205Lu cells were seeded in 6 well plates and grown in phenol–red free RPMI 1640 (Invitrogen, Inc.) supplemented with 1% (v/v) antibiotics/antimycotics (Invitrogen), 2 mmol/L of L-glutamine (Invitrogen), and 10% (v/v) FCS (fetal calf serum) (PAA Laboratories). The DBD plasma treatment procedure was identical to the treatment of HTori-3 cells. Additionally, 1205Lu cells seeded in another 6 well plate were incubated with ex-situ plasma treated PBS $Mg^{2+}Ca^{2+}$. For indirect treatment 2 ml

of PBS $Mg^{2+}Ca^{2+}$ were treated in 6 well plate without the cells and then treated medium was directly droped on cells. The third treatment procedure consisted in cell incubation with equivalent H_2O_2 concentrations. Before all three direct, indirect and H_2O_2 treatments, the culture medium was removed and cells were twice washed with warm PBS $Mg^{2+}Ca^{2+}$. Before the direct treatment the cells were incubated for 15 min with 2 ml of PBS $Mg^{2+}Ca^{2+}$ at 37 C. Afterwards, cells were exposed to three plasma doses of 29, 41 and 68 J/ml. Indirect (ex-situ) treatment was done by exposing of 2 ml of PBS $Mg^{2+}Ca^{2+}$ without cells to the same plasma doses and then treated medium was immediately dropped on the cells. For the third treatment three H_2O_2 doses of 30, 60 and 90 µM were prepared beforehand from standard solution in 2 ml of PBS $Mg^{2+}Ca^{2+}$ and dropped on cells. In order to determine the role of ROS produced by the cells exposed to direct, indirect and equivalent doses of hydrogen peroxide, another three 6 well plates with 1205Lu cells were preincubated with 10 µM of DPI (diphenyleneiodonium, inhibitor of intracellular ROS production) 45 min before the treatment. For all treatment conditions cells were incubated over 30 min after the treatment at room temperature.

Hydrogen peroxide dosage was done 5, 15 and 30 min after the treatment for all three treatment protocols on the normally grown cells and cell incubated with 10 µM of DPI. Figure 10 summarizes temporal evolution of hydrogen peroxide concentration for the lowest directly and indirectly applied plasma dose of 29 J/ml resulted in about 40 µM of H_2O_2 and 30 µM of H_2O_2 obtained from the standard solution. Similarly to HTori-3 line, incubation of 1205Lu cells in treated medium led to decrease in H_2O_2 concentration. More than 50 % of plasma produced H_2O_2 was absorbed by the cells over 30 min after the treatment. Evolution of H_2O_2 in the medium after ex-situ treatment (Figure 10) demonstrated about 50 % higher final concentration of H_2O_2 as compared to directly treated cells. It was already mentioned in previous chapter that pulsed nanosecond electric field of 5 kV/cm can induce formation of nanometer size pores in plasma membrane. In our conditions we expect to have even greater electric field strength as seen

by the cells. Therefore, we cannot neglect eventual permeabilization of cells membranes under electric field of the DBD device. However, more tests would be needed to clarify the role of electric field in supposed membrane poration and to eliminate the possibility of partial membrane peroxidation by short-lived ROS arising from radiolysis of the medium.

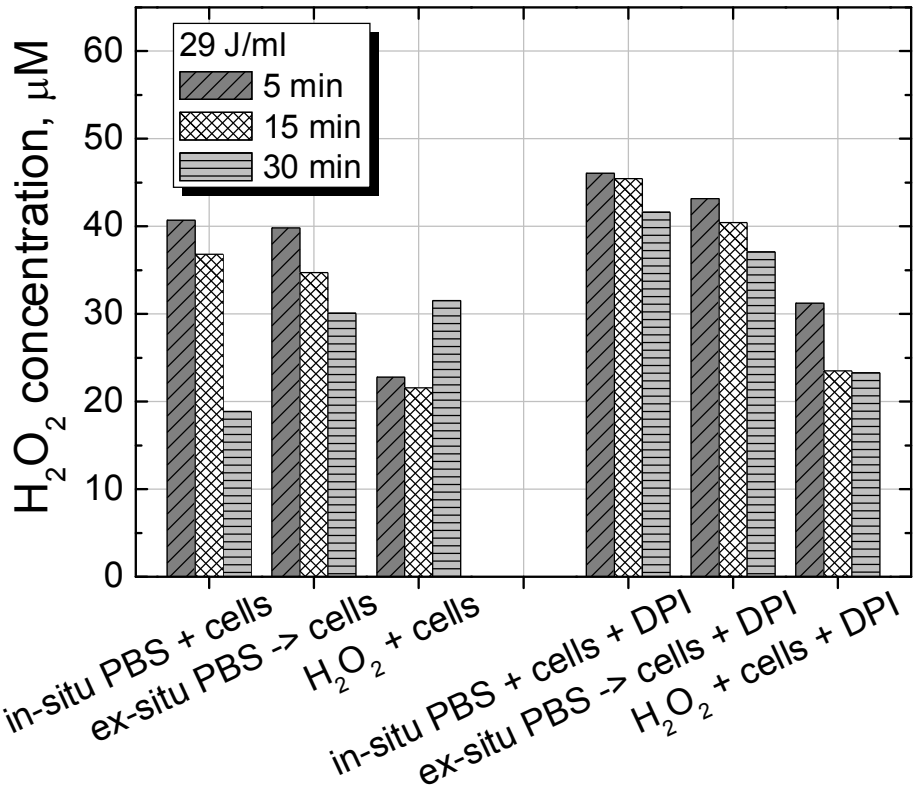

Figure 10 Time evolution of hydrogen peroxide concentration in 2 ml of PBS $Mg^{2+}Ca^{2+}$ with normally grown 1205Lu cells and cells preincubated with 10 μM of DPI 45 min before the treatment. The cells were exposed to in-situ(directly), ex-situ (indirectly, without cells) DBD plasma doses of 29 J/ml and 30 μM of H_2O_2 obtained from standard solution. Cells were seeded at a density of 10^5 cells/well in 6 well plates the day before treatment.

Surprisingly, preincubation of 1205Lu cells with DPI resulted in opposite effect on H_2O_2 concentration as one could expect from the treatment of HTori-3 cells. Direct and indirect treatment for the same plasma dose of 29 J/ml gave 7 – 10 % higher concentrations of hydrogen peroxide (Figure 10). Only sight 10 – 15 % decrease in total

H_2O_2 concentration was observed 30 min after the treatment. It seems likely that DPI prohibited H_2O_2 entry in the cells, however the mechanism of this effect is unclear and would need deeper investigation.

The treatment of the 1205Lu cells with 30 µM of H_2O_2 from standard solution showed nonmonotonous evolution of hydrogen peroxide concentration with time of incubation (Figure 10). Measured over first 15 min H_2O_2 concentration was found to be 21 – 22 µM, while after 30 min of incubation it exceeded 30 µM. Given that accuracy of H_2O_2 dilution and dosage was always better than 10 % it seems reasonable to assume some nonunifromity of H_2O_2 distribution in the volume of well when it was dropped in 2 ml of PBS $Mg^{2+}Ca^{2+}$. We did not used vortexing or extensive mixing to avoid disturbing adherence and viability of the cells. Premixed PBS/H_2O_2 aliquotes will be used in future experiments.

Viability of the 1205Lu cells directly and indirectly treated with DBD plasma and by H_2O_2 obtained from standard solution was analyzed with WST-1 proliferation assay following the described above protocol. 10^4 of viable cells 1 hour after the treatment were seeded in 96 well microtiter supplied with 200 µL of fresh complete medium. The day of analysis the medium was replaced with 100 µL of fresh one supplied with 10 µL/well of WST-1 proliferation reagent (Roche). Cells were incubated for 2 H at 37º C and then the absorbance of formazan produced by the enzymatic cleavage of WST-1 was measured at 450 nm on Perkin Elmer Victor 3 microplate reader (photometer/fluorimeter). The results of cell viability measurements 24, 48 and 72 hours after the treatment are shown in Figure 11. The signal was normalized for absorbance of untreated control measured 24 hours after the treatment and expressed as a percentage of number of viable cells.

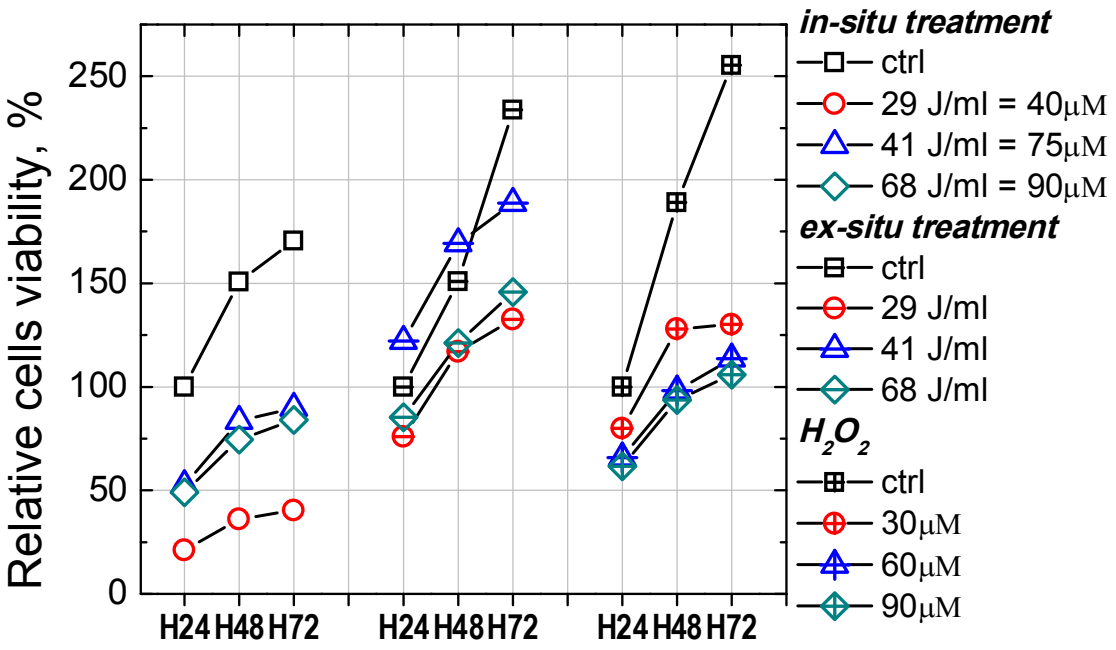

Figure 11 Viability of 1205Lu cells related to the untreated control after in-situ (directly, with cells), ex-situ (undirectly, without cells) DBD plasma exposure and equivalent doses of H_2O_2 determined by WST-1 assay 24, 48 and 96 hours after the treatment. Normally treated cell and cells preincubated over 45 min with 10 μM of DPI before the treatment.

Similarly to the case of HTori-3 cells direct plasma treatment of melanoma 1205Lu line resulted in very pronounced decrease in number of viable cells for the lowest plasma dose of 29 J/ml, while for plasma doses of 41 and 68 J/ml the number of metabolically active cells was almost doubled. The time course of viability curve for all three plasma doses indicated that some fraction of directly treated cells were able to proliferate at least up to 72 hours after the treatment. Surprisingly, ex-situ (indirect) plasma treatment affected viability of only 15 – 25 % of cells when the lowest and the highest plasma doses were applied (Figure 11). At the same time, the medium dose of 41 J/ml resulted, at the contrary, in enhanced proliferation as seen at H24 and H48. The difference in cytotoxic effect of direct and indirect treatment pointed to the fact that besides hydrogen peroxide production which was found to be equal in both cases, some other plasma produced factors must be

taken into consideration. However, as it was demonstrated by plasma treatment of HTpori-3 cells in the presence of catalase, those factors alone cannot affect cell viability and, hence, they should act synergistically increasing the effect of hydrogen peroxide. Plasma membrane permeabilization by nanosecond electric field or by short-lived hydroxyl radicals as was mentioned above seems to be a reasonable explanation. The fact that no difference was observed between direct and indirect treatment of glioblastoma (U87MG) cells (Vandamme *et al* 2012) by similar DBD device and close plasma doses of 10 and 20 J/ml (the treated volume was equal to 500 µl), but driven by microsecond voltage pulses of 23 kV supports this assumption. Actually, there is no experimental evidence of nanopores formation by microsecond voltage pulses (Weaver *et al* 2012).

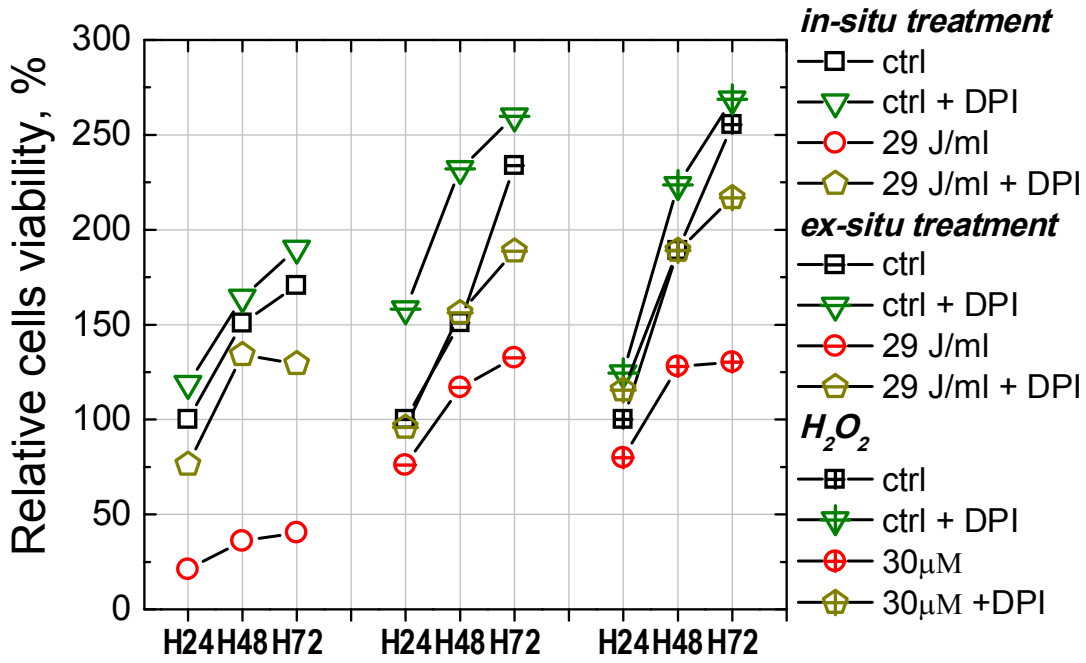

Figure 12 Viability of 1205Lu cells related to the untreated control after in-situ (directly, with cells), ex-situ (undirectly, without cells) DBD plasma exposure and equivalent doses of H_2O_2 determined by WST-1 assay 24, 48 and 96 hours after the treatment. Normally treated cells and cells preincubated over 45 min with 10 µM of DPI before the treatment.

The treatment of 1205Lu cells with 30 µM of hydrogen peroxide gave similar result as the lowest dose of indirect plasma treatment. However 60 µM and 90 µM of H_2O_2 showed stronger cytotoxicity as oppose to two higher ex-situ plasma doses producing close amount of H_2O_2. This result shows that the mechanism of plasma action cannot be fully explained only by formation of hydrogen peroxide even if H_2O_2 seems to play the primary role. Eventual production of nitrogen oxides in plasma (NO, NO_2, NO_3, N_2O, N_2O_5) (Sakiyama *et al* 2012) should lead to high nitrate concentration and acidification of the medium (Oehmigen *et al* 2010). Hereby, more complex plasma induced chemistry should be taken into account for proper interpretation of these results.

As in the case of HTori-3 cells DPI was able to enhance considerably survivability of 1205Lu cells exposed to the lowest plasma dose of 29 J/ml as well as indirectly treated cells and cells exposed to 30 µM of H_2O_2 (Figure 12). The protective role of DPI seems to consist in inhibition of oxidative stress induced by upregulation of intracellular ROS production mediated by extracellular H_2O_2.

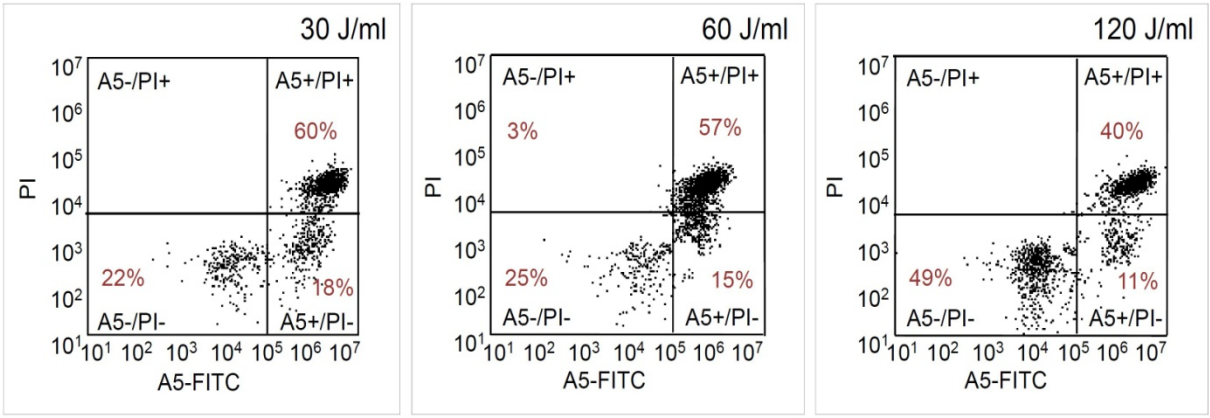

Figure 13 Cell apoptosis measured by Annexin V – Propidium iodide labeling 4 hours after DBD plasma treatment of 30, 60 and 120 J/ml. $8 \cdot 10^4$ cells were seeded in 24 well plate the day before the treatment and exposed to plasma with 300 µl of PBS Mg^{2+} Ca^{2+}.

WST-1 proliferation assay provides information on number of viable cells and their proliferation rate if measurements are done at several time moments. However, it completely ignores the way cells die as well

as the exact number of dying cells. To know whether plasma treatment induced activation of apoptotic pathway in our conditions AnnexinV – Propidium iodide (AV-PI) labeling (BD Bioscience) was used. Melanoma 1205Lu cells were seeded at density of $8 \cdot 10^4$/well in 24 well plate the day before treatment and grown in complete medium at 37 C. Plasma treatment was performed according to standard protocol as discussed above. After the treatment cells were incubated for 30 min in 300 µl of treated PBS $Mg^{2+}Ca^{2+}$ before the medium was replaced with 500 µL of RPMI supplied with 10% FCS and cells were incubated for another 3 hours at 37 C. Before the detachment cells were twice washed with PBS (without $Mg^{2+}Ca^{2+}$) while supernatant was collected in 15 ml tubes (BD Falcon). For detachment cells were supplied with 500 µL of PBS containing 5 mM of EDTA (Ethylene-diamine-tetra-acetic acid, Ca^{2+} chelator) and 5 mM of EGTA (ethylene glycol tetra-acetic acid, Ca^{2+} chelator) and were incubated for 3-5 min before detachment became visible. Detached cells were collected in 15 ml tube re-suspended in 10 ml of complete medium and centrifuged at 1500 rpm. For Annexin V – Propidium iodide labeling cells were re-suspended in 100 µl of binding buffer (BD Bioscience) in 5 ml flowcytometry polystyrene tubes (BD Bioscience) and labeled with 5 µl of FITC – AnnexinV and 5 µl of Propidium iodide reagents (BD Bioscience). After incubation in the dark over 15 min and adding of 200 µl of binding buffer, the cells were analyzed with BD Accuri C6 flowcytometer. FITC-AV fluorescence was measured on FL1 channel at 533 nm, while PI was detected at 630 nm with FL3 channel. Obtained PI-AV plots for 3 plasma doses of 30, 60 and 120 J/ml are given by Figure 13. Cells excluding AV and PI were considered as viable, while AV positive and PI negative and both AV and PI positive cells were related to early and late apoptosis respectively. The cells that stained with only propidium iodide are attribute to necrotic death. As one can see plasma doses of 30 and 60 J/ml induced apoptosis in 70 – 80 % of the cells already 4 hours after the treatment. Meanwhile, only 50 % of the cell exposed to the highest plasma dose of 120 J/ml demonstrated apoptotic pattern (Figure 13). No necrotic cells were detected. This result shows that

plasma produced hydrogen peroxide at concentration of 20 – 50 µM can effectively induced apoptosis, and confirms that higher H_2O_2 doses of about 100 µM lead to delay in apoptosis induction due to oxidative inactivation of caspases as was discussed in previous chapter.

7.3.3.1 Conclusions on plasma treatment of melanoma Lu1205 cells

Plasma treatment of cancerous melanoma 1205Lu cells demonstrated similar to normal HTori-3 cells dose dependant effect on cell viability.

- Almost 80 % of the cell colony died after plasma dose of 30 J/ml which was equivalent to extracellular hydrogen peroxide concentration of 40 µM.
- AnnexinV – Propidium iodide labeling suggested that cells were dying by apoptosis.
- The poorer cytotoxicity of indirect treatment supports the role of nanosecond electric field in eventual cellular membrane permeabilization.
- Exposure of the cells to equivalent doses of hydrogen peroxide obtained from standard solution indicated that production of nitrogen reactive species (RNS) and change in medium pH must be taken into account.

7.3.4 Influence of cell seeding protocol

These first results obtained on two cell lines: immortalized normal thyroid epithelial cells (HTori-3) and cancerous metastatic melanoma cells (1205Lu) showed very similar responses to plasma treatment of two cell cultures that one may expect to have very different tolerance to oxidative stress. As it follows from experimental findings, nanosecond DBD plasma induces oxidative stress which could be strengthened by synergetic effect of nanosecond electric field on membrane permeabilization. The key to this apparent contradiction may be found if one remembers that adherent cells in the colony are not developing as independent individuals but actively interact with each other by means

of chemical messengers. The speed and effectiveness of such interaction, obviously depends on number of cells and the distance between them. The cells having a straight contact with the neighborhood can more easily adapt to the change in environment by receiving and transferring the preventive signals. Cell adherence to the substrate is one of the parameters that to a considerable extent can define cell resistivity for the given conditions. It was shown that detachment of endothelial cells led to a rapid increase in intracellular ROS production that could activate caspases and induce cell death, termed anoikis, if the cells remained in suspension (Li *et al* 1999). Obviously, higher cell density provides higher concentration of cell adhesion proteins and, therefore, better overall adhesion of the cells. Cells integrated in living tissues have highest possible cell adaptiveness.

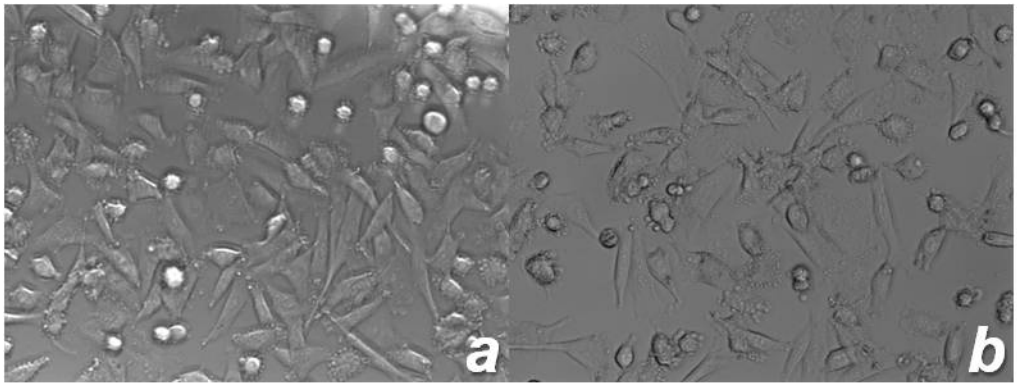

Figure 14 Confluency of 1205Lu cell layer. $8 \cdot 10^4$/well were seeded in 24 well plate and grown for 2 days. a) peripheral part of the well, b) center of the well. Phase contrast microscopy.

To illustrate how cell adhesion may influence the results of plasma treatment $8 \cdot 10^4$/well 1205Lu cells were seeded in 24 well plate and incubate for two days prior to plasma exposure (instead of 1 day incubation as was done for all previously presented data). The day of the treatment cells were at 60 – 80 % confluency (relative coverage of Petri dish by the cells) with slightly higher density at well periphery (Figure 14 a) comparing to the central part (Figure 14 b).

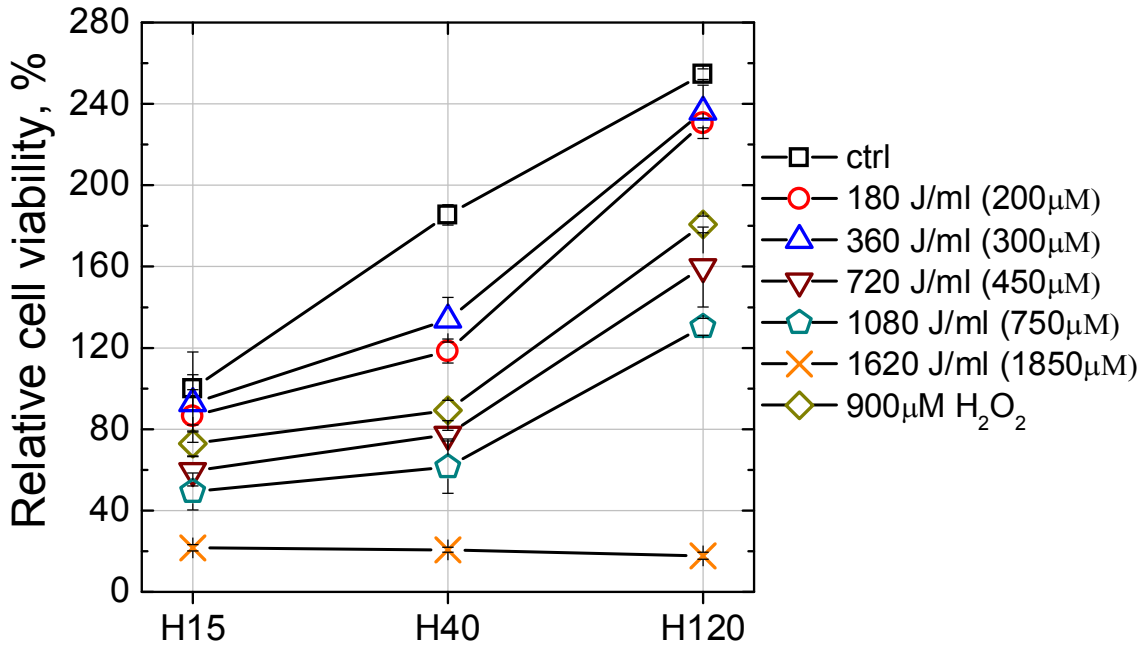

Figure 15 Viability of 1205Lu cells related to the untreated control after DBD plasma treatment and exposure to 900 μM of H2O2 determined by WST-1 assay 15, 40 and 120 hours after the treatment.

Cells were treated for 5 plasma doses, the highest dose of 1620 J/ml (90 s at 300 Hz) resulted in 1850 μM of hydrogen peroxide produced in 300 μl of treated PBS $Mg^{2+}Ca^{2+}$ (Figure 5). Cell viability was analysed by WST-1 proliferation assay at 15, 40 and 120 hours after the treatment (Figure 15). As one may see, more than 10 times higher plasma dose of 720 J/ml (450μM of H_2O_2) was needed to induce 50 % mortality as compared to treatment of 1205Lu cells incubated over 1 day before the plasma exposure. Only the highest plasma dose of 1620 J/ml induced 100 % cell mortality, while for lower doses some fraction of cells was able to withstand the oxidative stress and proliferate at least 120 hours after the treatment. Similarly to already discussed results, hydrogen peroxide alone demonstrated 20 – 30 % lower cytotoxicity than plasma treatment producing equivalent concentration of H_2O_2. It points to the role of nanosecond electric field even for rather high concentration of hydrogen peroxide.

This short discussion aimed to demonstrate that the choice between two experimental protocols, which both may seem proper would lead to drastically different results. It implies that not only the use of different cold plasma sources may be at origin of some divergence of results from different groups working on the subject, but also more attention must be paid to details of treatment procedure.

8 General conclusions and perspectives

This thesis deals with two subjects: physical phenomena occurring in electrical discharges in liquids and application of cold plasmas for treatment of living cells. The latter topic combines plasma chemistry of plasma interacting with liquid substrate with molecular biology of cell response. Two discharge devices based on nanosecond high voltage pulse technique were developed; namely device with microscopic point electrode for liquid discharge and atmospheric air dielectric barrier discharge.

Here we provide the summary of main results obtained in this thesis.

8.1 Initiation and development of nanosecond discharge in liquid dielectric

Time resolved optical shadowgraph visualization with spatial resolution of about 2 µm and temporal resolution of 2 ns was developed to study the initiation and dynamics of nanosecond discharge in liquid dielectrics. The discharge was initiated by application of short (30 ns) high voltage pulses (1.5 – 9.5 kV) of positive polarity on the point electrode having radius of curvature of 1 µm. Three different scenarios have been observed in polar dielectrics under In deionized water ($\varepsilon = 80$) and ethanol ($\varepsilon = 27$): i) formation of gaseous spherical cavity, ii) initiation of slower bush-like iii) and faster tree-like discharges could be observed on the point electrode depending on applied voltage amplitude.

Initiation phase

We have shown that under nanosecond positive HV pulse three different phenomena occur depending on voltage amplitude.

- At low applied voltage of 3.5 kV – 4.5 kV (field of the order of $8 \cdot 10^8$ – 10^9 V/m) the cavitation process was observed in deionized water ($\varepsilon = 80$) and ethanol ($\varepsilon = 27$) presumably due to the strong electrostrictive effect. In n-pentane cavitation is

observed at higher applied voltage of 10 kV-12 kV ($2.4 - 2.9 \cdot 10^9$ V/m).

- The size of cavitation zone was found to be about 4 µm in all tested liquids which is in a good agreement with the predictions of electrostriction based mode proposed by other authors.
- Expansion of cavitation bubble can be approximated by Rayleigh dynamics in deionized water at 3.5 kV and in ethanol at 4 kV. Calculated initial pressure in the case of deionized water and ethanol equals to 3 MPa and 1 MPa respectively.
- Slow bush-like mode seems to ignite in the gaseous void formed by cavitation process and separated from the point electrode by a layer of compressed liquid.
- Fast filamentary tree-like mode ignites on the point electrode as supported by occurrence of strong plasma emission.

In order to understand the different physical phenomena occurring in bush-like and tree-like discharge, we will consider the propagation dynamics of these two modes in the following section.

Discharge propagation

- Bush-like and tree-like discharge in deionized water demonstrate rather different propagation dynamics. Bush-like discharge propagation is found to be less sensitive to the amplitude of the applied voltage, while a probability to observe the bush-like discharge decreases with the HV pulse amplitude. The bush-like discharge demonstrates an order of magnitude lower propagation velocity as compared to the tree-like discharge. Visualization of the discharge emission demonstrates three orders of magnitude lower plasma emission intensity in the case of bush-like discharge that is too weak to obtain time resolved evolution. Difference in propagation dynamics suggests that the mechanisms responsible for the propagation of the bush-like and the tree-like discharges are essentially different.
- Maximal velocity at ignition of the bush-like discharge varies between 2 km/s and 4.5 km/s at 4 – 15 kV of applied voltage.

Propagation velocity decreases exponentially during the applied voltage pulse. A spherical shock wave produced at the ignition of the bus-like discharge degenerates to the acoustic wave during the applied voltage pulse. At high voltages (9 kV and higher) the propagation of the discharge filaments produces weaker shock waves. At voltage of 4 kV the discharge channels collapse at the trailing edge of HV pulse. Current of the bush-like discharge is much smaller than the detection limit.

- Tree-like discharge has maximal propagation velocity of 60 km/s at 15 kV. For the tree-like mode propagation of the discharge channels is accompanied by strong light emission and formation of a series of shock waves. Emission pattern demonstrates filamentary structures starting from 10 ns that are similar in size and form with discharge shadow structures. Light emission intensity was found to have two maxima: about 15 ns during the plateau of applied HV pulse and at the voltage drop over the trailing edge. Light emission intensity is correlated with current signal demonstrating a negative current spike at the trailing edge of the applied HV pulse. It is suggested that the back-discharge due to the charge accumulation occurs in gaseous channels. Maximal direct discharge current is 1.5 A and back-discharge current has an amplitude of 2 A. The total discharge energy is about 0.2 mJ for one pulse.
- In ethanol the difference in propagation dynamic between bush and tree-like mode was less evident. Maximum propagation velocity of bush-like discharge was found to be 2 – 3 km/s that was only 30% lower than the tree-like discharge velocity at given voltage amplitude.
- In n-pentane propagation velocity of tree-like discharge at 12kV and 18kV was 2.2 km/s and 4.6 km/s which was comparable with the tree-like discharge velocity in ethanol at 5.5 kV and 9 kV respectively.

Discharge pressure measurements

- Two methods were applied to estimate the gas pressure inside the tree-like discharge channels in deionized water at 6 kV. Model based on shock wave pressure measurements and model describing the expansion of a long cylindrical cavity provided consistent values of the maximal pressure of 0.3 – 0.4 GPa.
- Pressure evolution during the HV pulse and in the postdischarge phase demonstrates rapid relaxation down to 10^6 Pa already at 200 ns.
- At higher voltage amplitude of 15 kV shock wave pressure measurements give 4.2 km/s for maximal velocity which corresponds to 5.8 GPa of initial pressure.
- Obtained results demonstrate a strong dependence of the discharge pressure in the tree-like mode on the amplitude of applied voltage.

Discharge development under successive pulses

Shadowgraph and optical emission visualization of the successive discharges occurring under the reflected pulses of negative and positive polarity is done using two iCCD camera arrangement. Obtained results show that

- Negative discharge was confined in the channels of initial bush-like or tree-like structure. No formation of new structure or propagation of existed channels was observed. Formation of pressure waves at the extremities of all bush-like channels and at several tree-like filaments together with channel expansion was observed. Energy input was supported by strong light emission from several discharge channel in the case of tree-like discharge, while rather weak emission intensity was detected for bush-like discharge.
- Under the third pulse of the positive polarity new bush-like and tree-like discharges can be observed at the interface of gaseous cavity formed by the initial bush-like and tree-like structures.

Spectroscopic analysis of tree-like discharge

We attempted to apply optical emission spectroscopy to study evolution of plasma parameters, i.e. N_e, during applied HV pulse and under successive pulses.

Based on preliminary spectroscopic results it was shown that

- Emission spectra of first positive pulse consisted of intense continuum between 300 nm and 800 nm and strongly broadened lines of hydrogen Balmer series and atomic oxygen triplet bands OI at 725 nm and 777 nm. Baseline of spectrum can be approximated with the black body emission curve for T = 7000 K.
- The total width of hydrogen alpha line observed during second (negative) pulse demonstrated a more than three times decrease which is consistent with the pressure relaxation inside the discharge channel.
- H_α profile observed under the third (positive) HV pulse consists of a two Lorentzian components of 30 nm (FWHM) and 1 nm (FWHM). Two profiles can be attributed to emission from the spatially distinct denser high pressure plasma in newly created channels and the discharge in relaxed channels. No continuum emission is observed in this case.
- Weakly broadened (0.6 nm) hydrogen alpha profile detected under the fourth (positive) pulse is consistent with the pressure relaxation inside the discharge channel
- During the first (positive) discharge H_α profile demonstrates asymmetrical red wing and can be approximated with two shifted Lorentzian profiles. Two Lorentzian functions are ascribed to direct and back discharge inside the discharge channels. Each profile is assumed to be a sum of the combined action of the Stark and the Van der Waals broadening. Based on this assumption we obtained the electron density equal to $1.3*10^{26}\ m^{-3}$ for the direct discharge and $2*10^{25}\ m^{-3}$ for the back discharge.
- Because of long time of acquisition comparing to formative time of the discharge channel obtained electron densities seem to be

rather approximative. Time resolved measurement have to be done in the future

A systematic parametric investigation of several classes of polar and non-polar liquids under nanosecond pulse with variable amplitude and rising time should be done in the future to calibrate the models. The precise differential measurements of discharge current would help to discern between purely hydrodynamic phenomena and processes driven by active current. Scaling down to nanometer size electrodes (Staack *et al* 2008) seems to have a great potential application in growing field of plasma medicine and for industrial use in chemical modification of liquid hydrocarbons.

8.2 DBD plasma induced cell death mediated by production of ROS in cell medium

In the framework of this thesis two collaboration were established with the group working on cancer pathophysiology (Hopital St Louis, Inserm UMR-S 728) and group studying the role of ROS in radiocancerogenesis (UMR 8200).

DBD device: Nanosecond dielectric barrier discharge was specifically designed for in-vitro and in-vivo cell treatment. Developed DBD produce rather uniform plasma without substantial gas heating allow precise control of energy input. The typical energy dissipated in plasma was about 18 mJ for one pulse and did not depend on the frequency in the range 100 – 900 Hz.

DBD treatment of living cells (Hopital St Louis)

- For in-vitro tests flowcytometry based cell viability assay with two markers AnnexinV and Propidium iodide (PI) was applied 5 and 24 h after exposure to plasma. In-vitro treatment of cultured Jurkat and HMEC cells demonstrated a dose dependent induction of apoptosis at doses up to 250 J/cm for circulating

Jurkat cells and 340 J/cm for adherent HMEC. At higher doses a pattern was mostly necrotic.

- In vivo, on hematoxylin-eosin sections, significant lesions appeared for doses above 113 J/cm² for the epidermis, 281 J/cm² for the dermis, and 394 J/cm² for the hypodermis and muscle. Thus, the higher the dose, the deeper is the effect in the tissue. On the epidermis, pathological analysis on ultra-thin sections was consistent with apoptosis for medium doses (113 J/cm²) and necrosis for higher doses (281 J/cm²).

Study of mechanisms (IGR)

- In order to determine the effect of ROS on cell viability the quantitative dosage of H_2O_2 was performed using Amplex Red and Horseradish peroxidase in phosphate buffered saline with MgCO3 and CaCO3 (PBS $Mg^{2+}Ca^{2+}$) directly exposed to nanosecond DBD plasma. Plasma treatment resulted in reproducible and dose dependent production of hydrogen peroxide in the range 10 – 2000 µM for plasma doses between 14 and 1600 J/ml. For standard 6 and 24 well plates with respectively 2 ml and 300 µl of medium H2O2 production was determined mainly by volumetric power density.
- It is found that plasma induced cell death of normal HTori-3 cells is mediated by extracellularly produced hydrogen peroxide. The addition of 400 U/ml of catalase in the medium before the plasma treatment completely protects the cells. Preincubation of cells with DPI shows that metabolically produced ROS and ROS released in response to oxidative stress contribute additively with plasma generated H_2O_2 in the overall cytotoxic effect.
- Test done with cancerous melanoma Lu1205 cells demonstrated that almost 80% of the cells die after plasma dose of 30 J/ml which is equivalent to extracellular hydrogen peroxide concentration of 40 µM. AnnexinV – Propidium iodide labeling suggests that cells are dying by apoptosis. The role of electric field is elucidated by indirect treatment consisted in exposure to plasma of culture medium (PBS) without cells and then drop of

treated medium on the cells. Indirect treatment results in poorer cytotoxicity which accentuated the role of nanosecond electric field in eventual cellular membrane permeabilization. It is demonstrated that exposure of the cells to equivalent doses of hydrogen peroxide obtained from standard solution results equally in lower cytotoxicity which points to the role of nitrogen reactive species (RNS) and change in pH.

- Obtained results demonstrate the primary role of plasma generated reactive oxygen species (ROS) in the cytotoxic effect. In the case of cells treatment in the liquid medium the main ROS produced is H_2O_2. The electric field seems to play a role in H_2O_2 inside the cells by creating a transient pores in the cell membrane. Other ROS and RNOS, i.e. peroxynitrite and nitrate, presumably contribute to acidification of culture medium. Those species have to be identified in the future.

8.3 Perspectives

Discharges in liquids

Despite the long history of research in the field of electrical discharges in liquid; many fundamental aspects of plasma formation remain unexplained. The quantitative analysis and generalization of existing results is often complicated by strong spread in experimental approaches applied by different research groups. As it was shown in this thesis two different discharge modes can be observed in polar liquids under exactly the same conditions. This observation points to the complexity of physical phenomenon that combines atomic-level ionization and dissociation mechanisms with electro-hydrodynamic, cavitation and phase transition processes occurring on the sub-micronic scale.

A systematic parametric investigation of several classes of polar and non-polar liquids under nanosecond and sub-nanosecond pulses with variable amplitude and rising time should be done in future to calibrate the models. Fast picosecond iCCD cameras and streak cameras could be used in future for more detailed analysis of discharge initiation. The

precise differential measurements of discharge current would be helpful to discern between purely hydrodynamic phenomena and processes driven by active current. One of the big issues in spectroscopic analysis of Submicron electrodes have to be tested for understanding of spatial scale effects on discharge formation. Scaling down to nanometer size electrodes allows remote generation of plasma in liquids (Staack *et al* 2008) and seems to have a great potential application in growing field of plasma medicine and for industrial use in chemical modification of liquid hydrocarbons.

Atmospheric pressure plasma for biomedical applications

Application cold atmospheric plasmas for treatment of living cells and tissues has a great potential as new anticancer therapy (Vandamme *et al* 2010). First prominent results obtained in this thesis and by other authors demonstrated effective induction of apoptosis in treated cells in dose dependent manner. Moreover recent studies demonstrated selectivity of plasma treatment in respect to cancer cells (Zirnheld *et al* 2010).

The primary role of plasma produced ROS, namely H_2O_2, is demonstrated in this thesis. Pulsed nanosecond electric field of DBD is believed to induce formation of nanometer size pores in the cell membrane. However, peroxidation of lipid bilayer can be also responsible for membrane permeabilization.

In the future work other plasma produced ROS and RNOS have to be identified and quantified in extra and intracellular medium. Specially designed molecular probes should be applied in order to separate plasma produced ROS from ROS resulting from cell metabolism. Parametric study has to be done in future in order to clarify the effect of electric field in membrane permeabilization. Long term and by-stander effect of plasma treatment must be considered in the future.

9 Bibliography

Aka-Ngnui T and Beroual A 2001 Bubble dynamics and transition into streamers in liquid dielectrics under a high divergent electric field *J. Phys. D. Appl. Phys.* **34** 1408–12 Online: http://iopscience.iop.org/0022-3727/34/9/318

Albonetti C, Cavallini M, Massi M, Moulin J F and Biscarini F 2005 Electrochemical fabrication of cobalt and nickel tips for scanning tunneling microscopy *J. Vac. Sci. Technol. B Microelectron. Nanom. Struct.* **23** 2564 Online: http://link.aip.org/link/JVTBD9/v23/i6/p2564/s1&Agg=doi

Ameziane-El-Hassani R, Boufraqech M, Lagente-Chevallier O, Weyemi U, Talbot M, Métivier D, Courtin F, Bidart J-M, El Mzibri M, Schlumberger M and Dupuy C 2010 Role of H2O2 in RET/PTC1 chromosomal rearrangement produced by ionizing radiation in human thyroid cells. *Cancer Res.* **70** 4123–32 Online: http://www.ncbi.nlm.nih.gov/pubmed/20424115

An W, Baumung K and Bluhm H 2007 Underwater streamer propagation analyzed from detailed measurements of pressure release *J. Appl. Phys.* **101** 053302 Online: http://link.aip.org/link/JAPIAU/v101/i5/p053302/s1&Agg=doi

Arvengas A, Herbert E, Cersoy S, Davitt K and Caupin F 2011 Cavitation in heavy water and other liquids. *J. Phys. Chem. B* **115** 14240–5 Online: http://www.ncbi.nlm.nih.gov/pubmed/21988220

Bårmann P, Kröll S and Sunesson A 1997 Spatially and temporally resolved electron density measurements in streamers in dielectric liquids *J. Phys. D. Appl. Phys.* **30** 856–63 Online: http://iopscience.iop.org/0022-3727/30/5/018

BD Biosciences 2006 BD FACSCanto II Flow Cytometer *Ref. Man.* 158

Beebe S J, Fox P M, Rec L J, Willis E L K and Schoenbach K H 2003 Nanosecond, high-intensity pulsed electric fields induce apoptosis in human cells. *FASEB J.* **17** 1493–5 Online: http://www.ncbi.nlm.nih.gov/pubmed/12824299

Beroual a. 1993 Electronic and gaseous processes in the prebreakdown phenomena of dielectric liquids *J. Appl. Phys.* **73** 4528 Online: http://link.aip.org/link/JAPIAU/v73/i9/p4528/s1&Agg=doi

Beroual A 1992 Behavior of charged and uncharged bubbles in dielectric liquids subjected to electric stress *J. Appl. Phys.* **71** 1142–5

Beroual A, Zahn M and Badent A 1998 Propagation and structure of streamers in liquid dielectrics *IEEE Electr. Insul.* **14** 6–17 Online: http://ieeexplore.ieee.org/xpls/abs_all.jsp?arnumber=662781

Bienert G P, Schjoerring J K and Jahn T P 2006 Membrane transport of hydrogen peroxide. *Biochim. Biophys. Acta* **1758** 994–1003 Online: http://www.ncbi.nlm.nih.gov/pubmed/16566894

Bitbol M, Fellmann P, Zachowski A and Devaux P F 1987 Ion regulation of phosphatidylserine and phosphatidylethanolamine outside-inside translocation in human erythrocytes *Biochim. Biophys. Acta* **904** 268–82 Online: http://www.sciencedirect.com/science/article/pii/0005273687903762

Bluhm H 2006 *Pulsed power systems* (Springer-Verlag) Online: ftp://77.41.96.12/torrent/work/Books/Electronics Collection/Pulsed Power Systems - H. Bluhm (Springer, 2006) WW.pdf

Bolsover S R, Hyams J S, Shephard E A, White H A and Wiedemann C G 2004 *CELL BIOLOGY A Short Course* (Wiley-Liss)

Breton M and Mir L M 2012 Microsecond and Nanosecond Electric Pulses in CancerTreatments *Bioelectromagnetics* **33** 106–23

Briels T M P, Kos J, Winands G J, Veldhuizen E M and Ebert U 2008 Positive and negative streamers in ambient air: measuring diameter, velocity and dissipated energy *J. Phys. D. Appl. Phys.* **41** 234004 Online: http://iopscience.iop.org/0022-3727/41/23/234004

Bruggeman P and Brandenburg R 2013 Atmospheric pressure discharge filaments and microplasmas: physics, chemistry and diagnostics *J. Phys. D. Appl. Phys.* **46** 464001 Online: http://stacks.iop.org/0022-3727/46/i=46/a=464001?key=crossref.c6cee071903fdc61bc7f15a5d1dc9cc8

Bruggeman P, Schram D C, Kong M G and Leys C 2009 Is the Rotational Temperature of OH(A- “X) for Discharges in and in Contact with Liquids a Good Diagnostic for Determining the Gas Temperature? *Plasma Process. Polym.* **6** 751–62 Online: http://doi.wiley.com/10.1002/ppap.200950014

Bruggeman P, Verreycken T, González M Á, Walsh J L, Kong M G, Leys C and Schram D C 2010 Optical emission spectroscopy as a diagnostic for plasmas in liquids: opportunities and pitfalls *J. Phys. D. Appl. Phys.* **43** 124005 Online: http://stacks.iop.org/0022-3727/43/i=12/a=124005?key=crossref.70fd6f76a71be2c78864ed4bc16a12ad

Bunkin N F and Bakum S I 2006 Role of a dissolved gas in the optical breakdown of water *Quantum Electron.* **36** 117–24

Bunkin N F and Bunkin F V 1992 Bubbstons: stable microscopic gas bubbles in very dilute electrolytic solutions *Zh. Eksp. Teor. Fiz.* **101** 271–8

Bunkin N F, Suyazov N V, Shkirin A V, Ignatiev P S and Indukaev K V 2009 Nanoscale structure of dissolved air bubbles in water as studied by measuring the elements of the scattering matrix Nanoscale structure of dissolved air bubbles in water as studied *J. Chem. Phys.* **130** 134308–1–12

Ceccato P, Guaitella O, Shaper L, Graham B and Rousseau a. 2009 Time resolved imaging of a pulsed plasma discharge in water *2009 IEEE Pulsed Power Conf.* 866–71 Online: http://ieeexplore.ieee.org/lpdocs/epic03/wrapper.htm?arnumber=5386375

Chin C F and Yeong F M 2010 Safeguarding entry into mitosis: the antephase checkpoint. *Mol. Cell. Biol.* **30** 22–32 Online: http://www.pubmedcentral.nih.gov/articlerender.fcgi?artid=2798306&tool=pmcentrez&rendertype=abstract

Clément M V, Ponton a and Pervaiz S 1998 Apoptosis induced by hydrogen peroxide is mediated by decreased superoxide anion concentration and reduction of intracellular milieu. *FEBS Lett.* **440** 13–8 Online: http://www.ncbi.nlm.nih.gov/pubmed/9862415

Collins-Underwood J R, Zhao W, Sharpe J G and Robbins M E 2008 NADPH oxidase mediates radiation-induced oxidative stress in rat brain microvascular endothelial cells. *Free Radic. Biol. Med.* **45** 929–38 Online: http://www.pubmedcentral.nih.gov/articlerender.fcgi?artid=2603423&tool=pmcentrez&rendertype=abstract

Cram L and Mullan D 1985 Formation of the H-alpha absorption line in the chromospheres of cool stars *Astrophys. J.* **294** 626–33 Online: http://adsabs.harvard.edu/full/1985ApJ...294..626C

Daleke D L 2003 Regulation of transbilayer plasma membrane phospholipid asymmetry. *J. Lipid Res.* **44** 233–42 Online: http://www.ncbi.nlm.nih.gov/pubmed/12576505

Darzynkiewicz Z, Juan G and Li X 1997 Cytometry in cell necrobiology: analysis of apoptosis and accidental cell death (necrosis). *Cytometry* **27** 1–20 Online: http://www.ncbi.nlm.nih.gov/pubmed/9000580

Dekker A, Reitsma K, Beugeling T, Bantjes A, Feijen J and van Aken W G 1991 Adhesion of endothelial cells and adsorption of serum proteins on gas plasma-treated polytetrafluoroethylene. *Biomaterials* **12** 130–8 Online: http://www.ncbi.nlm.nih.gov/pubmed/1878448

Devins J, Rzad S and Schwabe R 1981 Breakdown and prebreakdown phenomena in liquids *J. Appl. Phys.* **52** 4531–45 Online: http://ieeexplore.ieee.org/xpls/abs_all.jsp?arnumber=5110212

Dobrynin D, Fridman G, Friedman G and Fridman A 2009 Physical and biological mechanisms of direct plasma interaction with living tissue *New J. Phys.* **11** 115020 Online: http://stacks.iop.org/1367-2630/11/i=11/a=115020?key=crossref.518f10daf4439017689fe0b7141d1c29

Dobrynin D, Seepersad Y, Pekker M, Shneider M, Friedman G and Fridman A 2013 Non-equilibrium nanosecond-pulsed plasma generation in the liquid phase (water, PDMS) without bubbles: fast imaging, spectroscopy and leader-type model *J. Phys. D. Appl. Phys.* **46** 105201 Online: http://stacks.iop.org/0022-3727/46/i=10/a=105201?key=crossref.c7b1628a0b7bf94c6265d9acd868896c

Dumitrescu L, Lesaint O and Bonifaci N 2001 Study of streamer inception in cyclohexane with a sensitive charge measurement technique under impulse voltage *J. Electrostat.* **53** 135–46

Ehlbeck J, Schnabel U, Polak M, Winter J, von Woedtke T, Brandenburg R, von dem Hagen T and Weltmann K-D 2011 Low temperature atmospheric pressure plasma sources for microbial decontamination *J. Phys. D. Appl. Phys.* **44** 013002 Online: http://stacks.iop.org/0022-3727/44/i=1/a=013002?key=crossref.0390e970db31e45f99a7ac0921a7d924

Emmert S, Brehmer F, Hänßle H, Helmke A, Mertens N, Ahmed R, Simon D, Wandke D, Maus-Friedrichs W, Däschlein G, Schön M P and Viöl W 2013 Atmospheric pressure plasma in dermatology: Ulcus treatment and much more *Clin. Plasma Med.* Online: http://linkinghub.elsevier.com/retrieve/pii/S2212816612000042

Farazmand B 1961 Study of electric breakdown of liquid dielectrics using Schlieren optical techniques *Br. J. Appl. Phys.* **12** 251–4 Online: http://iopscience.iop.org/0508-3443/12/5/310

Fisher A 2009 Redox signaling across cell membranes *Antioxid. Redox Signal.* **11** 1349–56 Online: http://online.liebertpub.com/doi/abs/10.1089/ars.2008.2378

Foster K W, Moy R L and Fincher E F 2008 Advances in plasma skin regeneration *J. Cosmet. Dermatol.* **7** 169–79

Frayssines P and Bonifaci N 2002 Streamers in liquid nitrogen: characterization and spectroscopic determination of gaseous filament temperature and electron density *J. Phys. D …* **35** 369–77 Online: http://iopscience.iop.org/0022-3727/35/4/313

Fridman G, Friedman G, Gutsol A, Shekhter A B, Vasilets V N and Fridman A 2008 Applied Plasma Medicine *Plasma Process. Polym.* **5** 503–33 Online: http://doi.wiley.com/10.1002/ppap.200700154

Fridman G, Shereshevsky A, Jost M M, Brooks A D, Fridman A, Gutsol A, Vasilets V and Friedman G 2007 Floating Electrode Dielectric Barrier Discharge Plasma in Air Promoting Apoptotic Behavior in Melanoma Skin Cancer Cell Lines *Plasma Chem. Plasma Process.* **27** 163–76 Online: http://link.springer.com/10.1007/s11090-007-9048-4

Fridovich I 1983 Superoxide radical: an endogenous toxicant *Annu. Rev. Pharmacol. Toxicol.* **23** 239–57 Online: http://www.annualreviews.org/doi/pdf/10.1146/annurev.pa.23.040183.001323

Gamaley I a and Klyubin I V 1999 Roles of reactive oxygen species: signaling and regulation of cellular functions. *Int. Rev. Cytol.* **188** 203–55 Online: http://www.ncbi.nlm.nih.gov/pubmed/10208013

Garton C G and Krasucki Z 1964 Bubbles in Insulating Liquids: Stability in an Electric Field *Proc. R. Soc. A Math. Phys. Eng. Sci.* **280** 211–26 Online: http://rspa.royalsocietypublishing.org/cgi/doi/10.1098/rspa.1964.0141

Gavrilov I M, Kukhta V R, Lopatin V V and Petrov P G 1994 Dynamics of prebreakdown phenomena in a uniform field in water *IEEE Trans. Dielectr. Electr. Insul.* **1** 496–502 Online: http://ieeexplore.ieee.org/xpls/abs_all.jsp?arnumber=300293

Geiger R and Staack D 2012 Microsparks Generated by Charged Particles in Dielectric Liquids *GEC* (Austin, Texas)

Gournay P and Lesaint O 1993 A study of the inception of positive streamers in cyclohexane and pentane *J. Phys. D. Appl. Phys.* **26** 1966–74 Online: http://iopscience.iop.org/0022-3727/26/11/019

Halpern B and Gomer R 1969 Field Emission in Liquids *J. Chem. Phys.* **51** 1031 Online: http://link.aip.org/link/?JCP/51/1031/1&Agg=doi

Hamdan A, Audinot J-N, Migot-Choux S, Noel C, Kosior F, Henrion G and Belmonte T 2013 Interaction of Discharges in Heptane with Silicon Covered by a Carpet of Carbon Nanotubes *Adv. Eng. Mater.* **15** 885–92

Hampton M B and Orrenius S 1997 Dual regulation of caspase activity by hydrogen peroxide: implications for apoptosis *FEBS Lett.* **414** 552–6 Online: http://linkinghub.elsevier.com/retrieve/pii/S0014579397010685

Heinlin J, Isbary G, Stolz W, Morfill G, Landthaler M, Shimizu T, Steffes B, Nosenko T, Zimmermann J and Karrer S 2011 Plasma applications in medicine with a special focus on dermatology. *J. Eur. Acad. Dermatol. Venereol.* **25** 1–11 Online: http://www.ncbi.nlm.nih.gov/pubmed/20497290

Helbig V and Kusch H 1972 Broadening and Shift of Magnesium Lines by van der Waals Interaction with Argon Atoms and by Microflelds *Astron. Astrophys.* **20** 299–304 Online: http://medcontent.metapress.com/index/A65RM03P4874243N.pdf

Herbert E, Balibar S and Caupin F 2006 Cavitation pressure in water *Phys. Rev. E* **74** 1–22 Online: http://link.aps.org/doi/10.1103/PhysRevE.74.041603

Hernandez-Avila J L, Bonifaci N and Denat A 1994 Hot electron phenomena in liquid and gaseous Ar and N2 in divergent electric fields *IEEE Trans. Dielectr. Electr. Insul.* **1** Online: http://ieeexplore.ieee.org/xpls/abs_all.jsp?arnumber=300283

Hoentsch M, von Woedtke T, Weltmann K-D and Barbara Nebe J 2012 Time-dependent effects of low-temperature atmospheric-pressure argon plasma on epithelial cell attachment, viability and tight junction formation in vitro *J. Phys. D. Appl. Phys.* **45** 025206 Online: http://stacks.iop.org/0022-3727/45/i=2/a=025206?key=crossref.0c3f3a512f178cf3911d9d9f919a0408

Van der Horst R M, Verreycken T, van Veldhuizen E M and Bruggeman P J 2012 Time-resolved optical emission spectroscopy of nanosecond pulsed discharges in atmospheric-pressure N2 and N2/H2O mixtures *J. Phys. D. Appl. Phys.* **45** 345201 Online: http://stacks.iop.org/0022-3727/45/i=34/a=345201?key=crossref.cc4921bbe7513c0a62d709570703b668

Hutchinson I 2002 *Principles of plasma diagnostics* (Cambridge University Press) Online: http://books.google.com/books?hl=en&lr=&id=pUUZKLR00RIC&oi=fnd&pg=PP1&dq=principles+of+plasma+diagnostics&ots=Wxm55DFF-p&sig=_S22RuayrWKBf8-3Z-QfXlQ06wc

Ingebrigtsen S, Bonifaci N, Denat a and Lesaint O 2008 Spectral analysis of the light emitted from streamers in chlorinated alkane and alkene liquids *J. Phys. D. Appl. Phys.* **41** 235204 Online: http://stacks.iop.org/0022-3727/41/i=23/a=235204?key=crossref.fda66675cf02c75e5ef34005290a292d

Isbary G, Morfill G and Zimmermann J 2011 Cold atmospheric plasma: a successful treatment of lesions in Hailey-Hailey disease *Arch. Dermatol. Res.* **147** 388–90 Online: http://archderm.ama-assn.org/cgi/reprint/147/4/388.pdf

Kalghatgi S, Friedman G, Fridman A and Clyne A M 2010 Endothelial cell proliferation is enhanced by low dose non-thermal plasma through fibroblast growth factor-2 release.

Ann. Biomed. Eng. **38** 748–57 Online: http://www.ncbi.nlm.nih.gov/pubmed/20013154

Katsuki S, Tanaka K, Fudamoto T, Namihira T, Akiyama H and Bluhm H 2006 Shock Waves due to Pulsed Streamer Discharges in Water *Jpn. J. Appl. Phys.* **45** 239–42 Online: http://jjap.jsap.jp/link?JJAP/45/239/

Kattan R, Denat a. and Lesaint O 1989 Generation, growth, and collapse of vapor bubbles in hydrocarbon liquids under a high divergent electric field *J. Appl. Phys.* **66** 4062 Online: http://link.aip.org/link/JAPIAU/v66/i9/p4062/s1&Agg=doi

Keidar M, Walk R, Shashurin a, Srinivasan P, Sandler a, Dasgupta S, Ravi R, Guerrero-Preston R and Trink B 2011 Cold plasma selectivity and the possibility of a paradigm shift in cancer therapy. *Br. J. Cancer* **105** 1295–301 Online: http://www.ncbi.nlm.nih.gov/pubmed/21979421

Kellogg E W and Fridovich I 1975 Superoxide ,Hydrogen Peroxide , and Singlet Oxygen in Lipid Peroxidation by a Xanthine Oxidase System *J. Biol. Chem.* **250** 8812–7

Khan A U and Kasha M 1994 Singlet molecular oxygen in the Haber-Weiss reaction. *Proc. Natl. Acad. Sci. U. S. A.* **91** 12365–7 Online: http://www.pubmedcentral.nih.gov/articlerender.fcgi?artid=45438&tool=pmcentrez&rendertype=abstract

Kim C-H, Bahn J H, Lee S-H, Kim G-Y, Jun S-I, Lee K and Baek S J 2010a Induction of cell growth arrest by atmospheric non-thermal plasma in colorectal cancer cells. *J. Biotechnol.* **150** 530–8 Online: http://www.ncbi.nlm.nih.gov/pubmed/20959125

Kim G J, Kim W, Kim K T and Lee J K 2010b DNA damage and mitochondria dysfunction in cell apoptosis induced by nonthermal air plasma *Appl. Phys. Lett.* **96** 021502 Online: http://link.aip.org/link/APPLAB/v96/i2/p021502/s1&Agg=doi

Kim W, Woo K-C, Kim G-C and Kim K-T 2011 Nonthermal-plasma-mediated animal cell death *J. Phys. D. Appl. Phys.* **44** 013001 Online: http://stacks.iop.org/0022-3727/44/i=1/a=013001?key=crossref.cbc39f182a3236afa063145b48262489

Kogelschatz U 2002 Filamentary , Patterned , and Diffuse Barrier Discharges *IEEE Trans. Plasma Sci.* **30** 1400–8

Korobeinikov S, Melekhov A and Besov A 2002 Breakdown initiation in water with the aid of bubbles *High Temp.* **40** 652–9 Online: http://link.springer.com/article/10.1023/A%3A1020420216579

Krysko D V, Vanden Berghe T, D'Herde K and Vandenabeele P 2008 Apoptosis and necrosis: detection, discrimination and phagocytosis. *Methods* **44** 205–21 Online: http://www.ncbi.nlm.nih.gov/pubmed/18314051

Kuskova N I 2001 Spark discharges in condensed media *Tech. Phys.* **46** 182–5 Online: http://link.springer.com/10.1134/1.1349273

Lakowicz J R 2006 *Principles of Fluorescence Spectroscopy* (Springer)

Latimer P 1982 Light scattering and absorption as methods of studying cell population parameters *Annu. Rev. Biophys. Bioeng.* **11** 129–50 Online: http://www.annualreviews.org/doi/abs/10.1146/annurev.bb.11.060182.001021

Laux C O, Spence T G, Kruger C H and Zare R N 2003 Optical diagnostics of atmospheric pressure air plasmas *Plasma Sources Sci. Technol.* **12** 125–38 Online: http://stacks.iop.org/0963-0252/12/i=2/a=301?key=crossref.c1d6e6ee041199344a20baea814fcdac

Leduc M, Guay D, Leask R L and Coulombe S 2009 Cell permeabilization using a non-thermal plasma *New J. Phys.* **11** 115021 Online: http://stacks.iop.org/1367-2630/11/i=11/a=115021?key=crossref.1593ad46563317de62c58b469ef06ff0

Lee H J, Shon C H, Kim Y S, Kim S, Kim G C and Kong M G 2009 Degradation of adhesion molecules of G361 melanoma cells by a non-thermal atmospheric pressure microplasma *New J. Phys.* **11** 115026 Online: http://stacks.iop.org/1367-2630/11/i=11/a=115026?key=crossref.464c2e3717ce437220e44bf349cd334b

Lesaint O and Gournay P 1994a Initiation and propagation thresholds of positive prebreakdown phenomena in hydrocarbon liquids *IEEE Trans. Dielectr. Electr. Insul.* **1** 702–8 Online: http://ieeexplore.ieee.org/lpdocs/epic03/wrapper.htm?arnumber=311713

Lesaint O and Gournay P 1994b On the gaseous nature of positive filamentary streamers in hydrocarbon liquids. I: Influence of the hydrostatic pressure on the propagation *J. Phys. D. Appl. Phys.* **27** 2111–6 Online: http://iopscience.iop.org/0022-3727/27/10/019

Lesaint O and Jung M 2000 On the relationship between streamer branching and propagation in liquids: influence of pyrene in cyclohexane *J. Phys. D. Appl. Phys.* **33** 1360–8 Online: http://iopscience.iop.org/0022-3727/33/11/315

Lewis T J 1998 A new model for the primary process of electrical breakdown in liquids *IEEE Trans. Dielectr. Electr. Insul.* **5** 306–15 Online: http://ieeexplore.ieee.org/lpdocs/epic03/wrapper.htm?arnumber=689419

Lewis T J 2003 Breakdown initiating mechanisms at electrode interfaces in liquids *IEEE Trans. Dielectr. Electr. Insul.* **10** 948–55 Online: http://ieeexplore.ieee.org/lpdocs/epic03/wrapper.htm?arnumber=1255771

Li a. E, Ito H, Rovira I I, Kim K-S, Takeda K, Yu Z-Y, Ferrans V J and Finkel T 1999 A Role for Reactive Oxygen Species in Endothelial Cell Anoikis *Circ. Res.* **85** 304–10 Online: http://circres.ahajournals.org/cgi/doi/10.1161/01.RES.85.4.304

Li Y and Trush M a 1998 Diphenyleneiodonium , an NAD(P)H Oxidase Inhibitor , also Potently Inhibits Mitochondrial Reactive Oxygen Species Production *Biochem. Biophys. Res. Commun.* **253** 295–9 Online: http://www.ncbi.nlm.nih.gov/pubmed/9878531

Lide D R 2005 *CRC handbook of chemistry und physics* vol 2003 (CRC Press) Online: http://www.hbcpnetbase.com

Lisitsyn I V, Nomlyama H, Katsuki S and Akiyama H 1999 Thermal processes in a streamer discharge in water *IEEE Trans. Dielectr. Electr. Insul.* **6** 351–6 Online: http://ieeexplore.ieee.org/xpls/abs_all.jsp?arnumber=775622

Lu X, Cao Y, Yang P and Xiong Q 2009 An RC plasma device for sterilization of root canal of teeth *IEEE Trans. Plasma Sci.* **37** 668–73 Online: http://dee.hust.edu.cn/plasma/pdf/2009/J-TPS-An RC Plasma Device for Sterilization of Root Canal of Teeth.pdf

Luque A, Ratushnaya V and Ebert U 2008 Positive and negative streamers in ambient air: modelling evolution and velocities *J. Phys. D. Appl. Phys.* **41** 234005 Online: http://stacks.iop.org/0022-3727/41/i=23/a=234005?key=crossref.b6c5e6259f2a7c9b1cddeb7a6690262c

Malik M A, Ghaffar A and Malik S A 2001 Water purification by electrical discharges *Plasma Sources Sci. Technol.* **10** 82–91 Online: http://stacks.iop.org/0963-0252/10/i=1/a=311?key=crossref.c7c482e5bb00b582d51382d67603f310

Marinov I, Guaitella O, Rousseau A and Starikovskaia S M 2013 Modes of underwater discharge propagation in a series of nanosecond successive pulses *J. Phys. D. Appl. Phys.* **46** 1–9 Online: http://stacks.iop.org/0022-3727/46/i=46/a=464013?key=crossref.a5393802b655a72a6029ae0920cd62da

Massines F, Gherardi N, Naudé N and Ségur P 2009 Recent advances in the understanding of homogeneous dielectric barrier discharges *Eur. Phys. J. Appl. Phys.* **47** 22805 Online: http://www.epjap.org/10.1051/epjap/2009064

McKenny P and McGrath P 1984 Anomalous positive point prebreakdown behavior in dielectric liquids *IEEE Trans. Electr. Insul.* **EI-19** 93–100 Online: http://ieeexplore.ieee.org/xpls/abs_all.jsp?arnumber=4081203

Melo F De, Molognoni F and Jasiulionis M 2013 The Role of Oxidative Stress in Melanoma Development, Progression and Treatment *Recent Advances in the Biology, Therapy and Management of Melanoma* ed L M Davids (InTech) p 375 Online: http://dx.doi.org/10.5772/46052

Menashi W P 1968 Treatment of surfaces *US Pat. 2,337,329* Online: http://www.google.com/patents?hl=en&lr=&vid=USPAT2337329&id=3T5YAAAAEBAJ&oi=fnd&dq=Treatment+of+surfaces&printsec=abstract

Metzger G and Vabre J-P 1969 *Transmission lines with pulse excitation* (Academic Press) Online: http://www.sciencedirect.com.sci-hub.org/science/book/9780124930506

Monici M 2005 Cell and tissue autofluorescence research and diagnostic applications *Biotechnol. Annu. Rev.* **11** 227–56

Morrison J 1977 Electrosurgical method and apparatus for initiating an electrical discharge in an inert gas flow *US Pat. 4,040,426* Online: http://www.google.com/patents?hl=en&lr=&vid=USPAT4040426&id=hJosAAAAEBAJ&oi=fnd&dq=Electrosurgical+method+and+apparatus+for+initiating+an+electrical+discharge+in+an+inert+gas+flow&printsec=abstract

Nagayama K, Mori Y, Shimada K and Nakahara M 2002 Shock Hugoniot compression curve for water up to 1 GPa by using a compressed gas gun *J. Appl. Phys.* **91** 476 Online: http://link.aip.org/link/JAPIAU/v91/i1/p476/s1&Agg=doi

Namihira T and Sakai S 2007 Electron temperature and electron density of underwater pulsed discharge plasma produced by solid-state pulsed-power generator *IEEE Trans. Plasma Sci.* **35** 614–8 Online: http://ieeexplore.ieee.org/xpls/abs_all.jsp?arnumber=4237270

Naugolnykh K A and Roy N A 1974 *Elecfrical Discharges in Water. A Hydrodynamic Description* (translated from Russian)

Nieto-Salazar J, Bonifaci N, Denat A and Lesaint O 2005 Characterization and spectroscopic study of positive streamers in water *International Conference on Dielectric Liquids (ICDL)* (IEEE) pp 89–92 Online: http://ieeexplore.ieee.org/lpdocs/epic03/wrapper.htm?arnumber=1490034

Nuccitelli R, Chen X, Pakhomov A G, Baldwin W H, Sheikh S, Pomicter J L, Ren W, Osgood C, Swanson R J, Kolb J F, Beebe S J and Schoenbach K H 2009 A new pulsed electric field therapy for melanoma disrupts the tumor's blood supply and causes

complete remission without recurrence. *Int. J. Cancer* **125** 438–45 Online: http://www.pubmedcentral.nih.gov/articlerender.fcgi?artid=2731679&tool=pmcentrez&rendertype=abstract

Ochkin V N 2009 *Spectroscopy of Low Temperature Plasma* (Berlin: Wiley-VCH)

Oehmigen K, Hähnel M, Brandenburg R, Wilke C, Weltmann K-D and von Woedtke T 2010 The Role of Acidification for Antimicrobial Activity of Atmospheric Pressure Plasma in Liquids *Plasma Process. Polym.* **7** 250–7 Online: http://doi.wiley.com/10.1002/ppap.200900077

Pai D Z, Lacoste D a. and Laux C O 2010 Transitions between corona, glow, and spark regimes of nanosecond repetitively pulsed discharges in air at atmospheric pressure *J. Appl. Phys.* **107** 093303 Online: http://link.aip.org/link/JAPIAU/v107/i9/p093303/s1&Agg=doi

Pakhomov A G, Bowman A M, Ibey B L, Andre F M, Pakhomova O N and Schoenbach K H 2009 Lipid nanopores can form a stable, ion channel-like conduction pathway in cell membrane. *Biochem. Biophys. Res. Commun.* **385** 181–6 Online: http://www.pubmedcentral.nih.gov/articlerender.fcgi?artid=2739132&tool=pmcentrez&rendertype=abstract

Pankov R and Yamada K M 2002 Fibronectin at a glance *J. Cell Sci.* **115** 3861–3 Online: http://jcs.biologists.org/cgi/doi/10.1242/jcs.00059

Paris P, Aints M, Valk F, Plank T, Haljaste A, Kozlov V K and Wagner H-E 2005 Intensity ratio of spectral bands of nitrogen as a measure of electric field strength in plasmas *J. Phys. D. Appl. Phys.* **38** 3894–9

Poling B E, Prausnitz J M and O'Connell J P 2001 *The properties of gases and liquids* (McGraw-Hill) Online: http://www.osti.gov/energycitations/product.biblio.jsp?osti_id=6504847

Pryor W 1986 Oxy-radicals and related species: their formation, lifetimes, and reactions *Annu. Rev. Physiol.* **48** 657–67 Online: http://www.annualreviews.org/doi/pdf/10.1146/annurev.ph.48.030186.003301

Qian J, Joshi R P, Kolb J, Schoenbach K H, Dickens J, Neuber A, Butcher M, Cevallos M, Krompholz H, Schamiloglu E and Gaudet J 2005 Microbubble-based model analysis of liquid breakdown initiation by a submicrosecond pulse *J. Appl. Phys.* **97** Online: http://link.aip.org/link/JAPIAU/v97/i11/p113304/s1&Agg=doi

Reuter S, Tresp H, Wende K, Hammer M U, Winter J, Masur K, Schmidt-Bleker A and Weltmann K-D 2012 From RONS to ROS: Tailoring Plasma Jet Treatment of Skin

Cells *IEEE Trans. Plasma Sci.* **40** 2986–93 Online: http://ieeexplore.ieee.org/lpdocs/epic03/wrapper.htm?arnumber=6269937

Robert E, Barbosa E, Dozias Sã©, Vandamme M, Cachoncinlle C, Viladrosa R and Pouvesle J M 2009 Experimental Study of a Compact Nanosecond Plasma Gun *Plasma Process. Polym.* NA–NA Online: http://doi.wiley.com/10.1002/ppap.200900078

Sakamoto S and Yamada H 1980 Optical study of conduction and breakdown in dielectric liquids *IEEE Trans. Electr. Insul.* **EI-15** Online: http://ieeexplore.ieee.org/xpls/abs_all.jsp?arnumber=4080725

Sakiyama Y, Graves D B, Chang H, Shimizu T and Morfill G E 2012 Plasma chemistry model of surface microdischarge in humid air and dynamics of reactive neutral species *J. Phys. D. Appl. Phys.* **45**

Sato M 1996 Formation of chemical species and their effects on microorganisms using a pulsed high-voltage discharge in water *IEEE Ind. Appl.* **32** 106–12 Online: http://ieeexplore.ieee.org/xpls/abs_all.jsp?arnumber=485820

Sensenig R, Kalghatgi S, Cerchar E, Fridman G, Shereshevsky A, Torabi B, Arjunan K P, Podolsky E, Fridman A, Friedman G, Azizkhan-Clifford J and Brooks A D 2011a Non-thermal plasma induces apoptosis in melanoma cells via production of intracellular reactive oxygen species. *Ann. Biomed. Eng.* **39** 674–87 Online: http://www.pubmedcentral.nih.gov/articlerender.fcgi?artid=3268344&tool=pmcentrez&rendertype=abstract

Sensenig R, Kalghatgi S, Cerchar E, Fridman G, Shereshevsky A, Torabi B, Arjunan K P, Podolsky E, Fridman A, Friedman G, Azizkhan-Clifford J and Brooks A D 2011b Non-thermal plasma induces apoptosis in melanoma cells via production of intracellular reactive oxygen species. *Ann. Biomed. Eng.* **39** 674–87 Online: http://www.pubmedcentral.nih.gov/articlerender.fcgi?artid=3268344&tool=pmcentrez&rendertype=abstract

Shneider M N and Pekker M 2013a Cavitation in dielectric fluid in inhomogeneous pulsed electric field *J. Appl. Phys.* **114** 214906 Online: http://link.aip.org/link/JAPIAU/v114/i21/p214906/s1&Agg=doi

Shneider M N and Pekker M 2013b Dielectric Fluid in Inhomogeneous Pulsed Electric Field *Phys. Rev. E* **87** 1–7

Shneider M N, Pekker M and Fridman A 2012 Theoretical study of the initial stage of sub-nanosecond pulsed breakdown in liquid dielectrics *IEEE Trans. Dielectr. Electr. Insul.* **19** 1579–82 Online: http://ieeexplore.ieee.org/lpdocs/epic03/wrapper.htm?arnumber=6311503

Silve A, Leray I and Mir L M 2012 Demonstration of cell membrane permeabilization to medium-sized molecules caused by a single 10 ns electric pulse. *Bioelectrochemistry* **87** 260–4 Online: http://www.ncbi.nlm.nih.gov/pubmed/22074790

Silver I A 1975 Measurement of PH and Ionic Composition of Pericellular Sites *Philos Trans R Soc L. B Biol Sci.* **271** 261–72 Online: http://rstb.royalsocietypublishing.org/content/271/912/261.short

Sretenović G B, Krstić I B, Kovačević V V., Obradović B M and Kuraica M M 2011 Spectroscopic measurement of electric field in atmospheric-pressure plasma jet operating in bullet mode *Appl. Phys. Lett.* **99** 161502 Online: http://link.aip.org/link/APPLAB/v99/i16/p161502/s1&Agg=doi

Staack D, Fridman A, Gutsol A, Gogotsi Y and Friedman G 2008 Nanoscale corona discharge in liquids, enabling nanosecond optical emission spectroscopy. *Angew. Chem. Int. Ed. Engl.* **47** 8020–4 Online: http://www.ncbi.nlm.nih.gov/pubmed/18756561

Stacey M, Stickley J, Fox P, Statler V, Schoenbach K, Beebe S . and Buescher S 2003 Differential effects in cells exposed to ultra-short, high intensity electric fields: cell survival, DNA damage, and cell cycle analysis *Mutat. Res. Toxicol. Environ. Mutagen.* **542** 65–75 Online: http://linkinghub.elsevier.com/retrieve/pii/S1383571803002328

Stalder K R and Woloszko J 2007 Some Physics and Chemistry of Electrosurgical Plasma Discharges *Contrib. to Plasma Phys.* **47** 64–71 Online: http://doi.wiley.com/10.1002/ctpp.200710010

Starikovskiy A 2013 Pulsed nanosecond discharge development in liquids with various dielectric permittivity constants *Plasma Sources Sci. Technol.* **22** 012001 Online: http://stacks.iop.org/0963-0252/22/i=1/a=012001?key=crossref.75d3057593f7fd56a923db4c96e8cb36

Starikovskiy A, Yang Y, Cho Y I and Fridman A 2011 Non-equilibrium plasma in liquid water: dynamics of generation and quenching *Plasma Sources Sci. Technol.* **20** 024003 Online: http://stacks.iop.org/0963-0252/20/i=2/a=024003?key=crossref.67ab7f8b2adcbc4c51e30652f96192ae

Stoffels E, Kieft I and Sladek R 2003 Superficial treatment of mammalian cells using plasma needle *J. Phys. D Appl. …* **36** Online: http://iopscience.iop.org/0022-3727/36/23/007

Sun P, Pan J, Tian Y and Bai N 2010 Tooth whitening with hydrogen peroxide assisted by a direct-current cold atmospheric-pressure air plasma microjet *IEEE Trans. Plasma Sci.* **38** 1892–6 Online: http://ieeexplore.ieee.org/xpls/abs_all.jsp?arnumber=5409600

Sunka P, Babický V and Clupek M 1999 Generation of chemically active species by electrical discharges in water *Plasma Sources Sci. Technol.* **8** 258–65 Online: http://iopscience.iop.org/0963-0252/8/2/006

Sunka P, Stelmashuk V, Benes J, Pouckova P and Kralova J 2007 POTENTIAL APPLICATIONS OF TANDEM SHOCK WAVES IN CANCERS THERAPY *IEEE Pulsed Power Conference* pp 1074–7

Suresh S J, Satish A V and Choudhary A 2006 Influence of electric field on the hydrogen bond network of water. *J. Chem. Phys.* **124** 74506 Online: http://www.ncbi.nlm.nih.gov/pubmed/16497056

Tahmasebipour G, Hojjat Y, Ahmadi V and Abdullah a 2009 Effect of fabrication process parameters on the apex-radius of STM tungsten nanotip. *Scanning* **31** 65–74 Online: http://www.ncbi.nlm.nih.gov/pubmed/19191264

Tamada Y and Ikada Y 1993 Cell adhesion to plasma-treated polymer surfaces *Polymer (Guildf).* **34** 2208–12 Online: http://linkinghub.elsevier.com/retrieve/pii/003238619390752V

Tao S, Kaihua L, Cheng Z, Ping Y, Shichang Z and Ruzheng P 2008 Experimental study on repetitive unipolar nanosecond-pulse dielectric barrier discharge in air at atmospheric pressure *J. Phys. D. Appl. Phys.* **41** 215203 Online: http://stacks.iop.org/0022-3727/41/i=21/a=215203?key=crossref.8cc358606d58d54fd7b56c5eed0c9415

Thannickal V and Fanburg B 2000 Reactive oxygen species in cell signaling *Am. J. Physiol. - Lung Cell. Mol. Physiol.* **279** 1005–28 Online: http://ajplung.physiology.org/content/279/6/L1005.short

Ushakov V Y, Klimkin V F and Korobeynikov S M 2007 *Impulse Breakdown of Liquids* (Berlin Heidelberg New York: Springer)

Vallee P, Lafait J, Legrand L, Mentre P, Monod M-O and Thomas Y 2005 Effects of Pulsed Low-Frequency Electromagnetic Fields on Water Characterized by Light Scattering Techniques : Role of Bubbles *Langmuir* **21** 2293–9

Vandamme M, Robert E, Lerondel S, Sarron V, Ries D, Dozias S, Sobilo J, Gosset D, Kieda C, Legrain B, Pouvesle J-M and Pape A Le 2012 ROS implication in a new antitumor strategy based on non-thermal plasma. *Int. J. Cancer* **130** 2185–94 Online: http://www.ncbi.nlm.nih.gov/pubmed/21702038

Vandamme M, Robert E, Pesnel S, Barbosa E, Dozias S, Sobilo J, Lerondel S, Le Pape A and Pouvesle J-M 2010 Antitumor Effect of Plasma Treatment on U87 Glioma

Xenografts: Preliminary Results *Plasma Process. Polym.* **7** 264–73 Online: http://doi.wiley.com/10.1002/ppap.200900080

Vegiri A 2004 Reorientational relaxation and rotational–translational coupling in water clusters in a d.c. external electric field *J. Mol. Liq.* **110** 155–68 Online: http://linkinghub.elsevier.com/retrieve/pii/S0167732203002447

Vernier P T, Sun Y, Marcu L, Salemi S, Craft C M and Gundersen M a 2003 Calcium bursts induced by nanosecond electric pulses *Biochem. Biophys. Res. Commun.* **310** 286–95 Online: http://linkinghub.elsevier.com/retrieve/pii/S0006291X03017601

Volotskova O, Hawley T S, Stepp M a and Keidar M 2012 Targeting the cancer cell cycle by cold atmospheric plasma. *Sci. Rep.* **2** 636 Online: http://www.pubmedcentral.nih.gov/articlerender.fcgi?artid=3434394&tool=pmcentrez&rendertype=abstract

Watson P K and Chadband W G 1988 The dynamics of pre-breakdown cavities in viscous silicone fluids in negative point-plane gaps *IEEE Trans. Electr. Insul.* **23** 729–38 Online: http://ieeexplore.ieee.org/lpdocs/epic03/wrapper.htm?arnumber=7346

Weaver J C, Smith K C, Esser A T, Son R S and Gowrishankar T R 2012 A brief overview of electroporation pulse strength-duration space: a region where additional intracellular effects are expected. *Bioelectrochemistry* **87** 236–43 Online: http://www.ncbi.nlm.nih.gov/pubmed/22475953

Weltmann K D, Kindel E, von Woedtke T, Hähnel M, Stieber M and Brandenburg R 2010 Atmospheric-pressure plasma sources: Prospective tools for plasma medicine *Pure Appl. Chem.* **82** 1223–37 Online: http://iupac.org/publications/pac/82/6/1223/

Weltmann K-D, Polak M, Masur K, von Woedtke T, Winter J and Reuter S 2012 Plasma Processes and Plasma Sources in Medicine *Contrib. to Plasma Phys.* **52** 644–54 Online: http://doi.wiley.com/10.1002/ctpp.201210061

Weyemi U and Dupuy C 2012 The emerging role of ROS-generating NADPH oxidase NOX4 in DNA-damage responses. *Mutat. Res.* **751** 77–81 Online: http://www.ncbi.nlm.nih.gov/pubmed/22580379

Wu A S, Kalghatgi S, Dobrynin D, Sensenig R, Cerchar E, Podolsky E, Dulaimi E, Paff M, Wasko K, Arjunan K P, Garcia K, Fridman G, Balasubramanian M, Ownbey R, Barbee K a, Fridman A, Friedman G, Joshi S G and Brooks A D 2013 Porcine intact and wounded skin responses to atmospheric nonthermal plasma. *J. Surg. Res.* **179** e1–e12 Online: http://www.ncbi.nlm.nih.gov/pubmed/22480830

Yu Q S, Li H, Ritts A C, Yang B, Chen M, Hong L, Xu C, Yao X and Wang Y 2012 Plasma for Bio-Decontamination, Medicine and Food Security *Plasma for Bio-*

Decontamination, Medicine and Food Security ed Z Machala, K Hensel and Y Akishev (Dordrecht: Springer Netherlands) pp 215–28 Online: http://www.springerlink.com/index/10.1007/978-94-007-2852-3

Zhang X, Li M, Zhou R, Feng K and Yang S 2008 Ablation of liver cancer cells in vitro by a plasma needle *Appl. Phys. Lett.* **93** 021502 Online: http://link.aip.org/link/APPLAB/v93/i2/p021502/s1&Agg=doi

Zirnheld J L, Zucker S N, Disanto T M, Berezney R and Etemadi K 2010 Nonthermal Plasma Needle : Development and Targeting of Melanoma Cells *IEEE Trans. Plasma Sci.* **38** 948–52

Zucker S N, Zirnheld J, Bagati A, DiSanto T M, Des Soye B, Wawrzyniak J a, Etemadi K, Nikiforov M and Berezney R 2012 Preferential induction of apoptotic cell death in melanoma cells as compared with normal keratinocytes using a non-thermal plasma torch. *Cancer Biol. Ther.* **13** 1299–306 Online: http://www.ncbi.nlm.nih.gov/pubmed/22895073

10 Annex

10.1 Composition of commercial culture media

Dulbecco's phosphate buffered saline with $MgCl_2$,$CaCl_2$ (D-PBS Mg^{2+} Ca^{2+})

Components	Molecular Weight	Concentration (mg/L)	mM
Inorganic Salts			
Calcium Chloride (CaCl2) (anhyd.)	111	100	0.90 1
Magnesium Chloride (MgCl2-6H2O)	203	100	0.49 3
Potassium Chloride (KCl)	75	200	2.67
Potassium Phosphate monobasic (KH2PO4)	136	200	1.47
Sodium Chloride (NaCl)	58	8000	138
Sodium Phosphate dibasic (Na2HPO4-7H2O)	268	2160	8.06

Roswell Park Memorial Institute (RPMI 1640 w/o phenol red)

Components	Molecular Weight	Concentration (mg/L)	mM
Amino Acids			
Glycine	75	10	0.133
L-Arginine	174	200	1.15
L-Asparagine	132	50	0.379
L-Aspartic acid	133	20	0.15
L-Cystine 2HCl	313	65	0.208
L-Glutamic Acid	147	20	0.136
L-Glutamine	146	300	2.05
L-Histidine	155	15	0.0968

L-Hydroxyproline	131	20	0.153
L-Isoleucine	131	50	0.382
L-Leucine	131	50	0.382
L-Lysine hydrochloride	183	40	0.219
L-Methionine	149	15	0.101
L-Phenylalanine	165	15	0.0909
L-Proline	115	20	0.174
L-Serine	105	30	0.286
L-Threonine	119	20	0.168
L-Tryptophan	204	5	0.0245
L-Tyrosine disodium salt dihydrate	261	29	0.111
L-Valine	117	20	0.171
Vitamins			
Biotin	244	0.2	0.00082
Choline chloride	140	3	0.0214
D-Calcium pantothenate	477	0.25	0.000524
Folic Acid	441	1	0.00227
Niacinamide	122	1	0.0082
Para-Aminobenzoic Acid	137	1	0.0073
Pyridoxine hydrochloride	206	1	0.00485
Riboflavin	376	0.2	0.000532
Thiamine hydrochloride	337	1	0.00297
Vitamin B12	1355	0.005	0.0000037
i-Inositol	180	35	0.194
Inorganic Salts			
Calcium nitrate (Ca(NO3)2 4H2O)	236	100	0.424
Magnesium Sulfate (MgSO4) (anhyd.)	120	48.84	0.407
Potassium Chloride (KCl)	75	400	5.33
Sodium Bicarbonate (NaHCO3)	84	2000	23.81
Sodium Chloride (NaCl)	58	6000	103.45

Sodium Phosphate dibasic (Na2HPO4) anhydrous	142	800	5.63
Other Components			
D-Glucose (Dextrose)	180	2000	11.11
Glutathione (reduced)	307	1	0.00326